Investigation of polyetherimide's thermal degradation and fabrication of thermal end-of-life sensor for fire protective clothing

by

Chungyeon Cho

A thesis submitted in partial fulfillment of the requirements for the degree of

Doctor of Philosophy

In

Materials Engineering

Department of Chemical and Materials Engineering
University of Alberta

Abstract

Typically, protective clothing are made of materials that have a high temperature resistance, good mechanical and chemical properties. However, some high-performance textiles – including those used in protective clothing – age silently, undergoing a gradual reduction in their protective properties. In order to estimate the lifetime of protective clothing, especially for fire fighters, this dissertation proposes a non-destructive method to monitor the aging level of outer shell fabrics. It is hypothesized that an electrically conducting layer that loses its conductivity systematically under aging conditions can be used as the basis for an end-of-life-sensor for textiles. This sensor is fixed as a patch on the fire protective clothing; the mechanism of sensing is based on the loss of conductivity of a graphene layer on a high temperature resistant polymer during thermal aging. This sensor also can be used to monitor the condition of polymeric materials under extreme environments.

The first study introduced a simple method to prepare conductive tracks on a meta-aramid woven fabric using reduced graphene oxide (rGO). The simple "dip and dry coating" method was used to coat rGO on a meta-aramid fabric. While 15 iterations of rGO coating cycles were needed to completely wrap each m-aramid fiber with rGO sheets, 10 cycles were sufficient to establish electrical conductivity. This conductivity remained stable for up to 10 laboratory wash cycles. The conductivity of these rGO coated fabrics also remained stable during immersion in water. Furthermore, a fabrication protocol was developed for patterning both single- and two-sided rGO tracks on the m-aramid fabric. Assessment with a Martindale abrasion tester revealed that the single-sided rGO-track lost its conductivity after 150 abrasion cycles, whereas the two-sided rGO-tracks survived 3000 abrasion cycles. These results demonstrate that a simple rGO coating technique can be used to prepare end-of-life sensors for high-performance textiles.

In a second study, the selection of a high temperature resistant polymer for use in a thermal end-of-life sensor was performed. Polyetherimide (PEI) was chosen since it has a similar thermal degradation behavior as m-aramid fibers. This study investigated the thermal aging behavior of PEI at elevated temperatures. During thermal aging, PEI underwent a change in both its mechanical and chemical properties. Crosslinking and chain scission reactions took place in the PEI specimens, which in turn affected the ultimate tensile strength (UTS), functional groups, and glass transition (T_g) temperature. Furthermore, cracks formed on the PEI surface and propagated during aging, likely due to chain scission. The UTS was used to construct a time-temperature-superposition master curve. The activation energy corresponding to the decrease in the UTS was calculated to be 112 kJ/mol.

The third study proposed a design for a thermal aging sensor for fire protective clothing. A conducting layer was formed by laser irradiation to convert the top layer of a PEI film into graphite, creating a laser-induced-graphene (LIG) layer. The electrical conductivity of this graphitic layer decreased during aging at temperatures above the glass transition of PEI. At temperatures below PEI's T_g, the electrical resistance of the LIG layer was observed to decrease due to contact annealing. This sensor showed a stable response over 10 heating and cooling cycles. Finally, the washing stability of this sensor was assessed over 10 washing cycles; the results suggest the need for a better encapsulation strategy.

Overall, this dissertation explores a novel non-destructive method to monitor the level of thermal aging of high performance fabrics. The washing stability of the sensor still needs to be improved but it offers a very large potential for outer shell fabrics used in fire protective clothing as the high temperature resistant polymer selected for the sensor has a similar thermal degradation

behavior and activation energy as outer shell fabrics and the thermal aging monitoring only relies

on the measurement of the electrical conductivity of the conductive layer.

Preface

This thesis is organized in seven chapters. Chapter 1 is the introduction. Chapter 2 and 3 provide the background/literature review. Chapter 4, 5, and 6 describe the work on the thermal aging sensor conducted as part of the project "Graphene-based end-of-life sensors for fire protective fabrics"[1]. The overall conclusions of the thesis are summarized in Chapter 7.

Chapter 4 (NSERC Strategic Project STPGP 521866 – 18) corresponds to preliminary work for the project and has been published as C. Cho, A.L. Elias, J. Batcheller, P. Dolez, H.-J. Chung., "Electrical conduction of reduced graphene oxide coated meta-aramid textile and its evolution under aging conditions". Journal of Industrial Textiles. 2019. C. Cho wrote the manuscript with iterated revisions and instructions from P. Dolez, H.-J. Chung, A.L. Elias, and J. Batcheller.

Chapter 5[2](NSERC Strategic Project STPGP 521866 – 18) of this thesis will be further refined and submitted to a journal as C. Cho, J. Batcheller, A.L. Elias, H.-J. Chung, P. Dolez. "The investigation of accelerated thermal aging behavior of polyetherimide and lifetime expectation at elevated temperature". C. Cho, H.-J. Chung, and P. Dolez conceived the idea, and C. Cho performed the experiments and carried out data interpretation with instructions from A.L. Elias, J. Batcheller, H.-J. Chung, and P. Dolez. In addition, there will be another manuscript that focuses on the chemometrics analysis of FTIR spectra. Our collaborators in J. Harynuk group in the department of chemistry, S-L. Nam and P. de la Mata led the chemometrics analysis and will prepare a separate manuscript with C. Cho, H.-J. Chung and P. Dolez.

Chapter 6[3] (NSERC Strategic Project STPGP 521866 – 18) of the thesis will be further refined and submitted to a journal as C. Cho, J. Batcheller, A.L. Elias, P. Dolez and H.-J. Chung, "The

---

[1] These studies are funded by NSERC Strategic Project Grant (STPGP 521866 - 18)
[2] The author names are only tentative and the auther sequence has not been decided yet.
[3] The author names are only tentative and the auther sequence has not been decided yet.

fabrication of polyetherimide-based thermal aging indicators for the monitoring of fire protective clothing's outer shell". C. Cho, A.L. Elias, P. Dolez and H.-J. Chung conceived the idea. C. Cho performed the experiments and carried out data interpretation.

In addition to the above, I also contributed to one of my group members' publications (not included in this thesis): S. Qiu, T-G. La, L. Zheng, C. Cho, A.L. Elias, J. Rieger, H.-J. Chung., "Mechanically and electrically robust stretchable E-textiles by controlling the permeation depth of silver-based conductive Inks" Flexible and Printed Electronics, 4, 025006 (2019). In this publication, my contribution included the characterization of the amount of silver-ink penetration into stretchable textiles by using helium-ion microscopy.

To my family and Jeonghyun

Acknowlegment

First of all, I would like to thank Dr. Hyun-Joong Chung for giving me the opportunity to join and work in his group. He has been always supported me to broaden the scope of my work and project. He always inspires me with his enthusiasm and dedication for research. He cares student's problem from his experience, and he is a great educator and a research supervisor. I also do thank to Dr. Anastasia Elias for her dedication, inspiration to all my projects, and she is an excellent listener and supporter. Finally, I deeply appreciate to Dr. Patricia Dolez, who organizes entire project plans with Dr. Chung, and support me a lot.

I also would like to thank everyone in Dr. Chung and Dr. Elias group, Dr. Thanh Giang La, Dr. Tanushree Ghosh, Dr. Xinda Li, Dr. Syed Asad Manzoor Bukhari, Dr. Wendy Tran, Amit Kumar, Li Liu, Hemant Charaya, Fanghui Liu, Shide Qiu, Dinara Zhalmuratova, Lelin Zheng (our former students and PDF), Rosmi Abraham, Ankit Saha, Pradipika Natamai Vasudevan, Dr. Zahra Barikbin, Dr. Ben Nearingburg, Dr. Preetam Anbukarasu, Dr. Diana Martinez Tobon, Dr. Adrian Lopera, Dan Li, Joseph Caputo, Joshua Cunningham, Anuja Tripathi, Sim Yee Chen, Sina Momeni, and Valeria Hernandex Salgado. It was invaluable time that we have been together, and I wish your success in future. I am also very thankful to Ng E Khoon in Malaysia for his support.

Many thanks to the staff of CME department: Lily Laser. I always appreciate your kind smiles. I do thank the staff in the nanoFab: Dr. Aaron Hryciw, Stephanie Bozic, Scott Munro, Dr. Nancy Zhang, Shiau-Yin Wu, Dr. Dr. Shihong Xu and Peng Li. Your effort on my trainings and trouble shootings made my degree success. I appreciate Dr. Paulina de la Mata and PhD student Seo Lin Nam of Dr. James Harynuk's group in the Department of Chemistry for their chemometrics analysis for my study.

After finishing my master's degree from Department of Chemistry, I have started long journey to achieve my PhD degree. I remember everything I felt happiness, struggling and challenging. I do thank my parents and my sister, brother-in-law for their unconditional supports and love all though my life. Lastly, I truly appreciate my fiancée, Jeonghyun Lim with her patience, understanding and consideration for my entire 5 years. She believes in me to reach my achievement.

Table of Contents

LIST OF TABLES

LIST OF FIGURES

CHAPTER 1   Introduction

1.1 Introduction

Fabrics made with high-performance fibres are used to manufacture protective clothing for firefighters and workers subjected to extreme conditions, including heat, flame or radiation exposure [1]. These protective garments are critical for ensuring the safety of people who are wearing them. For that purpose, high performance fibers have been developed over the last 50 years that display inherently flame/high temperarature resistance, great mechanical properties, and improved chemical resistance [2]. Even though these fibers exhibit excellent performance when new, their properties may be affected over time when used under extreme conditions (e.g., heat, flame, or UV) [3]. In addition, these changes may not be visible to the naked eye [4]. Figure 1.1 illustrates the two levels of degradation in textile materials. The performance limit is the limit below which the textile performance does no longer meet the requirements it was initially intended to meet [5]. The visual limit indicates when degradation (e.g., color, tears) becomes visually obvious. However, the visual limit may be reached later than the performance limit, which raises large safety issues in the case of protective clothing.
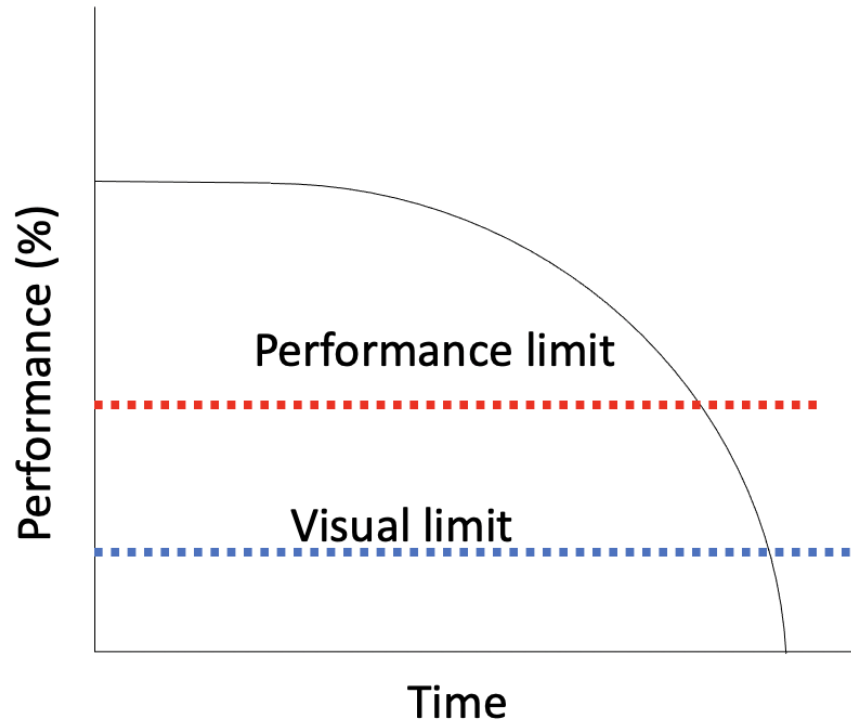
Figure 1.1 Change in performance as a function of time in textile materials reproduced from [5].

For structural firefighters' protective clothing, the requirements in terms of performance are described in the National Fire Protection Agency (NFPA)'s standard NFPA 1971 [6]. Particularly, outer shell fabrics are evaluated in terms of flame resistance, heat and thermal shrinkage resistance, tear resistance, cleaning shrinkage resistance, breaking strength, and water absorption resistance. This assessment is mostly done using destructive testing. However, destructive tests are not practical to assess the change in the protective clothing performance in service. Furthermore, testing a limited number of pieces of fire protective clothing cannot provide a representation of the condition of all clothing in a fire department, and cannot predict the level of damage to individual pieces of clothing [7]. Therefore, strategies for the non-destructive assessment of the performance of fire protective clothing in service are needed and must be developed. Non-destructive testing have been implemented in many other engineering applications, such as for the evaluation of the performance of cable materials in nuclear power plants [8]. If non-destructive tests can be used to

monitor the level of degradation in fire protective clothing performance, this information could be used to make decisions on the retirement of individual pieces of clothing without destroying usable pieces [7]. Currently, non-destructive test methods currently investigated are color measurement and near infrared spectroscopy. Some success has been achieved to correlate the results provided by these test methods with those by destructive methods [9,10]. However, these non-destructive tests still require sample preparation and additional testing equipment. Therefore, this thesis proposes cost effective and simple to use aging monitoring sensors for fire protective clothing under thermal aging.

The proposed sensor consists of a film of polyetherimide (PEI) with a conductive track of laser-induced-graphene (LIG), and an encapsulation layer. PEI was selected because of its high glass transition and degradation temperature. Due to high glass transition temperature and degradation temperature, PEI resists long-term exposure under high temperature. Graphene was selected as the conductive layer material because it can be produced by simple laser irradiation of PEI, which is converted to graphitized carbon [11].When the PEI sensor is exposed to heat or fire, PEI thermally ages. As a result, the PEI film may exhibit a change in its mechanical or chemical properties. These changes may create a disruption of the LIG layer physical integrity and lead to a decrease in the electrical conductivity of the LIG layer. If the thermal aging kinetics of the sensor is matched with that of the fire protective clothing, this sensor can inform when the fire protective clothing needs to be replaced. The overarching goal of this thesis is that developing a thermal aging sensor for monitoring an aging level of fire protective clothing as a non-destructive method by measuring electrically conductivity of LIG layer that loses its conductivity systematically under aging conditions. This thermal aging sensor can be used as the basis for an end-of-life-sensor for textiles.

The summarized objectives of this thesis are:

1. reduced-Graphene-Oxide (rGO) coating on meta-aramid fabric for electrically conductive fabric and perform washing or water immersion stability of rGO layer to investigate the stability of rGO layer, and rGO patterning on the fabric to investigate its abrasion resistance.

2. Investigation of the accelerated thermal aging behavior of a high temperature resistance polymer, PEI.

3. Fabrication of a PEI thermal aging sensor for fire protective clothing outer shell fabrics as a non-destructive tool for monitoring the level of thermal aging of the outer shell fabric with conductive track deposition.

The organization of the thesis is as follows: Chapter 2 provides a background and literature review of polymer/textile degradation. Chapter 3 provides a introduction and literature review of e-textiles and their applications. In Chapter 4, a simple and cost-effective method of preparing an rGO coating and patterning on a common outer shell fabric was developed to make the fabric electrically conductive. We investigate the stability of the graphene coated fabric under water immersion, washing, and abrasion. Chapter 5 describes a candidate polymer, PEI, for the thermal aging sensor. PEI was exposed to accelerated aging conditions and its thermal aging behavior was studied. Chapter 6 illustrates the fabrication of the thermal aging sensor for fire protective clothing with PEI. Finally, the overall conclusions and future works of this thesis are summarized in Chapter 7.

CHAPTER 2   Literature review on polymer and textile materials, and their degradation

2.1 Introduction

Chapter 2 provides a brief literature review and a general description of the concept of degradation of textiles and polymers, including the causes of degradation, the degradation mechanisms, and the effects of degradation. This chapter will also cover the methods of assessment of degradation in textile and polymers. It may be noted that, since many textile materials are made of polymers, the mechanisms of degradation of textiles and polymers may overlap. In order to distinguish between the degradation of textiles and polymers, the aging of textile materials will described in terms of macroscopic changes, such as visual changes, while the aging of polymers will be described in terms of micro/nanoscopic changes in the polymer network, such as mechanical or chemical changes.

2.2 Degradation and aging in textiles

The general term of degradation in the textile field implies that a material becomes less desirable, weaker, or experiences some changes of properties as a result of usage [12]. The degradation of textile materials may be due to changes in the molecular structure, including main and side chains or functional groups. These changes can lead to a deterioration in the physical or chemical properties such as strength, color, and resistance to abrasion. The difference between degradation and aging only relates on whether a specified-time-period is involved or not. The Internationl Union of Pure and Applied Chemistry (IUPAC) defines aging as "Processes that occur in a polymeric material during a specified period of time, and that usually result in changes in physical and/or chemical structure and the values of the properties of the material", and

degradation is defined as "Chemical changes in a polymeric material that result in undesirable changes in the values of in-use properties of the material [13]." However, for the sake of simplicity, from now on, this dissertation will not make the distinction between degradation and aging. The aging process of materials, including textiles, is inevitable and while changes can be decelerated, they cannot be halted. The results of degradation and aging may affect the service life of the clothing or the comfort of the wearer [12].

2.3   The causes of degradation in textiles

The essence of textile aging lies at the molecular level [12]. There are three types of degradation; 1) cleavage of one or more end-groups in a molecule, 2) breakage of the side chains, and 3) scission in the main chain. These degradations are sensitive to various characteristics such as the arrangement (orientation, crystallinity, etc) of the molecules in the fibers, the organization of the fibers in the yarn, and the way the yarns are structured to make a fabric. For instance, the yarn twist, fabric thickness, and spacing in weave can change the way in which the fabric is degraded upon abrasion. On the other hand, the molecular orientation in a fiber can modify the way in which the fabric is affected by water-borne reagents that can potentially attack the fiber.

One of the main factors that can influence textile degradation is the crystallinity of the fiber. Atalla suggested that cellulose possesses a one-dimensional order in an individual chain, and a three-dimensional order in an aggregate of chains ([14] cited in [12]). The authors found that the crystallinity of the cellulose material increases during the isolation of the native cellulose from biological sources such as wheat straw, sugarcane, hemp, rice husk ([15] cited in [12]). After the isolation process, the material becomes brittled due to increased crystallinity ([14] cited in [12]). Okamba-Diogo et al. studied the degradation process of the semi-crystalline polyamide 11 (PA 11) [16]. The general degradation process starts with chain scission, which causes a reduction in molar

mass, and can also lead to crystallization. Due to the increasing degree of crystallinity, the interlamellar distance decreases as well, and the polymer becomes brittled.

Another factor in textile degradation is the pre-treatment history of fibers [12]. Pre-treatment can also influence the fibers' ability to resist molecular changes and their tendency to degrade during use. This process may start even before the fiber is produced from the raw material. The production process may affect the degradation at a later stage, potentially contributing to or reducing degradation. One study showed that for two types of wool fibers (with high and low degrees of waviness), wool fibers from sheep with a low nutritional level are associated with an increased swelling in formic acid, and a reduced sulfur content and fiber diameter ([17] cited in [12]). This study also found that low crimp fibers disintegrate more easily than high crimp fibers. Furthermore, the authors showed that the rate of disintegration was accelerated in wools from sheep with low nutrition levels.

As the degradation process depends on the chemical structure of the fiber, it can be assumed that the entire degradation process depends on the fiber type, production conditions, and mode of use [12]. Therefore, it is necessary to consider separately each aspect of the production and use of articles made from specific fibers. The following sections review in detail various aspects of degradation conditions during fabric production, maintenance and storage, regular use, and exposure to extreme conditions.

2.3.1 Degradation during fabric production

Before the manufacturing of fabrics has even been completed, fabric degradation may begin [12]. This degradation can occur in response to harmful treatments during the production process or at any moment from fiber preparation to the delivery of produced textile goods. At the

early stage of the production process, the fibers are often exposed to mechanical or chemical actions that cause a loss or decline of desired properties. For example, the abrasive action of a machine or chemical reagents will affect the fabrics' molecular structure. Deshpande reviewed the significant causes of damage to wool fibers during wet processing ([18] cited in [12]). Possible causes of damage were scouring and bleaching by hydrogen peroxide, dyeing with various colors, and various finishing processes (pressing or coatings). These treatments have some influence on the degradation process.

Synthetic fibers are typically manufactured by filament extrusion and drawing [12]. During the manufacturing, the level of drawing can influence the subsequent behavior of the material produced from the filaments, the molecular structure of the fibers, and the fiber degradation. For example, the ester linkages in polyester fibers are susceptible to wet heat treatment ([19] cited in [12]); therefore when polyester fibers are temperature-set with steam, the materials end up with a lower molecular weight than those treated using a conventional dry setting.

The last stages of both synthetic and natural fiber manufacturing are the finishing and dyeing processes [12]. These processes also affect the fabric properties. Holmes-Brown et al. studied the effect of dyeing processes at various pH, temperature, and pressure (including steam) conditions on the degradation of wool ([20] cited in [12]). They found that extreme conditions can lead to the bending or breaking of fibers depending on the processing time of the wool fibers in the dyeing solution. Furthermore, the pH of the solution influences the fiber's morphological changes. Herrling et al. described that the cell-membrane complex is an important morphological component in wool fibers ([21] cited in [12]); this membrane allowes the fibers to interpenetrate as a continuous network. It consistes of two lipid layers with a protein layer in the center. This cell membrane is important for textile manufacturing as it affects the fiber's mechanical properties. If

this membrane is damaged by the dyeing process under various pH conditions, the tensile strength and abrasion-resistance of the wool fibers are eventually reduced.

The finishing process covers drying, curing, and other surface treatments such as crease-resistant (wrinkle-resistant) and mercerization, especially for cellulose fibers [12]. Mercerization is the textile finishing process for cellulose, cotton, or flax that improves dye uptake and tear strength, and reduces fabric shrinkage. For example, at the drying/curing stage of the cellulose fiber processing, the temperature is the main cause of degradation ([22] cited in [12]). On the other hand, surface treatments, mercerization, and scouring involve chemistry that affects the cellulose fibers and enhance their tensile strength ([23] cited in [12]).

2.3.2   Degradation during transportation and storage

Although manufacturers may try to minimize degradation agents during fiber or textile production, it is important to note that undesirable changes can also happen during the transportation and storage of items [12]. For example, during long-term shipping, stored wool fibers can be damaged by mechanical action, leading to changes such as discoloration, a decrease in tensile strength, and increase in grease content ([24] cited in [12]). Furthermore, the quality of ventilation and humidity may increase the tendency of fibers to produce dust, which will cause problems in subsequent processing of wool fibers ([25] cited in [12]). However, synthetic fibers are not very likely to change their properties as their finishing treatments are designed to protect them from degradation-causing factors.

2.3.3 Degradation during care and maintenance

Generally, textile materials have to undergo care and maintenance treatment to remain at an acceptable level of quality prior to and in between uses [12]. Maintenance of textile includes brushing, laundering, dry-cleaning, or bleaching; during these processes textiles are subjected to chemical and/or mechanical action. Laundering is a standard method to maintain textile products in which they are subjected to combined chemical and mechanical actions. Laundry detergents are mostly of alkaline nature. They can change the surface condition of textiles in water so that soil particles can be washed out by the water flow inside a washing machine. Detergents intensify the stain removal and brightness of textile products. During a chemical reaction with detergents, fibers in a textile can be adversely affected by the chemical compounds, leading to an accelerated degradation process. For example, wool fabric is degraded rapidly at high pH, high temperature, and extended washing time ([26] cited in [12]). Sodium perborate in the detergent improves the brightness of cotton, but it may decrease its degree of polymerization, which leads to a decrease in tensile strength and weight loss ([27] cited in [12]). The mechanical action in the washing process provides physical agitation to separate soil from the fabric through the mingling of the water. During mechanical agitation, the textile undergoes frictional contact with the walls of the washing machine drum and/or other textiles. This contact leads to abrasive contact and mechanical degradation such as a loss in tensile strength for silk, acetate, and nylon ([28] cited in [12]).

2.3.4 Degradation during normal use

There are numerous sources of degradation that can occur during the normal use of textiles [12]. These include mechanical action, ultra-violet (UV) radiation, moisture, and heat. Garments are commonly exposed to abrasive action by the body movement during wearing. Different

pressures are applied to the garments as a result of body movement; for instance, large pressures are applied when sitting or moving in a chair ([29] cited in [12]). In general, the effect of abrasion on textiles is a decrease in strength and weight. Depending on the amount of abrasion and the fabric type, the fabric thickness may increase due to fiber breakage, e.g., entanglement of broken fibers, broken fiber fillings pores, while air permeability may decreases ([4] cited in [12]).

The exposure of textile materials to UV radiation (e.g. by sunlight) is the most common and inevitable cause of degradation [12]. To each type of fiber corresponds an energy that results in the breaking of bonds within the fibers' polymer chain. For example, one study exposed nylon and polyester fibers to light from a xenon arc lamp, and compared the aging behavior of the two fabrics [30]. The author observed that nylon had a slower degradation rate with the xenon lamp than in sunlight while it was the reverse for the polyester fibers. The xenon lamp has a lower relative intensity above 330 nm, where the dissociation energies of the nylon bonds are located, compared to noontime sunlight. On the other hand, the dissociation energies for the polyester bonds are situated below 330 nm, where the relative intensity of the xenon arc lamp is slightly higher. Simpson et al. found that the most significant degradative effect on wool fibers occurs in the range of UV light (310- 400 nm) with the WeatherOmeter (accelerated weathing experiments device) and at the 11:00 am to 12:00 pm time under sunlight ([31] cited in [12]). A similar study by Boboev et al. studied the photodegradation of silk and nylon 6 exposed to UV light in the 254-365 nm range to determine the changes in mechanical property due to photoaging. The results showed that the tensile strength decreased by 36 % for silk and 20 % for nylon after 60 hours of exposure ([32] cited in [12]).

Textile materials also experience weathering during normal use [12]. They are often used or left outdoors, and therefeore have inevitable contact with the combination of stimuli including

light, water, dust, and atmospheric component (i.e., oxygen) that are associated with weathering and can cause degradation in fabrics. Various fabrics, including cotton, wool, polyester, and nylon, were exposed to weathering conditions corresponding with outdoor exposure ([5] cited in [12]). They experienced significant losses in tensile strength, tear strength and abrasion resistance.

An other source of degradation in textiles is heat. Thermal degradation can cause a decrease in strength ([33] cited in [12]) and/or degree of polymerization ([34] cited in [12]), and create yellowing ([35] cited in [12]). The thermal degradative process may be combined with hydrolysis or photodegradation. A detailed description of the mechanisms corresponding to the different degradative factors listed in this section will be discussed in the next section.

2.4 Degradation mechanisms in polymers and textile materials

Many textile fibers are made of organic, high molecular weight polymeric materials such as polyester, polyamide and polyolefins [10]. For their part, cotton, flax, and other cellulosic fibers consist of a carbohydrate polymer while silk and wool are composed of a protein polymer. Therefore, the degradation of textile materials can be associated with the degradation of polymers. Thus this section introduces the degradation mechanism of polymeric materials.

2.4.1 Mechanical degradation

Mechanical degradation in polymeric materials is a result of external mechanical loads. As described in section 2.3, when fibers are manufactured, stored, and used, textile materials are subjected to mechanical actions such as compression, abrasion, or tensile stress. When mechanical actions are experienced in polymers, sub-microcracks can form in the amorphous or crystalline region [36,37]. Furthermore, the mechanical degradation that occurs depends on the number of atoms in the chain, activation energy for bond scission (chain-scission), and orientation of the

molecules in material. After several cycles of compressive force have been applied to textile materials, changes in fiber diameter or tenacity may occur, with the recovery not being perfect because of the chemical changes in the structure [38]. Some factors depend upon the length of time during which a certain force is applied rather than on the number of cycles. These factors include the fatigue of single fibers, yarns, and small ropes in creep-rupture mode.

In a solid polymer system, defects in the amorphous and crystalline phase as well as external impurities influence the formation and behavior of radicals [39,40]. "Mechano-radicals" are generated when mechanical stress is applied to a polymer. When polymers are in the glassy state, the mobility of the macromolecules is limited so that the chain scission of bonds is localized. This chain scission will occur near the site of the formation of primary radicals. The chain-scission reaction may propagate quickly, initiating degradation and allowing local sites to easily collapse when stress is applied to the polymer. Locally degraded sites can lead to the formation of sub-microcracks, as shown in Fig. 2.1. First, when a stress is applied, a polymer chain can break, forming two end radicals (Fig.2.1 (a)). Next, the end radicals interact with neighboring macromolecules receiving an electron to form a stable end group (Fig.2.1 (b)). Further degradation occurs as some internal radicals from the chain scission form stable end groups and others form free radicals (Fig.2.1 (c)), and this sequence leads to sub-microcracks (Fig.2.1 (d)). If a new strain is applied at a higher loading, then new radicals are formed [39,41]. Microcracks are propagated at the weakest links of polymer networks and cause anisotropic orientation and chain extension. Furthermore, mechanical stress can cause changes in the chemical reactivity of polymers and their physical properties. These changes affect chain breaks and radical formation, which can initiate degradative processes, including microcracks and oxidation.
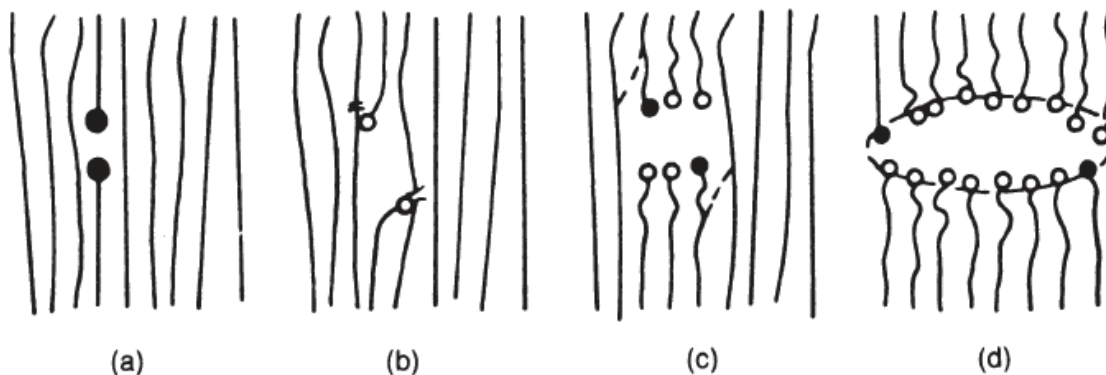
Figure 2.1 The sub-microcrack formation in a stressed polymer network. Symbols correspond to end radicals (•-), free radicals (-×-), and stable end groups. (o-) Reprinted from [40]

2.4.2 Photodegradation

Photodegradation can cause chemical changes in polymers by photoenergy-induced initiation of radicals [42–44]. In order to initiate the degradation, the molecules have to be activated by the absorption of radiation energy with sufficient activation energy. The photodegradation principle stems from the energy of photons: every photon that can be absorbed by the material will cause a physical process or chemical reaction. The energy of a photon is expressed by the equation (2-1).

$$E = h\nu \; or \; \frac{hc}{\lambda} \qquad (2\text{-}1)$$

where ν is the frequency of the electromagnetic energy, λ is the wavelength, c is the speed of light, and h is Plank's constant. Thus, when a chemical species in a polymer chain absorbs a photon with sufficient energy, a chain breakage reaction occurs, which generates radicals as described by reaction (2-2),

$$ROOH \xrightarrow{h\nu} RO\cdot + \cdot OH \qquad (2\text{-}2)$$

This reaction is called photolysis or photolytic breaking of the bond: chain scission is the primary process of the photochemical reaction. The bonds that have a higher bond energy will require

14

higher energy photons to initiate chain scission reactions. Light in the UV-C region, which corresponds to 100–280 nm, has a higher energy than light at longer wavelengths, and thereore has the highest potential of inducing photolytic chain scission. Higher energy bonds such as C-C (aromatic), C=C, C-H and O-H, cannot be broken upon exposure to near UV light, which corresponds to wavelengths between 400 and 315 nm. Some bonds that have a low bond energy such as C-O and O-O can undergo chain scission reactions in the near UV range. Therefore, depending on the bond energy, various wavelengths of light can initiate chain scission reactions in polymer chains. Table 2.1 and Table 2.2 summarize the wavelengths corresponding to the dissociation of various primary bonds and different polymers, respectively.

Table 2.1 Dissociation energy and corresponding radiation wavelength for various primary bonds. Reproduced from [43]

Bond	Bond energy (kJ/mol)	Wavelength (nm)
C ≡ N (nitrile)	875	136.8
C = C	837	142.9
C = O (Ketone)	729	164.3
C – C (aromatic)	519	230.6
C – H (acetylene)	506	236.3
C – H (ethylene)	444	269.7
O – H	460	260.0
C – O	364	328.6
N – H	352	340.4
C – C (aliphatic)	335	357.4
C – O (ether)	331	361.9
O – O (peroxide)	268	446.7
C – N (amide)	222	539.5

Table 2.2 UV wavelengths that induce the maximum degradation in various polymers. Reproduced from [43]

Polymer	Effective wavelength in the UV light range [nm]
Polyester	315
Polystyrene	318 and 340
Polyvinylchloride	310 and 370
Polyvinyl acetate	< 280
Cellulose acetobutyrate	295 to 298
Polyamide	250 to 310
Polyethylene	300

Carbonyl groups in aldehyde and ketone absorb at 187 nm and in the range of 280-320 nm, respectively, while carbon-carbon bonds absorbs at 195 nm and in the range of 230-250 nm [43]. The hydroxyl group absorbs at 230 nm, and primary carbon-carbon absorbs in the 135 nm range. For example, when a carbonyl group absorbs UV light, the C=O bond will break and form a radical (lone electron). This photochemical reaction is shown in reaction (2-3).

$$ (2\text{-}3) $$
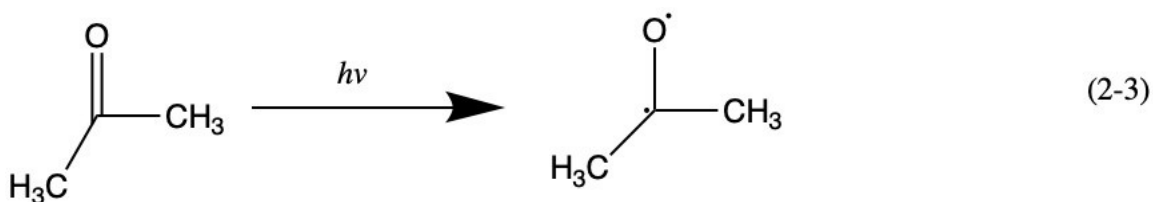
Photodegradation experienced by materials also depends on the energy (and wavelength) of the incident light [44]. When molecules absorb UV light, they are activated for a short time. If a molecule is modified or decomposed when a single photon of light is absorbed, the quantum efficiency is equal to unity. When the chain reaction is initiated in polymer chains, the quantum yield becomes exceptionally high due to the formation of peroxide radicals, as shown in equation (2-2) [44]. Also, the excited molecules can transfer the absorbed energy to near-neighbor

molecules. However, sometimes these molecules may lose the absorbed energy though different processes, for instance [44]:

1) the release of heat;

2) the emission of radiant energy of phosphorescence or fluorescence;

3) chemical changes in a molecule;

4) breaking of a chemical bond;

5) transferring energy to another molecule,

where 1), 2) are considered photophysical processes, and 3) to 5) are considered photochemical processes. Even though the transferred energy may initiate chemical changes, called the secondary process in a photochemical reaction, the collision with neighboring molecules may also dissipate the absorbed energy so that the quantum efficiency decreased.

The first step of the photochemical processes caused by the absorption of radiation is the formation of free radicals or non-radicals (monomer units) [44,45]. If free radicals are formed then secondary processes that do not require light can allow the reaction to propogate. For a better understanding, here is an example of primary and secondary processes of the photochemical reactions by which dye molecules in cellulose are degraded by peroxide radicals. The primary process is initiated after the dye molecule absorbs UV light [44],

$$\text{HD (Dye molecule)} \xrightarrow{h\nu \text{ (UV light)}} \text{HD} \cdot \text{ (activated dye)} \tag{2-4}$$
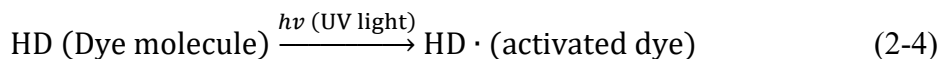
This activated dye molecule will transfer its excited energy to oxygen,

$$\text{HD} \cdot + O_2 \rightarrow O_2 \cdot \text{ (radical generated)} \tag{2-5}$$

After an oxygen radical is formed, the secondary process will initiate between oxygen and water and generate hydrogen peroxide.

$$O_2 \cdot + 2H_2O \rightarrow 2H_2O_2 \text{ (hydrogen peroxide)} \tag{2-6}$$
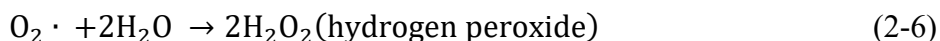
In the next step of the secondary process, the hydrogen peroxide causes cellulose to become oxycellulose and/or the dye molecule to bleach:

$$H_2O_2 + Cellulose \rightarrow H_2O + Oxycelluose \qquad (2\text{-}7)$$

$$H_2O_2 + HD \rightarrow H_2O + HOD \text{ (bleached dye)} \qquad (2\text{-}8)$$

We can see that the presence or absence of oxygen and water will influence the secondary process. Water is consumed in reaction (2-6) but regenerated during reactions (2-7) and (2-8). This will speed up the oxidation of the cellulose or dye molecule. UV degradation is therefore another contributor to chemical changes that occur in textile materials (and polymers).

2.4.3 Chemical degradation

Sometimes, textile materials are subjected to extreme conditions during their normal use that can accelerate the process of degradation [12]. This situation is particularly relevant for protective clothing against high temperature, radiations, corrosive compounds, and toxic environments. Acids and alkalis can easily cause the degradation of textile fibers during spillage events and other accidental exposure in an industrial situation where these kinds of reagents are likely to come into contact with garments [43,44,46]. Exposure to acid reagents may lead to an exothermic reaction, or to hydrolysis. For example, when cellulose fibers react with sulfuric acid, hydrolysis occurs in the fibers. This reaction will lead to chain breakage and affect the amorphous regions in the fiber [47]. Furthermore, this reaction will be accelerated by chain breakage, crosslinking, or branching. Regarding alkali reagents, mercerization is a well-known cellulose treatment with sodium hydroxide. Sodium hydroxide makes cellulose fibers swell, causing a change in the crystallinity and molecular orientation of the fibers after further drying of the fibers [48].

2.4.4 Thermal degradation

The thermal degradation of polymers/textile materials may be called thermolysis or pyrolytic degradation [12]. A pyrolytic reaction only takes place in the absence of oxygen, ideally in an inert and dry atmosphere; it is not a relevant process in aging/weatherability studies as oxygen is usually present [43,44]. In real-life situations also, thermal degradation will occur in the presence of oxygen. Thus, it is also called thermally-induced oxidative degradation, which is represented in Fig. 2.2.
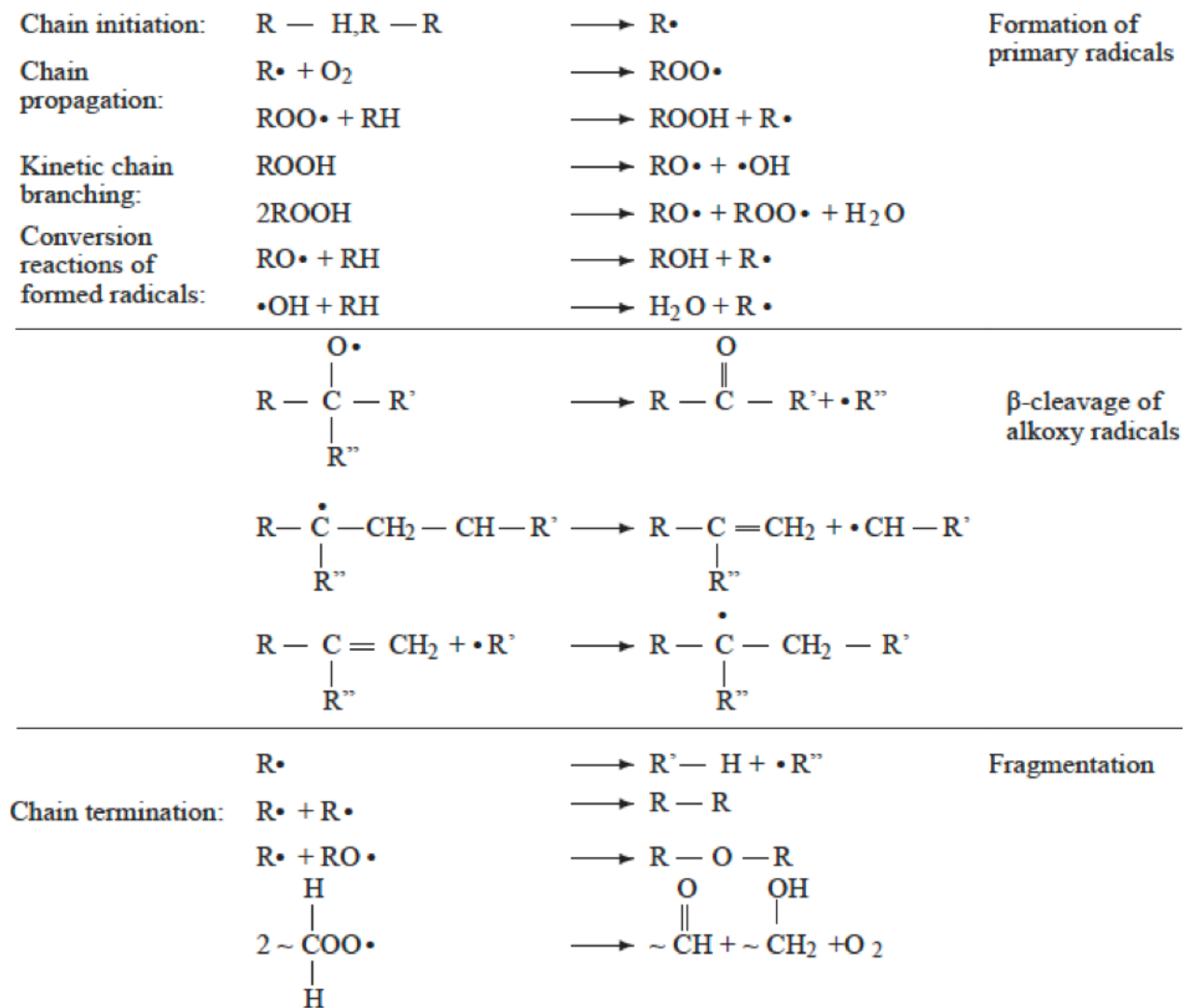
Figure 2.2 Mechanism of thermally-induced oxidative degradation in polymers. Reproduced from [43]

As heat is applied to the polymer, it starts to evaporate the residual solvent, water, or oligomers [43]. At higher temperatures, side group and backbone cleavage begins, and irreversible depolymerization occur in the entire polymer chain. Chain cleavage does not initiate uniformly but depends on the position in the chain (bond energy) and chain length. Bonds can be cleaved either in a side chain or in the main backbone. Ultimately, the thermally activated chain cleavage, will leave only carbon, because the high activation energy corresponding to heat breaks every bond within the polymer structure. Crosslinking is caused by the macro radical formation and occurs at a lower temperature than side-chain cleavage [43]. Therefore, the mechanisms of thermal degradation and chemical degradation are the same, even if the cause of the radical formation is different. Figure. 2.3 shows the thermal degradation process of polyethylene [49]. In the first step, peroxide radicals are formed by thermal activation. In the second step, the polyethylene chain breaks and forms radicals by reacting with peroxide radicals. Crosslinking reactions will also occur between radicals in the polyethylene chain in the second step. The crosslinking reaction is dominant at the beginning of the second step. Later, the chain scission reaction becomes dominant compared to the crosslinking reaction, so the net effect is chain scission in the polymer chains. At the third step, all radicals are consumed by combination or disproportionation.

Step 1. Initiation

$$R\!-\!\!OOR \longrightarrow R\!-\!\dot{O} \quad + \quad R\!-\!\dot{O}$$
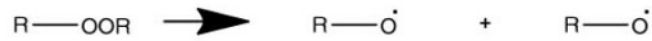
Step 2. propagation
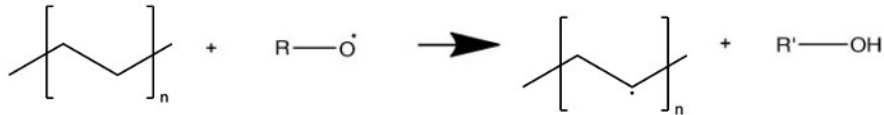
Step 3. Termination
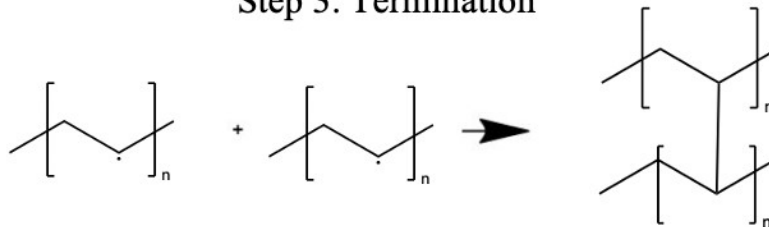
Figure 2.3 Thermal degradation process of polyethylene. Reproduced from [49]

2.4.5 Moisture-induced degradation

The presence of water is another factor that initiates polymer degradation by hydrolysis [12]. Polymers containing ester, ether, or amide groups are prone to hydrolysis reactions. It occurs in two steps. The first step is the hydrolysis of ester or amide bonds in the polymer chain. In the second step, chain breakage between polymer chains may occur. As a result of hydrolysis, chemical changes, such as a reduction in molecular weight or in mechanical properties, may occur. The mechanism of hydrolysis of amide or ester groups are shown in reaction (2-9) and (2-10), respectively. Materials are generally exposed to moisture or humidity in the air [50]. Moisture may adsorbed at the surface of a fiber, be absorbed, and start the degradation reaction. Water can also

be generated by chemical reactions such as the oxidation of cellulose by hydrogen peroxide represented in reaction (2-7).

$$(2\text{-}9)$$

$$(2\text{-}10)$$
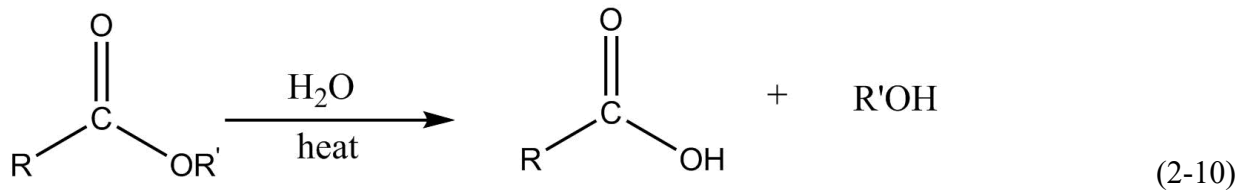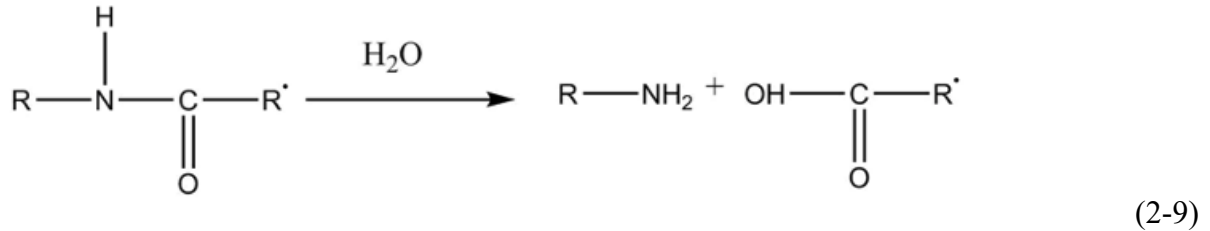
2.5 The effect of degradation in textile materials

When textile and polymeric materials are degraded, several noticeable changes may appear, either in appearance and in other properties [12]. For example, these changes may include color fading after laundering or dry-cleaning, or a mass loss due to a chemical reaction. Changes resulting from degradation can also reduce the chemical or mechanical performance of materials, thereby reducing their lifespan and period of usage. As described previously, various environmental factors lead to the degradation of materials; this section will describe the mechanical and chemical changes that can occur.

When polymeric materials are subjected to degradation processes, a common effect of degradation is a reduction in molecular weight [51–53]. The scission of chain bonds results in a decreased average molecular weight. The molecular weight of polymer can be calculated by equation 2-11.

$$\overline{M_n} = \frac{\sum N_i M_i}{\sum N_i} = \frac{\sum w_i}{\sum N_i} \tag{2-11}$$

where N_i is the number of molecules and w_i is the mass of the molecules with a molecular weight M. A decrease in molecular weight will also result in a decrease in the tensile strength (σ) of the polymer as their relationship can be represented by the following equation:

$$\sigma = \sigma_\infty - \frac{A}{M_n} \qquad (2\text{-}12)$$

with σ is the tensile strength of the polymer, σ_∞ is the tensile strength of polymer with a molecular weight of infinity, and A is constant. From equation 2-12, polymeric materials become easily deformed and break under at low stress when their molecular weight is reduced. This process is called embrittlement.

Regarding of the strength of yarns, yarns are composed of either continuous long fibers (continuous filament yarn) or short staple fibers (spun yarn) [54]. For both types of yarns, the relative tensile strength of the yarn can be estimated by the yarn-to-fiber modulus ratio (equation 2-13).

$$\frac{\text{Yarn modulus}}{\text{Fiber modulus}} = \frac{E_y}{E_f} = cos^2\alpha\,(1 - k\,cosec\,\alpha) \qquad (2\text{-}13)$$

where E_y is the yarn modulus, E_f is the modulus of the corresponding fiber and α is the twist angle of the yarn. The parameter k is a local bulk modulus of the fibril assembly and is expressed by the following equation 2-14:

$$k = \frac{\sqrt{2}}{3L_f}\left(\frac{aQ}{\mu}\right)^{\frac{1}{2}} \qquad (2\text{-}14)$$

where L_f is the fiber length, a is the fiber radius, Q is a constant, and μ is the coefficient of friction among the fibers in the yarn. Equation 2-13 includes two separate terms which are dependent on the twist level (α) [54,55]. The $cos^2\alpha$ term leads to a decreasing strength with an increasing twist angle ($0 < \alpha < 90$ °); this component is only applied for continuous filament yarns as the response of spun yarns is too complexe to be described by such a simple term. The ($1 - k\,cosec\,\alpha$) term yields

to an increase in strength with an increase in the twist angle due to increased friction among fibers. When the level of twist is constant, the strength of yarn is largely dependent on the k value ([55] cited in [54]). A higher k value will result in a lower strength ratio. It depends on the length and diameter of the fiber. Therefore a change in the fiber length or diameter that takes place during the degradation process will affect the k value, which means that the strength of the fiber will change as a result of the degradation process. There are two major mechanisms for yarns failure, fiber slippage or pullout and fiber breakage. The fiber slippage is influenced by changes in the twist angle of yarn. An increase in the twist angle causes an increase in the interfiber friction. This is shown by equations 2-13 and 2-14. Hence, higher twist levels tend to result in a predominance of fiber breakage, and lower twist levels tend to result in an increase in fiber slippage.

In textile materials, shape and color change can also result from degradation in addition to loss in strength ([56] cited in [12]). Shape change can result from insufficient fiber's elasticity. The surface appearance changes because of the abrasive (mechanical degradation) removal of small fragments from fibers or of entire fibers from the surface. Weaker fibers on the surface break and stronger ones generate pills. The breakage of the weaker fibers shortens the fiber length. This change in fiber length results in a decrease in the strength of yarns according to equation 2-13 and 2-14. Color loss is the result of chemical degradation, essentially through a cission of side groups.

Photodegradation leads to chain scission of polymers and can cause new crosslinks to form between polymer chains as well [57]. At the beginning of the photodegradation, both the strength and the toughness of the material can increase slightly. After further degradation, after the polymer has undergone an increase in the crosslinking density, the strength may be strongly increased but the elasticity may have decreased, leading to an increase in the brittleness of the material.

In textile materials, different types of degradation have been shown to affect different properties [46]. The influence of crosslinking on cotton fiber durability was investigated by comparing the properties of crosslinked cotton and regular cotton; crosslinked cotton was found to be insoluble in water and more brittle than regular cotton fibers. For wool textiles, UV triggered degradation leads to a decrease in tensile strength, breaking elongation, and abrasion resistance [57]. When acrylic and nylon 6 fibers were exposed to mechanical degradation, changes in the crystalline structure occurred preferentially at lower temperature and higher moisture content [58]. This mechanical degradation caused the reorganization of bonding forces, resulting in a reduced symmetry in fibers. During the degradation of Kevlar 49 fibers by hydrolysis, fibers underwent a slight reduction in strength [59].

In moisture-induced degradation, water plays a role as a plasticizer and can be responsible for the swelling and deterioration of the polymer [43]. In addition, the presence of water leads to accelerated oxidation reactions, which results in further degradation. Water can cause a cleavage of polymer chains or catalyze polymers that have hydrolysable groups, such as polyester and polyamides. This causes a reduction in molecular weight, which has a significant impact on the mechanical properties of the polymer. Sometimes, water may not be the main driver of the degradation, but rather accelerate hydrolysis reactions when combined with acidic or basic environments. Cyclical absorption of humidity (or water) can cause a succession of swelling and deswelling events in the polymer and can lead to crack formation.

2.6   Fire protective clothing and their degradation

2.6.1   Fire protective clothing and their properties

Personal protective equipment (PPE) is defined by Health Canada as an 'equipment or clothing worn to minimize exposure to chemical hazards in the workplace' [60]. Therefore PPE does not reduce or remove workplace hazards and should be used as a last line of defense after all other available risk control strategies – i.e. engineering controls and administrative measures - have been implemented [61]. Protective clothing is a category of PPE. It has three main functions:

1) Protection: protects the wearer from environmental hazards;

2) Comfort: provides comfort to the wearer, including tactile and thermal comfort;

3) Mobility: preserves the wearer's mobility to allow them performing their tasks.

Firefighter protective clothing are fire protective clothing designed to protect firefighters from various hazards associated with their occupation, including heat, flame, abrasive objects, and accidental chemical exposure [62]. Fire protective clothing are manufactured using specific polymeric materials in the form of fibers and membranes. These materials become charred instead of melting, dripping, or igniting when the temperature is elevated. Furthermore, they decompose at a much higher temperature than other polymers, and they are designed to be inherently flame resistant [7]. High performance fibers commonly used in firefighter protective clothing include aramids [2]. Poly(meta-phenylene isophthalamide) or meta-aramid was initially marketed as Nomex®. Poly(para-phenylene terephthalamide) or para-aramid is commercialized as Kevlar® for instance. Polybenzimidazole (PBI) is another inherently flame resistant polymer which also has an aromatic structure and forms a synthetic fiber with high thermal stability and high chemical resistance [7]. Aramids and PBI are the backbones of flame-resistant fabrics used in firefighter protective clothing. In addition, polytetrafluoroethylene (PTFE) is a common material used in

moisture barriers [7]. In its expanded form, it contains micropores big enough to allow water vapor, which is generated by perspiration, to pass through the fabric while preventing the entry of liquids. These four materials' chemical structures are illustrated in Fig. 2.4. Table 2.3 list some of their mechanical properties. It also includes other fire resistant fibers and membrane materials.
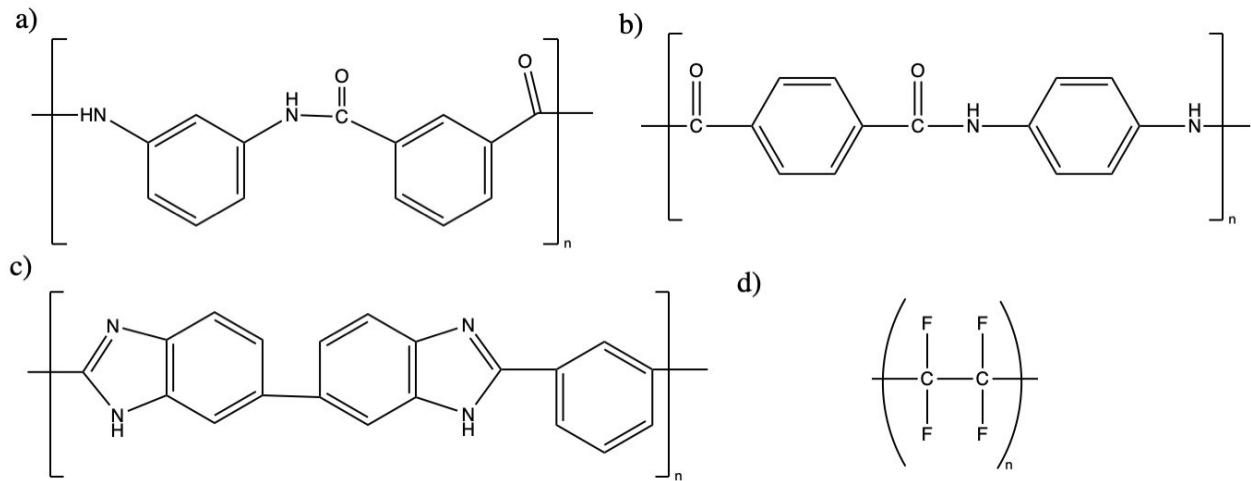
Figure 2.4 Chemical structure of a) meta-aramid, b) para-aramid, c) PBI, and d) PTFE

Table 2.3 Mechanical properties of fire protective fibers. This information is taken from manufacturers' literature and Ref. [63]

Fiber or membrane	Tenacity (N/tex)	Initial modulus (N/tex)	Breaking extension (%)	Tensile strength (GPa)	Initial modulus (GPa)
m-aramid (Nomex)	0.485	7.5	20	0.34-3	N/A
Kevlar 29	2.1	58	4.4	3.0	83
Kevlar 49	2.1	80	2.9	3.0	115
Kevlar 149	1.6	98	2.5	2.3	141
Polybenzimidazole (PBI)	0.24	2.8	28.5	0.16	N/A
Polyimide (P84)	0.35-0.38	3-4	33-38	0.14-0.15	N/A
Polyamide-imide (Kermel)	0.25-0.59	4.9-9.4	8-20	0.11-0.19	N/A
poly(p-phenylene-2,6-benzobisoxazole (Zylon)	3.7	116.9	2.5-3.5	5.8	N/A
Melamine-formaldehyde (Basofil)	0.2-0.4	6	15-20	0.25	N/A
Novoloid phenolic resin (Kynol)	0.12-0.16	2.6-3.5	30-50	0.16-0.2	N/A
Glass-E	1.4	2.9	4.8	3.5	72
Glass-S	1.8	35	5.4	4.6	87
Silicon Carbide Niccalon	1.0	81	1.5	2.7	210
Silicon carbide Whisker	3.2	220	1.2	8.4	580
Nextel	0.63	56	1.1	1.7	150
Alumina-FP	0.36	97	0.4	1.4	380
Polytetrafluoroethylene (PTFE)	0.14	N/A	20	0.031	N/A
Polyvinylidene chloride (PVDC)	0.2	0.44-0.68	15-30	0.016	N/A

In North America, firefighter's protective clothing generally includes three layers, an outer shell (OS), a moisture barrier (MB), and a thermal liner (TL), as illustrated in Fig.2.5. The outer shell is the outmost layer and designed to offer resistant to flame and heat, as well as protection against mechanical hazards . This layer is made of high strength and excellent thermal resistive

polymer fibers [7,64]. It may also have a finish with water repellent properties. The TL layer is the innermost layer and functions as a thermally insulating layer, providing thermal protection from heat or cold environments. It is usually produced with a non-woven insulating structure or highly porous padding fixed on an inner layer of woven fabric that reduces the friction with the skin. Even though thicker TL offers better heat protection, it may be heavy and bulky, making it less comfortable. In addition, the slippery woven surface of the TL provides ease of donning and doffing to firefighters and improved mobility and agility during firefighting operations. The MB layer is typically the middle layer between the TL and OS layers. It resists water, chemicals, and other liquids such as body fluids, which may permeable through the OS layer. At the same time, it allows water vapor to pass through, either thanks to a microporous structure or by diffusion across a solid membrane [7,64]. This reduces heat stress as well as the risk of steam burns on the skin. Usually the MB layer is made of a film barrier laminated on thin aramid woven or non-woven backing substrate for mechanical support [61]. Tables 2.4-2.6 give the main characteristics of products used as OS, TL, and MB layer in firefighter protective clothing, respectively.
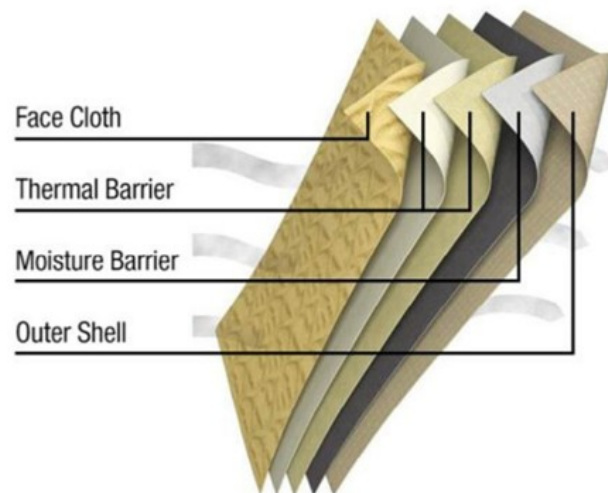
Figure 2.5 The layers of fire-protective clothing. Reprinted from [65]

Table 2.4 Composition and properties of commercial outer shell fabrics. Reprinted from Ref. [61]

Brand	PBI gold	PBI MATRIX	Nomex® IIIA	BASOFIL®
Materials	40 % PBI™, 60 % Kevlar®	40 % PBI™, 60 % Kevlar®, includes an array of Kevlar filaments	93% Nomex®, 5% Kevlar®, 2% antistatic fibers	40% BASOFIL®, 60% Kevlar®
Fabric weight (oz./yd^2)	7.5	7.5	N/A	7.5
Thermal stability	Superior	Superior	Basic	Excellent
Tensile strength (MPa)	Very good	Excellent	Very good	Good
Abrasion resistance	Very good	Excellent	Good	N/A
Water repellency		Durable water repellent SST finish		

Table 2.5 Commercially available moisture barrier materials for fire protective clothing. Reprinted from [61]

Brand	CROSSTECH® 2-Layer	CROISSTECH® 3-Layer	GORE RT7100™	CROSSTECH® S/R Fabric
Substrate	Nomex ® fabric woven from spun fibers (pyjama check)	Top: Nomex® fabric woven from spun fibers (pyjama check) Bottom: Nomex® fabric woven from spun fibers	Nomex® non-woven spun lace	Nomex® fabric
Film	Enhanced bicomponent ePTFE membrane	Enhanced bicomponent ePTFE membrane	Bi-component ePTFE membrane	Enhanced bicomponent ePTFE technology
Overall thermal performance	The highest THL[1] /TPP[2] combinations	Best durability/THL/ TPP combinations	N/A	Flame- and Heat resistant, Meets NFPA 1951 and NFPA 1999
Liquid resistant	Best	Best	Better	N/A
Breathability	Breathable	N/A	Breathable	Most Breathable
Durability	Very good abrasion resistance	Most durable flex and abrasion resistance		Most durable in abrasion, cuts, and puncture

THL: total heat loss, TPP: Thermal protective performance

Table 2.6 Commercially available thermal liners for fire protective clothing. Reprinted from Ref. [61]

Brand	QUANTsUM3D ™ (2-layer)	QUANTUM3D ™ (1-layer)	CALDURA R SL2	CALDURA R SL3
Face cloth	Nomex® blend of filament and spun fibers	Nomex® blend of filament and spun fibers	Nomex® fabric woven from a blend of filament and spun fibers	Nomex® blend of filament and spun fibers
Batting	Two layers of Nomex®, Kevlar® blend spun lace (1 layer 2.3 oz./ yd2 with 3D waffle design and one layer 1.5 oz./yd 2)	One layer of Nomex®, Kevlar® blend spun lace (2.3 oz./yd 2 with 3D waffle design)	Two layers of Nomex® E-89 ™ (1 layer each of 2.3 with 3D waffle design and 1.5 oz./yd 2)	Three layers of Nomex® E-89 ™ (each layer is 1.5 oz. yd 2)
Donning/doffing properties	Excellent	Excellent	Excellent	Excellent
Flexibility	Most flexible, thin and lightweight	Most flexible, thin and lightweight	Lightweight and flexible	The most flexible choice for this much insulation
Thermal protection per unit weight	More thermal protection	N/A	N/A	N/A
Wickability and quick drying	Excellent	Excellent	Very good	Very good

2.6.2   Aging of fire protective clothing

In section 2.2, aging and degradation were defined. During the aging, irreversible changes occur that may reduce the functionality of clothing. As described in section 2.6, the performance of each layer of the fire protective clothing has a significant influence on the level of the protection provided. In general, the protection performance of the fire protective clothing is expected to change over time as a result of exposure to service conditions [7]. Unfortunately, it is still unclear when the fire protective clothing starts aging and how long it can continue to protect firefighters when performing their work. A major factor that affects the evaluation of the performance of the protective clothing over time is the material and weight of each layer of the fire protective clothing. When textiles are exposed to high temperatures, heat flux, or UV radiation at the same conditions and for the same durations, different fiber blends and weights of fabrics will age differently. Likewise, abrasion will affect different fabrics differently. Firefighters (and their clothing) are exposed to extreme conditions in terms of heat and flame; this exposure can provide sufficient energy for chain scission and the formation of volatile products due to degradation [66].

Several studies have characterized the thermal aging of fire protective clothing. Table 2.7 provides the main results of some of them. Iyer et al. studied the effect of thermal exposure on para-aramid fabrics [67,68]. Fabric specimens were aged in a series of isothermal tests in a furnace between 150 °C and 550 °C (the decomposition temperature of the polymer fibers) for times ranging between 0.5 and 7000 hrs. Folowing this exposure, a decrease in both tensile strength and weight was measured. At the beginning of the aging stage, grooves and peel-offs formed on the fabric surface. Holes and protrusions occurred at a later aging stage. These morphological changes were associasted to both weight loss and decrease in the tensile strength of the fabric specimens.

Day et al. examined the effect of thermal aging on the mechanical and thermal protective properties of some fabrics (Nomex III, Polyamide/FR viscose blend, FR cotton and FR wool) used in fire protective clothing [66]. Samples were taken from the outer shell and moisture barrier materials. Thermal aging was conducted between 150 °C and 250 °C for 5 min to 7 days. The consequence of thermal aging on the fabrics was thermal shrinkage and weight loss, the extent of which depended on the fabric type. Meta-aramid was shown to undergo 1 % thermal shrinkage and less than 5 % weight loss. However, the tear strength of this material decreased by approximately 20 %. While outer shell specimens underwent a significant reduction in tear strength, the tear strength of the moisture barrier specimens increased after thermal exposure, which was caused by crosslinking reactions.

Jain and Vijayan investigated the effect of thermal aging on meta-aramid specimens between 240 °C and 400 °C for 0.5 to 2000 hrs [69]. They observed microgrooves on the fiber surface after thermal exposure at 300 °C for 400 hrs. This study revealed that a decrease in crystallinity and tensile strength, and and increase in weight occurred due to the thermal aging of meta-aramid fibers.

Thorpe also evaluated the performance of fire protective clothing upon exposure to extreme conditions. The author thermally exposed specimens, including three-layer fabrics, to radiant heat flux values of 5 to 30 kW/m^2 for a time ranging from 30 to 3600 s [10]. The result showed that the tensile strength of the outer shell specimens decreased with higher heat flux values and longer exposure times. The Conductive and Compressive Heat Resistance (CCHR) rating of the specimens (which describes the amount of heat energy transferred by a protective fabric by thermal conduction to the wearer) increased when specimens were exposed to higher heat flux values and

longer exposure time. Air pockets formed inside the fabric after thermal exposure caused an increase in the CCHR rating as well as the fabric stiffness.

Arrieta et al. studied the thermal aging of Kevlar®/PBI fiber blend fabric and yarn samples under various temperatures (190 °C, 220 °C, 275 °C, and 320 °C) for up to 2 weeks [70]. The author measured the breaking force retention and looked for possible chemical changes after thermal aging. The thermal life of the materials corresponding to a 50 % reduction in the original breaking force was 12 days at 190 °C and 1 hour at 320 °C. The Arrhenius model was applied to the accelerated thermal aging data using the 50% performance loss criterion; it led to a value of the activation energy of 137 kJ/mol. The data were also analysed using the time-temperature superposition (TTS). With the TTS model, the activation energy was measured to be 107 kJ/mol. The FTIR technique was used to look for a change in the chemical properties during thermal aging, but no significant change in the absorbance was recorded.

Dolez et al. investigated the effect of thermal aging on the mechanical performance of fire protective clothing [3]. This study examined seven different fabrics used in fire protective clothing, which were thermally exposed between 150 °C and 300 °C for up to 500h. A significant decrease in tear strength was observed for all specimens, even at 150 °C. This study used a combination of the TTS principle with the Arrhenius model to compute the values of the activation energy corresponding to thermal aging of these different fabrics. They ranged between 81 and 113 kJ/mol depending on the fiber content.

Tests have also been conducted on firefighter protective clothing subjected to service use. Vogelpohl examined pieces of real firefighters' suits that had been used for lengths of time varying from one year to more than five years [71]. The author found that used outer shell materials absorbed more than 10 % water, while new specimens did not absorb an appreciable amount of

water. Moisture barrier specimens taken on the used garments absorbed water within an hour, much faster compared to the new material. The moisture barrier specimens also failed the water penetration resistance test. Both outershell and moisture barrier materials underwent a decrease in tensile strength (average of 40 % reduction in outer shell specimens and 10 % in moisture barrier specimens) as a result of use.

McQuerry et al. describes the results of an investigation of used firefighter protective clothing from 2 to more than 10 year old [72]. The researchers characterized the residual performance of the outershell, moisture barrier, and thermal liner layers according to the test methods in NFPA 1851 and NFPA 1971. This included visual inspection, tear and breaking strength measurement, water penetration evaluation, and flammability test. The authors found that the outer shell fabrics of age 10 years or greater from the manufacturer date were in poor to fair condition. Thermal liner fabrics 10 year old and more failed the visual inspection. In terms of tear strength 75% of the fabrics failed to meet the minimum 100 N required by NFPA 1971. Regarding breaking strength, 17 % of the outer shell fabrics failed to meet the minimum requirement by NFPA 1971, which is 623 N; the average breaking strength was 845 N for outer shell fabrics between the ages of 2 and 10 years and 725 N for outer shell fabrics between the ages of 10 and 22 years. All the less than 10-year-old outer shell fabrics and 98 % of the less-than-10-year-old moisture barrier and thermal liner fabrics passed the flammability test. For the more than 10-year-old garments, 23 % of the moisture barrier fabrics failed the flammability requirements while all the outer shell and thermal liner fabrics passed it.

Table 2.7 Studies on thermal aging of fire protective clothing in the literature. Reproduced from Ref.[73]

Author(s)	Material/Aging conditions	Duration of thermal aging	Assessment methods	Summary of the main results
Iyer et al [67,68,74]	Para-aramid Exposure to 150-550 °C in a furnace	0.5 – 7000 hrs	– X-ray diffraction – Weight – Tensile strength – Microstructural features	– The decrease in crystallinity, tensile strength, and weight and the damage to the surface of the fibers depended on the duration of each stage in a multiple-stage exposure.
Day et al. [66]	Meta-aramid, Flame resistant wool, PBI/para-aramid blend Exposure to 150-250 °C in an oven	5 min to 7 days	– Thermal shrinkage – Weight – Char length – After flame time – Tear strength	– The thermal shrinkage and weight loss depended on the fabric type; – The char length, after flame time, and TPP rating changed only slightly; – The tear strength of the outer shell specimens decreased, while the tear strength of the moisture barrier specimens increased.
Jain and Vijayan [69]	Meta-aramid Exposure to 240-400 °C in a furnace	0.5 – 2000 hrs	– X-ray diffraction – Weight – Tensile strength – Microstructural features	– The decrease in crystallinity, tensile strength, and weight, and the damage to the surface of the fibers depend on both the temperature and the duration of thermal exposure.
Thorpe [10]	Para and meta-aramid Exposure to 5–30 kW/m^2 using radiant panel	30–3600 s.	– CCHR rating – Tensile and tear strength – Water penetration resistance	– The increase in CCHR rating, decrease in tensile strength, and decrease in water penetration resistance depend both on heat flux and duration.

Vogelpohl [71]	100% meta-aramid 40/60 PBI/para-aramid 50/50 PBI/para-aramid 40/60 meta-aramid/para-aramid Evaluated used firefighters' protective clothing	$1-5^+$ years in service	– After flame time – Char length – TPP rating – Water absorption – Water penetration resistance – Mechanical properties	– The tear strength of used outer shell specimens is lower than for new specimens; – The tear strength of used moisture barrier and thermal liner specimens is higher than for new specimens; – The tensile strength of used specimens lower than for new specimens; – After flame time, char length, and TPP rating of used clothing were higher than for new clothing; – Most moisture barrier specimens failed the NFPA requirements for new clothing; – The outer shell of used clothing absorbed more water than new clothing.
Arrieta et al. [70]	60/40 para-aramid/PBI 190, 220, 275, and 320 °C	2 weeks	– Breaking force retention – Chemical structure changes	– The time to reach 50% of breaking force retention was 12 days for 190 °C and 1h for 320 °C. – No significant changed in FTIR spectra The activation energy for thermal aging was 137 kJ/mol using a 50% tensile strength retention criterion and 107 kJ/mol using the TTS principle
Dolez et al. [3]	100% Kevlar spun yarn fabric	Up to 500 hrs	– Chemical structure changes	– Decrease in tear strength; – Not clear evidence of changes in the chemical structure for FTIR;

	93% Nomex, 5% Kevlar, 1% carbon (Nomex IIIA) spun yarn fabric 60% Kevlar/40% Nomex IIIA spun yarn fabric 60% Kevlar/20% Nomex/20% PBO spun yarn fabric 60% Kevlar/40% Basofil spun yarn fabric 100% Nomex spun yarn fabric 60% para-aramid/40% PBI spun yarns/Kevlar filament fabric Accelerated thermal aging at 150, 190, 210, 235, and 300 °C.		– Tear strength retention – Decomposition rate	– Values characterizing the effect of temperature and the kinetics of thermal aging using a combination of the TTS principle, the Arrhenius model and a fit by the Hill equation.
McQuerry et al. [72]	Used garments in fire departments (donated, volunteered)	2 ~ +10 years	– Tear strength – Average breaking strength – Flammability test	– 75 % fabrics below 100 N tear strength – Average breaking strength: 845 N for 2~ 10 yrs fabrics, 725 N for 10 ~ 22 yrs fabrics. – Flammability test: 100% and 98 % passed for MB and TL aged less than 10 yrs, 77 % of MN (aged + 10) passed,100 % for OS, TL (aged +10)

2.7 The assessment of textile materials aging

The assessment of textile materials' aging is complicated by the fact that the aging process is not necessarily linear, and is a very delicate process [75]. Even though the aging process of textile materials may not be noticeable on a short time scale, significant changes may accumulate, and eventually the items will become unserviceable and have to be discarded. Therefore, it is important to be able to estimate when any article will no longer satisfy its intended function. However, it is not easily achieved. Various types of destructive testing can be performed to estimate the service life of textiles, but this type of testing is limited because of the cost associated with damaging the articles during the analysis. This section will introduce some test methods allowing the assessment of the effect of aging on textiles and their properties that can be used to predict the useful service life and suggest a replacement schedule. Table 2.8 presents some of these properties along with the corresponding measurement methods.

Table 2.8 Testing methods for polymer aging. This table is reproduced from [76]

Category	Characteristics	Measurement methods
Surface properties	Color, transparency, cracks	UV/VIS spectrophotometry, Optical microscopy, Scanning electron microscopy
Mechanical properties	Elongation at break, tearing force, ultimate tensile strength	Tensile test
Chemical properties	Chemical structure, crystallinity, molecular weight	FTIR, XRD[1], GPC[2]
Thermal properties	Thermal stability	TGA[3], DSC[4]

[1]XRD:X-Ray Diffraction, [2]GPC: Gel Permeation Chromatography, [3]TGA: Thermogravimetric analysis, [4]DSC: Differential scanning calorimetry

2.7.1   Mechanical property measurement

Three significant mechanical properties in textiles are tensile strength, tearing strength, and abrasion resistance [12]. All these properties are easily measured, but the tensile behavior of fibers is a universal way to recognize degradation. Changes in the tensile strength or other properties associated with tensile stress (work of rupture, Young's modulus, or elongation at break) are always indicative of the presence of some aging process in progress.

In general, tensile strength is represented on a stress-strain curve (Fig. 2.6). The behavior of an individual fiber under a gradually increasing force is also expressed on the stress-strain curve [63]. Conventional stress is given by equation 2-15. Due to the spacing and the presence of voids between fibers, the cross-section area of textile yarns and fabrics is not well defined. For single fibers, the cross-section area is obtained indirectly from the mass and density of the specimen. Therefore, it is more convenient to use the linear density, which is the mass per unit length, instead of the cross-section area to express the stress of fibers and yarns. This expression of the stress is called specific stress (equation 2-16). The tensile strain is expressed as a function of the elongation according to equation 2-17.

$$\text{stress} = \frac{\text{load}}{\text{area of cross section}} \tag{2-15}$$

$$\text{specific stress} = \frac{\text{load}}{\text{linear density}} \tag{2-16}$$

$$\text{tensile strain} = \frac{\text{elongation}}{\text{initial length}} \tag{2-17}$$

The conventional stress is expressed in terms of force per unit area and has a unit of Pascal (Pa). But in the textile community, the specific stress is preferred, with a unit of N/tex [63]. The correspondence between the different units for the stress-strain curve of a fiber is expressed in Fig. 2.6.
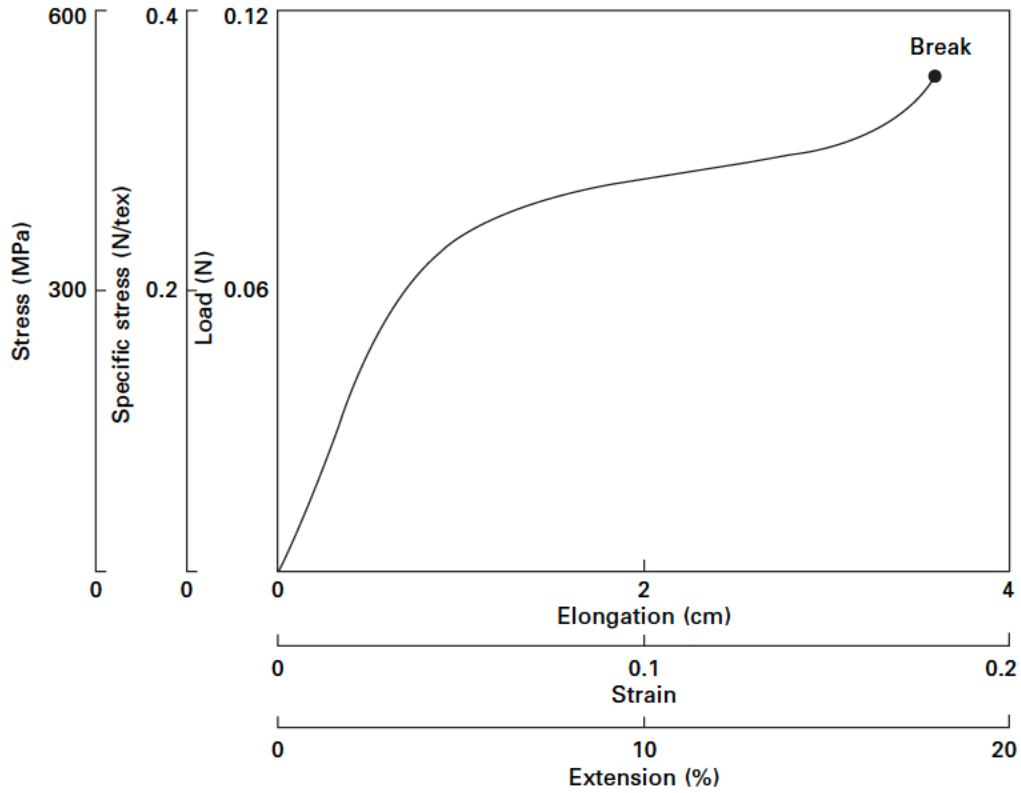
Figure 2.6 Example of true stress-strain curve for a 0.3 tex fiber with a 1.5 g/cm^3 density. Reprinted from [63]

For individual fibers, the work of rupture is defined as the energy needed to break the fiber [63]. The physical meaning of the work of rupture also called toughness is illustrated in Fig. 2.7. The toughness of a fiber will be proportional to its linear density (through the load) and its length (through the elongation). In order to compare with different materials, the specific work of rupture defined by equation 2-19 is preferred instead of the general work of rupture (equation 2-18).

$$\text{Work} = \text{Force} \times \text{displacement,}$$

$$\text{Total work spent in breaking the fiber (work of rupture)} = \int_0^{\text{break}} F \cdot dl \qquad (2\text{-}18)$$

$$\text{Specific work of rupture} = \frac{\text{Work of rupture}}{\text{linear density} \times \text{initial length}} \qquad (2\text{-}19)$$
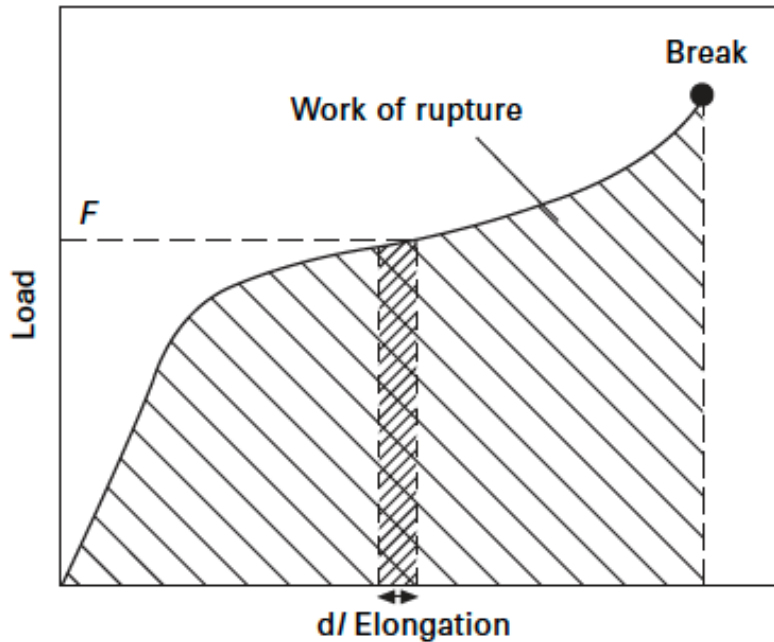
Figure 2.7 Work of rupture illustrated on a load-elongation curve. Reprinted from [63]

The specific work of rupture is given by the area under the curve of the specific stress-strain curve (Fig. 2.7). It may be expressed in N/tex or kJ/g [63]. It represents the energy in Joules required to break a 1 m long filament of 1 tex.

The mechanical properties such as the tensile strength, elongation at break or work of rupture can be obtained by applying a constant rate of strain to a specimen and measuring the stress, and strain at the breaking point of a specimen. These properties may be modified as a result of aging, and a change in the mechanical properties may be indicative of an aged polymer. In this dissertation, the ultimate tensile strength (MPa) will be used as the main property to characterize the change in the polymer due to aging.

2.7.2 Physical and chemical properties

The chemical changes that occur as a result of aging are often used to monitor the level of aging [43]. Both reductions in molecular weight and chemical analyses can be used to identify the changes of chemical functional groups to inform about the processes of polymers' aging. Viscosity measurements are a simple, fast, and reliable indicator of changes in the molecular weight of a polymer. Viscosity is related to the average size of the molecules in a polymer chain. From the Mark-Houwink equation, the viscosity [η] is expressed in terms of the average molecular weight (M_v) (equation 2-20).

$$[\eta] = K M_v^{\alpha} \tag{2-20}$$

where K and a are constants relative to the polymer and the solvent [77]. The degree of polymerization (DP_n) is expressed by equation 2-21.

$$DP_n = \frac{M_n}{M_0} \tag{2-21}$$

where M_n is the number-average molecular weight, and M_0 is the molecular weight of the monomer unit. A change in the molecular weight will affect the degree of polymerization. Based on the two equations above, viscosity measurements will provide information on a change in molecular weight.

During the aging process, polymers undergo changes in their chemical structure. Infrared spectroscopy (IR) has been widely used for the study of aging (or degradation) of polymers [76]. The beauty of using IR characterisation in polymer aging studies is that all the changes in functional groups (including the generation or consumption) can be tracked by their unique IR spectrum. Furthermore, the absorption is proportional to the concentration of species following the Beer-Lambert Law. Thus, IR spectroscopy is a powerful tool for investigating the kinetics of the process involved in the aging of a polymer. In general, the determination of the rate of aging by

IR spectroscopy is conducted by monitoring the formation of carbonyl groups (I_{CO}) at 1720-1710 cm^{-1}, and/or hydroxyl groups (I_{OOH}) at 3450-3400 cm^{-1} ([78] cited in [76]). During aging, carboxyl radicals are generated or consumed (referred to as "formation of primary radicals" in Fig 2.2) so that the rate of aging can be calculated using the following equations (Eq. 2-22, 2-23)

$$I_{OOH} = \frac{\text{Absorbance at } 3450-3400 \text{ cm}^{-1}}{\text{Absorbance of a reference peak}} \tag{2-22}$$

$$I_{CO} = \frac{\text{Absorbance at } 1720-1710 \text{ cm}^{-1}}{\text{Absorbance of a reference peak}} \tag{2-23}$$

In summary, the molecular weight of polymers has an effect on the viscosity, degree of polymerization, and molecular size of polymer chains, and the molecular weight of a polymer will be reduced during the aging process. Furthermore, identifying the formation or consumption of functional groups in polymer chains during aging by IR spectroscopy will lead to a better understanding of the chemical changes that occur. In Chapter 5, the change in the FTIR peak area (functional group formation or consumption) is characterized to analyze the aged polymer.

2.8 Lifetime expectation of textiles and polymeric materials

In daily use, it is necessary to be able to predict the service life of garments so that users know when garments should be replaced [43]. The effect of aging depends both on temperature and time, so it is necessary to establish an aging model that describes the rate of aging at different temperatures. The Arrhenius model can be used to investigate the effect of temperature on the rate of chemical reactions [44]. The Arrhenius equation is expressed by equation 2-24.

$$f(T) = A \cdot e^{-\frac{E_a}{RT}} \quad or \quad \ln k = -\frac{E}{RT} + \ln A \tag{2-24}$$

where E_a is the activation energy, k is the reaction rate, T is the temperature, R is the ideal gas constant, and A is a constant. The measurement of the rate of reaction is performed at various

temperatures, and the logarithm of those rates is plotted versus 1/T, the inverse of the absolute temperature. The resulting plot is a line declining with 1/T, with the rate of chemical reactions and processes increasing exponentially with temperature. Thus, a low-temperature exposure will lead to a slower aging reaction, and increased temperatures will cause an accelerated aging reaction. In order to apply the Arrhenius model, it is assumed that the rate of a polymeric material's aging is determined by a unique chemical reaction or physical process at a certain temperature. According to equation 2-24, the slope of the Arrhenius plot, $-E_a/R$, is used to calculate the activation energy.

However, there are two assumptions for the Arrhenius model to apply. First, the rate of reaction should be constant over the period of the time where the aging process was measured [43,44]. In other words, it is a single step reaction. Second, the activation energy should be independent of the temperature, i.e. be constant over the range of temperatures of interest. In order to predict the lifetime of polymeric materials, plotted curves can be shifted along the time axis (expressed on a log scale) to create a master curve of well-known properties such as tensile strength at various temperatures. This shift of temperature-dependent individual curves on a master curve is called time-temperature superposition. This time-temperature superposition (TTS) causes time compression and is expressed using a time shift factor α_T in equations 2-25 and 2-26.

$$\alpha_T = \frac{t}{t_{\text{ref}}} \tag{2-25}$$

$$log \frac{t}{t_{\text{ref}}} = \frac{E}{2.303R}\left(\frac{1}{T_{\text{ref}}} - \frac{1}{T}\right) \tag{2-26}$$

where α_T is the time-shift factor, t is the time, t_{ref} is the reference time, R is the ideal gas constant, E is the activation energy, T_{ref} is the reference temperature, and T is temperature. In practice, the curves with a log time scale corresponding to the aged polymer residual performance at various temperatures are shifted along the time axis until all curves become congruent. Thus a "master curve" is obtained at a certain reference temperature T_{ref}. The principle of construction of the

master curve is illustrated in Fig 2.8. Therefore, generating the master curve using the TTS will provide the activation energy of aging of polymeric materials, and the estimate lifetime at a specific temperature under service [79].
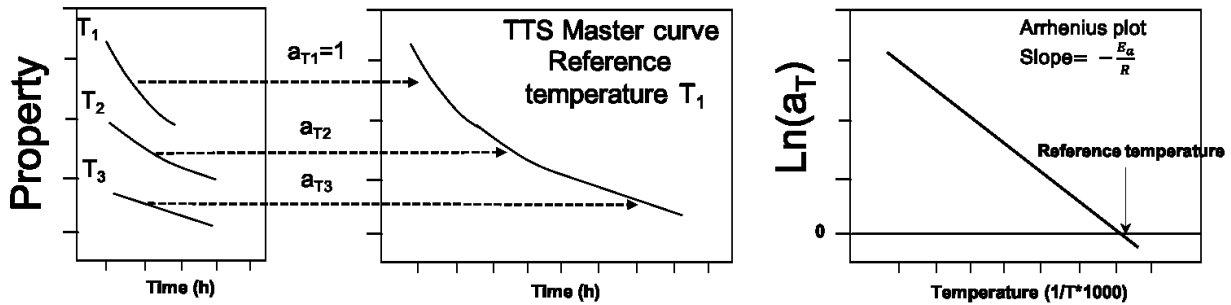
Figure 2.8 Arrhenius curves at three different temperatures (T_1, T_2, and T_3) on the left, master curve plotting in the middle, and Arrhenius plot with the temperature shift factors on the right. Reproduced from [43]

2.9 Summary

In conclusion, the degradation of textile materials/polymers is caused by various factors. In a macroscopic view of textile aging, textile materials exposed to heat, chemical, or mechanical load experience chemical changes during the multiple steps of the manufacturing process. After the manufacturing process, textile materials are exposed to mechanical and chemical actions during the use, maintenance, and storage. When the articles are folded and stored, tensile and abrasive loads may be applied. Also, when the articles are cleaned by laundering, dry-cleaning, or bleaching, they are exposed to a reactive chemical environment. During normal use, textile materials are also exposed to stimuli from daily activities, including heat, UV, and moisture.

On a micro/nanoscopic scale, textile aging is considered as a polymer aging mechanism. The aging mechanism includes the following steps: initiation, chain propagation, branching, or crosslinking between polymer chains, and termination. The critical step is an initiation. It is caused by the formation of radicals due to absorbed energy by the weakest chemical bonds. This energy

can come from different aging factors, e.g. heat, UV, mechanical actions, or moisture. Once chemical bonds break and generate radicals, the degradation process will be accelerated.

After investigation of the mechanisms of aging, various fire protective clothing materials and data available in the literature on their aging behavior were described. In section 2.7, a brief introduction was given of the assessment methods of textile materials' aging. The change in certain properties that occurs due to aging can be tracked at certain temperatures. The data will be expressed in terms of property change at different temperatures. Then, these curves will be superposed to create a master curve by applying time-shift factors. This master curve will provide information about the activation energy of the aging of textile materials and an estimated lifetime of clothing materials.

CHAPTER 3   Literature review and background on E-textiles, fabrication methods and their applications

3.1   Introduction

Traditionally, textiles have mostly been used to make clothings to protect humanity from the environment. In the later 20th century, textiles have develop into electronic textiles (E-textiles) by incorporating electronic components to fulfill unmet needs [80]. E-textiles are a subset of smart textiles, and is a promising component in making wearable electronics. Smart textiles are textile articles that has abilities to detect or adapt the changes in environment [81]. Since late 1990's, researchers have been developing garments that can monitor physiological signals for healthcare, military, or aerospace applications. One of the early demonstration was a Wearable Motherboard Garment, which had having rigid electronic components attached to a fabric substrate for Personalized Mobile Information Processing (PMIP), which came with a catchy phrase of "Fabric is the computer [82]." Since 2010's, advances in the reseaches of electronic soft materials are converting the rigid and non-flexible electronic products to flexible and wearable formats; E-textiles are gradually achieving form factors that are fully compatible with traditional garments with a broad spectrum of functions [81].

The growth of E-textiles is also aided by the implementation of conductive polymers and transistor-based technologies [83,84]. Furthermore, the use of electrically functional yarns has led to a facile integration with electronic components with E-textiles. Advances in material science and electronics have led E-textiles to be worn comfortably while fulfilling aesthetic and functional requirements [81,83]. Figure 3.1 shows a timeline for the evolution of E-textiles [83]. The first generation of E-textiles was based on adding external circuitry or electronics to a garment, and it

introduced the concept of "wearing a computer". The second generation of E-textiles implemented functional fabrics containing switches or sensors with wiring interconnects. In third generation, functional yarns have been utilized (e.g. LED yarns) [83,85]. The various types of conductive fibers have been used in each generation.
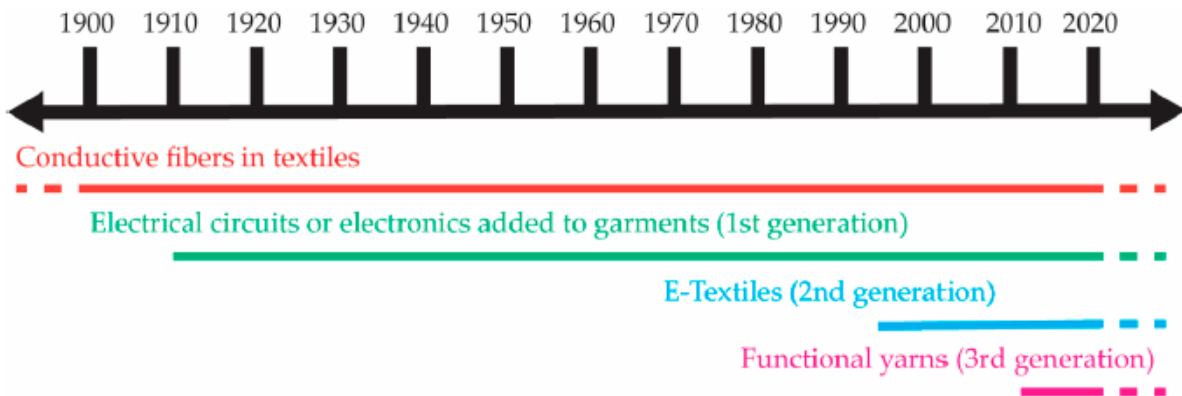
Figure 3.1 A timeline of the 1st to 3rd generation of E-textiles. Reprinted from [83]

E-textiles consist of sensor, actuators, and power source (battery). The sensor offers the information (signals) about the wearer, environment or the textile itself, actuator acts upon the detected information (signals), and the power source operates entire system [86]. This information can be transmitted by a wireless connection (Bluethooth®) [87]. In order to communicate among components, all components must be connected to each other with stable interconnects. Conductive fibers or fabrics can be used for these interconnects. The next section will introduce how to fabricate conductive fibers/fabrics.

3.2 Fabrication of electrically conductive components in E-Textiles

Nanomaterials can be integrated in textiles to achieve various functionalities [88]. One of the major challenges in E-textile research is obtaining and maintaining electrical conductivity in textile assemblies [89]. Several strategies, including metalized fabrics, coatings of conductive polymers, and conductive particles/polymer composites, have been pursued. The conductive traces can be fabricated in the form of fibers/yarns or printed patterns [89,90]. For example, graphene-based materials, carbon nanotubes (CNTs), or carbon nanofibers (CNFs) have been coated on textiles to make textiles electrically conductive. As another example, the electro/melt spinning technique has been utilized to produce of carbonized polymeric micro/nanofibers, followed by a spinning and then weaving processes to fabricate conductive carbon fabrics. Conductive fibers or yarns may be interlaced to textiles by sewing, embroidery, weaving, or knitting [81,91,92]. Table 3.1 shows a list of fabrication techniques of e-textile and their attributes.

Table 3.1 Comparison of e-textile fabrication techniques and their attributes. Reproduced from [93]

Fabrication techniques	Machinery costs	Material costs	Process complexity	Resistance to wear
Coating	High	Low	Low	Low
Embroidery	High	Low	High	High
Braiding	Low	Low	Low	High
Spinning	Low	Low	Low	Low
Knitting	Low	High	High	Low
Non-Woven	Low	Low	Low	Low
Weaving	Low	High	High	High
Sewing	Low	Low	Low	High

3.2.1 Electroplating and electroless plating of metal layer

Electroplating and electroless plating of metallic coating layer are among commonly used methods to produce textiles with electrical conductivity [94]. The electroplating methods require the externally applied electric current to grow metal layer on a cathodic surface, whereas electroless plating harnesses autocatalytic reduction of metal cations in liquid bath without the necessity of electric current. A few notable reports include an electroplating of gold layer on Kevlar® fibers and an electroless plating of copper layer deposition on cotton yarns, which achieved the conductivity of 1.02 S/cm and 1 S/cm, respectively [95,96]. The metal plating methods have a merit of high purity and conductivity values, but their reported limitations include coating duarbility, production cost, and surface uniformity [94].

3.2.2 Coating of conductive polymers and nanomaterials

Various non-electrochemical coating methods are utilized to produce conductive fibers [81,97,98]. Vacuum deposition method, such as sputtering of copper is among the commonly used methods [99]. The solutions of conducting polymers or polymer composites with conductive components are versatile in many economic production methods such as ink-jet printing [100], wet spinning [101], screen printing [102], micro-contact printing [103], spray coating [104], and dip coating [101].

Conducting polymers such as polypyrrole (PPy) [105], polyaniline (PANI) [106], and polythiophene (PT) are commonly used in E-textile-based sensor and actuator applications [107]. In some cases, conductive polymers contributes in improving the mechanical properties of the fabric substrates. For example, PPy coated on cotton enhanced the tensile strength of the fabric by 30 % [108]. PANI has three different redox forms depending on its oxidation level, whose conductivity level varies by one to 10 orders of magnitudes, which renders the material suitable

for various sensing applications [109]. PT and its derivatives can be either conductive or semiconductive; semiconductive forms are commonly used in field-effect transistors on flexible logic circuits [110–112]. Due to low-cost production, lightweight, and flexibility, these conductive polymers can be easily integrated into textiles.

However, there is still a challenge for finding a balance between the electrical conductivity, comfort, and flexibility of textiles [110]. Carbon-based nanomaterials coatings have been addressing this challenge to develop imparting electrical conductivity to textile and maintaining conductivity of coated textiles during the service. A polyelectrolyte/multiwall carbon nanotube composite coating applied to cotton threads had a capacitance 20 times higher than that of pristine CNT fibers [113]. Another approach to achieve the balance has used a combination of gold nanoparticle and poly(3,4-ethylene dioxythiophene (PEDOT) for conformal coating of cotton fibers [114]. In situ polymerization of PEDOT created a polymeric bridge between nanoparticles, which provided stability to the material under mechanical deformation.

A common method for coating graphene onto fibers and fabrics is dip coating [115]. Due to its easiness in the processing method of graphene oxide reduction by immersing the fabrics in graphene oxide (GO) solution and then reducing the GO with reducing agents, graphenic materials are popular in the E-textile field. Graphene coatings have been applied onto various fabrics including Nylon 6 [116], cotton [116], and lycra [117]. Reduced graphene oxide (rGO) has excellent mechanical strength and coating stability. The π-π stacking structure in rGO layers provided strong interaction between rGO sheets and other nanoparticles [117]. This interaction results in the formation of a stable coating and improvements in the mechanical strength of the coated substrate. Table 3.2 lists examples of the applied coating techniques on various textiles to achieve electrical conductivity.

Table 3.2 Textile coating techniques and coating materials. Reproduced from [97]

Coating technique	Textile material	Coating material
Dip coating	Polyamide fibers	PEDOT[118]
Inkjet printing	Nylon66	PEDOT:PSS[119]
Chemical polymerization	Woven Fabric	PPy/PET[120]
Wet spinning	Fabricated microfibers	PEDOT:PSS [121]
Electrochemical deposition	Nylon, Polyester	Polyaniline[122]

3.2.3 Printing of conductive inks

Generally, conductive inks contain a high fraction of highly conductive metallic components such as gold nanoparticles, silver, and copper, binder and solvent [81]. Formulated inks can be printed on various substrates, including textiles, to make electrically-conductive patterns. Among the printing methods, screen printing is attractive due to its capability of producing patterns quickly [123–125]. Screen printing can be applied on flat or cylindrical substrates to provide conducting lines on inorganic materials for circuit boards or antennas with a lateral resolution of 30 microns. Inkjet printing has been commonly used for low-cost and high-precision work to print conductive-ink materials on various substrates [126]. The viscosity of inks is an important factor that affects the resolution of inkjet printing; low viscosity inks typically achieve 50 μm range of resolution, which may be an issue for applications that require a high density of electronic components. High viscosity inks can be used to achieve smaller resolution, but tend to contain dispersed particles or inorganic metals that may result in a clogging issue during printing. Thus, it is necessary to optimize the ink formulation before actual printing on a substrate.

After the printing of patterns from nanoparticles-based inks, these nanoparticles are typically sintered to attain electrical percolation [127]. For example, the sintering temperature of inks with gold nanoparticles has been reported to be around 130 °C, for 1 h [128], but ink with silver nanoparticles can be formulated without sintering process or room temperature [129,130]. Another point to consider is whether the conductive inks can maintain is electrical conductivity under mechanical deformation such as bending, stretching or twisting, and the repitative exposure to the deformation modes [131]. Thus, conductive inks have been developed to be retain electrical connection between printed-patterns and electrically active components (such as integrated cicuit (IC) chips, antennas, light emitting diodes (LEDs), etc) on a textile substrate under applied mechanical stress. Thus, inks may contain additives that tune their properties for increased performance, which could include their adhesion to substrates, or the dispersion of the particles in the ink medium. In summary, an ideal conductive-ink for printing textile substrate can be characterized with the following requirements;

1. High electrical conductivity

2. Excellent adhesion to the substrate

3. Excellent printability without the risk of clogging the nozzle of the printing head

In Soft Material and Device Laboratory (SMDL) at the University of Alberta, Kumar et al. investigated the formulation of intrinsically stretchable inks that contain Au micro-particles, fluorine rubber, triethanolamine, and ketone-based co-solvent, and applied the ink to print antennas and interconnects on elastomeric substrates [132]. Qiu et al. developed an optimized formulation of stretchable conductive ink to be applied on porous electrospun polyurethane substrates, followed by jet printing to fabricate high durability E-textiles [133]. These E-textiles were used to

monitor physiological indicators of surface electromyogram (sEMG) and electroencephalogram (EEG) for human health monitoring.

3.3 Applications of E-textiles

There are several notable reviews that summarizes the applications of E-textiles [83,89,134,135]. E-textiles have been predominantly used in the field of wearable electronics, such as touch sensors [136], pressure sensors [137], electrocardiography (ECG) [138], and electromyography (EMG) [139]. The main communication method between E-textile and a remote receiver can be Wi-Fi or Bluetooth® with an additional power source. The power source should consist of thin, flat or flexible batteries that can endure washing, drying dry cleaning or ironing [140].

The most widely used E-textile application is a sensor that transduces the external stimuli into electrical signals [81]. The most notable example of the stimulus is mechanical strain due to applied pressure [137]. Even tiny pressure changes due to breathing has been detected [141]. Such strain sensors are commonly used for monitoring the movement of joints by achieving close contact to the skin [81]. It is notable that the anisotropic nature of knitted textile is the key to efficient strain sensing. For example, metal fibers were knitted to construct a piezoresistive textile that can discern the direction of deformation [134]. Here, the increase of resistance was due to the change in contact between the knitted fibers that occurs upon the stretching. After the initial increase in resistance, the resistance decreased as the gaps between the strands of yarn were reduced, allowing better contact of parallel conductivity paths [142]. This sensing concept can be applied to other types of conductive fibers, those that incorporate including conductive elastomer [143] or carbon [142]. In a similar approach, interlacing sensing fibers with non-sensing fibers can

be an effective method to achieve high sensitivity to mechanical stimuli owing to the intrinsic structural motif of the fabric [144].

In piezoresistive coating, the change in electrical resistance will be represented as a result of the applied strain to the substrate [124]. This change can be measured by the gauge factor, a measure of sensitivity of a strain sensor. The gauge factor is dependent on both the piezoelectric properties of the material itself and how the fabric substrate is deformed under applied strain. This type of material was used in the application of gloves wired to the computer that collects to finger gesture data from the user. The performance of piezoresistive sensors will depend on how many coatings performed on the substrate. Table 3.3 is listed on fiber and yarn strain sensor and their attributes.

Table 3.3 Fiber and yarn strain transducer and their attributes. Reproduced from [144]

Type	Coating material	Measurement	Sensitivity	Strain range	Characteristic
Metal fiber knitted sensor[99]	Stainless-steel fibers	Electrical resistance/surface contacts	0.75 Ω/% elongation. In linear range (10-30%)	0-30%	Knitted
Carbon knitted sensor[142]	Stabilized carbon fibers	Electrical resistance /surface contacts	3.9 tubular, 6.6 single warp	0-30% tubular 0-15% single warp	Knitted tubular and single warp
Polymer knitted fiber[145]	Carbon filled fibers in course direction	Electrical resistance/elastic deformation	Linear range ~ 1-8mm, 0.014 MΩ/mm	0-12mm extension	Flat-knitted sensor with pre-tension
Conductive thread knitted[143]	Conductive yarn, Nylon 6 with carbon	Conductive contact	Gauge factor 1.42 in 7.6-26% linear range	0-65% strain	Made with intarsia technique

In medical applications, smart fabric transducers also being used for a short-term and a long-term monitoring of patients' health conditions [146,147]. Typically, patients prefer to be treated at home, minimizing discomfort and inconvenience as possible. E-textile-based health monitoring devices fulfill these requirements, and patients can wear the device for long periods with comfort. The electro-physiological signals of patients such as electrocardiogram (ECG), electromyogram (EMG) and electroencephalogram (EEG) are collected by devices which are made of conductive electrodes embedded into the textile substrate. These devices are then worn on the relevant location on the patients' bodies. Electro-physiosignals are also useful information in the military or extreme environment fields. People who work in conditions requiring high levels of activity and /or extreme environments may experience dehydration, which can be monitored by low levels of sodium in their sweat [148]. Therefore, monitoring devices can be used to detect dehydration, fatigue, or exhaustion of people working under these conditions. Wearable electrodes can be used to collect sodium levels in sweat and process the signal to convert the electrical information. ECGs can measure the heart rate, and the electrodes for measuring heart rate can be made of textile-based with conductive yarn or stainless steel yarns integrated into on garment [149]. These electrodes must have good contact on target body sites to obtain accurate signals. Thus, embedding textile-based electrodes in tight-fitting wearable garments can help to fix the position of the electrodes during measurement of signals [150]. The EMG signal measurements are a useful technique to assess physiotherapy treatment of gait cycle disorders or stroke rehabilitation [151]. In addition, EMG technique can be used in prosthetic devices, and neuromuscular diagnostic tests. Myoelectric signals are collected on the localized skin surface over skeletal muscles.

EEG is a non-invasive technique to monitor brain activity in real-time [152,153]. It measures postsynaptic potential activities of pyramidal neuron and collects biopotential signals

from surface electrodes on the scalp. For EEG recording, two types of devices may be used: (1) bulky EEG acquisition systems used in clinical settings, or (2) portable devices that do not interrupt a patient's daily routine. In order to optimize the wearability of EEG systems, textile-based electrodes are being used in EEG systems instead of conventional electrodes. Textile electrodes face a challenge in recording EEG waves due to hairs on the scalp [154]. Hence, textile electrodes are usually placed on the forehead because signals (alpha and beta waves) are collected from the frontal lobe without hairs. Table 3.4 is showed that the summary of various integrated textile-based sensors for ECG, EMG, and EEG lists and detail of their fabrication techniques.

Table 3.4 Several fabrication techniques of textile-based ECG, EMG, and EEG for the acquisition of biopotentials. Reproduced from [150]

Biopotential signal	Fabrication techniques	Conductive material	System integration	Electrode location
ECG[155]	Graphene-coated textile	Graphene	Wristband	Left and right arms
ECG[156]	Printing	PEDOT:PSS	Kimono	Chest and wrists
ECG[157]	Weaving and Knitting	Silver yarns	Chest band	Chest
EMG[158]	Knitting	Silver-plated yarn	band	Flexor carpi ulnaris
EMG[139]	Knitting	Stainless Steel	Sleeve	Upper arm and forearm
EMG[159]	Weaving	Silver-plated copper yarn	eyeglasses	Temporalis muscle
EEG[160]	Screen printing	Carbon-loaded rubber	headband	forehead
EEG[161]	Screen printing	Ag-particle/fluoropolymer composite ink	Stand-alone	Behind the ears

3.4 Summary

This chapter described the development of E-textile systems and their fabrication techniques. E-textiles started with the integration of bulky electronic components on textiles, and has since progressed towards minimizing the size of these components while meeting comfort and aesthetic requirements. Section 3.2 mainly focused on the fabrication of the main component of E-textiles: conductive yarns/fibers. In section 3.3, a brief review was given of E-textile applications in sensing or medical fields. This chapter will help to understand chapter 5, which describes the fabrication of a textile-based thermal aging sensor.

CHAPTER 4   Electrical conduction of reduced graphene oxide coated meta-aramid textile and its evolution under aging conditions[4]

4.1 Introduction

High-performance fibers are used for personal protective equipment for workers exposed to heat and fire, cold temperatures, mechanical hazards, and electric arcing [162]. In addition, these high-performance fibers are used in the automotive and aerospace industries, among others. However, these fibers may gradually lose their performance as a result of exposure to various environmental factors (heat, UV, humidity, abrasion, etc.). In fact, studies done on used firefighter protective garments, some retired and some still in service, have shown significant reductions in both mechanical performance and resistance to water penetration [72]. Large losses in the mechanical performance of fire resistant fabrics made with these high performance fibers were also observed using accelerated thermal [70,163], UV [66], and moisture[164] aging programs. Therefore, monitoring the aging process of these high-performance fibers/fabrics is critical. Still, although significant efforts have been devoted towards this goal over the last 20 years [73], there is currently no non-destructive test method that enables assessment of the residual performance of these fabrics as a result of aging [165]. End users may use perceivable physical alterations, such as visible wear or discoloration, as an indicator; however some fabrics used for firefighters' protective clothing exposed either to radiant or convective heat were reported to undergo a reduction in mechanical strength of 40 to 79% before a discoloration could be detected [163]. Other aging monitoring strategies, e.g. using sensors, should thus be explored to help ensure the

---

[4] A version of this chapter has been published as:
C. Cho, A.L. Elias, J. Batcheller, P. Dolez, H.-J. Chung., Electrical conduction of reduced graphene oxide coated meta-aramid textile and its evolution under aging conditions. Journal of Industrial Textiles. 2019.

safety and function of these materials. Graphenic nanomaterials offer interesting properties that can be applied in the development of sensors for textiles [144]. One potential application is to implement textile-based wearable electronic devices (e-textiles) in which patterned graphenic nanomaterials act as conductive traces between various components. Because of hydroxyl and carboxylic functional groups in the graphenic nanomaterials, a good bonding is obtained with fabrics and can lead flexible, washable, and wearable e-textiles [81,90,166–169]. In order to establish electrical connections between active device components, various textile manufacturing techniques, including embroidery [92], weaving [170], knitting [91], screen inkjet printing [90], and yarn coating [106], have been suggested. Among these techniques, the yarn coating method is a low-complexity process because it utilizes a finished fabric without requiring specialized printing equipment. For instance, textile electrical components have largely been produced by simply coating textiles with metals or conductive polymers [93]. Recently, graphene-coated textiles have generated much interest due to the ease of the coating and reducing process [93,171]. In particular, the "dip and dry" method and further reduction with ascorbic acid has been adopted for conventional reduced graphene oxide (rGO) coating fabrication [115,172,173]. For schematic illustration of the coating mechanism, interested readers may refer to Figure 1 in Ref [115] and Figure 1 in Ref [173].

In this study, we investigated the production of conductive tracks on fire protective fabrics using rGO coatings. The stability of the rGO tracks was studied following exposure to water immersion, laundering, and abrasion. The ultimate objective is to produce graphene-based end-of-life sensors for fire protective fabrics.

4.2 Experimental section

4.2.1 Materials

The fabric used in this study is a woven meta-aramid fabric (weave: 2/1 twill; mass: 222 g/m^2; fabric count: 31 warp x 26 weft yarns/cm; thickness: 0.38 mm). In order to investigate the scouring effect on the graphene coating process, the fabric was used as received as well as after being subjected to a pre-washing treatment involving 10 washing/drying cycles according to Procedure IIIE (40°C, tumble dry) of CAN/CGSB 4.2 No 58 [174].

The graphene oxide (GO) solution (4 mg/mL) was purchased from Graphenea, Spain. L-ascorbic acid (L-AA) from Sigma-Aldrich (Oakville, ON, Canada) was used as a reducing agent for graphene oxide. 2-propanol (IPA) was purchased from Sigma-Aldrich (Oakville, ON, Canada).

4.2.2 Preparation of the rGO coated m-aramid fabric

The m-aramid fabric (as-received or pre-washed) was cut into 2 cm x 2 cm pieces with a laser cutter (Versalaser Engraver, ULS, AZ, USA). The specimens were cleaned using deionized (DI) water and IPA, and dried at 65°C for 15 min. The specimens were then dipped into 10 mL of graphene oxide solution for 15 min and dried at 65 °C for 30 min. This "dip and dry" coating procedure was repeated to obtain different add-on masses of rGO coating on the fabric specimens (1, 5, 10, and 15 dips). Between each rGO coating, the dry specimens were reduced by immersion in 40 mg/mL of L-AA at 90 °C for 4 h. They were then rinsed with DI water and IPA, and placed in an oven (Symphony-VWR, Vacuum brand 2 C) at 80°C for 30 min. An illustration of the rGO coating process on the m-aramid fabric specimen is provided in Fig. 4.1. Except for the results shown in Fig. 4.3, the specimens were exfoliated with adhesive tape at the end of each dip-dry-reduce cycle in order to remove the rGO flakes not firmly attached to the fabric substrate.

The rGO add-on ratio can be calculated using equation (1):

$$\text{Add} - \text{on ratio} = \frac{m_n - m_0}{m_0} \times 100 \qquad (1)$$

where m_0 is the mass of the uncoated fabric specimen and m_n is the mass of "n"-time rGO-coated fabric specimen.

| Uncoated m-aramid fabric | GO coated m-aramid fabric | Reduction with L-AA | rGO-coated m-aramid fabric |
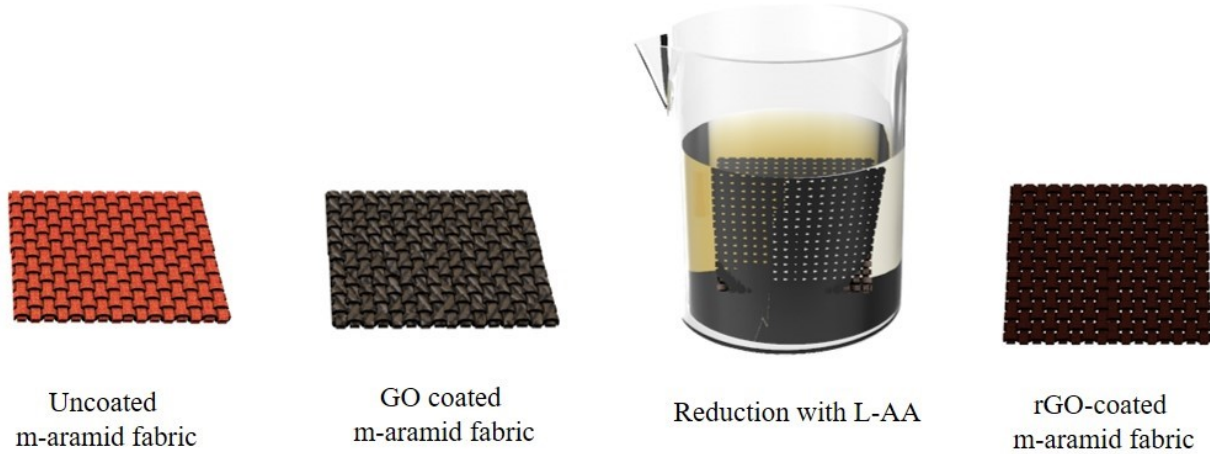
Figure 4. 1 Scheme of rGO coating process on m-aramid fabric.

4.2.3 Preparation of rGO tracks on the m-aramid fabric

To pattern rGO on a single side of the fabric specimen, a 3-inch diameter wax film was first printed on a polyethylene terephthalate (PET) film by wax printer (ColorQube 8570, Xerox). The printed wax pattern was transferred to the back side of the fabric specimen using a Bench Top Standard Heated Press (Carver, Inc, IN, USA) at 65 °C for 5 min, as illustrated in Fig. 4.2(a); this wax layer protected the back surface of the fabric during subsequent processing. Then, the wax-transferred fabric specimen was sandwiched between two round acrylic molds, one solid and the other bearing three tracks (with dimensions of 1.5 cm × 3 cm, (width, length, respectively).The mold with the tracks was positioned on the face side of the fabric, i.e. the side without the wax film. Fig. 4.2(b) shows the detail of the rGO-patterning process.

Once the molds were in place, 200 μL of GO solution was deposited onto the front side of fabric, and heat-pressure-transferred wax layer on backside acted as a mask, which was localizing the GO solution in the patterned area. The specimen was left for 30 min in an oven at 65 °C to dry specimen. After drying, the GO-tracks were reduced by immersion in 40 mg/mL L-AA solution at 90 °C for 4 h. After reduction, loose rGO was exfoliated with adhesive tape as described in section 4.2.2. This process of coating, drying, reducing, and exfoliating the rGO comprises one coating cycle and was repeated 15 times. The heat-pressure-transferred wax layer remained intact with well-defined features over all 15 coating cycles; no blurring was observed in the rGO pattern.

To prepare rGO tracks on both sides of the fabric specimens, the rGO patterning process was conducted by sandwiching the fabric between two acrylic molds bearing the three rectangular tracks. Great care was taken to ensure that the position of the tracks in the two molds corresponds. 200 μL of GO solution was used to pattern the tracks on both sides of the fabric, with a 30 min at 65 °C drying period between each side. The rest of the process was similar to what was used to prepare the single-sided tracks, including the number of coating cycles applied.
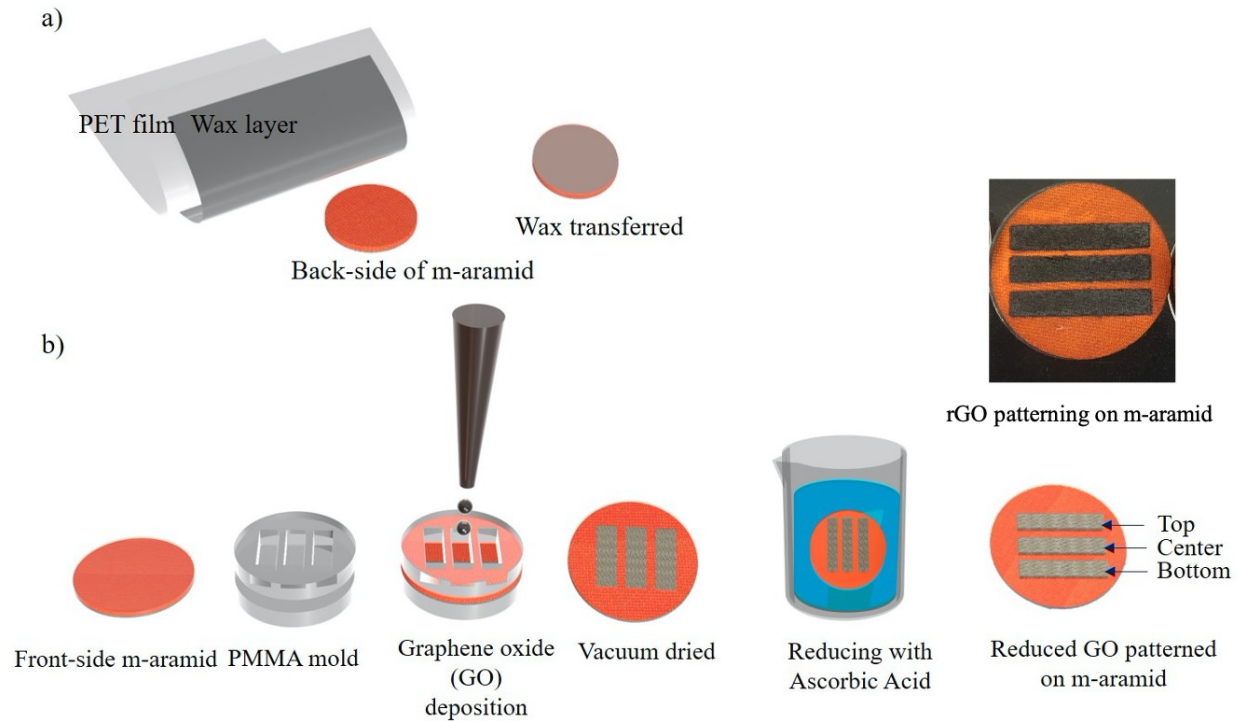
Figure 4.2 Scheme of rGO patterning on fabric specimen (a) Wax layer deposition, (b) Patterning and reduction process.

4.2.4 Specimen general characterization

The surface morphological details of the rGO-coated textile were observed by a field emission scanning electron microscope (FE-SEM, Zeiss Sigma) and Helium Ion Microscope (HIM) (Zeiss Orion NanoFab, Zeiss Sigma). The sheet resistance (R_s, unit of Ohm/□) of the rGO-coated textile was measured using a 4-point-probe (Pro4 4000, Lucas Labs, CA, USA). Three measurements were made for each specimen/condition, and the results were averaged.

The electrical resistance of the rGO-tracks was measured with a digital multimeter (Fluke 77-4 Industrial Multimeter, NC, USA). Three measurements were carried out on each rGO track, and the results were averaged. A piece of adhesive conductive silver strip was installed on each end of the rGO track. The measurement of the electrical resistance of the rGO-track was conducted by connecting the digital multimeter between the conductive silver strips under the assumption

that the resistance of the silver conductive strips and the contact resistance with the rGO track is negligible compared to the resistance of the rGO track itself.

4.2.5 Washing fastness of the rGO-coated fabric

Tests were conducted to assess the effect of repeated laundering on the electrical conductivity of the rGO tracks on the fabric. Accelerated washing was performed with a Launder-Ometer (Atlas, IL, USA) following the ISO 105-C06 standard and test procedure A1S [174]. One cycle of accelerated washing using the Launder-Ometer is equivalent to 1 cycle of domestic laundering.[5] According to this standard, 150 mL of washing solution prepared with 4 g/L of detergent was used to wash the specimens with 10 steel balls at 40 °C. Three specimens were collected from the canister after a predetermined number of washing cycles (1, 3, 5, 7, 9, and 10 cycles), where each cycle lasted 6 min. Immediately after being collected, the specimens were rinsed with DI water and dried at 65 °C for 15 min. Then, the R_s value was measured on each of the three replicates. The surface morphology of the rGO-coated fabric (before and after the different number of washing cycles) was observed by scanning electron microscope.

4.2.6 Martindale abrasion resistance test of the rGO-coated fabric

The resistance of the rGO coatings to wear was assessed by submitting the specimens to abrasion cycles using a Martindale abrasion tester and then measuring the residual electrical conductivity. The abrasion test was carried out with a M235 Martindale Abrasion Tester (SDL Atlas, Rock Hill, SC, USA) following the ASTM D4966 standard [175]. In accordance with the standard, the rGO-coated fabric specimens were abraded using standard wool abradant fabric with

---

[5] The published paper mistakenly reported that the washing cycle applied in this study using the Launderometer was equivalent to 5 cycles of domestic laundering. In addition, test procedure of ISO 105-06 standard was reported A1M. The correction has been made here that the washing cycle applied is equivalent to 1 cycle of domestic laundering, and that the test procedure is A1S.

a 47.5 rpm abrading speed. In order to accommodate the small size of the specimens, they were mounted on the three top (mobile) fabric holders while the wool abradant fabric was installed on the bottom (stationary) fabric holders. After a defined number of cycles, the abrasion tester was stopped, the specimen was removed from its holder, and the specimen's electrical conductivity was measured. Then, the specimen was mounted again on the specimen holder for another series of cycles. The test was conducted on specimens bearing single- and double-sided rGO tracks.

4.2.7 Water immersion resistance of the rGO-coated fabric

The resistance of the rGO-coated fabric to water immersion was assessed by measuring the electrical resistance R_s of the specimens after a 24 h immersion in DI water at room temperature followed by 30 min drying at 65 °C in an oven. The 24 h immersion was repeated 5 times on each specimen, for a total of 120 h.

4.2.8 Statistical Analysis

Measurements were generally performed three times, and average values and standard deviations are reported. Where applicable, statistical significance was evaluated using the single factor ANOVA analysis.

4.3 Results and discussions

4.3.1 Effect of rGO-coating conditions

As the initial fabric condition may affect the rGO-coating performance, trials were conducted using the m-aramid fabric in two conditions: as-received and pre-washed (see procedure in Section 4.2.1). Pre-washing is considered a scouring process as it removes non-permanent textile finishes and other impurities from the surface of the as-received fabric [176]. The removal of strongly hydrophobic contaminants from the surface of the fabric may enhance its affinity for GO, but may also create a rougher surface which is harder to coat with a small number of layers.

Fig. 4.3 shows the variation in the rGO coating sheet resistance as a function of the number of coating cycles for the two initial conditions of the fabric. When collecting this data, no exfoliation was applied between the coating cycles. For each type of fabric, an increase in the number of coating cycles – and correspondingly the amount of rGO deposited – led to a reduction in the rGO sheet resistance.

Fig. 4.3 also showed markedly different R_s values up to the 2nd rGO coating for the as-received and pre-washed fabric conditions: the rGO coating on the pre-washed m-aramid initially had a lower R_s than the rGO coating on the as-received fabric. This indicates that the washing treatment was effective at improving the GO affinity and bonding with the m-aramid fibers. The difference in R_s between the two initial fabric conditions disappeared after the 2nd rGO coating cycle. This implies that two coating cycles were sufficient to coat the m-aramid fibers at the surface of the fabric with rGO sheets. Further coating cycles added new GO layers on top of the underlying rGO layers, i.e. without any contact with the m-aramid fabric. This can be evidenced by the lower drop in the rGO coating sheet resistance and the absence of significant difference between the as-received and pre-washed conditions after the 3rd coating cycle (see inset in Fig. 4.3). After 15 coating cycles, the sheet resistance of the rGO coating on the m-aramid fabric reached a value in the range of 10 $\Omega/\square$. As a comparison, the sheet resistance of uncoated m-aramid fabric is more than 10^{16} $\Omega/\square$.
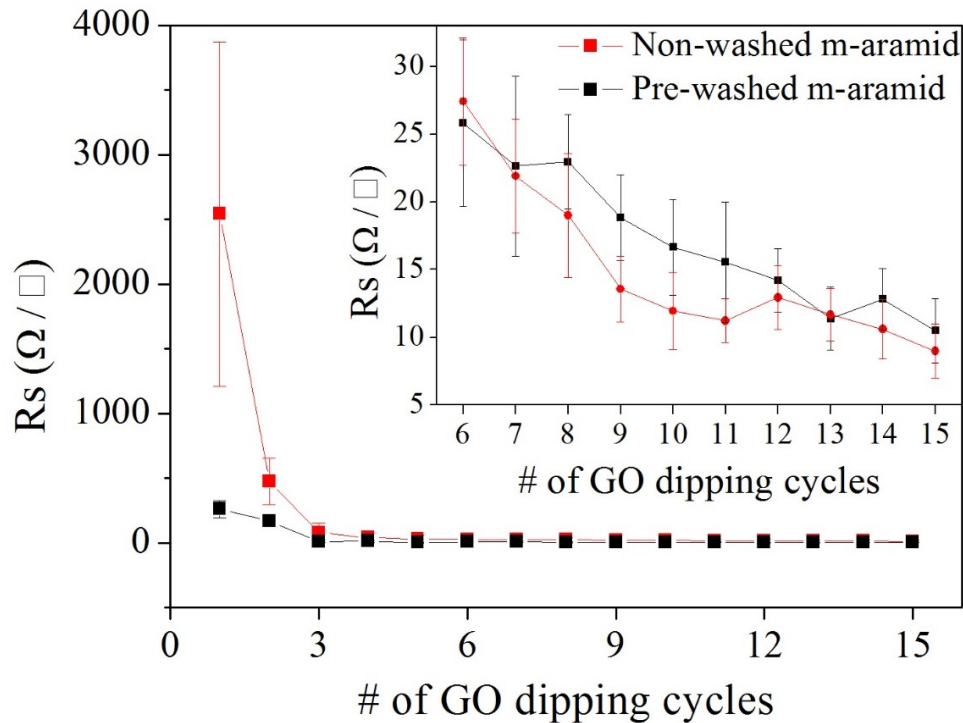
Figure 4.3 Sheet resistance (R$_s$) of rGO coating as a function of the number of coating cycles (including coating, drying, and reduction, but without the exfoliation step) for the two initial conditions of the m-aramid fabric, as-received and pre-washed (Inset: scale-up of the low resistance part of the curve)

The left column of Fig. 4.4 shows FE-SEM images of the rGO-coated m-aramid fabric after five, 10, and 15 successive coating cycles without the exfoliation step. With successive rGO coatings, the shape of the fibers becomes less and less pronounced, suggesting that the rGO sheets first covered the m-aramid fibers and then built up in layers; after the 15th rGO coating (Fig. 4.4(c)), the fibers are no longer visible as the rGO has created a smooth surface layer. However, these stacked rGO layers would likely be easily damaged when the fabric is bent or folded (the large crack in the middle of Fig. 4.4(c) may have resulted from mechanical deformation). In addition, the images of the layers produced without exfoliation suggests the presence of a number of loosely attached rGO sheets on the fabric surface. Ideally, the rGO layers should not cover the entire fabric surface but should wrap around the individual fibers. Consequently, the coating process was

modified to include an rGO exfoliation step between each coating cycle (see Section 4.2.2). The right column of Fig. 4.4 shows FE-SEM images of the rGO-coated m-aramid fabric (after 5, 10, and 15 successive coating cycles) with this added exfoliation step. These specimens were prepared using the as-received fabric. A comparison between left and right column of Fig. 4.4 shows that for the coatings prepared with the exfoliation step, rGO sheets appear to wrap around the individual m-aramid fibers and the number of loosely attached graphene sheets is strongly reduced. The HIM image in Fig. 4.5 illustrates that the rGO sheets completely and conformally cover the surface of individual m-aramid fibers. Here, a stark contrast is achieved between insulating (m-aramid) and conducting (rGO) components as HIM imaging is free from charging-inflicted artefacts in the insulating regions.
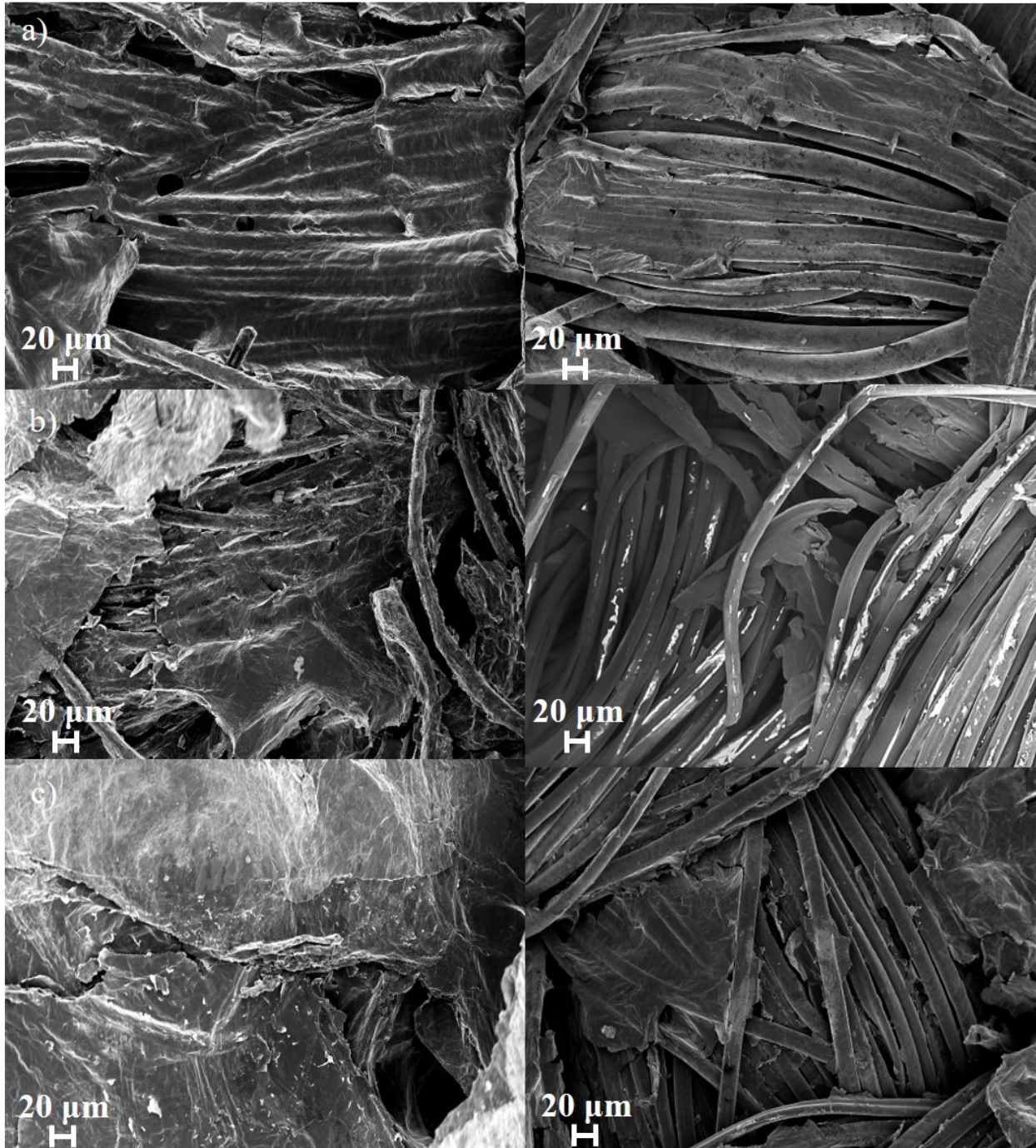
Figure 4.4 FE-SEM images of rGO coating on as-received m-aramid fabric prepared (left column) without and (right column) with the exfoliation step. Samples were imaged after a) 5th rGO coating, b) 10th rGO coating, and c) 15th rGO coating.
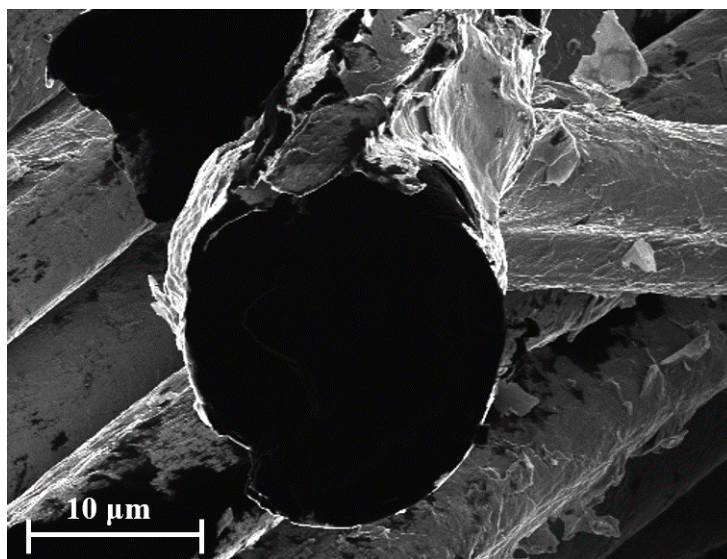
Figure 4.5 Helium-ion microscope (HIM) image of rGO wrapped individual m-aramid fiber. The black area in the center of the image corresponds to the uncoated cross-section of the fiber.

The rGO add-on ratio as a function of the number of rGO coating cycles is shown in Fig. 4.6. The specimens were prepared using the as-received m-aramid fabric. The specimen preparation included the added exfoliation step after the rGO reduction step. It is observed that the rGO add-on percentage increases with the increasing number of rGO coating cycles. The rGO add-on ratio was 9 ($\pm$ 1) % after 15 rGO-coating cycles, corresponding to an add-on weight of 7.3 ($\pm$ 0.99) μg. Previous studies reported rGO add-on weight percent on woven cotton fabric of 3.31 % with 15 coating cycles of immersion in a 2.25 wt% GO solution concentration [171]. The higher add-on ratio observed in our study may be due to the difference in the GO content in the coating solution, which was 4 wt% in our study.

The inset in Fig. 4.6 shows the R_s values of the corresponding rGO coating at the 5th, 10th, and 15th dipping obtained with the added exfoliation step included in the coating cycles. The resistance values observed for a given number of cycles are much higher than for the same number of cycles without exfoliation (Fig. 4.3). This can be attributed to the fact that exfoliation removed

the extra rGO sheets loosely deposited over the fabric surface, leaving only a coating around the individual fibers. Even if the exfoliation process leads to a decrease in conductivity of the rGO track, it is essential to ensure that the fabric normal use conditions (folding, bending, etc.) do not affect the electrical performance due to the presence of loosely bonded rGO sheets.
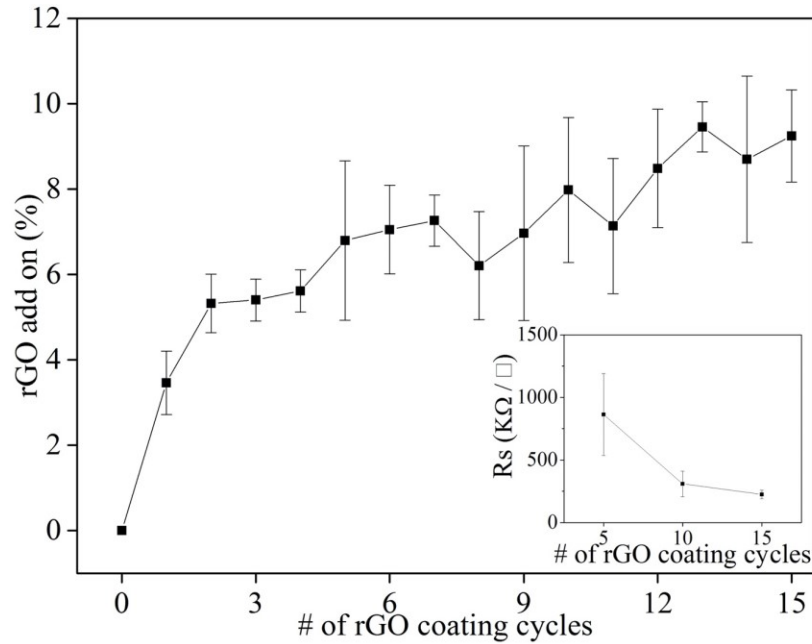
Figure 4.6 Variation in the rGO add-on as a function of the number of rGO cycles for the as-received m-aramid fabric (where the exfoliation step was included between each coating cycle) (Inset: sheet resistance (R_s) versus the number of rGO cycles)

4.3.2 Washing fastness

One of the greatest challenges for a textile-based sensor is related to launderability. The mechanical stresses applied during the washing process may destroy the electrical interconnects [177]. The presence of water, high temperature and detergent chemicals may also affect textile-based sensors, particularly if the sensors cannot be coated by a protective layer without affecting their function (as is the case for our devices). In order to investigate the washing resistance of the rGO-coated meta-aramid fabric, the R_s of rGO-coated textiles was characterized after selected numbers of washing cycles. As shown in Fig. 4.7, the average R_s of the rGO-coated m-aramid

textile with 5 rGO coating cycles (including the exfoliation step) was 863 ($\pm$ 179) kΩ/$\square$ before washing, and increased to 1.3 ($\pm$ 0.4) MΩ/$\square$ after 10 washing cycles. On the other hand, the R_s values of the samples that underwent 10 and 15 coating cycles increased by only 3.3% and 11.2%, respectively, after 10 washing cycles. An single factor ANOVA was performed on the data. The results of the ANOVA identify no statistical difference in R_s between the number of washing cycles for samples with 10 and 15 rGO coating cycles, with p-values of 0.16, and 0.29 (Total sample size n = 42) respectively. On the other hand, for samples with 5 rGO coating cycles, the p-value is 7.68×10^{-6} (Total sample size n = 42), which points to statistical differences in R_s between the washing cycles. This implies that 5 rGO coating cycles are not enough to obtain stable electrical conductivity, and a minimum of 10 rGO coating cycles is required if that the rGO-coating on the m-aramid fabric will endure at least 10 domestic laundering cycles without a significant loss in electrical conductivity.

Fig. 4.8 and Fig. 4.9 show FE-SEM images of fabric samples prepared with 5 and 15 rGO coatings, both before washing and after 1, 5, and 10 washing cycle(s). For samples prepared with 5 GO coating cycles (Fig. 4.8 (a) to (d)), the rGO coated layer on m-aramid fabric became cracked as the number of washing cycles increased. It is possible to see some rGO sheets partially peeling away from the fibers after 10 washing cycles (Fig. 4.8d). This failure of the rGO fiber covering explains the increase in the electrical resistance with the number of washing cycles for the 5 rGO coated samples that was observed in Fig. 4.7. On the other hand, for samples prepared using 15 rGO coating cycles (Fig. 4.9 (a) to (d)), no signs of cracking or delamination are observed, and the rGO sheets remain wrapped around the fibers. This observation is in agreement with the stable resistance recorded for up to 10 washing cycles.
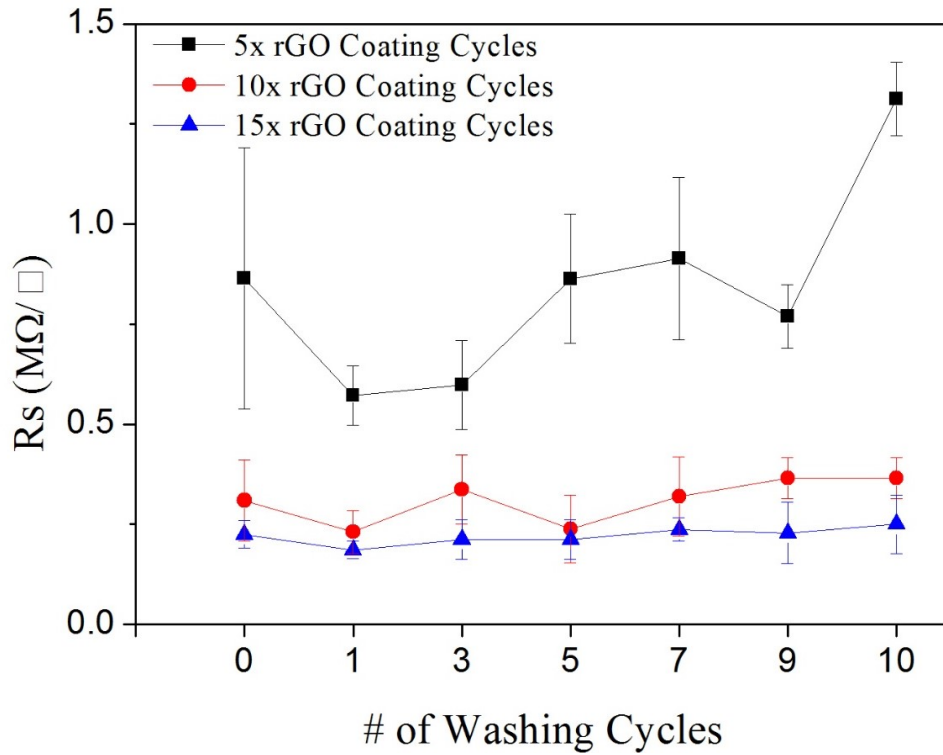
Figure 4.7 Effect of up to 10 accelerated washing cycles on the sheet resistance (R_s) of m-aramid fabric with 5, 10, and 15 rGO coatings
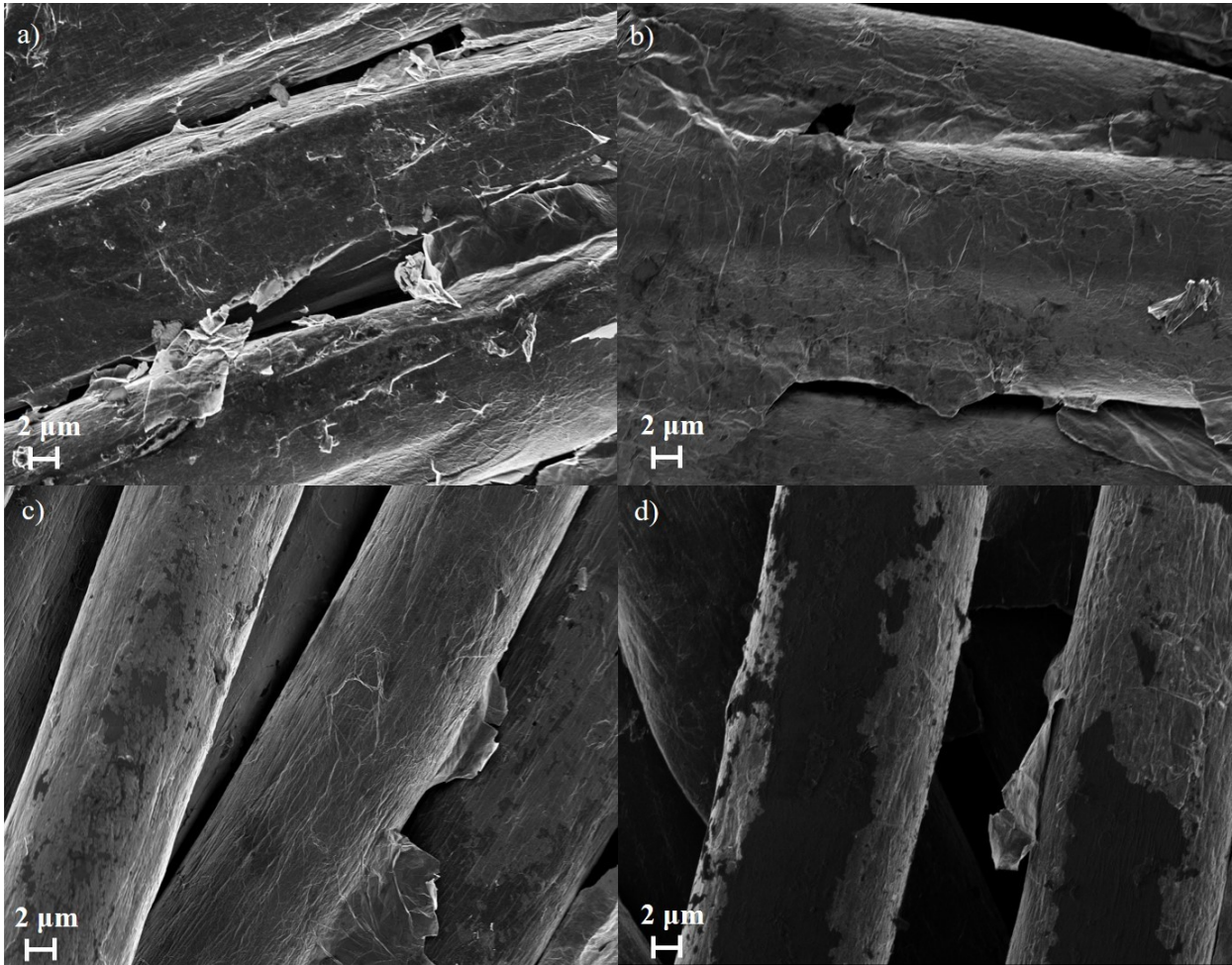
Figure 4.8 FE-SEM images of m-aramid fabric with 5 rGO coatings on m-aramid textile a) before washing, b) after 1, c) 5, and d) 10 accelerated washing cycles.
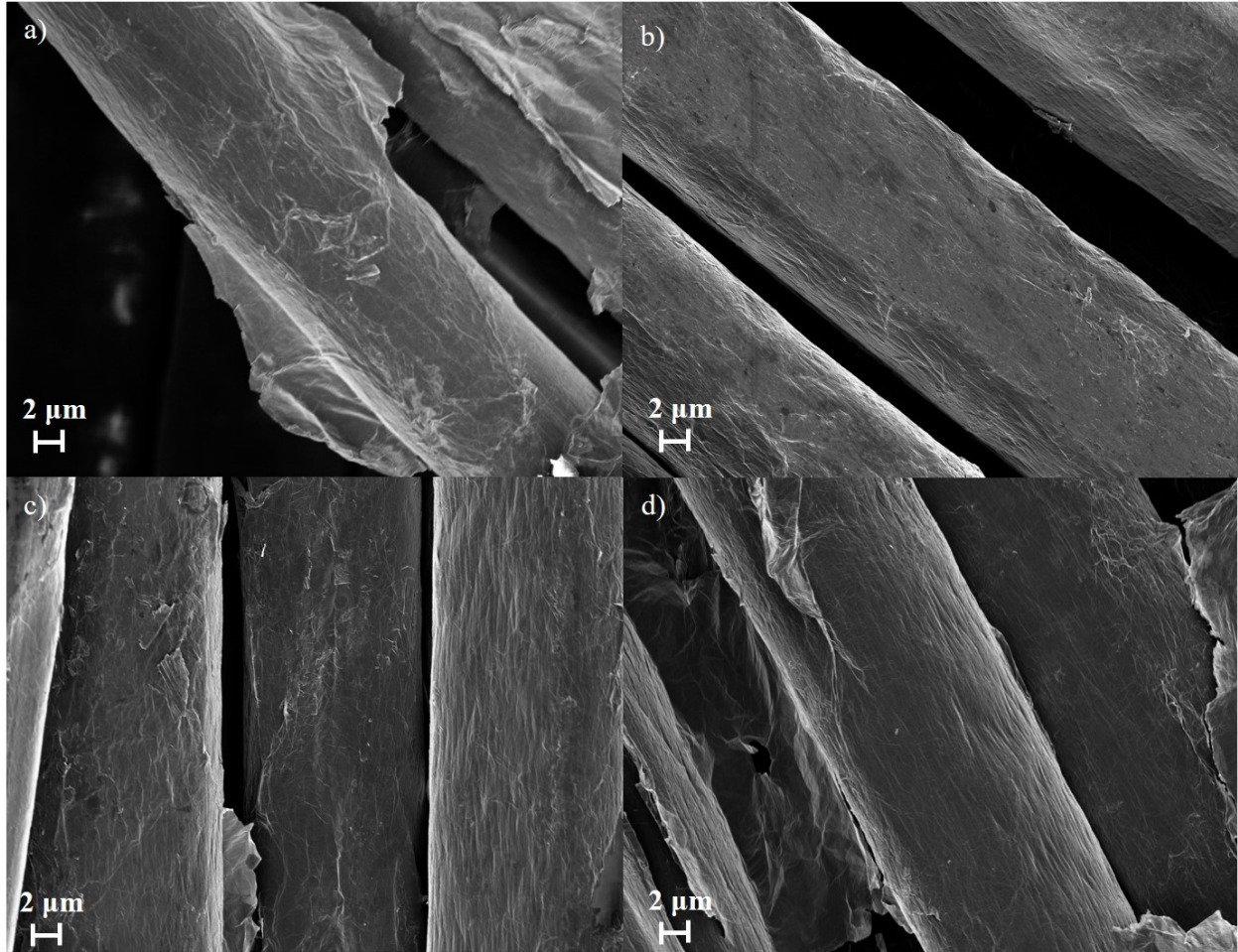
Figure 4.9 FE-SEM images of m-aramid fabric with 15 rGO coatings on m-aramid a) before washing, b) after 1, c) 5, and d) 10 accelerated washing cycles.

4.3.3 Stability of the rGO coating upon water exposure

During use, fire-resistant fabrics may be exposed to varying sources of humidity including rainy environments, the wearer's perspiration, and immersion in water. One mechanism by which water can swell fibers is by generating voids and microcracks at the fiber-matrix interface [177,178]. Therefore, conductive traces on fabrics may be damaged when the textiles are exposed to water.

In order to study the rGO coating stability under water exposure, I immersed 2 cm × 2 cm, 15 rGO-coated m-aramid fabric specimens in water for up to 5 days, and the electrical resistance

of the fabric was measured every 24 h. Fig. 4.10 shows the R_s value of the specimens measured after each 24 h period. Differences in R_s measured after each 24 h period of immersion in water were not statically significant (with a p-value of 0.73, total sample size n = 18).
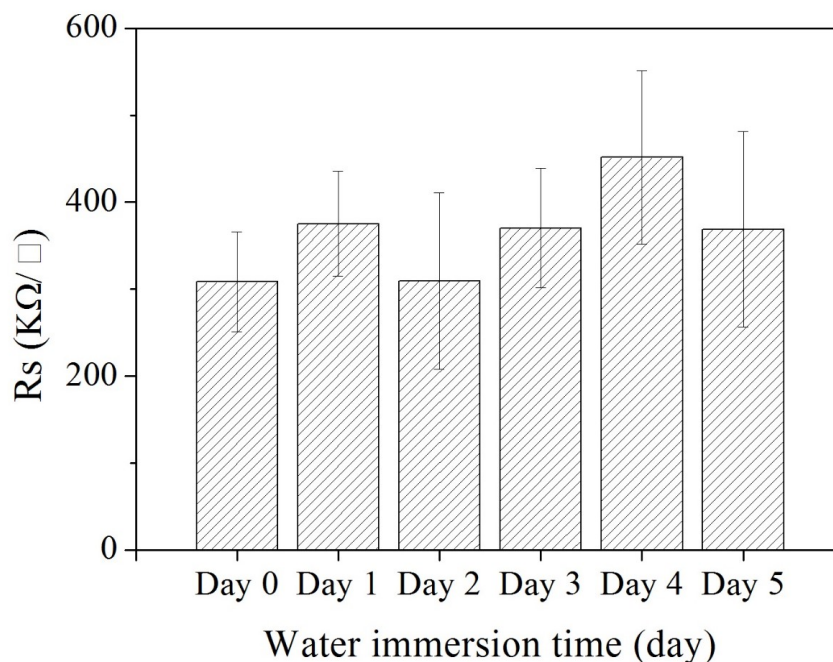
Figure 4.10 Variation in the sheet resistance of 15th time rGO-coated fabric as a function of immersion time in water

The moisture regain of meta-aramid fibers at 65% relative humidity and 21°C (standard conditions for textile testing) is reported to be 4.5% (by weight) [179]. In addition, a technical sheet on m-aramid paper reports that – as a result of moisture vapour absorption under 96% relative humidity at room temperature – the m-aramid fibers expand approximately 1%, 2.5% and 4% in the warp direction, the weft direction, and the thickness, respectively [180]. However, a close look at Fig. 4.5 reveals that the rGO coating on m-aramid fibers is rather scaly and that some free volume exists between the graphene layer and the fiber. The graphene sheets may also have the ability to slide relative to each other and accommodate the limited swelling of the aramid fibers upon water immersion. This may explain in part why the rGO coating layer was able to maintain

its electrical conductivity after water immersion for up to 5 days. In addition, the hydrophobic nature of the rGO coating may limit water adsorption on the fiber surface.

4.3.4 Resistance to abrasion

Abrasion resistance is an ability of textile materials to resist contact rubbing or surface wear. Thus, abrasion testing is an important assessment to predict the behavior of textiles in real life conditions [181]. In order to characterize the abrasion resistance of rGO-coating on m-aramid fabric, a coating procedure was developed to prepare rGO tracks on the m-aramid fabric (section 4.2.3). The abrasion testing was conducted in accordance with ASTM D4966 [175], using the methodology described in section 4.2.6.

Each specimen was patterned with three parallel, rectangular rGO tracks. The abrasion tester has discs of worsted wool abradant, and these discs rub the specimen with a trajectory of Lissajour curve[182]; in other words, the center part of the specimen is more frequently abraded compared to the peripheral parts. As a result, the resistance of the center rGO track increased more quickly than those of the top and the bottom ones. Fig. 4.11 (a) shows the variation in electrical resistance as a function of the number of abrading cycles for rGO tracks deposited on one side of the fabric. The resistance gradually increased with the number of abrasion cycles until it reached 150 cycles. Afterwards, the resistance jumped abruptly out of the instrument range (measuring up to 60 MΩ, corresponding to 1 M$\Omega/\square$ in R$_s$), which indicated that the electrical conductivity was completely lost. Fig. 4.11(a) also shows that above 50 cycles, a marked difference in conductivity loss occurs between the track situated in the center of the specimen and the two tracks on each side. This is attributed to the inhomogeneous pressure distribution across the abrasion sample holder surface area created by the foam padding between the sample holder and the specimen.

Below 50 abrasion cycles, the high resistance measurement variability prevents distinguishing between the behavior of the three tracks.

As an alternative approach to maintain electrical conduction against rGO loss from abrasion, tracks were formed on both sides of the fabric. The protocol developed (Section 4.2.3) ensured that the tracks on one face of the fabric were exactly superimposed over the tracks on the opposite face. Fig. 4.11 (b) shows that the two-sided rGO tracks undergo a moderate decrease in electrical conductivity with increasing number of abrasion cycles, but the rate is much lower compared to the single-sided rGO tracks: the resistance increase was less than a decade over 3000 abrasion cycles as compared with an increase of over two decades after only 150 cycles. This can be attributed to the almost complete penetration of the rGO coating through the fabric thickness as evidenced by the HIM cross section image of the two-sided rGO tracks shown in Fig. 4.12. The difference in the abrasion rate on the loss of electrical conductivity between the center track and the tracks on each side (labelled top and bottom) can also be observed in Fig. 4.11 (b). After 3000 abrasion cycles, the electrical resistance of the center track underwent 10-fold increase while those of the two other tracks increased by ~4 times.
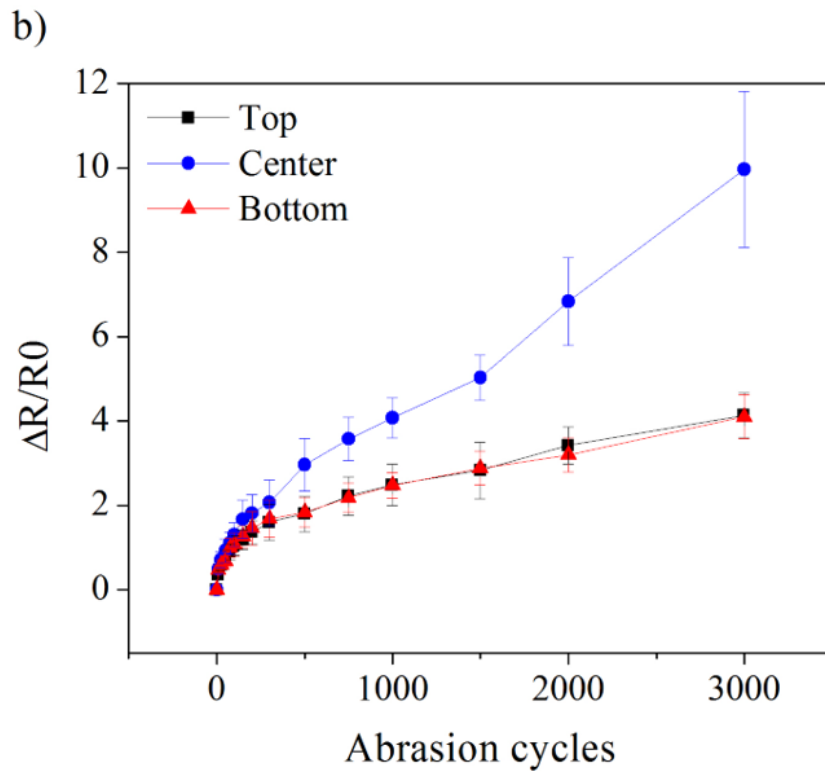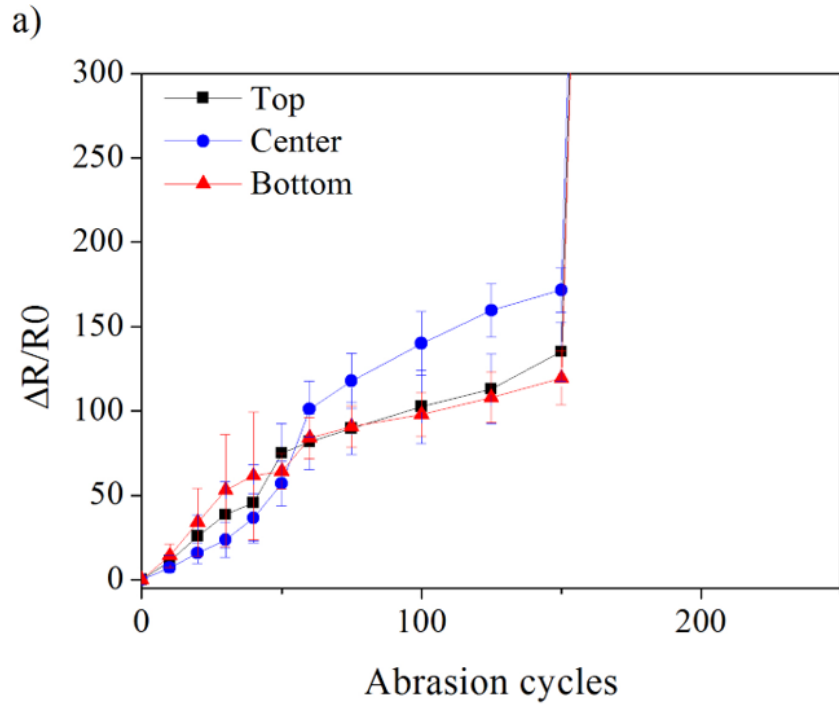
Figure 4.11 Influence of Martindale abrasion on resistance of a) single-sided rGO tracks, and b) double-sided rGO tracks. (Top, center, and bottom labels correspond to the location of the three tracks on the specimen).
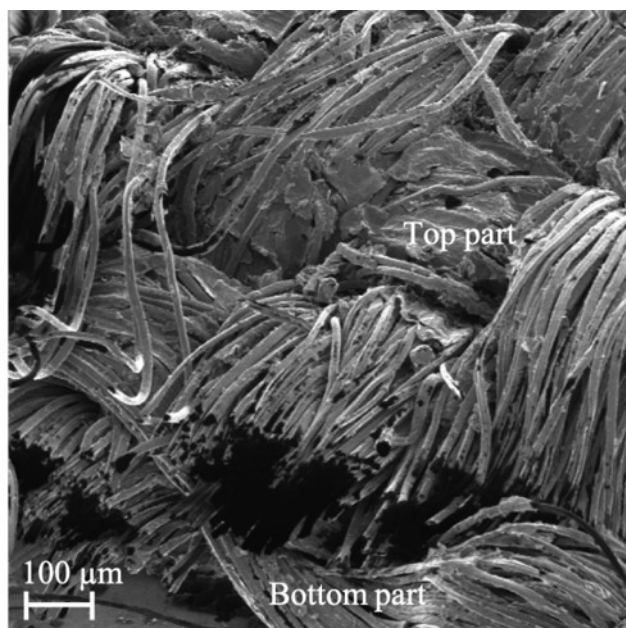
Figure 4.12 Bird's eye view (54° tilting) on the cross-sectional area of the m-aramid fabric sample with two-sided rGO tracks (top and bottom fabric parts are indicated; insulated area appears solid black). Helium Ion Microscopy (HIM) was used for imaging.

4.4 Conclusions

The objective of the present work with an m-aramid woven fabric was to establish a protocol of stable rGO coating that loses its conductivity by controlled abrasion. The underlying motivation of this study is to apply the stable rGO coating with controlled conductivity loss as a platform for an end-of-life sensor for high-performance textiles. In order to achieve the stable rGO coating, up to 15 iterations of "dip and dry" method was applied with exfoliation step at the end of each cycle. This wrapped rGO coating did not show any sign of degradation in conductivity under 10 accelerated washing cycles (equivalent to 10 domestic washing cycles) and under water immersion (up to 5 days). Under abrasion cycles, on the other hand, a systematic degradation behavior was observed.

Another point to highlight is our heat-pressure-transfer protocol of wax printed patterns. This simple technique allows selective coating of rGO on fabric to form high fidelity patterns, whereas the pattern can simply be fabricated by a commercial desktop wax printer.

In future studies, I envision that our rGO patterning technique can be used to prepare an aging

indicator for high-performance fabrics such as m-aramid. These laundering and abrasion

behavior of these rGO tracks can be tailored to match the requirements of the sensor design; this

opens large opportunities for the application of graphenic nanomaterials as end-of-life sensors.

CHAPTER 5 Investigation of the accelerated thermo-oxidative aging behavior of polyetherimide and lifetime prediction at elevated temperature

5.1 Introduction

High-performance polymers are often engineered to withstand extreme conditions, such as high temperature, ultraviolet (UV), chemical, or moisture, for various industrial applications such as the aerospace [183], automotive [184], or nuclear power plant industry [8]. For example, poly etheretherketone (PEEK) has high temperature and chemical stability [185], polysulfone (PSU) is flame retardant and has good chemical resistance properties [186], polyphenylene sulfide (PPS) is resistant to high temperatures and chemicals [187], polyimide (PI) has great mechanical properties, thermal stability, and chemical resistance [188], and polyetherimide (PEI) is a thermoplastic polymer with excellent mechanical and high temperature resistance properties [189]. Due to the potential catastrophic impact of a premature failure due to exposure to the service conditions, the estimated service life must be considered when selecting a particular polymer for a specific application.

Resistance to thermal aging and the prediction of service life are also critical components in the development of end-of-life sensors for fire protective fabrics. Therefore, if a high temperature resistant polymer has a similar thermal aging behavior and service life as outer shell fabrics used in fire protective clothing, this polymer can be used as the sensitive layer in a thermal end-of-life sensor for these fire protective clothing. PEI has been selected for this study because PEI and m-aramid (which is a widely used fiber in outer shell fabrics in fire protective clothing) produce the

same type of degradation by-products above 550 °C [190], and PEI also has a high temperature resistance.

PEI has several functional groups in its backbone: aromatic imides, propylidene, and ether groups, as illustrated in Fig 5.1. Aromatic imide groups provide stiffness and high thermal stability while the ether groups offer good processability due to low melt viscosities [184]. In addition, PEI has an excellent stability in hydrolytic environments, such as diluted bases and mineral acids (for short-term contact) [184]. Therefore, PEI has been used in applications under high temperature and moisture [191] such as electronics [192], automotive (i.e., vehicle headlamp) [184], medical [193] and aircraft applications.
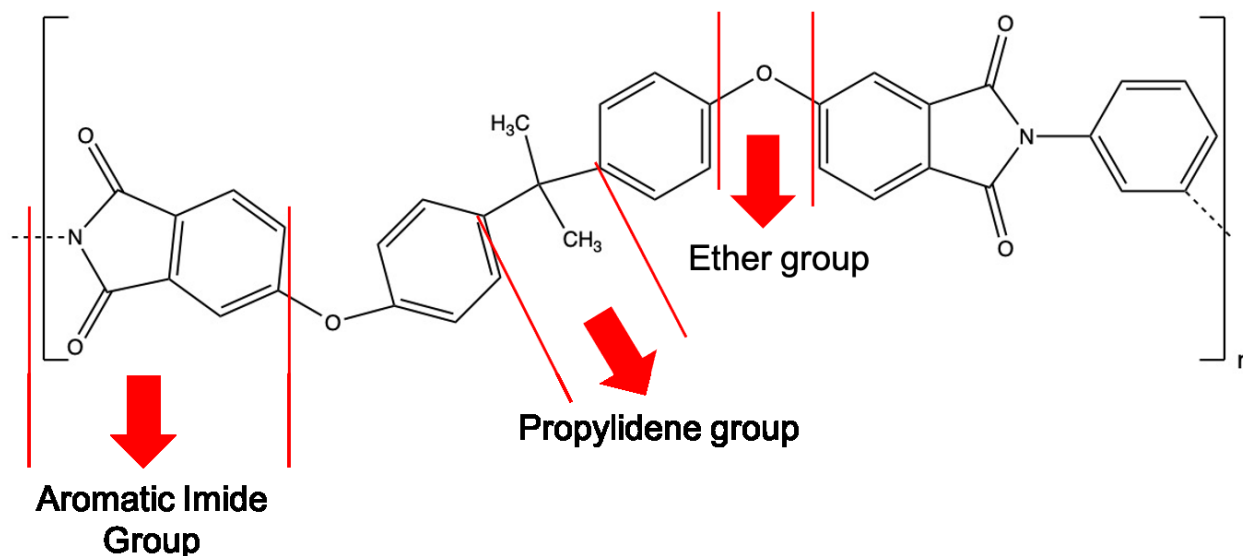
Figure 5.1 Chemical structure of PEI and its functional groups. Reprinted from [189]

The thermal degradation behavior of PEI has been studied and possible degradation mechanisms have been suggested [189,190]. Amancio-Filho et al. investigated PEI plates that were joined by friction riveting (FricRiveting) and thermally degraded because of that [189]. They observed that the chemical properties of the PEI plates changed depending on the rotating speed of the aluminum rivet. The heat generated led to a temperature increase of 350 °C to 475 °C

depending on the rotating speed of the rivet (1570 to 2200 rad/s). These temperatures are above the range of chain scission in PEI. This explains why the molecular weight decreased by 10 % at the highest rotating speed. FTIR analysis showed that the absorbance of the main groups of PEI decreased with increasing rotation speed.

Carroccio et al. investigated thermal degradation mechanism of PEI by direct pyrolysis with mass spectrometry [190]. Author used mass spectrometry for identifying pyrolysis compounds of PEI. Furthermore, the pyrolysis of m-aramid was performed for comparision, and it was found that m-aramid and PEI yield the same type of pyrolysis products beyond 550 °C.

A recent study looked at the thermal degradation behavior and lifetime estimation of PEI/carbon fiber composite [194]. When heated from 25 to 1000 °C at different heating rates (2,4,6,8, and 10 °C/min), PEI experienced a 17 to 21 % weight loss but the carbon fibers were relatively stable. This study defined the lifetime of PEI/carbon fiber composite as the time when the sample had experienced a 5 % weight loss in the thermogravimetry anaylsis. The lifetime was determined at 5.3×10^{17} years for PEI/carbon fiber composite parts kept at room temperature, and 1.3×10^{12} years when at 80 °C, which is the highest service temperature of commercial aircrafts, the main application for PEI/carbon fiber composites. However, this estimation was based on inert atmosphere, i.e. without including the effect of realistic aging conditions such as weather and mechanical loadings.

These existing studies are based on frictional heating or pyrolysis reactions; long-term degradation (aging) has not been studied well in conditions relevant to the thermal aging of fire protective fabrics, which involves thermo-oxidative aging. Yet, during the thermal aging of PEI, the mechanical and chemical properties may change. An understanding of the thermal aging of polyetherimide in air (thermo-oxidative aging) is thus critical to estimate the service life of PEI-

containing parts. This study investigates the thermo-oxidative aging behavior of PEI at different temperatures and the resulting changes in its mechanical and chemical properties. Based on the data obtained, the service life of PEI was estimated using the time temperature superposition principle. Furthermore, FTIR was used to suggest the mechanism of thermal aging of PEI. In the end, this study opens up a new field of research on the estimated service life and the aging mechanisms of high-performance polymers under extreme conditions.

5.2 Experimental section

The study involved subjecting PEI specimens to thermal aging at three different temperatures (190, 200 and 210 ℃) for 10 exposure times. These three temperatures were selected for specimens that used for characterization of mechanical property, surface, and 210 ° was selected for specimen that used for FTIR peak anaysls, differencial scanning calorimetry (DSC), and thermalgraviterics analysis (TGA). For each condition, eight replicates were produced. The effect of aging was assessed both in terms of mechanical performance through tensile testing and chemical changes through FTIR. The FTIR measurements were performed on the dog-bone-shaped specimens used for the tensile tests before the tensile test was carried out. Complementary surface analysis by SEM and atomic force microscopy (AFM) was conducted as well as thermal analysis by DSC and TGA. This section describes the different experimental protocols used.

5.2.1   Materials and specimen preparation

Eight 80 μm thick polyetherimide films (PEI, Ultem, Mcmaster Carr., Robbinsvile, NJ) were purchased from McMaster Carr. Dog-bone shape samples in accordance with ISO 527 were hand cut using a metal template to allow the measurement of the residual tensile strength after aging

[195]. The specimens have a gauge length of 25 mm, a width of 4 mm, a thickness of 0.8 mm and an overall length of 75 mm. This technique of preparation of the dog-bone specimens was selected as it yielded a lower variability in the strength results compared to the other strategies attempted.

A total of 41 dog-bone specimens were prepared with each PEI film. To minimize the effect of the inter-film variability, each film included one replicate for each condition: one specimen for the unaged condition, 30 specimens for the three different temperatures and 10 different aging times, and 10 extra specimens. The detail of dog-bone specimen preparation is discussed in Appendix (Section A1).

5.2.2 Accelerated thermal aging program

The thermal aging of the dog-bone specimens was undertaken at 190, 200 and 210 °C. They were suspended in a convection oven (Heratherm^{TM}, ThermoFisher Scientific, NC, USA) for designated time period (190 °C : 12 weeks, 200 °C: 16 weeks, and 210 °C: 8 weeks). The calibration of the oven temperature and detail of the distribution of the dog-bone specimens in the oven are discussed in Appendix (Section A2).

5.2.3 Mechanical characterization

A tensile testing frame (Instron 5943, Instron, Norwood, MA, USA) equipped with a 1 kN load cell was used to measure the ultimate tensile strength of the PEI dog-bone specimens. These dog-bone specimens were tested at a constant strain rate of 10 mm/min until failure according to the standard test method ISO 527. For each aging time and temperature condition, the ultimate tensile strength was measured on the eight replicates; average values and standard errors were determined. All tests were carried out at room temperature and atmospheric pressure.

5.2.4 Chemical analysis by Fourier Transform Infrared (FTIR) Spectroscopy with Attenuated Total Reflection (ATR)

The functional groups of the control specimens of PEI (three per film) and the different specimens subjected to accelerated thermal aging (using the dog-bone specimens prior to mechanical testing) were identified by ATR-FTIR (Nicolet 8700, Thermo Scientific, USA). The specimens were placed on a germanium crystal surface. For each measurement, 128 scans with a resolution of 4.0 per cm were performed over a wavenumber range between 600 and 4000 cm^{-1}.

Chemometrics anaylsis[6] was used to identify the absorption peaks undergoing a significant change as a result of the thermal aging of PEI. It is a qualitative analysis technique that is useful to conduct a statistical analysis on an entire spectrum of data [196]. Data are often obtained with multiple variables, and it is difficult to represent these data on a 2-dimensional (2-D) plot. A strategy to plot data with multiple variables in two dimensions involves selecting only the variables that undergo the largest changes. Principal component analysis (PCA) is a common tool in chemometrics to select two dominant variables to represent or classify data from multiple variations across the entire spectrum and between spectra [196,197]. These two dominant variables are called the first and second principal component. These two dominant variables can then be plotted in a 2-D representation, which is called a bi-plot [198]. The PCA model can be expressed by equation 5.1:

$$X = TP^T + E \tag{5.1}$$

where X represents the data matrix with m rows (samples) and n columns (variables), T represents the scores (describing how close to each other samples are, in other words the principal

---

[6] The chemometrics analysis of the data was performed by collaborator Dr. Paulina de la Mata and PhD student Seo Lin Nam of Dr. James Harynuk's group in the Department of Chemistry at the University of Alberta.

components), P^{T} is the loading vector (describing how close variables are to each other or have similar information), and E is the residual (encompassing all minor variables that are not selected as principal components). According to the PCA model, the first principal component (PC1) and the second principal component (PC2) are selected among the entire variables; they are the dominant factors that represent the differences among the spectra or data points. In the bi-plot, the more dominant component has the higher score (%), i.e. the score of PC1 is higher than the score of PC2. PCA modelling (plotting) produces linear combianations of the original variables [197,198]. Therefore, PCA bi-plots can also show outliers of the data set, which fall outside of a linear relationship. The outliers do not represent wrong data, but rather inconsistencies among data points.

Recently, FTIR spectra have been combined with chemometrics in food science to identify the origin or quality of foods [199–201]. This combination has also been applied in this project to reveal the progress of the polymer aging and identifying the peaks in the FTIR spectra undergoing to significant changes. The detail of the chemometrics analysis is not provided here and the results in terms of evolving peaks are directly used to inform about the aging mechanisms.

Once the peaks of interest were identified, they were deconvoluted so that their individual area is calculated. The details of the FTIR peak analysis are illustrated in Fig. 5.2 and Fig. 5.3. The raw FTIR spectra were deconvoluted and analyzed using the Peak Analyzer function in the Origin software. First, we performed a baseline correction of the FTIR spectrum by interpolation between linear sections at both extremities of the peak series. The software then performed the deconvolution of the FTIR spectrum into several Gaussian peaks. The areas of these peaks were calculated using the peak integration function in the software. To allow a comparison between different FTIR spectra, the peak area is divided by the area of a reference peak [189]. For PEI, the

reference peak correspond to the aromatic ring stretching at 838 cm^{-1}. In order to keep the reference

peak area constant between the different spectra measured, the spectra were normalized such that

the reference peak area was scaled to unity.
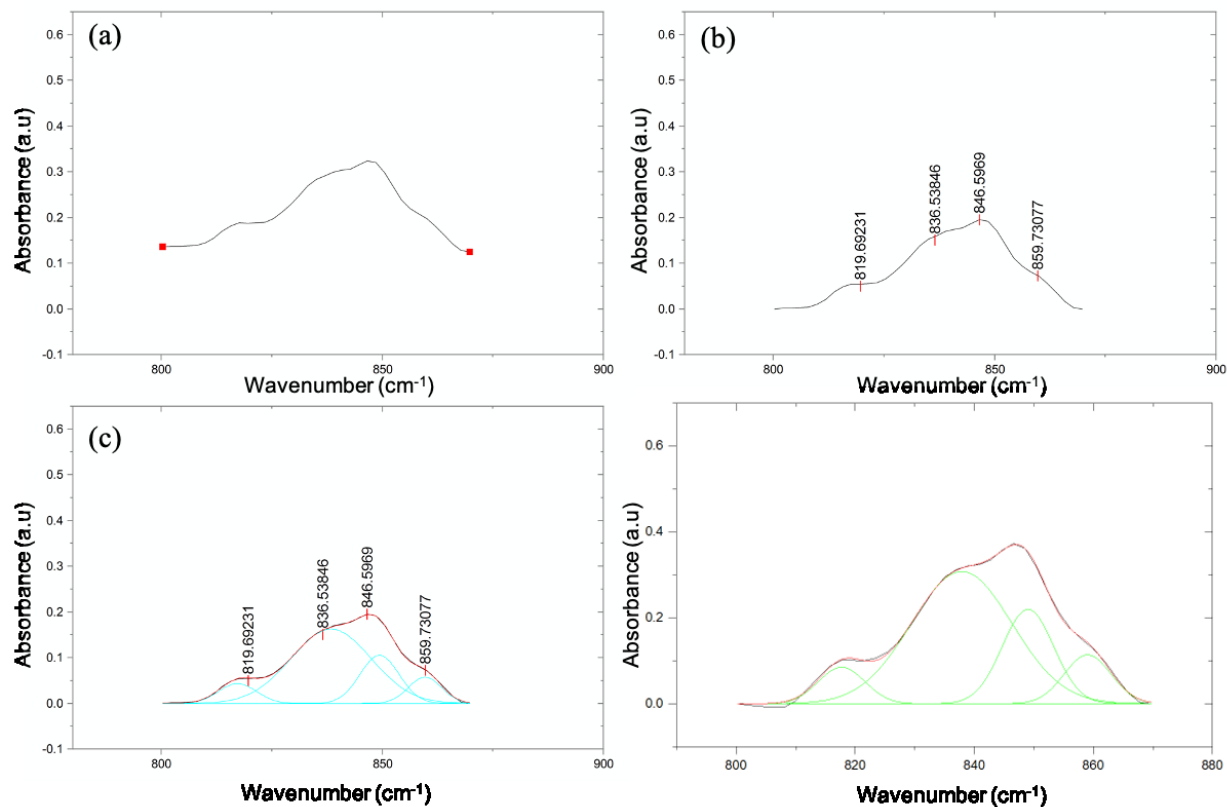
Figure 5.2 Process of deconvolution of the FTIR spectra: (a) selection of two points that encompass the overlapping peaks; (b) peak identification; (c) fitting of the Gaussian peaks; (d) deconvoluted peaks.
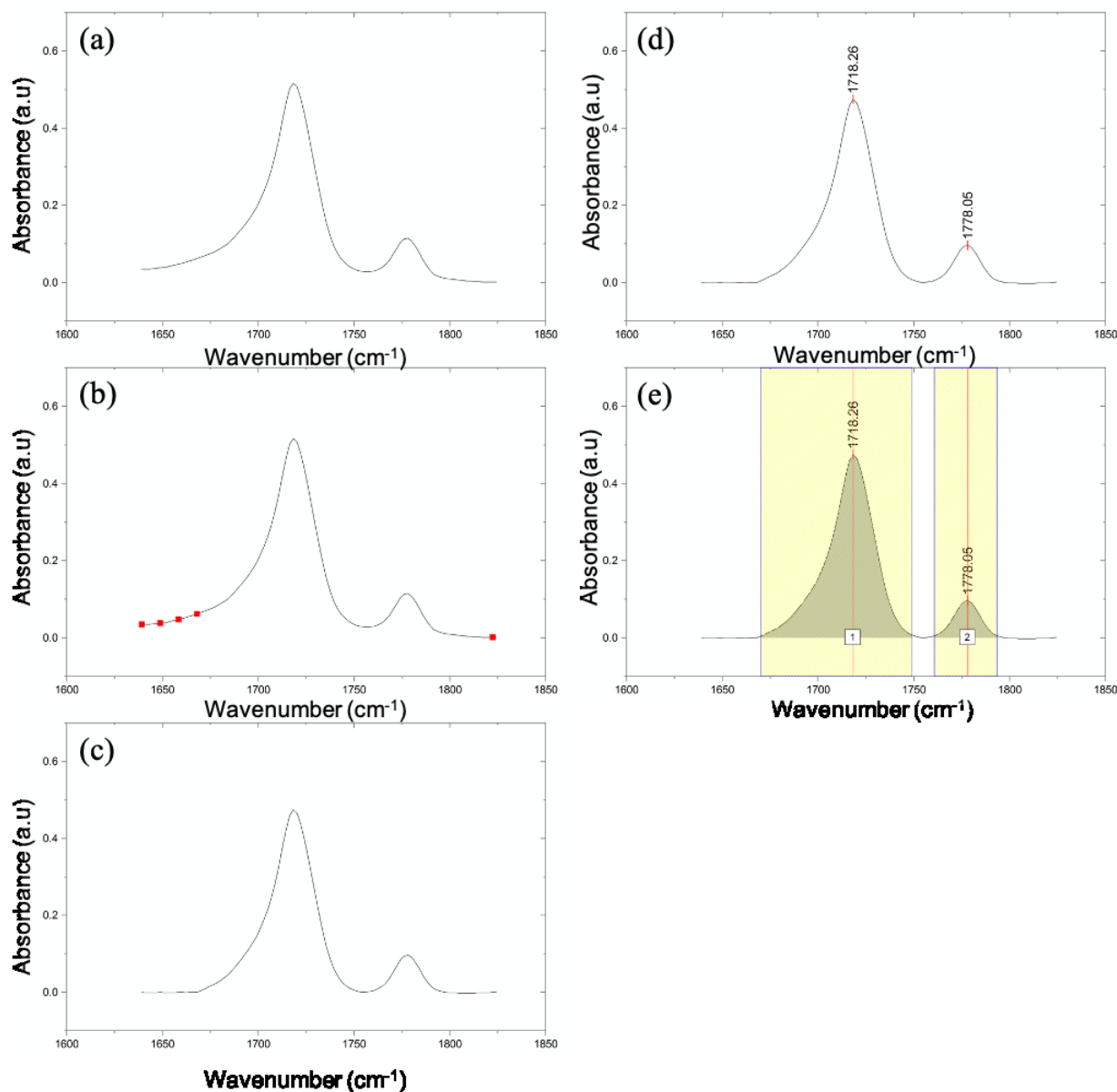
Figure 5.3 Calculation of the FTIR peak area: (a) selection of the wavenumber range; (b)-(c) baseline correction; (d) peak identification; (e) peak area integration.

For each aging time, spectra were collected for the eight replicates. Depending on the temperature, 8 or 10 aging times were used. When one adds the unaged condition (labelled as control), this leads to 72 or 88 spectra being compared (see the example in Fig. 5.4 a for the 210 °C case). To facilitate the comparison of the results at the different conditions, the eight spectra corresponding to the eight replicates measured for each condition were merged into one spectrum

using the SpectraGryph software (http://spectragryph.com, Oberstdorf, Germany). The merging process involves extrapolating between the gaps of the spectra and averaging the overlaps in the spectra. This process is shown in Fig. 5.4 in the case of the spectra for the specimens aged at 210 °C for the entire wavelength range (Fig. 5.4 a and b) and for the 1172 cm^{-1} peak (Fig. 5.4 c and d).
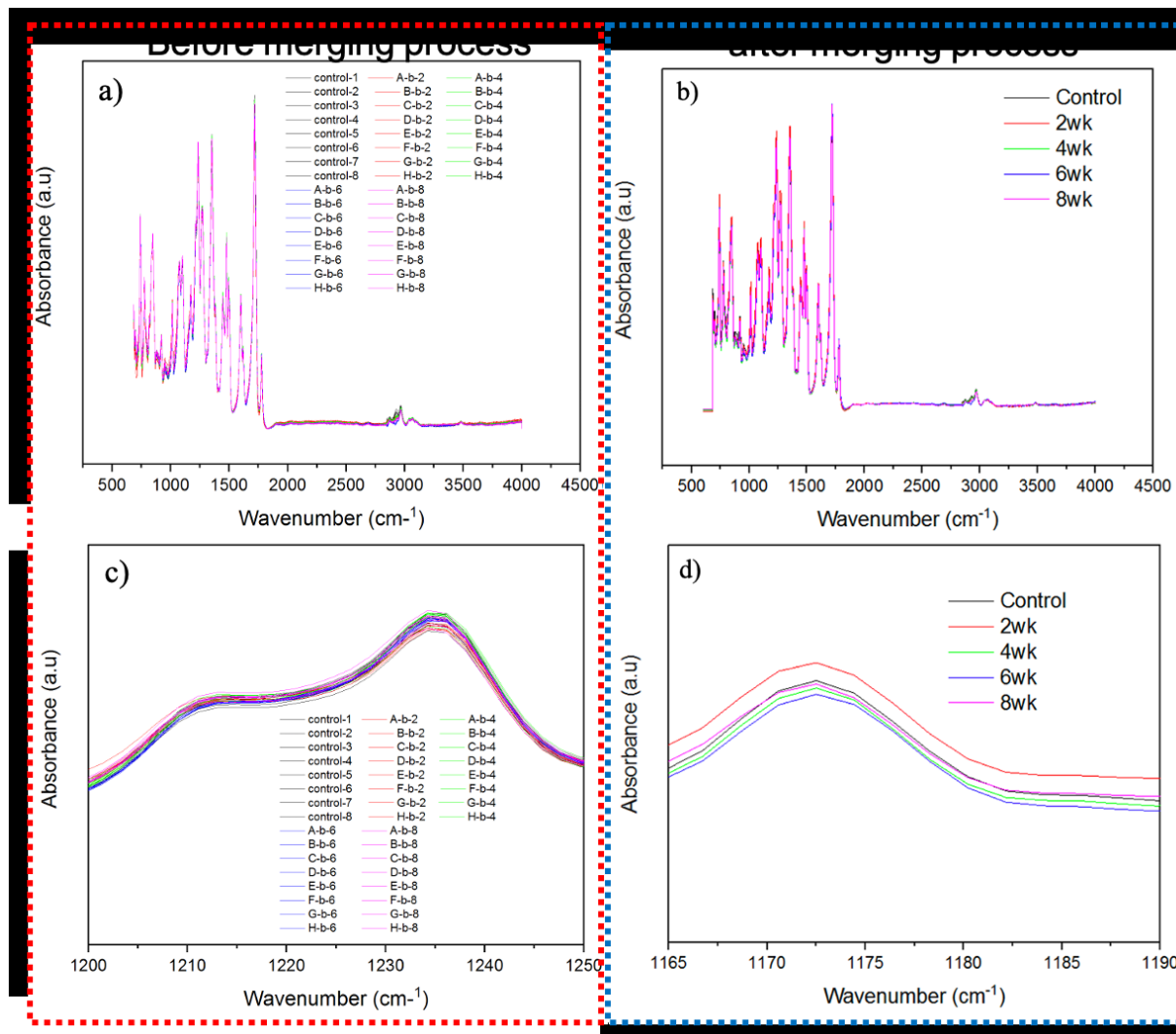
Figure 5.4 FTIR spectra for the unaged condition and for the specimens aged at 210 °C for 2, 4, 6 and 8 weeks: a) all 40 spectra over the entire wavelength range; b) after merging the spectra of the 8 replicates; c) at 1172 cm^{-1} peak for the 40 spectra; and d) after the merging process (5 spectra).

5.2.5 Scanning electron microscopy

The surface details of the control and aged PEI specimens were observed by a field emission scanning electron microscope (FE-SEM, Zeiss Sigma, Germany, 5 kV). Gold coating on PEI surface was made under 100 mTorr and 15 mA conditions for 1 mins sputtering (Denton Vacuum Sputter DESK II, Denton, NJ, USA). Finally, 8 nm gold layer was deposited on PEI.

The crack surface area on the aged PEI samples was determined on the SEM images. The five different spots in one sample (44.42 μm^2 per one spot area, 222.1 μm^2 for five spots area) were used to estimate crack surface area. The color histogram feature in the software ImageJ (NIH, Bethesda, MD, version 1.8.0.172) was used to perform the quantitative analysis of the crack surface area. First, the contrast and brightness were adjusted on the imported SEM image to intensify the crack area. Second, the color histogram feature in the software was used to display the cracks in black while the rest of the surface is red. This process is illustrated in Fig 5.5. The "Analyze histogram" feature of the software then gave access to the number of black and red pixels in the image. Finally, the ratio of black vs. red pixels in the image was calculated, and was used to determine the crack surface area, as described by equation 5.2.

$$\text{Crack surface area (\%)} = \frac{\text{Number of black pixels (crack)}}{\text{Total number of pixels in image}} \times 100 \qquad (5.2)$$
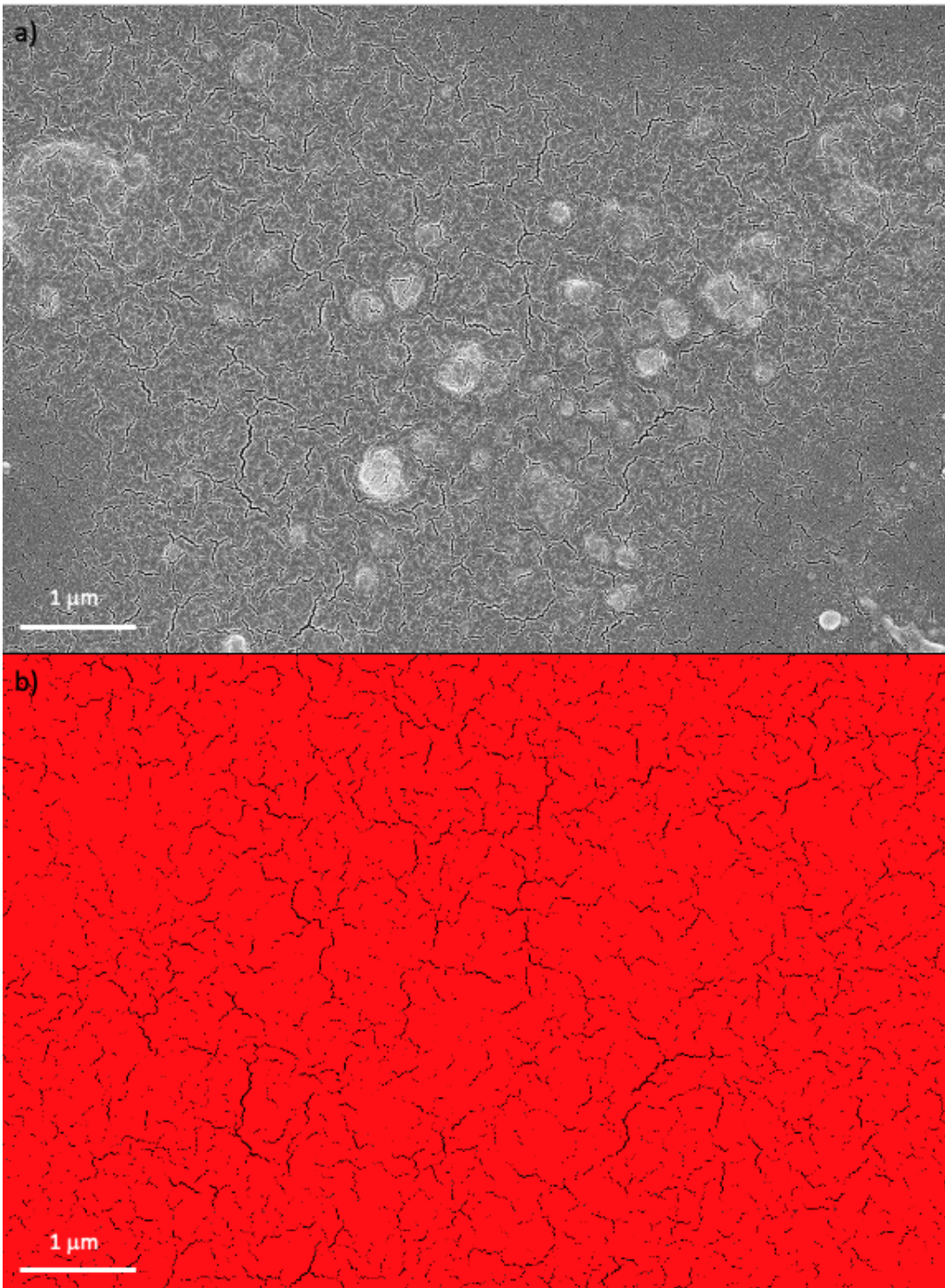
Figure 5.5 a) SEM image showing the cracks (8 weeks of aging at 210 °C); b) "color histogram" feature applied to the imported SEM image of the cracks, which the cracks being colored in black and the rest of the sample surface being colored in red.

5.2.6 Differential scanning calorimetry (DSC)

The effect of thermal aging on the glass transition temperature of PEI was determined by differential scanning calorimetry (DSC, Q1000, TA Instrunments, DE, USA). A small section of the dog-bone specimens after thermal aging was used for the DSC testing. For the measurement, a 2 mg sample was sealed in an aluminium sample pan and exposed to the following thermal conditions: (1) hold at 25 °C for 3 min, (2) heat from 25 °C to 350 °C at a rate of 20 °C/min, (3) hold at 350 °C for 3 min, (4) cool down to 25 °C at a rate of 20 °C/min. The heat flow as a function of the temperature was recorded. The onset and end points in the resulting DSC curve were determined using the Bi-Gaussian fitting provided by the Peak Analyzer function in the Origin software. It is the same method described in section 5.2.4 for the FTIR peak analysis, but without the peak deconvolution step. The curve fitting process is shown in Fig 5.6. After obtaining a fitted curve, the onset and end point temperatures were obtained from the tangential lines that were selected on the fitted curve using the Origin software (OriginLab, MA, USA) (Fig. 5.7). The glass transition temperature (T_g) was determined as the mid point between the onset and the end point.
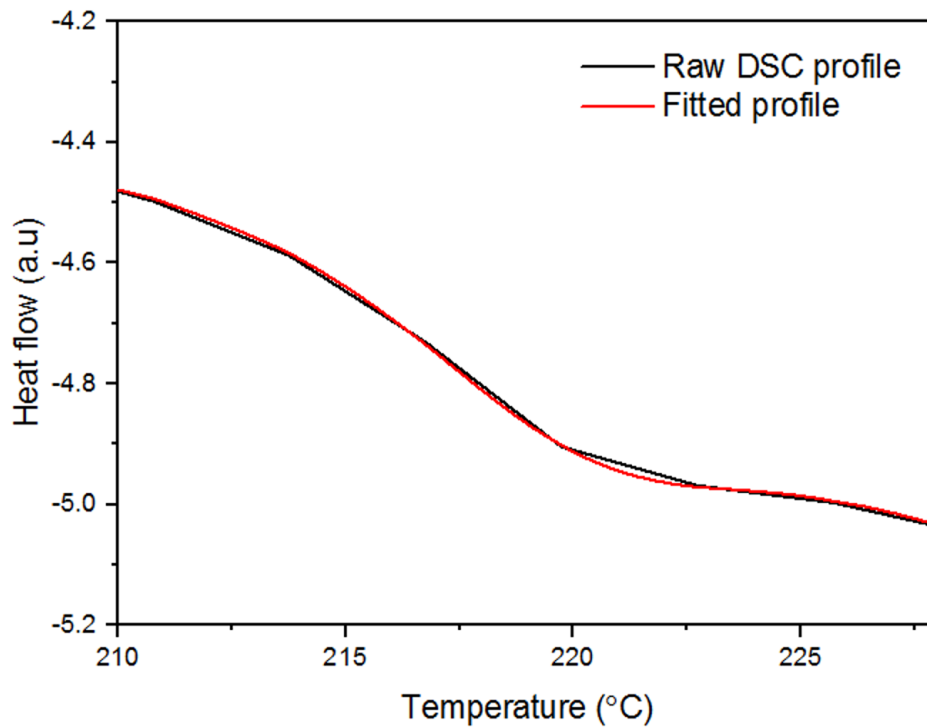
Figure 5.6 Bi-Gaussian fitting of the DSC curve
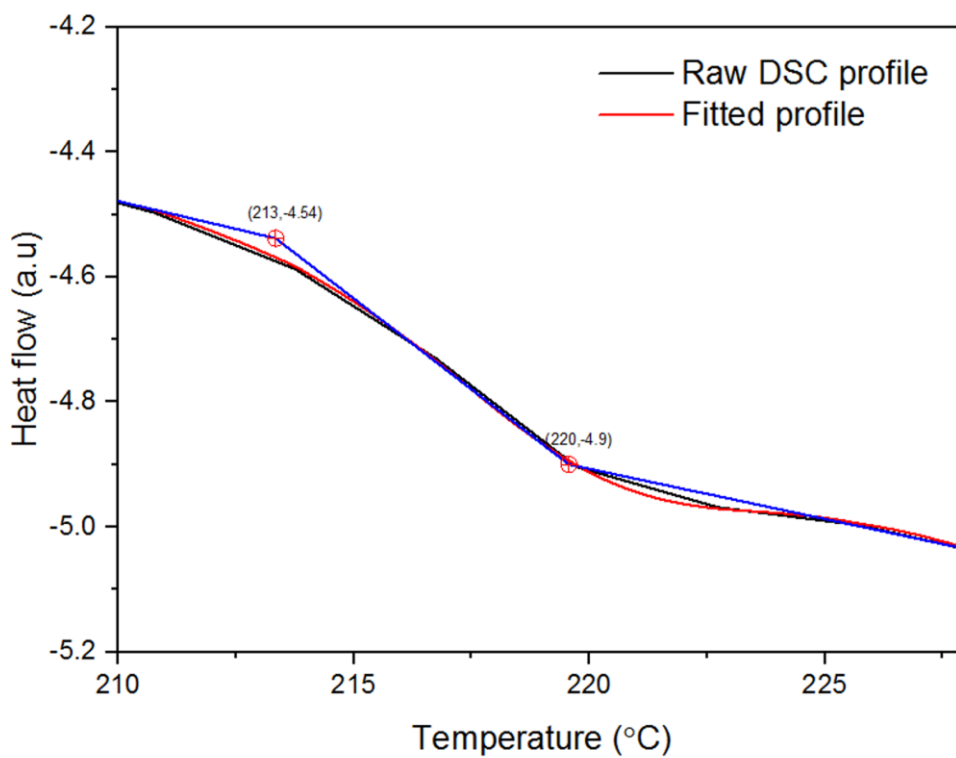
Figure 5.7 Determination of the onset and end point temperatures from the tangential lines on the fitted DSC curve.

5.2.7 Thermalgravimetrics analysis (TGA)

The effect of thermal aging on the thermal decomposition of PEI was studied by thermogravimetric analysis (Discovery TGA, TA Instruments, New Castle, DE, USA). Samples with a mass of 2 mg were taken from unaged and aged PEI dog-bone specimens. These samples were heated from 30 °C to 850 °C in air with a flow rate of 25 ml/min and a heating rate of 20 °C/min in the thermal analyzer. The variation in the sample weight was recorded as a function of the temperature.

5.2.8 Atomic Force Microscope (AFM) an optical microscope analysis

The surface roughness of the PEI samples was measured using an atomic force microscope (Dimension Edge^{TM}, Bruker). The microscope was run in the tapping mode and an area of 50 μm × 50 μm (512 × 512 points) was scanned at a scan rate of 0.6 Hz. The measurement was performed at five different points of the specimen surface and the result was averaged for each condition. In addition, the unique patterns on PEI film was observed using an optical microscope (Stereomaster, Fisher Scientific).

5.2.9 Statistical Analysis

Depending on experimental methods, measurements were generally performed 3 to 8 times and mean values are used to comparison for identifying changes. Where applicable, statistical significance was evaluated using the single factor ANOVA analysis. A confidence level of 0.05 was set to establish significance. Detailed results of statistical analysis for this chapter are included in Appendix, section A4.1 to A4.3

5.3 Results and discussions

5.3.1 Thermal properties

Figure 5.8 presents the effect of thermal aging on the thermal behavior of PEI as measured by DSC. The results shown in Fig 5.8 correspond to the following 4 conditions: unaged (control), and aged for 4, 6 and 8 weeks at 210 °C. The DSC curve shows an endothermic peak between 220 – 230 °C in the aged samples whereas the control did not show such a peak. DSC has previously been used by researchers to evidence the signs of physical aging in polymers [202]. In the case of the thermally aged PEI samples reported here, this DSC peak might have been changed by the crosslinking and chain scission reactions taking place during thermal aging. When a polymer is thermally aged, both crosslinking and chain scission reactions occur. At the beginning, it involves mainly crosslinking in the polymer network; in the second stage of aging, chain scission reactions break apart the polymer network, broken bonds create radicals and these radicals can react with either each other or oxygen and form new bonds [43]. Chemical bond formation reactions are exothermic reactions, and are accompanied by heat and energy loss [203]. When an aged polymer is heated above T_g like here during the DSC test, the polymer absorbs heat which may correspond to the amount of energy lost during thermal aging [204]. I thus potentially attribute the endothermic peak observed in the DSC curves of the aged specimens just above Tg to the energy lost through crosslinking and formation of new bonds during the aging process. The fact that the values of this endothermic peak area for samples aged at 210 °C for 4, 6 and 8 weeks are similar (99.65, 99.99, and 99.56, respectively) may point to the crosslinking reactions during the early stage of aging as the source of this phenomenon.
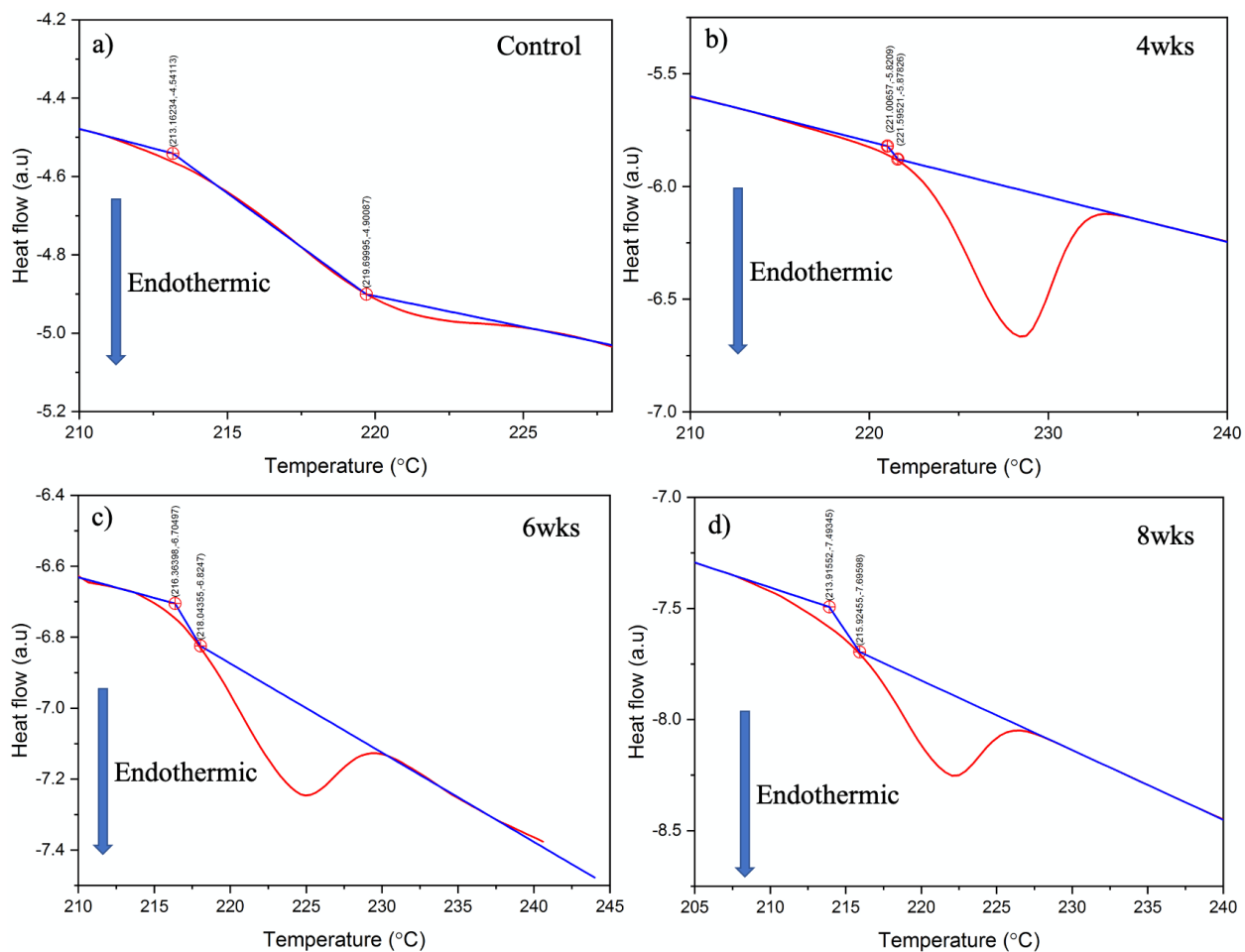
Figure 5.8 DSC curves (red curve) measured for PEI samples a) unaged and after thermal aging at 210 °C for b) 4 weeks c) 6 weeks and d) 8 weeks. The onset and end point are determined using the tangent technique (blue lines) and are indicated with red crosses.

Table 5.1 gives the values of T_g corresponding to the conditions shown in Fig 5.8. The value of T_g for the unaged PEI specimens is in agreement with the literature [205]. When comparing mean values, T_g is observed to increase slightly until 4 weeks, and decreasing during further aging. A statistical analysis of the results was made and shows that at least one condition is different from the other conditions. The details of the statistical analysis are given in Appendix, section A4.1. This behavior may be attributed to a crosslinking reaction at the beginning of the aging process that prohibits molecular mobility [206]. Further thermal aging (beyond 4 weeks) induced chain

scission; thus the value of T_g decreased after 6 weeks and 8 weeks of aging due to increased molecular mobility.

Table 5.1 Values of the glass transition temperature of PEI before aging and after thermal aging at 210 °C for 4, 6 and 8 weeks. The average value and standard deviation are calculated for 5 measurements.

Aging condition at 210 °C	Tg (°C)
Control	216.8±0.6
4 weeks	222.5±0.5
6 weeks	218.7±0.3
8 weeks	216.4±0.5

The TGA curves of aged PEI samples in the unaged condition and after thermal aging for 4, 6 and 8 weeks at 210 °C are shown in Fig 5.9. The PEI decomposition takes place in two stages [207]. The first stage corresponds to the decomposition of aliphatic chains . The second stage corresponds to the decomposition of aromatic groups. Fig. 5.10 and 5.11 show enlarged views in these two zones, respectively. The decomposition behavior of the PEI samples was characterized using the following parameters : $T_{5\%}$, which is defined as the decomposition temperature corresponding to a weight loss of 5 % [207]; $T_{initial}$, which is the first deflection point from the baseline; $T_{1st\ max\ rate}$, which is the temperature at which the highest rate of weight loss occurs in the first decomposition region; and $T_{2nd\ max\ rate}$, which is the temperature at which the highest rate of weight loss occurs in the second decomposition region.

The values of these parameters are shown in Table 5.2 for the unaged condition and after thermal aging for 4, 6 and 8 weeks at 210 °C. The values for the unaged PEI specimens are in agreement with the literature [190]. An 8% decrease in the mean-value of $T_{initial}$ is observed between the unaged condition and 8 weeks of aging at 210 °C. This decrease in the mean-value of $T_{initial}$ might be attributed to chain scission in PEI during thermal aging [207]. A slight decrease is

observed in the mean $T_{5\%}$ value between the unaged condition and 8 weeks of aging. $T_{1st\ max\ rate}$ (corresponding to the aliphatic groups) did not appear to change with increased aging times when looking at mean values, which may indicate that the thermal aging has not affected the aliphatic groups. The mean $T_{2nd\ max\ rate}$ values (corresponding to the aromatic groups) decreased by 3% between the unaged condition and 8 weeks of aging at 210 °C. The overall statistical analysis showed that the $T_{initial}$ and $T_{5\%}$ values have at least one condition that is statistically different from the other conditions, while the $T_{1st\ max\ rate}$ and $T_{2nd\ max\ rate}$ values are not statistically different. The details of the statistical analysis are shown in Appendix, section A4.2.
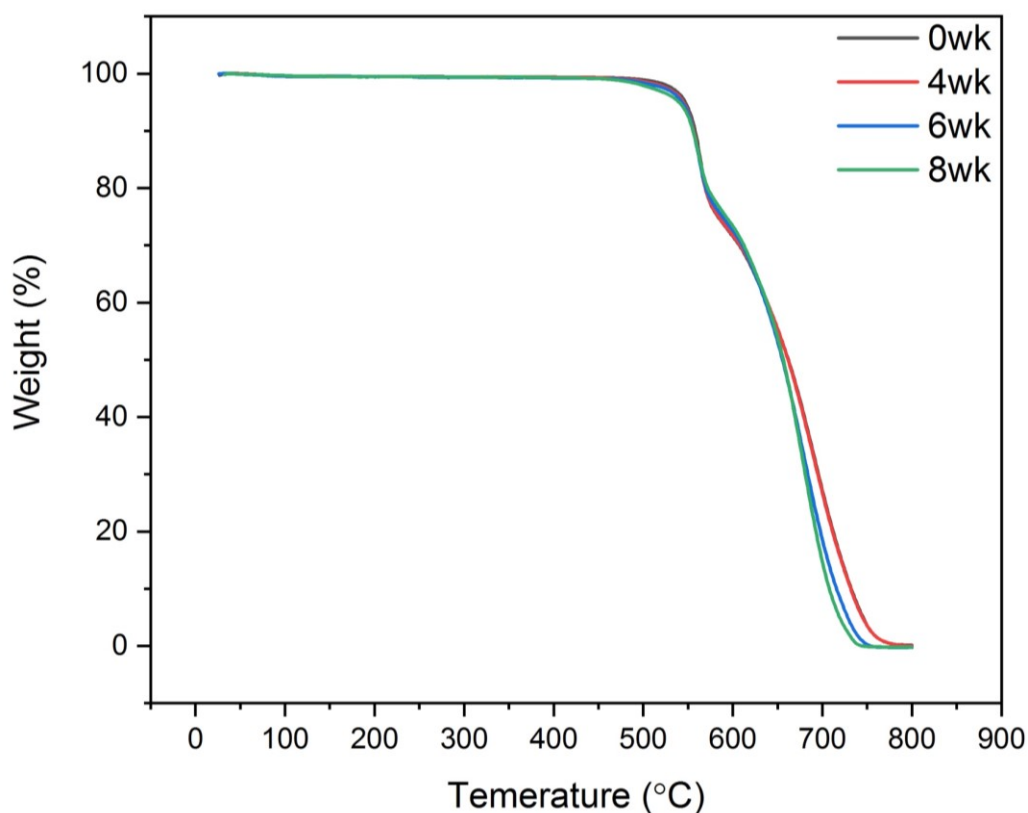
Figure 5.9 TGA curves of PEI in the unaged condition and after thermal aging for 4, 6 and 8 weeks at 210 °C.
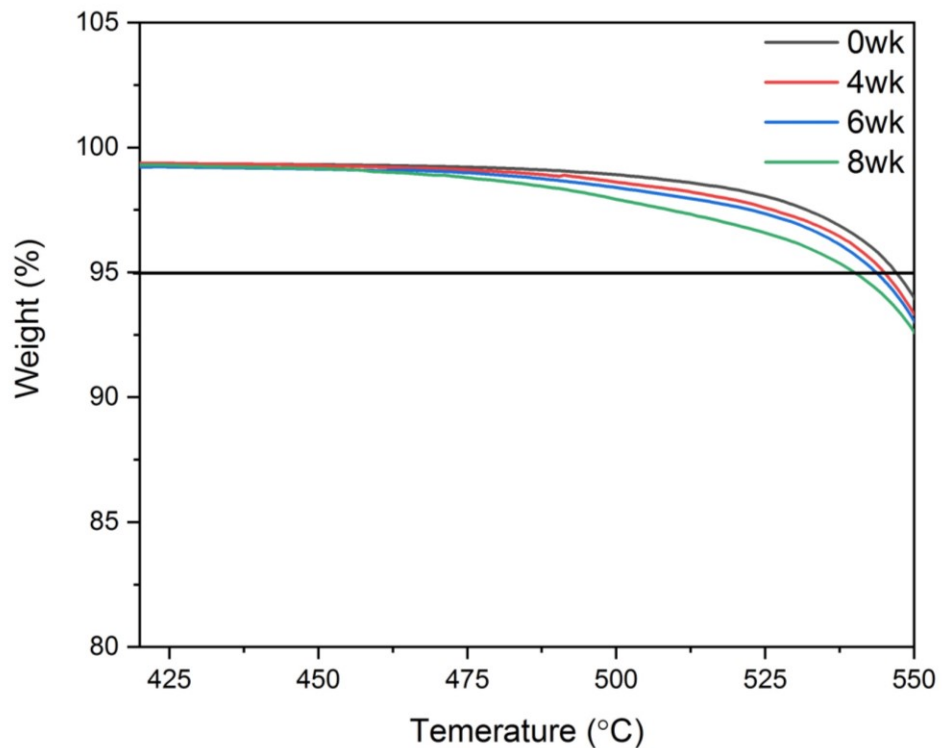
Figure 5.10 Enlarged view of Figure 5.9 corresponding to the first deflection point from the baseline. The black solid line indicates 5 % weight loss.
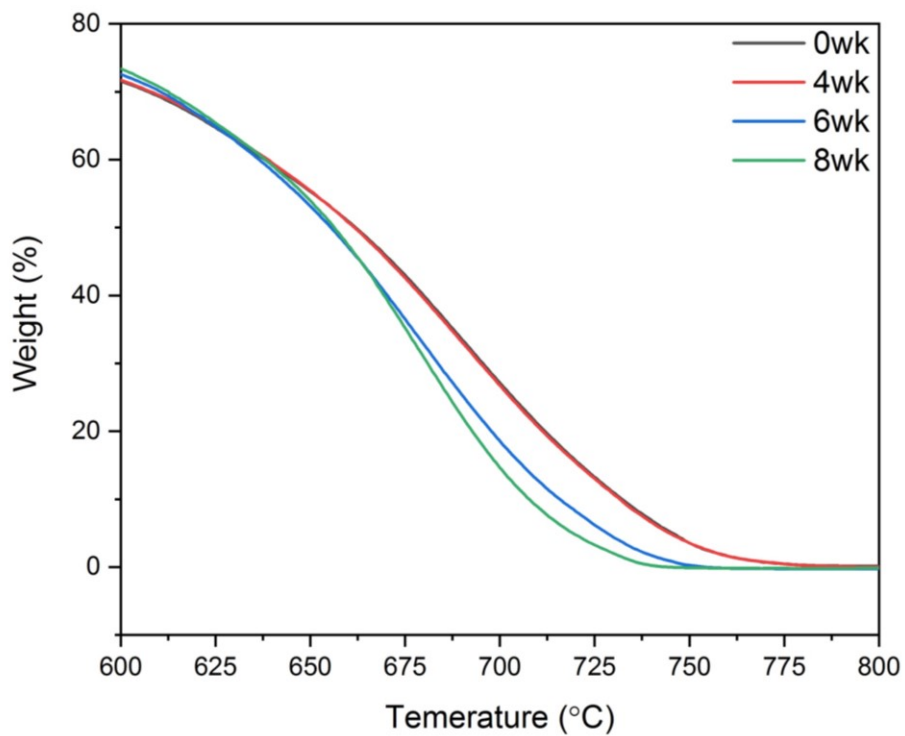
Figure 5.11 Enlarged view of Figure 5.9 corresponding to the decomposition of the aromatic parts of PEI.

Table 5.2 Values of the parameters extracted from the TGA curves for PEI in the unaged condition and after thermal aging for 4, 6 and 8 weeks at 210 °C.

Parameter / Condition	$T_{5\%}$ (°C)	$T_{initial}$ (°C)	$T_{1st\ max\ rate}$ (°C)	$T_{2nd\ max\ rate}$ (°C)
Control	548 ± 1	480 ± 3	562 ± 1	685 ± 8
4 weeks	545 ± 2	460 ± 6	564 ± 1	690 ± 2
6 weeks	544 ± 1	466 ± 8	560 ± 3	681 ± 3
8 weeks	540 ± 1	442 ± 6	565 ± 2	663 ± 2

5.3.2 Mechanical properties

The effect of thermal aging on the tensile properties of the PEI specimens were characterized for different aging times and temperatures: up to 12 weeks at 190 °C, up to 16 weeks at 200 °C, and up to 8 weeks at 210 °C. The ultimate tensile strength (UTS) was determined for each specimen. The variation of the UTS averaged over the eight replicated as a function of aging time and temperature is shown in Fig. 5.12. The individual data points corresponding to each replicate are also included. An example of stress-strain curve of an aged PEI specimen (210 °C, 8 weeks) is shown in Fig. A13 in Appendix.
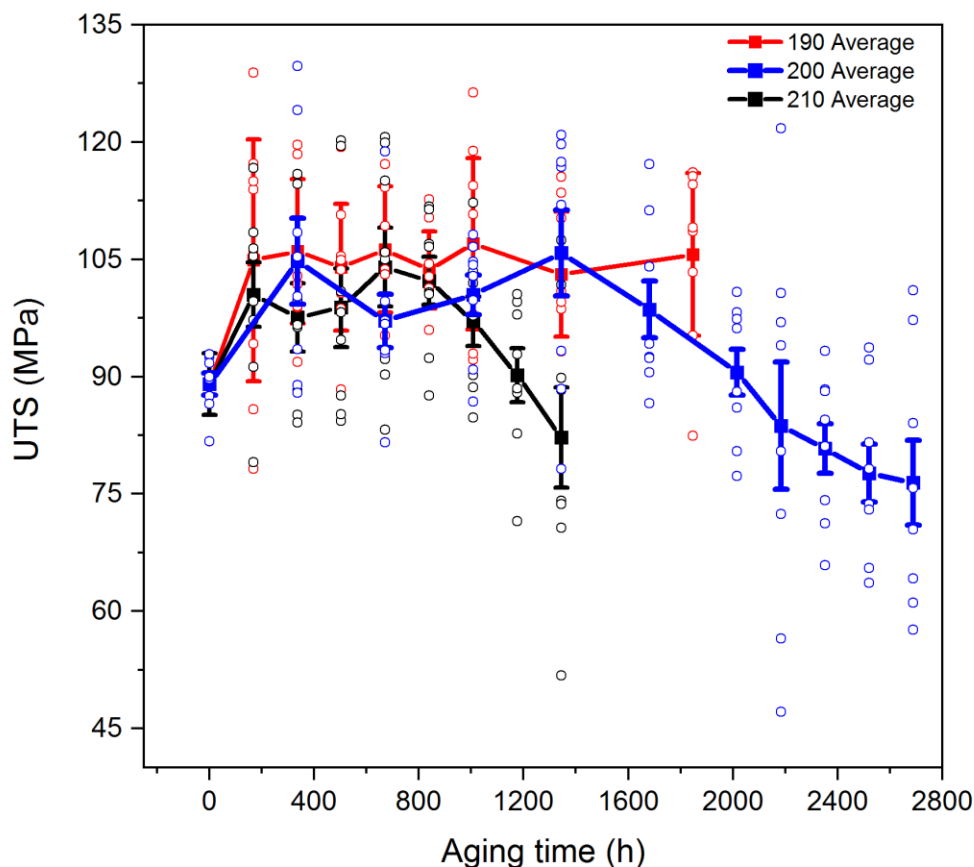
Figure 5.12 Variation of the specimen UTS as a function of aging time for three aging temperatures, 190, 200 and 210 °C (Different color the mean values are provided as a guide for the eye). The open circles correspond to individual UTS for the eight replicates, with their color referring to the relevant aging temperature.

The average UTS of the control PEI specimen (not exposed to thermal aging) was 90 ± 4 MPa. After the first week of aging, the UTS value increased by 13-17 % for all aging temperatures. This increase in the UTS is attributed to the crosslinking reaction that takes place during the initial stages of thermal aging [208]. In the case of thermal aging at 190 °C, the UTS remained at that 20% increased level compared to the unaged condition until the end of the aging program at 10 weeks. The increased scattering observed in the individual UTS values of the aged PEI specimens can be attributed to the fact that aging is by definition an inhomogenous process. For instance, in the thermo-oxidative aging of polymers, the oxygen diffusion can be a limiting factor when the

oxygen consumption rate is larger than its permeability [209,210]. As a result, the oxygen diffusing into polymers from the surrounding atmosphere is primarily consumed by the oxidation of the polymer surface, and does not reach the internal of the polymer part.

On the other hand, when thermal aging was performed at 200 and 210 °C, a decrease in the UTS of the PEI specimens was observed after the first increase and subsequent plateau. The decrease in the UTS value started after eight weeks of aging in the case of the 200 °C thermal aging and after 4 weeks of aging at 210 °C. These higher temperatures allowed the aging process to reach its second step, with the occurance of chain scission [211]. Other studies of thermal aging of polymeric materials have also shown similar changes in their mechanical properties as function of aging time and temperature. For instance, Yang et. al studied the effect of thermal aging on the mechanical properties of polyetheretherketone (PEEK). The tensile strength of PEEK increased during the short aging times, but decreased for longer aging times [212]. This study concluded that the increase of the mechanical properties was linked to crosslinking in the polymer network, while the decline in mechanical properties was due to chain scission. In the case of cross-linked polyethylene (PE), Mechri. et al. showed a decrease in tensile strength by 30 % to 70 % depending on the aging time and temperature [213]. Shrisinha et al. studied the effect of thermal aging on the mechanical properties of a chlorinated PE/Natural rubber blend. The different ratios of the PE/rubber blend underwent a decrease in tensile strength of 36 % to 50 % due to aging, with samples with higher rubber content undergoing a larger decrease [214]. Based on these results, we can hypothesize that the PEI samples will become brittle during the first phase of the accelerated thermal aging due to the crosslinking reaction. The embrittlement will further increase during the second phase of the aging process due to the chain scission reaction.

Following the work by Parkman who used it to analyse the creep and relaxation of a PEI cylinder subjected to constant radial deformation, the time temperature superposition (TTS) principle was used to construct a master curve from the UTS data for the specimens exposed to accelerated aging at 200 and 210 °C (Fig. 5.13) [215]. The values at 200 °C was used as the reference. The data at 190 °C could not be used as the second stage of the thermal aging process corresponding to the decrease in UTS had not been reached. The shift factors provided by the TTS transformation are displayed on an Arrhenius plot (inset in Fig. 5.13). If the UTS data can be described by an Arrhenius model, the plot of the logarithm of the shift fators as a function of the inverse of the absolute temperature will show a linear relationship [216]. Here, since only the data at two aging temperatures can be used to construct the TTS master curve, it is not possible to verify that the Arrhenius model applied for the thermal aging of PEI. However, several studies have successfully used the Arrhenius model to described the effect of thermal aging on the mechanical strength of various polymers, e.g. polychloroprene [217], polyamide [218], para-aramid/PBI blend yarns and fabrics [70], and various fire protective fabric blends [3]. In addition, the Arrhenius model was shown to apply to the flexural creep of PEI at different temperatures [219]. Therefore, it was used to compute the value of the activation energy corresponding to the effect of thermal aging on the UTS of PEI. The value provided by the TTS shift factors is 112 kJ mol^{-1}. This value is similar to the values of activation energy reported for fire protective fabric blends used as outer shell in firefighter protective clothing [3], with for instance an activation energy of 111 kJ mol^{-1} for a 60/40 Kevlar/PBI fabric and of 113 kJ mol^{-1} for a 60/40 Kevlar/Nomex IIIA (93% Nomex, 5% Kevlar, 2% carbon fibers) fabric. This indicates the relevance of the choice of PEI as the sacrificial polymer layer for the design of the end-of-life sensor for fire protective fabrics.

The data in Fig. 5.13 display a sigmoid shape. The common fitting model of sigmoid curves is the Hill equation [3]. In the case of Fig. 5.13, the 4-parameter Hill equation was used (equation 5.3).

$$y = Start + (End - Start)\frac{x^n}{x^n + k^n}$$
(5.3)

where n corresponds to the slope of fitted curve, Start and End are the very first and last data point-values, k relates to the inflection point, which indicates degradation rate (a higher k value retards as much as possible the degradation). Based on this fitting of the TTS master curve by the 4-parameter Hill equation, the following values were obtained for the parameters: n = 5.6, Start = 102 N, End = 46 N, k = 2670 h. The values of n and k are similar to the values obtained for the thermal aging of various outer shell fabrics [3].

Furthermore, if 50% of ultimate tensile strength retention is selected as the criterion for the termination of use (green star in Fig. 5.13) [216], the lifetime can be estimated to 188 days at 200 °C and 113 days at 210 °C.
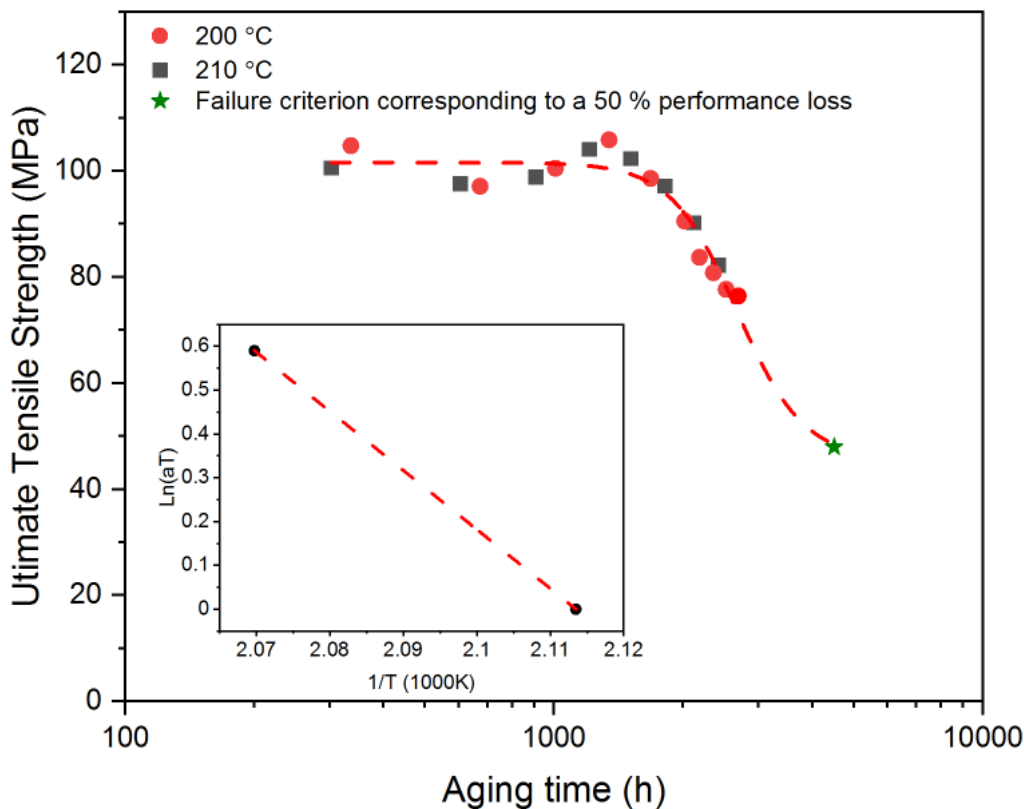
Figure 5.13 TTS master curve at a temperature of 200 °C for the thermal aging of PEI (insert: Arrhenius plot of the shift factors).

5.3.3 ATR-FTIR analysis

The chemical changes that took place in the PEI samples during thermal aging were investigated by ATR-FTIR spectroscopy. The pre-treated FTIR spectra (with the baseline correction and normalization by the reference peak area) at different thermal aging times (0, 2, 4, 6 and 8 weeks) for an aging temperature of 210 °C are shown in Fig. 5.14.
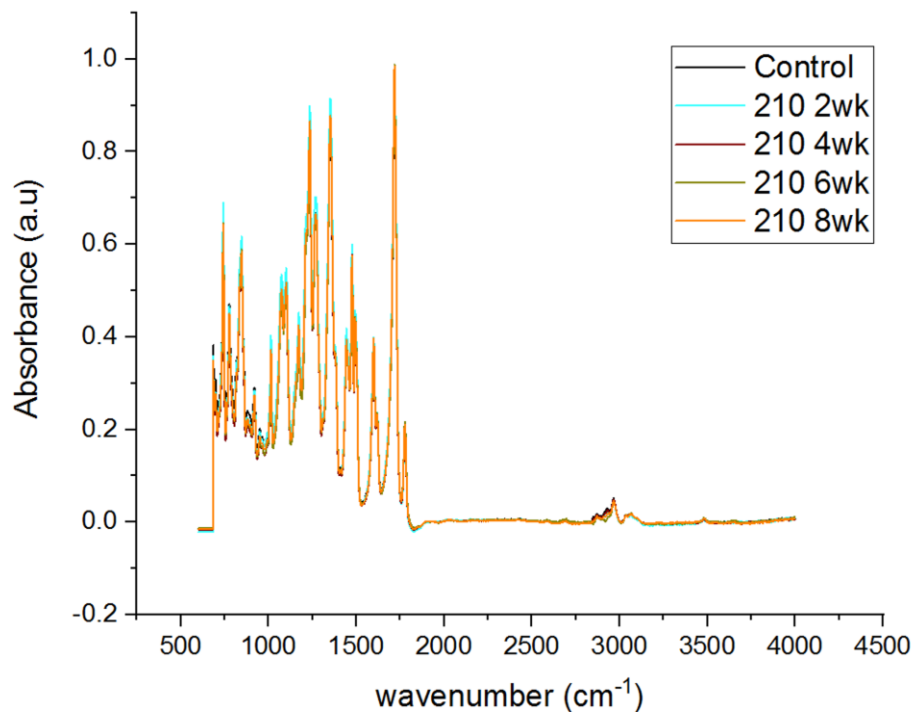
Figure 5.14 FTIR spectra at different thermal aging times (0, 2, 4, 6 and 8 weeks) for an aging temperature of 210 °C

The chemometrics technique[7] helped identify FTIR peaks experiencing a change as a result of the thermal aging of PEI at 210 °C. The location of these peaks along with the corresponding functional groups of PEI are shown in Table 5.3. This includes aryl-ether-aryl, isopropylidene, C-N stretching, C-H stretching, C=C vibration, and Carbonyl in imide group.

---

[7] Performed by collaborator Dr. Paulina de la Mata and PhD student Seo Lin Nam of Dr. James Harynuk's group in the Department of Chemistry at the University of Alberta.

Table 5.3 FTIR peaks experiencing a change as a result of the thermal aging of PEI and corresponding functional groups

Wavenumber (cm^{-1})	Functional group
1269, 1234, 1074, 1014	Ar-O-Ar (aryl ether aryl) [220,221]
1172	Isopropylidene [222]
1351, 1215	C-N stretching [223,224]
2965, 2873	C-H stretching [225,226]
1618, 1600,1494, 1444	C=C vibration [227–229]
1777, 1718	Carbonyl group in imide [229,230]

The area of each of these peaks was determined at the different aging times. The spectra had already been already normalized by the area of a thermally stable peak (838 cm^{-1}) during the pretreatment of the FTIR specta (section 5.2.4). The normalization of the individual peak area by the area of the stable peak (A_{peak}/A_{base} according to [189]) was thus not required at this stage.

Fig.5.15 shows the determination of the peak area for the peak at 1215 cm^{-1}, which corresponds to the C-N stretching in the pthalimide ring. This area is defined by a straight line corresponding to the spectrum baseline in that zone. The variation in this peak area as a function of the aging time at 210 °C is shown in Fig.5.16. The mean values of the peak areas did not appear to change much between 0 and 4 weeks (672 h) of aging. They started to decrease after 4 weeks, and showed a reduction of 4% in the peak area after 8 weeks of aging. This decrease in the FTIR peak area corresponding to the C-N stretching in the pthalimide ring can potentially be attributed to chain scission in the C-N bond as a result of the thermal aging process [190].
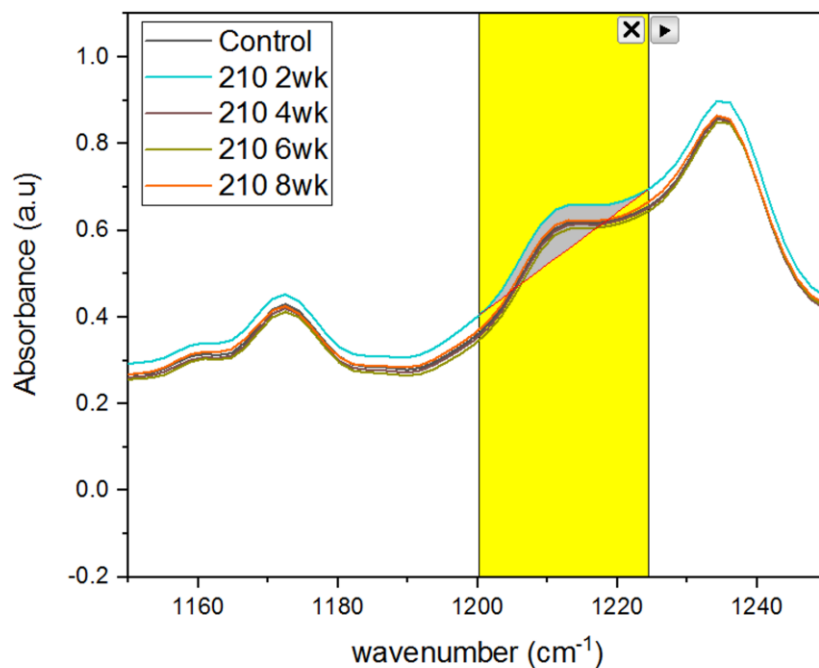
Figure 5.15 Determination of the peak area for the 1215 cm^{-1} peak associated to the C-N stretching in the pthalimide ring.
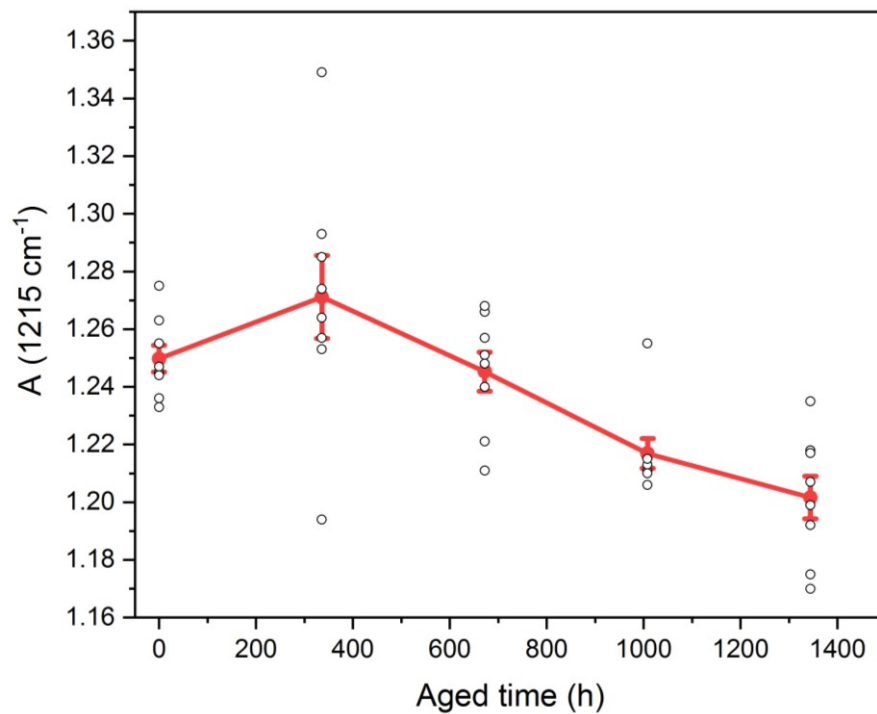
Figure 5.16 Variation in the 1215 cm^{-1} peak area associated to C-N stretching in the pthalimide ring as a function of the aging time at 210 °C. The open circles correspond to the values for the individual replicates.

Fig. 5.17 shows the determination of the peak area for the 1777 cm^{-1} peak associated with the carbonyl group (1777 cm^{-1}) in the phthalimide group. The variation in the peak area as a function of the aging time at 210 °C is shown in Fig. 5.18. A comparison of the mean values of the peak areas from 0 to 8 weeks shows an initial increase followed by a plateau. This result can be attributed to the fact that the thermo-oxidation of polymers is generally associated with an increase in the number of carbonyl groups because of the radicals formed under the application of thermal energy [76]. These C-O• radicals are then converted to C=O groups in the polymer network.
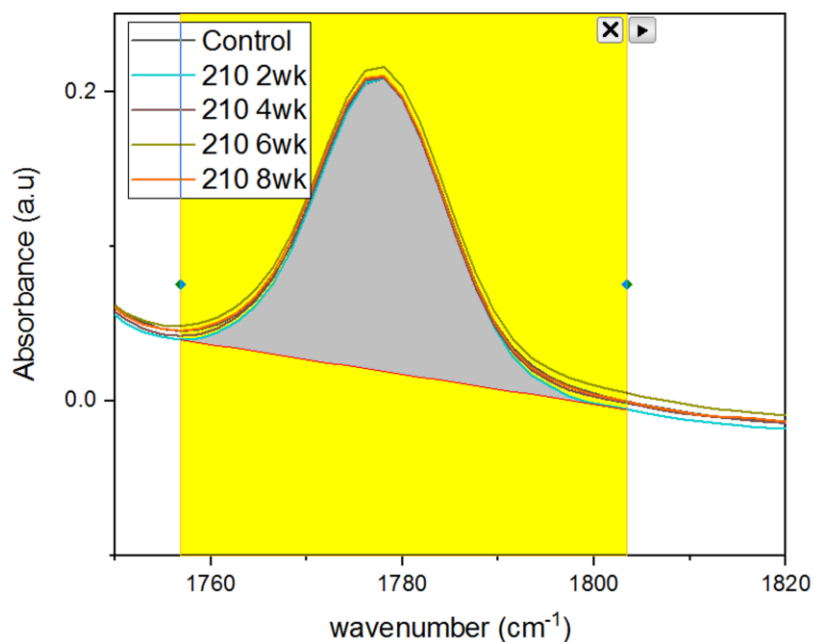
Figure 5.17 Determination of the peak area for the 1777 cm^{-1} peak associated with the carbonyl group in the pthalimide ring.
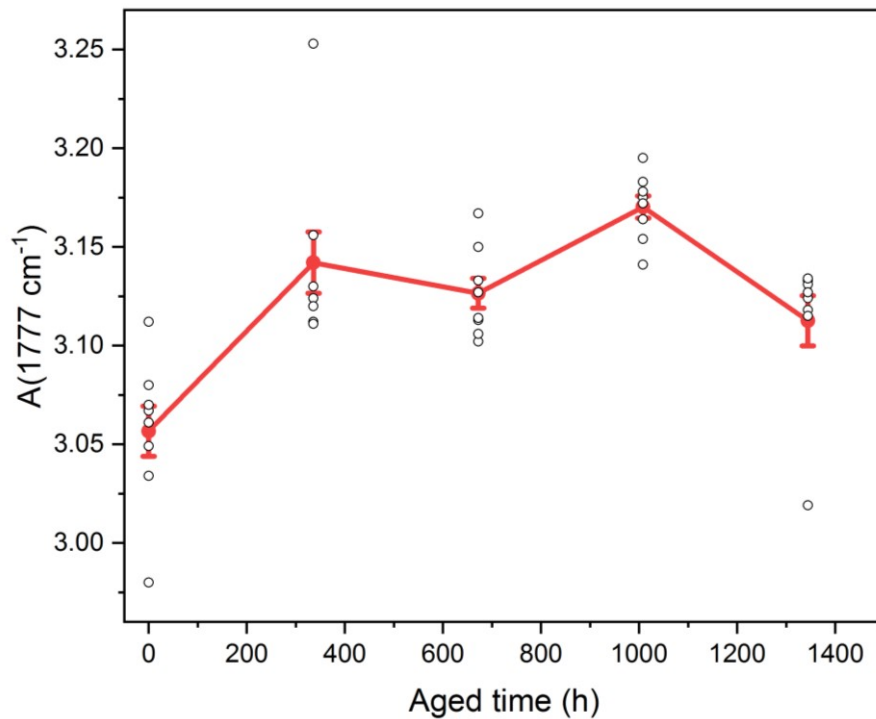
Figure 5.18 Variation in the 1777 cm^{-1} peak area associated with the carbonyl group in the pthalimide ring as a function of the aging time at 210 °C. The open circles correspond to the values for the individual replicates.

Fig 5.19 shows the determination of the peak area for the 1172 cm^{-1} peak associated with the isopropylidene group. The variation in the peak area as a function of the aging time at 210 °C is illustrated in Fig 5.20. The mean values of the peak areas show a decrease with aging time. This result can be attributed to the occurrence of chain scission of the isopropylidene group during thermal aging, in agreement with the conclusion of Carroccio et al. who investigated the thermal degradation mechanisms of PEI by pyrolysis [190].
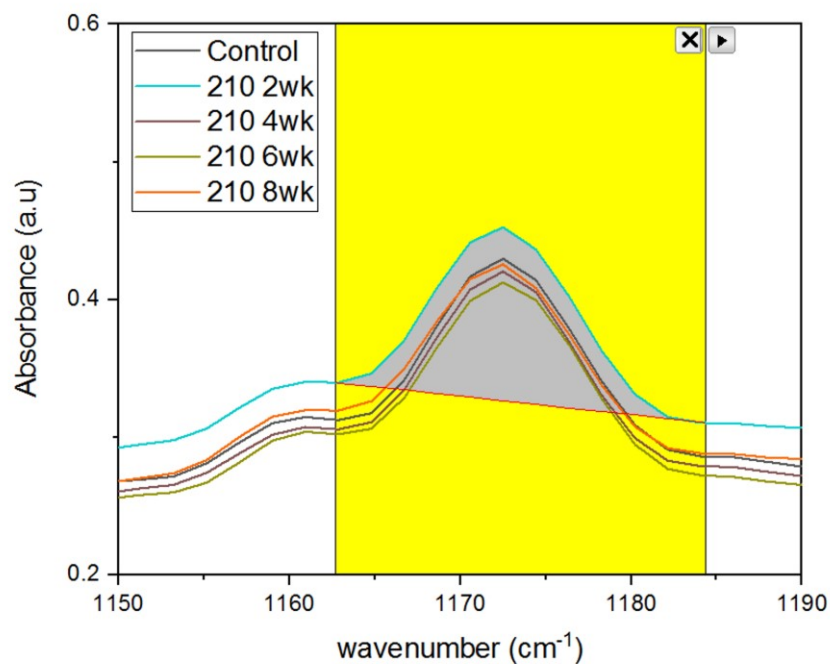
Figure 5.19 Determination of the peak area for the 1172 cm^{-1} peak associated with the isopropylidene group.
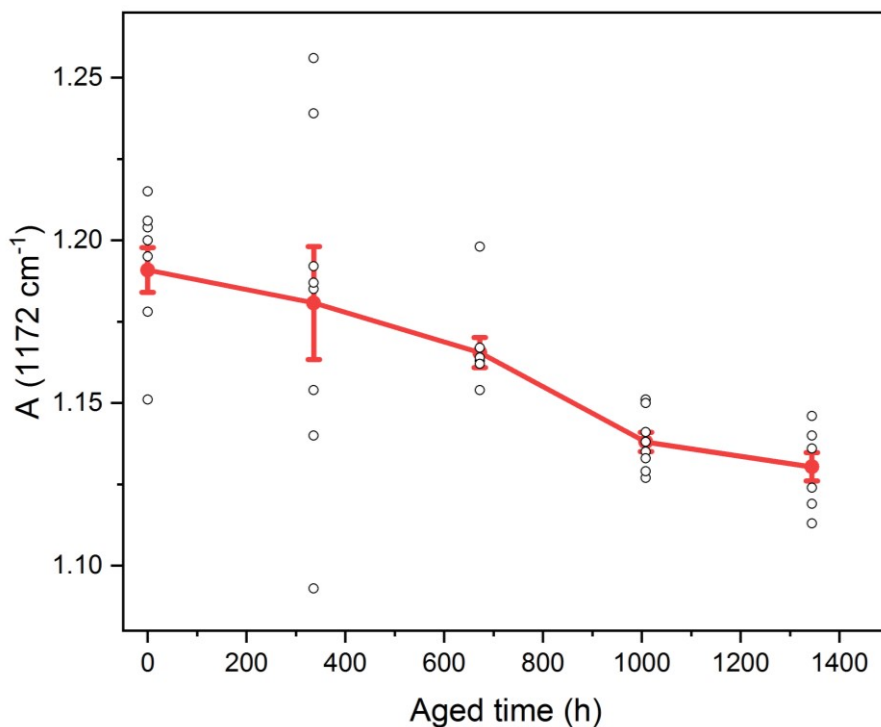
Figure 5.20 Variation in the 1172 cm^{-1} peak area associated to the isopropylidene group as a function of the aging time at 210 °C. The open circles correspond to the values for the individual replicates.

Based on the statistical analysis, we found that at least one aging condition was statistically different from the other aging conditions. The details of the statistical analysis are provided in Appendix, section A4.3. In addition, 2 weeks of aged PEI spectra in Fig 5.17 to 5.19 shows higher absorbance value over all other conditions becuase this value was obtained after the spectra are normalizeby the area of a thermally stable peak. This change in the FTIR peak areas corresponding to the phthalimide and isopropylidene groups as a result of thermal aging is in agreement with the results of Musto et al. [231]. It also points towards three specific reaction mechanisms for the thermal aging of PEI:

- N-H transfer from pthalimide ring (identified as R_5 in Fig. 5.21);

- C-H transfer after disproportionation in isopropylidene group (identified as R_3 in Fig. 5.21);

- Formation of carbonyl groups in the pthalimide ring.
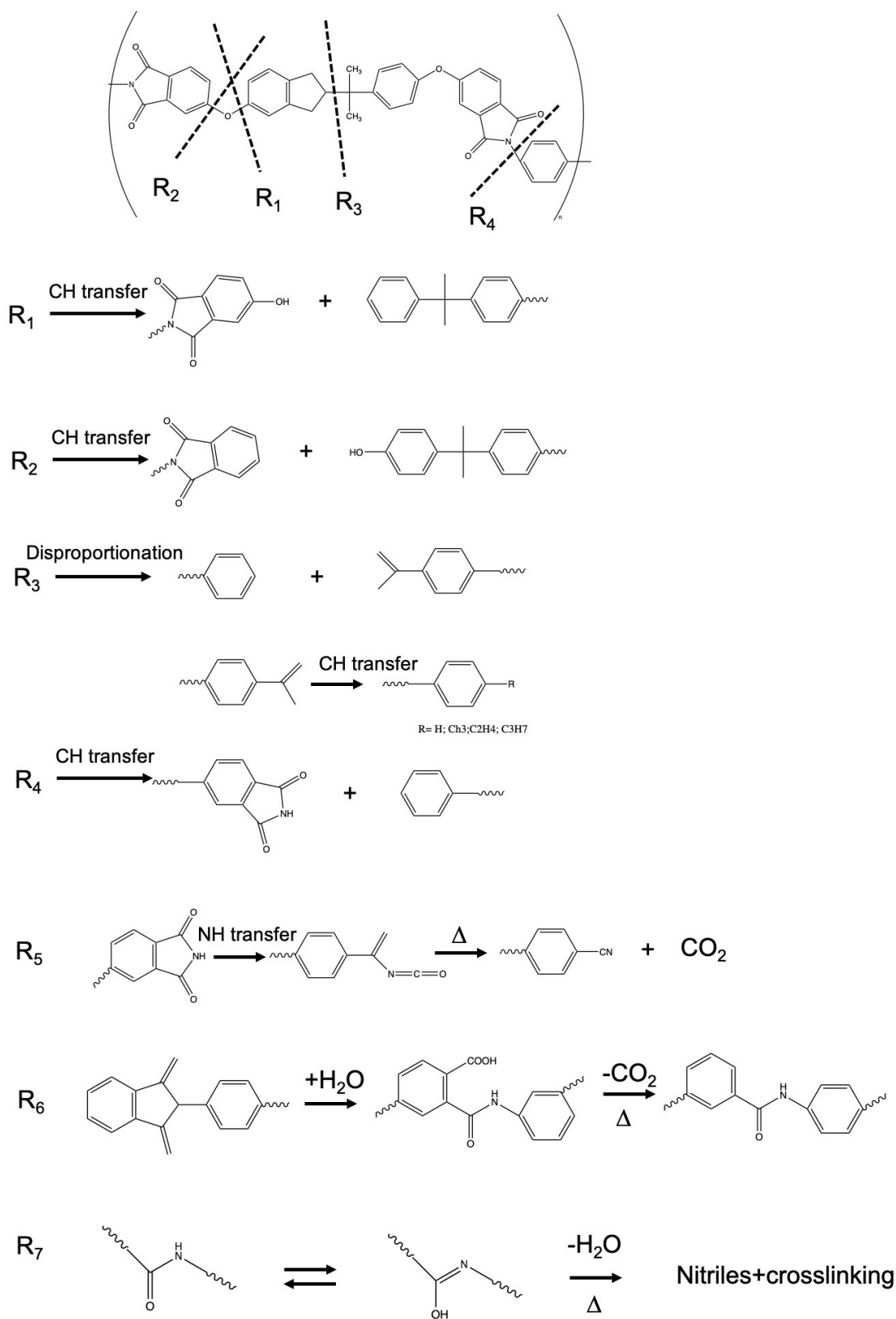
Figure 5.21 Possible mechanisms of thermal chain scission of PEI. Reprinted from [189] and [191]

5.4 Surface characterization of PEI

The influence of thermal aging on the polymer surface has been studied in various polymers and resins, micro cracks formation, surface cracking, and changed in surface roughness [232–234]. In order to investigate the effect of thermal aging on the surface of PEI samples, FE-SEM images were taken at different aging times and temperatures. Fig. 5.22 shows examples of results obtained for the unaged samples (Fig. 5.22 a), after 12 weeks of aging at 190 °C (Fig. 5.22 b) and 200 °C (Fig. 5.22 c), and after 8 weeks of aging at 210 °C (Fig. 5.22 d). A difference between the surface of the unaged and aged PEI samples is the emergence of cracks on the surface of the thermally aged PEI samples. The 12 weeks -190 °C condition (Fig 5. 22 b) can be associated with a few sub-micron cracks and some non-uniform areas. With 12 weeks of thermal aging at 200 °C (Fig. 5.22 c), both the surface area occupied by the crack-dense zones and the number of these crack-dense zones has increased. After 8 weeks of aging at 210 °C (Fig 5.22 d), sub-micron cracks are visible over the entire surface of the SEM image.
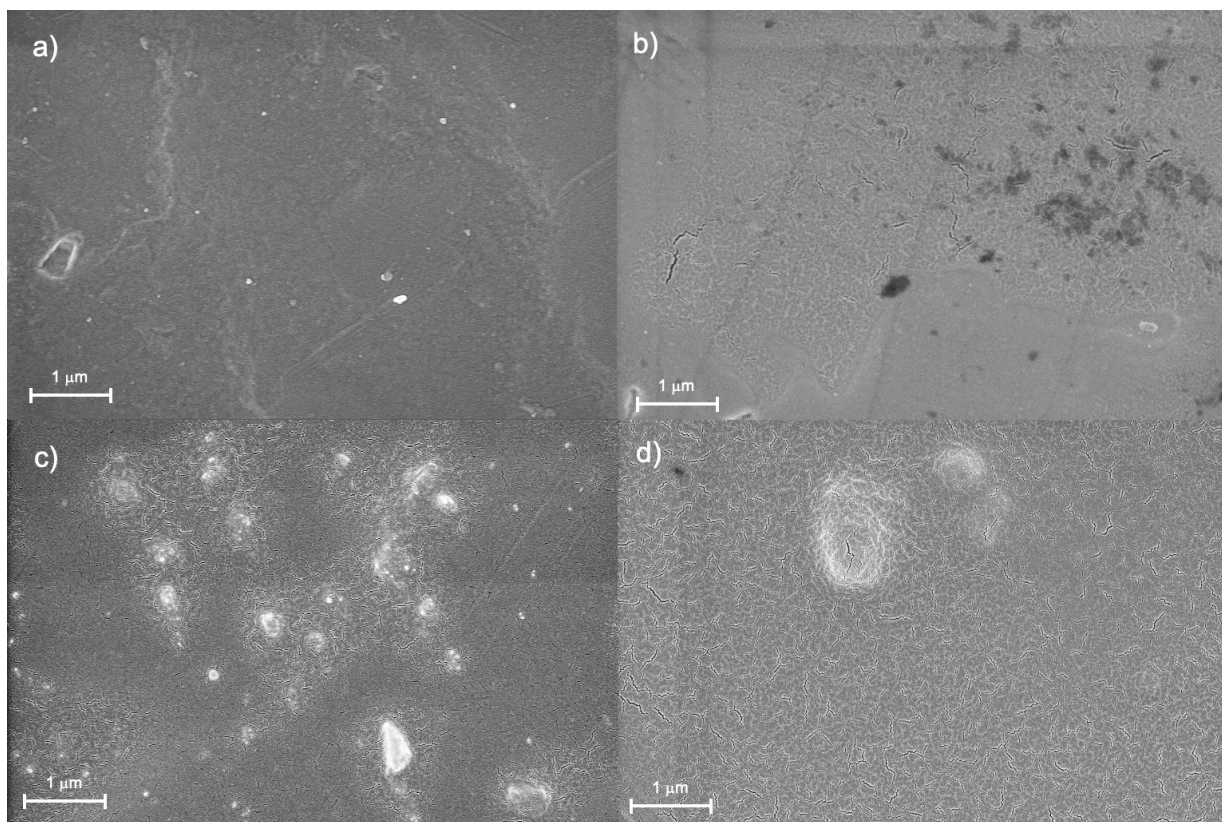
Figure 5.22 SEM image of the surface of thermally aged PEI specimens, a) unaged (0h), b) aged at 190 °C for 12 weeks, c) aged at 200 °C for 12 weeks, and d) aged at 210 °C for 8 weeks.

The surface area occupied by the cracks was quantified for the different thermal aging times and temperatures using the SEM images and the ImageJ software (section 5.2.5). Fig. 5.23 illustrates the variation between the crack area (%) and the aging time for the three aging temperatures. The crack area increases both with aging time and temperature. This suggests that chain scission occurred during thermal aging, causing some areas to weaken. When the specimens are removed from the oven after the aging period, the cooling from the aging temperature (190 °C to 210 °C) and room temperature generates thermal stress. This thermal stress is applied to areas weakened by thermal aging, cracks may formed and propagated [235]. This phenomenon of crack formation at the surface of the PEI film as a result of aging is a beneficial feature for the design of

the end-of-life sensor as it may favor the disruption of the conductive track at the surface of the PEI film.
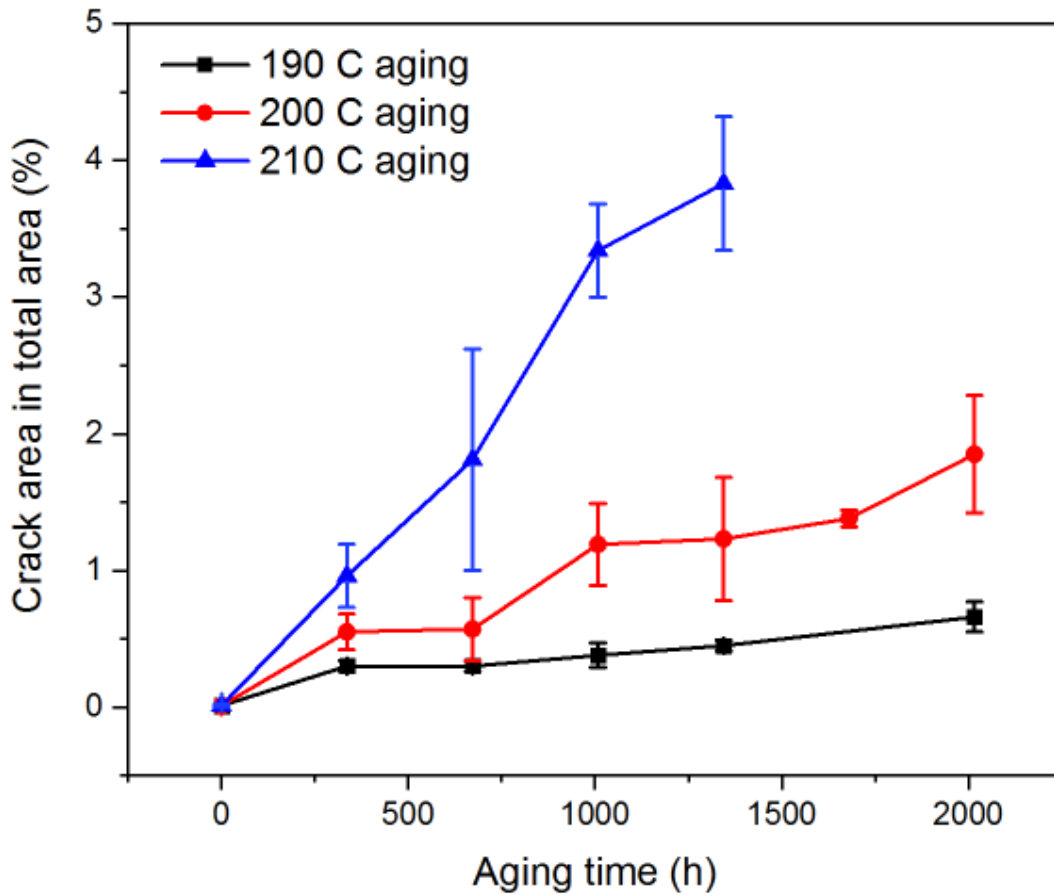
Figure 5.23 The percent of crack in area of 222.1 μm^2 of thermally aged PEI at different time /temperatures.

The surface roughness of the PEI samples before and after aging at the different conditions was also measured using AFM (section 5.2.8). In general, authors report that surface roughness increases after thermal aging because added matter or the formation of holes/cracks on the surface during aging [236]. In our case, the unaged PEI film had an unique pattern associated with the manufacturing process (Fig 5.24). The surface roughness was quantified using AFM. Fig 5.25 displays the image of the surface in 3D. The unaged PEI film has a surface roughness (Rq) of 0.16

± 0.01 mm (Table 5.4). After thermal aging, it is possible to observe both on the AFM images (Fig

5.25) and in Table 5.4 that the surface roughness decreased.

Figure 5.24 Optical microscope image of the unaged PEI film.
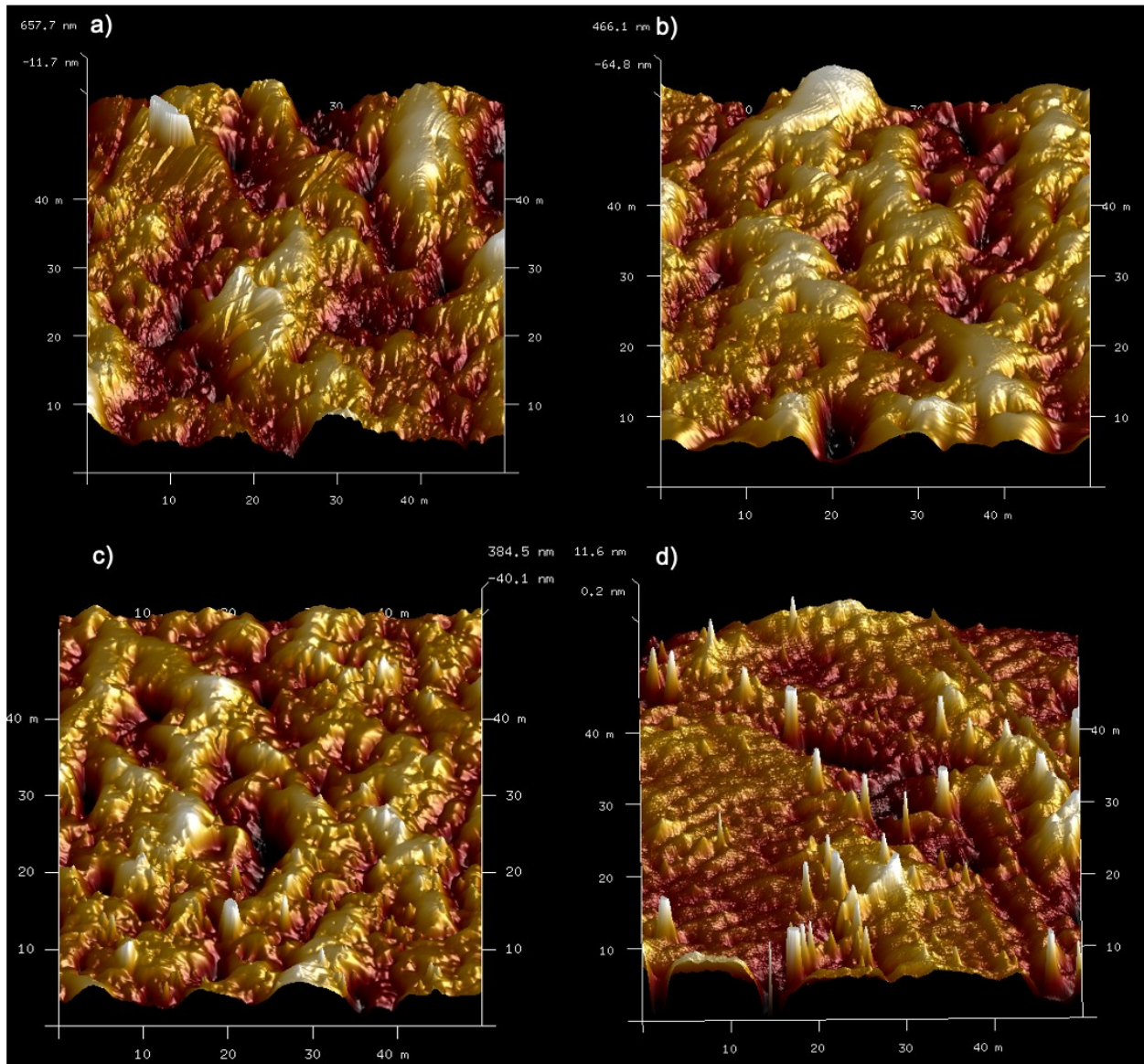
Figure 5.25 3D AFM images of PEI film surface in the a) unaged condition and after aging for 8 weeks at different temperatures b) 190 °C, c) 200 °C, d) 210 °C .

Table 5.4 Surface roughness of the unaged and thermally aged PEI film samples

Aging temperature/time	Surface roughness (Rq)
Control (unaged)	0.16 ± 0.01 mm
190 °C/8 weeks	0.16 ± 0.01 mm
200 °C/8 weeks	0.12 ± 0.01 mm
210 °C/8 weeks	0.03 ± 0.01 mm

A change in the PEI film was also observed visually. The neat PEI film was initially semi-transparent (Fig. 5.26 a). It became gradually transparent to visible light after thermal aging. This may be related to the apparent surface roughness reduction during thermal aging, which can be confirmed in Table 5.4 [237,238].
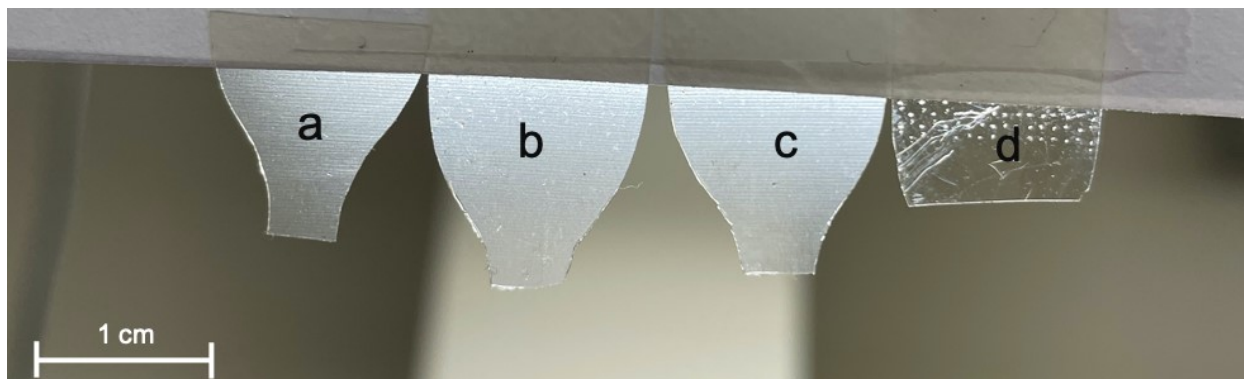
Figure 5.26 Change in the PEI film transparency after thermal aging for 8 weeks at different temperatures. a) unaged, b)190 °C, c) 200 °C, and d) 210 °C.

5.5 Conclusions

The accelerated thermal aging behavior of PEI has been investigated. Specimens taken from a PEI film were exposed to three different temperatures: 190, 200 and 210 °C, for times up to 16 weeks depending on the aging temperature. The FTIR analysis showed that the main functional groups in PEI are consumed due to chain scission. The formation of carbonyl groups resulting from oxidation reactions is also observed. The thermal aging was also shown to create microcracks on the surface of the PEI specimens. The surface area occupied by these cracks increased with longer aging times and higher aging temperatures. This phenomenon of crack formation at the surface of the PEI film as a result of aging is a beneficial feature for the design of the end-of-life sensor as it may favor the disruption of the conductive track at the surface of the PEI film. A irreversible deformation was also observed as a result of thermal aging, reducing the PEI film roughness and increasing its transparency to visible light.

In terms of mechanical behavior, the aged PEI showed changes in UTS as well. The first phase of the thermal aging generated an increase in UTS due to crosslinking reactions. This crosslinking evidenced by the initial increase in the UTS can also be associated with the initial increase in the glass transition temperature observed because the crosslinking reaction reduces the mobility of the polymer network. For longer aging times and higher aging temperatures, the UTS of PEI started to decrease because of chain scission. Using the UTS data, a master curves was constructed based on the application of the TTS principle. The shift factors yielded to a value of the activation energy of 112 kJ mol^{-1}. This value is similar to values of activation energy reported for fire protective fabric blends used as outer shell in firefighter protective clothing, with for instance an activation energy of 111 kJ mol^{-1} for a 60/40 Kevlar/PBI fabric and of 113 kJ mol^{-1} for a 60/40 Kevlar/Nomex IIIA (93% Nomex, 5% Kevlar, 2% carbon fibers) fabric. This indicates the relevance of the choice of PEI as the sacrificial polymer layer for the design of the end-of-life sensor for fire protective fabrics.

CHAPTER 6   The fabrication of polyetherimide-based thermal aging sensors for the monitoring of fire protective clothing's outer shell fabric

6.1 Introduction

Firefighters are often exposed to extremely hazardous environments such as high temperatures, heat flux, and flames during firefighting operations and emergency rescue. Under these conditions, firefighters may experience life-threatening injuries. There were 38,844 fires in the seven jurisdictions reporting to the National Fire Incident Database (NFID) in Canada, 2014 [239]. Due to these fires, the importance of firefighting techniques and safety of firefighters have gained attention. Firefighters have to wear fire protective clothing and other safety gear such as helmets and boots in structural (buildings, vehicles, aircraft interiors, vessels and enclosed structures), and wildland firefighting [6,240]. Fire protective clothing is designed to protect against heat and flames, and minimize the effects of life-threatening surfaces (sharp or abrasive surfaces) [241]. It play an important role in reducing injuries to firefighters. Fire protective clothing must also have the function of regulation of physiological reactions of the body, for example enabling the evaporation of perspiration [73]. However, not all of these requirements can be met completely by one layer of fabric in fire protective clothing, multi-layer clothing is therefore required.

Fire protective clothing generally consists of 3 layers: a thermal liner, a moisture barrier and an outer shell. The outer shell is the first protection layer from heat, flame, abrasion and cuts. The common materials for outer shells are para-aramid (commercialized for instance as Kevlar®), meta-aramid (commercialized for instance as Nomex®), polybenzimidazole (PBI), and their blends; these materials all provide high strength and thermal resistance [64]. The outer shell layer is the first line of defense against hazards, and this layer ages with normal use or exposure to high

temperature, and other conditions [7,10,242]. According to the National Fire Protection Association (NFPA) 1971 criteria, the minimum tear strength and breaking force of outer shell are 100 N and 623 N, respectively [6]. With these criteria, the aging of outer shell fabrics has been studied under various conditions, including high temperature, heat flux, exposure to water and UV [3,59,70,164,243]. It is very important to understand how the protective clothing ages and identify methods to indicate the progress of aging, so that the firefighters can be informed when this clothing needs to be replaced.

For polymeric materials, which are the ingredients of fire protective clothing in textile or coating forms, aging is defined as cumulative and irreversible changes with the passage of time that cause a decline in performance and/or improvement in/loss of functionality of fire protective clothing [244]. Fire protective clothing is exposed to a combination of thermal, ultraviolet (UV), and moisture aging environments among others. For firefighters, frequent exposure to high temperature atmospheres is one of the causes of the aging of their protective clothings (the typical temperature range that firefighters experience under operation is between 60 °C and 300 °C) [64,70,164]. In general, the thermal aging mechanism of polymeric materials has three steps: (i) radical formation, (ii) chain scission and crosslinking reactions caused by the radicals, and (iii) termination of the aging reactions by inactivation of the radicals [12]. Knowledge of the thermal aging behavior of polymeric materials can be used to predict the lifetime of these materials.

The assessment of aging of fire protective clothing is generally conducted using destructive testing methods, for instance the tensile and tear strength testing of constituting textiles [245,246]. Some authors have also measured the effect of aging on the liquid penetration [247]. While performance evaluation methods that lead to a destruction of the clothing provide reliable information to assess the progression of aging, such testing cannot be performed to monitor the

status of the fire-protective clothing during use as it would render the garment useless. Non-destructive methods, such as by monitoring the changes in color or in macromolecular chemistry, e.g. by infrared spectroscopy, have been investigated to evaluate the performance of the clothing at regular intervals over time [64,248]. However, these non-destructive test methods have not been able to provide a reliable assessment of the fabric's performance decrease. In addition, they require equipment not available in fire stations and thus cannot be easily implemented to allow the in-service condition monitoring of the protective clothing by firefighters. Therefore, new real-time monitoring methods that can be used to track the clothing condition continuously during service are desirable. Here, the integration of sensing layers within the protective clothing is proposed to serve as an indicator about the aging of the clothing. These sensing layers must have similar thermal properties as the fire protective clothing itself. In addition, all of the materials used in these sensors must be able to withstand the high temperatures to which the garments are exposed.

Polyetherimide (PEI), a thermoplastic polymer developed and commercialized in 1982 by General Electronics®, has excellent mechanical properties and a high temperature resistance ($T_g \sim$ 217 °C) [189,205,249]. PEI has the chemical structure of an aromatic imide with propylidene and ether groups in its backbone. Aromatic imide groups provide stiffness and high thermal stability, and the ether groups offer good processability due to low melt viscocities [184]. In addition, PEI has an excellent stability under hydrolytic environments, and can even withstand short-term contact with mineral acids and diluted bases [184]. Due to PEI's flame resistance and stability in liquid environments, PEI can be used in applications under harsh environments with a wide range of temperatures and exposure to moisture [191]. For example, PEI has been used in automotive (i.e., vehicle headlamp) [184], electronics [192], medical and aircraft applications [193].

The two leading chemical reactions that cause the thermal degradation of PEI are crosslinking and chain scission [250]. The crosslinking reaction in PEI networks is reported to happen frequently in the temperature range between 320 and 380 °C, whereas chain scission reactions are abundant above 400 °C with the highest decomposition rate occuring between 510 and 540 °C [251]. The pyrolysis products above 550 °C are the same for PEI and m-aramid, a common fire protective clothing material [190]; this implies that PEI and m-aramid may have similar thermal degradation behaviors.

The thermal decomposition temperatures of PEI and m-aramid were observed to be around 450 °C and above 400 °C, respectively [190,252]. In Chapter 5 of this thesis, the activation energy of PEI was found to be 112 kJ/mol. These results were obtained over the temperature range from 190 °C to 210 °C. On the other hand, Dolez et.al determined the activation energy of 7 different outershell fabrics with different fiber content composition and structure during thermal aging [3]. It was based on the change in tear strength of the fabrics after exposure to different temperatures between 150 and 300 °C. Among the 7 fabrics they studied, fabrics labelled "60% Kevlar/40% Nomex IIIA spun yarns", "60% Kevlar/20% Nomex/20% PBO spun yarn", and "60% para-aramid/40% PBI spun yarns/Kevlar filament" showed activation energies of 113 ± 7 kJ/mol, 103 ± 7 kJ/mol, and 111 ± 3 kJ/mol, respectively. The activation energy of 112 kJ/mol measured for PEI is thus within the range of what has been reported for these outershell fabrics. Therefore, since PEI has a similar thermal aging behavior as fire protective clothing fabrics, it can be expected that PEI can be used as the temperature-sensitive layer in the sensor for the aging assessment of fire protective clothing.

Recently, the Tour group has introduced the 'laser-induced-graphene' (LIG) technique in polyimide-based polymers. This technique allows 3D porous graphene to be patterned on these

polymers under ambient environment using a commercial CO_2 infrared laser scriber [11,253]. By irradiating the area of interest with a focused laser at a controlled intensity, the laser scriber carbonizes polyimide-based polymers by converting the sp^3-carbons in the polymer to sp^2-carbon atoms by a photothermal reaction [11,254,255]. The Tour group found that LIG can be applied to polymers including m-aramid, polyimide (Kapton®), polyetherimide, and polybenzimidazole [256]. The LIG technique can be used to create electrically conducting traces on the surface of PEI films so that they can be utilized in wearable sensor applications.

The present study is focused on the fabrication of thermal aging indicators (sensors) for fire protective clothing. This sensor is designed to be affixed on the fire protective clothing as a wearable patch; it will lose its electrical conductivity when a critical thermal aging temperature/time is reached. Compared to other non-destructive methods for the assessment of aging, this indicator does not require specimen preparation procedures for external characterization tools, such as Fourier-transform infrared spectroscopy (FTIR) optical microscopy, or colorimetry [3,64]. The proposed indicator, named as PEI-LIG sensor, consists of a PEI film, a conductive LIG layer, and a support fabric (figure 6.1). An encapsulation layer is included to protect the sensor during laundering.
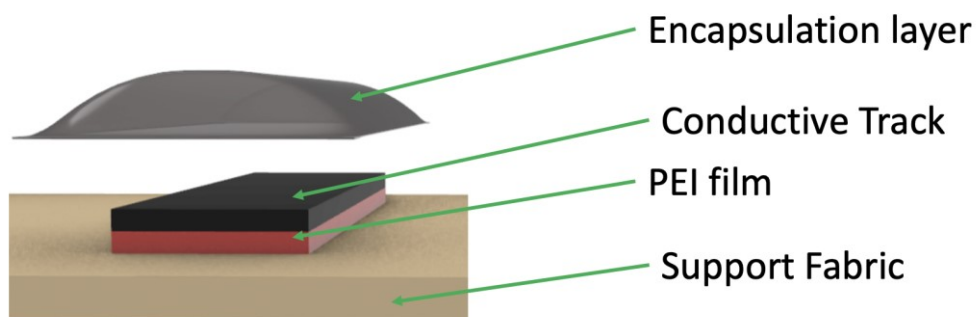
Figure 6.1 The layout of the thermal aging sensor for fire protective clothing

In the design of the PEI-LIG sensor, the PEI layer serves as a sensing layer that simulates the aging behavior of the fire protective clothing. The electrical conductivity of the LIG conductive layer, which is formed from the PEI substrate, is the aging indicator that will be monitored. In Chapter 5, we confirmed that microcracks are created as the PEI layer undergoes thermal aging. These microcracks may lead to a disruption of the physical integrity of the LIG layer and therefore a loss in its electrical conductivity. While Chapter 4 of the thesis evidenced a high stability of conductive rGO coatings on m-aramid fabrics (for e-textile applications) under mechanical deformation and abrasion [257], the aging indicator that was fabricated for the work described in Chapter 6 harnesses the conductivity loss of the LIG layer induced by the extrinsic factor of the thermal degradation (aging) of the PEI substrate layer for the assessment of fabric aging. Based on the activation energy calculations in Chapter 5, our PEI-LIG thermal aging indicator should offer the information about the aging status of the fire protective clothing simply by monitoring the change in electrical conductivity of the conductive trace to give an indication of when the fire protective clothing needs to be replaced. This indicator will be a useful tool to estimate when protective garments and other high performance textiles in other fields, such as aerospace or military applications, have reached the end of their life.

6.2 Experimental section

6.2.1 Laser-induced-Graphene (LIG) layer on polyetherimide film

A 250 μm thick polyetherimide (PEI) film was purchased from McMaster Carr, and placed in a 70 W 10.6 μm laser scribing system (PLS 6.150 D, Universal Laser System, Inc) equipped with a CO_2 laser for patterning. During the patterning of the graphitic layer on the PEI substrate, the speed and power were set to 5 % for patterning and 10 % for cutting, respectively. The value of

pulses per inch was fixed at 500 during the engraving process. A schematic represnetation of the LIG layer formation on the PEI film is provided in Fig. 6.2. The size of sensor was 3.8 cm in length and 0.8 cm in width. The dimensions of LIG layer were 3 cm in length and 0.5 cm in width.
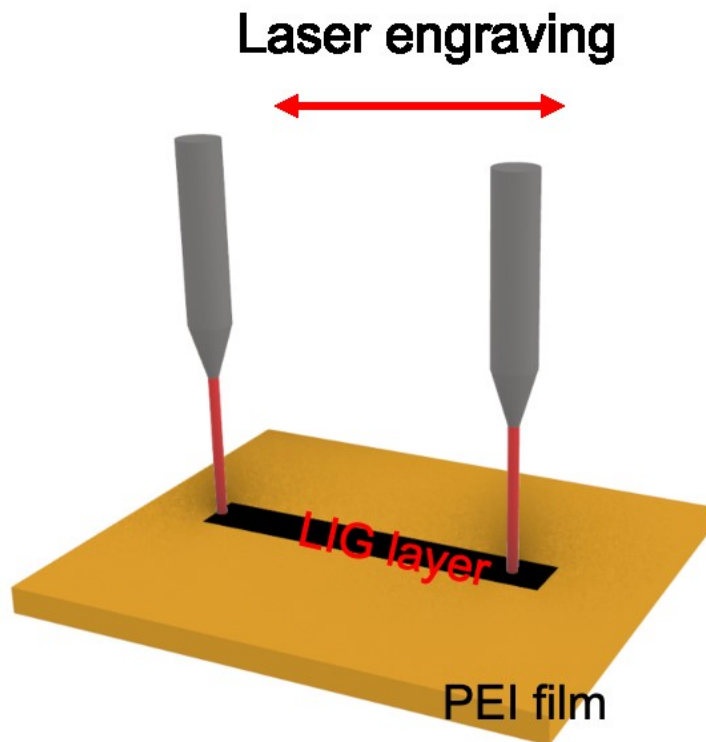
Figure 6.2 Laser-Induced-Graphene layer formation by laser patterning

6.2.2 Fabrication of the PEI-LIG sensor

In order to monitor the electrical resistance of the LIG layer on the PEI film, electrical connections were made by bonding copper strips to the LIG layer. A carbon adhesive (DAG-T-502, Ted Pella, CA, USA) was applied between the copper strips and the LIG layer. It was also used to cover the copper strips to prevent their oxidation during thermal aging. In the last step, a non-photosensitive polyimide encapsulant (PI 2574, HD MicroSystems, NJ, USA) was applied on the LIG layer by spin coating (Laurell Model WS-650MZ-23NPP) at 1000 rpm for 1 min. The PEI-LIG sensor fabrication process is illustrated in Fig. 6.3.
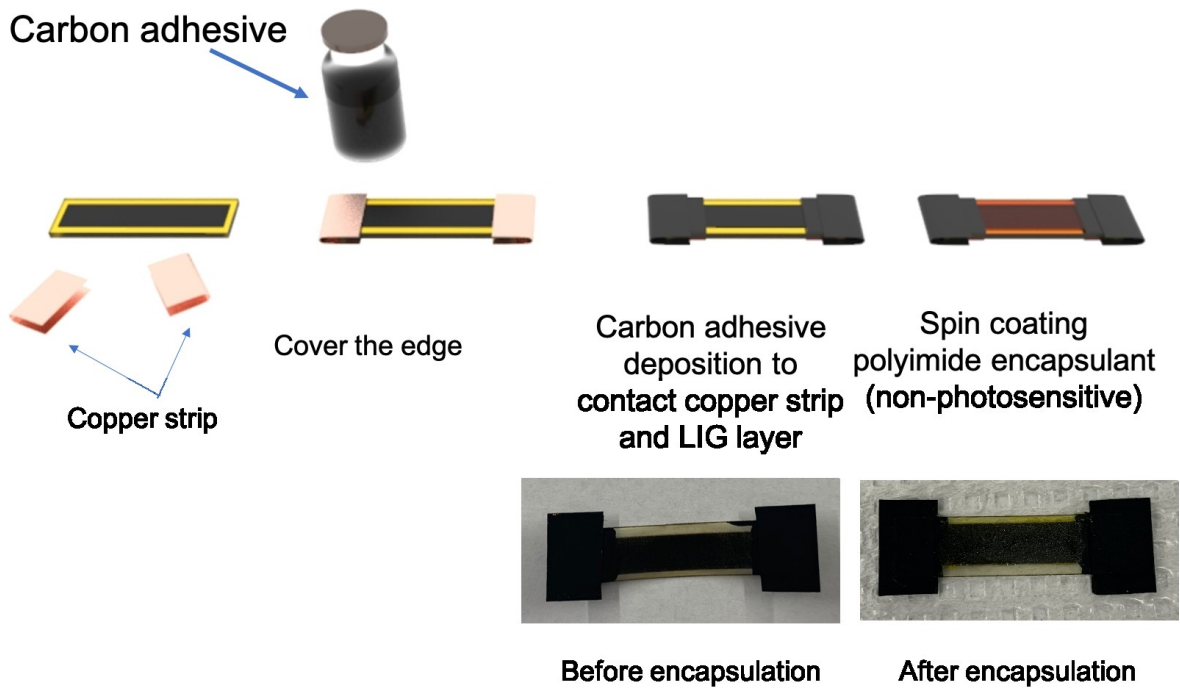
Figure 6.3 The fabrication process of the PEI-LIG sensor

A series of sensors were prepared for short/long term aging and washing stability assessment. Their initial resistance (R_0) values are listed in Table 6.1. Variations in R_0 values can be observed beween the different sensors produced. This can be attributed to the sensor fabrication process, in which some parameters may be more or less controlled. As a result, the results for these sensors are expressed in terms of the average normalized resistance R/R_0 by computing the average of the ratio of the residual resistance to the initial resistance for each sensor.

Table 6.1 Initial resistance of the sensors prepared for short/long term aging and washing stability assessment

Short term aging	210 °C	250 °C	260 °C	270 °C	280 °C
	2.66 kΩ	7.07 kΩ	3.16 kΩ	8.39 kΩ	44.3 kΩ
Initial resistance (R_0)	6.41 kΩ	3.41 kΩ	5.22 kΩ	55.6 kΩ	5.22 kΩ
	8.50 kΩ	2.57 kΩ	56.5 kΩ	2.94 kΩ	2.65 kΩ
Long term aging	**Group 1**	**Group 2**	**Group 3**	**Group 4**	**Group 5**
	2.10 kΩ	5.70 kΩ	3.05 kΩ	6.96 kΩ	11.15 kΩ
	3.53 kΩ	7.17 kΩ	3.75 kΩ	2.17 kΩ	4.69 kΩ
Initial resistance (R_0)	6.33 kΩ	3.63 kΩ	4.53 kΩ	3.35 kΩ	2.11 kΩ
	4.35 kΩ	4.83 kΩ	4.12 kΩ	10.7 kΩ	7.81 kΩ
	2.12 kΩ	7.90 kΩ	9.10 kΩ	10.5 kΩ	7.96 kΩ
Washing stability	**1 washing**	**3washing**	**5washing**	**10 wasing**	
	1.48 kΩ	0.485 kΩ	1.39 kΩ	2.13 kΩ	
	1.59 kΩ	0.963 kΩ	0.671 kΩ	1.96 kΩ	
Initial resistance (R_0)	1.90 kΩ	1.23 kΩ	1.68 kΩ	1.84 kΩ	
	1.22 kΩ	1.62 kΩ	1.48 kΩ	3.41 kΩ	
	2.21 kΩ	1.11 kΩ	1.81 kΩ	2.10 kΩ	

6.2.3 Accelerated thermal aging of the PEI-LIG sensor

Two different methods were used to induce thermal aging in the PEI-LIG sensor. In the first method, the fabricated PEI-LIG sensor was placed in a convection oven (Model 281 A Vacuum Oven, Fisher Scientific) set to a temperature of 270 °C. In order to observe the changes in resistance at different aging times, six groups of sensors were prepared (each group contained five samples) and each group was aged a different time (4 days for Group 1, 10 days for Group 2, 14 days for Group 3, 21 days for Group 4, and 28 days for Group 5). The resistance was measured for each group after different aging times. The samples were placed back into the oven between the measurements until a total time of 4 weeks was reached. The electrical resistance of the sensors

at the desired timepoints was measured by a Bench LCR meter (BK precision model 895, CA) by clipping the copper strips with alligator clips. For Group 1, the sensors were measured after 4, 10, 14, 21, and 28 days. For Group 2, the sensors were measured after 10, 14, 21, and 28 days. For Group 3, the sensors were measured after 14, 21 and 28 days. For Group 4, the sensors were measured after 21 and 28 days.

In the second method, the PEI-LIG sensors were placed on a hot plate (Corningr® Digital Hot plates, Corning, NY, USA) and thermally aged at 210, 250, 260, 270, and 280 °C for 80 h. The temperature of the samples was determined with an infrared camera; it remained at the set aging temperature throughout the aging process. The electrical resistance of the sensors was measured using the same method as above.

6.2.4 Stability of the PEI-LIG sensor under accelerated laundering

Accelerated laundering was conducted to assess the effect of repeated washings on the electrical conductivity of the PEI-LIG sensor. Accelerated washing was performed with a Launder-Ometer (Atlas, IL, USA) following the ISO 105-C06 standard and test procedure A1S [174]. According to the standard, one accelerated washing cycle (30 min) in the Launder-Ometer is equivalent to 5 cycles of domestic laundering. In our case, we divided the 30 min cycle into 6 min segments; therefore, one accelerated washing cycle applied here can be considered as equivalent to one cycle of domestic laundering. In accordance with the standard, 150 mL of washing solution prepared with 4 g/L of detergent was introduced in each canister with 10 steel balls. Four canisters of five sensors were prepared. The laundering was conducted at 40 °C. The five sensors were collected from the canister after the predetermined number of washing cycles (1, 3, 5, and 10 cycles), where each cycle lasted 6 min. Immediately after being collected, the specimens were

rinsed with DI water and dried at room temperature for 24 hours. Then, the electrical resistances of the five samples was measured.

6.2.5 Statistical Analysis

Depending on the test, between three and five replicates of the sensors were tested: three replicates for the short term aging and five replicates for the long term aging and the laundering. The mean values and standard deviations are reported. Where applicable, statistical significance was evaluated using the single factor ANOVA analysis. A confidence level of 0.05 was set to establish significance. The detailed results of the statistical analysis for this chapter are included in Appendix (section A4.4).

6.3 Results and discussions

6.3.1 Thermal aging of the PEI-LIG sensor

In order to assess the long-term thermal (up to a month) aging, five groups of five sensors were placed in the convection oven at 270 °C. All five groups have a total aging time of 28 days (672 hours), but each group has a distinct thermal history. Specifically, the thermal aging of each group was halted at different times (i.e., taken out of the convection oven to the room temperature); the interruptions were intentionally designed to confirm if there is a noticeable effect of intermittent heating/cooling cycles on the overall thermal aging. The black solid line in Fig. 6.4 follows the evolution of the average resistance values for Group 1, 2, 3, 4, and 5 sensors, which have undergone uninterrupted annealing times of 4, 10, 14, 21, and 28 days (i.e., 96, 240, 336, 504, and 672 hours), respectively. The uninterrupted thermal aging resulted in an increase of the normalized resistance values by 1.65, 3.24, 3.76, 6.79, and 10.6 times for Group 1, 2, 3, 4, and 5 sensors, respectively.
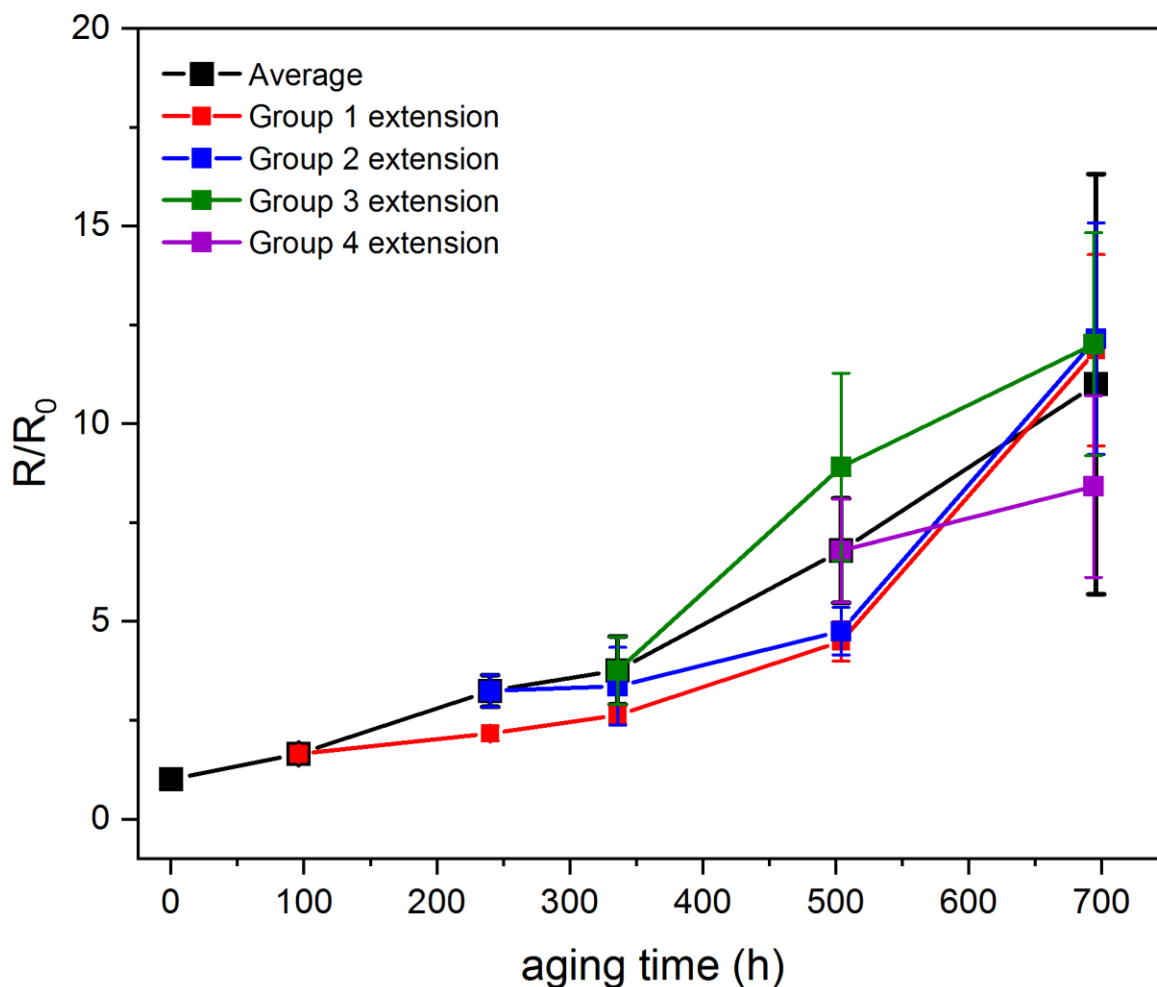
Figure 6.4 Resistance changes after accelerated thermal aging of PEI-LIG sensors at 270 °C for 4 weeks. The black line indicates the average values for each group at the designate time point (e.g. Group 1 at 4 days, Group 2 at 10 days, etc). The colored lines track each group after their initial designated time point as their aging was extended their aging to 4 weeks.

The effect of intermittent cooling to room temperature was studied by putting Groups 1, 2 ,3 and 4 sensors back in the oven after being measured; these samples were exposed to cooling/measuring/heating cycles periodically up until 28 days. When comparing mean values of resistance in each aging condition, the resistance is increased over the annealing time in both uninterrupt/interrupt annealing. A statistical analysis was conducted between the different aging conditions (table 6.2); it shows no statistically significant difference in resistance between the

results for the different sensor Groups. Therefore, subjecting the sensors to intermittent cooling does not seem to affect their overall thermal aging behavior in terms of electrical conductivity.

Table 6.2 Result of the statistical analysis (ANOVA) for the different series of aging conditions.

Aging time (h)	p-value (95% confidence level)
336h	0.49 (Total sample size n = 20)
504h	0.21 (Total sample size n = 25)
672h	0.90 (Total sample size n = 25)

The short-term aging experiment involved placing five groups of sensors on a hotplate; each group has three sensors. Each group of sensors was exposed to thermal aging on the hotplate for 80 h at a different temperature (210, 250, 260, 270 and 280 °C). The temperature of 210 °C was chosen to determine how the resistance changed at a temperature lower than the glass transition temperature (T_g) of PEI (T_g =215; as shown in Figure 5.19 in this thesis) [190]. All the other temperatures selected were above T_g; such high temperatures are often experienced by firefighters in operation.

Fig. 6.5 shows the change in the average normalized resistance of each group of sensors exposed to a different temperatures for 80 h. The resistance of the sensors exposed to an aging temperature below the T_g decreased after aging. This drop in resistance may be attributed to a contact annealing effect between the copper strips and the LIG layer [258]. At temperatures higher than T_g, the resistance values increased consistently with time; the level of increase became larger as the temperature increased from 250 °C to 280 °C. It is notable that the change in resistance observed after 80 h of aging at 270 °C in the short-term aging experiment on a hot plate ($R/R_0 = 1.77$; Figure 6.5) is similar to the value obtained after 100 h at the same temperature in the long-term aging experiment in a convection oven ($R/R_0 = 1.65$; Figure 6.4).
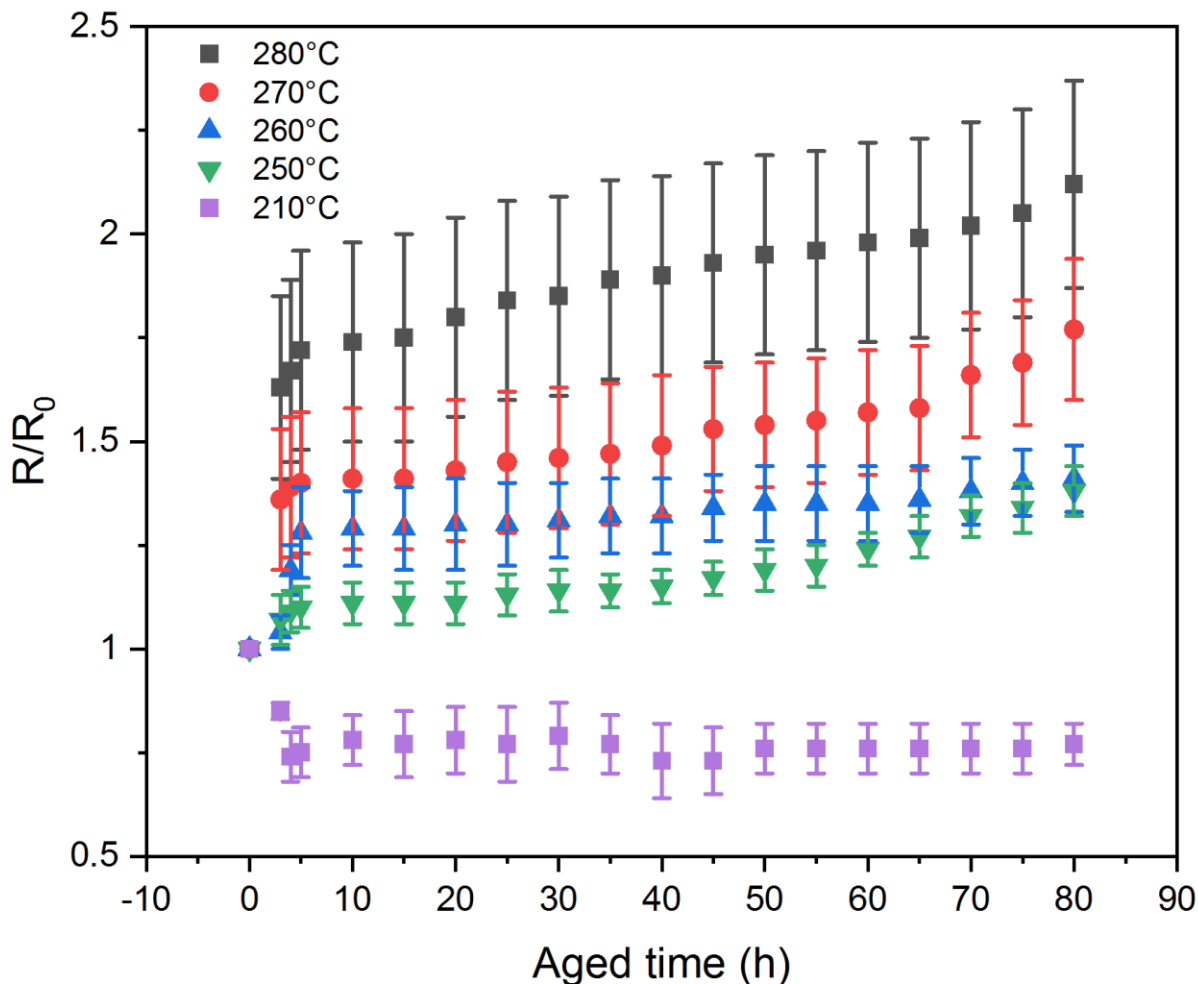
Figure 6.5 Change in normalized resistance values (R/R_0) of the PEI-LIG sensors after thermal aging on the hotplate with different temperatures.

6.3.2 Response of the PEI-LIG sensors to heating/cooling cycles

When firefighters are working near a fire, the high temperature exposure is often brief, followed by a cooldown in ambient air. In order to verify the reproducibility of the resistance values over several heating/cooling cycles, a PEI-LIG sensor was exposed to repeated cycles of heating at 270 °C for 30 min and subsequent cooling in ambient air for 30 min, as shown in Fig. 6.6. The results are expressed in terms of the change in the normalized resistance R/R_0. The normalized resistance values reached a steady state quickly upon heating. However, there were noticeable delays between the start of the cooling and the drop observed in the resistance. In Fig.

6.7, the transient curves showed that, out of 10 cooling cycles, six cycles showed fairly consistent cooling rates whereas four cycles show some scattering in the cooling trend. A possible explanation of this lack of consistency in the cooling curves is a non-uniform air flow in the lab during the cooling phase, which took place under uncontrolled cooling conditions. However, a promising result from the experiment is that the steady-state normalized resistance values at 270 °C are highly consistent at $R/R_0 = 1.28 \pm 0.02$ over 10 cycles.
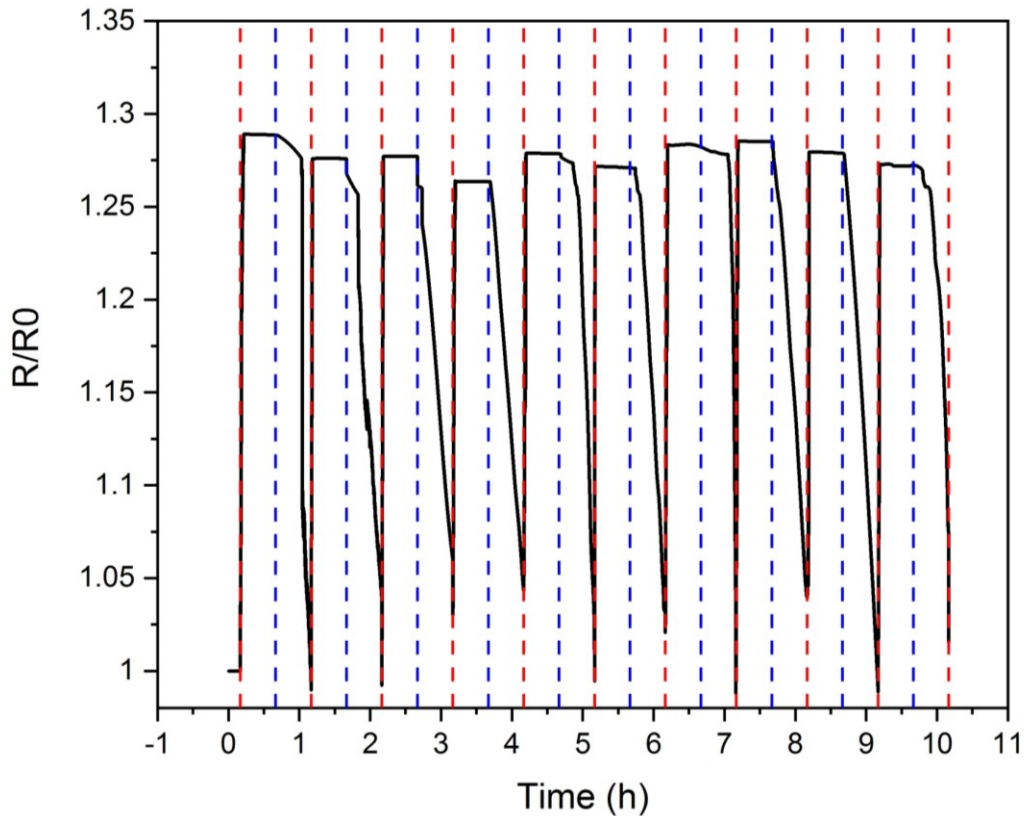
Figure 6.6 Ten heating/cooling cycles of a PEI-LIG sensor. Each cycle comprises 0.5 h heating (onset time: red dash line) and 0.5 h cooling in ambient air (onset time: blue dash line). The normalized resistance values, R/R_0, were plotted against time.
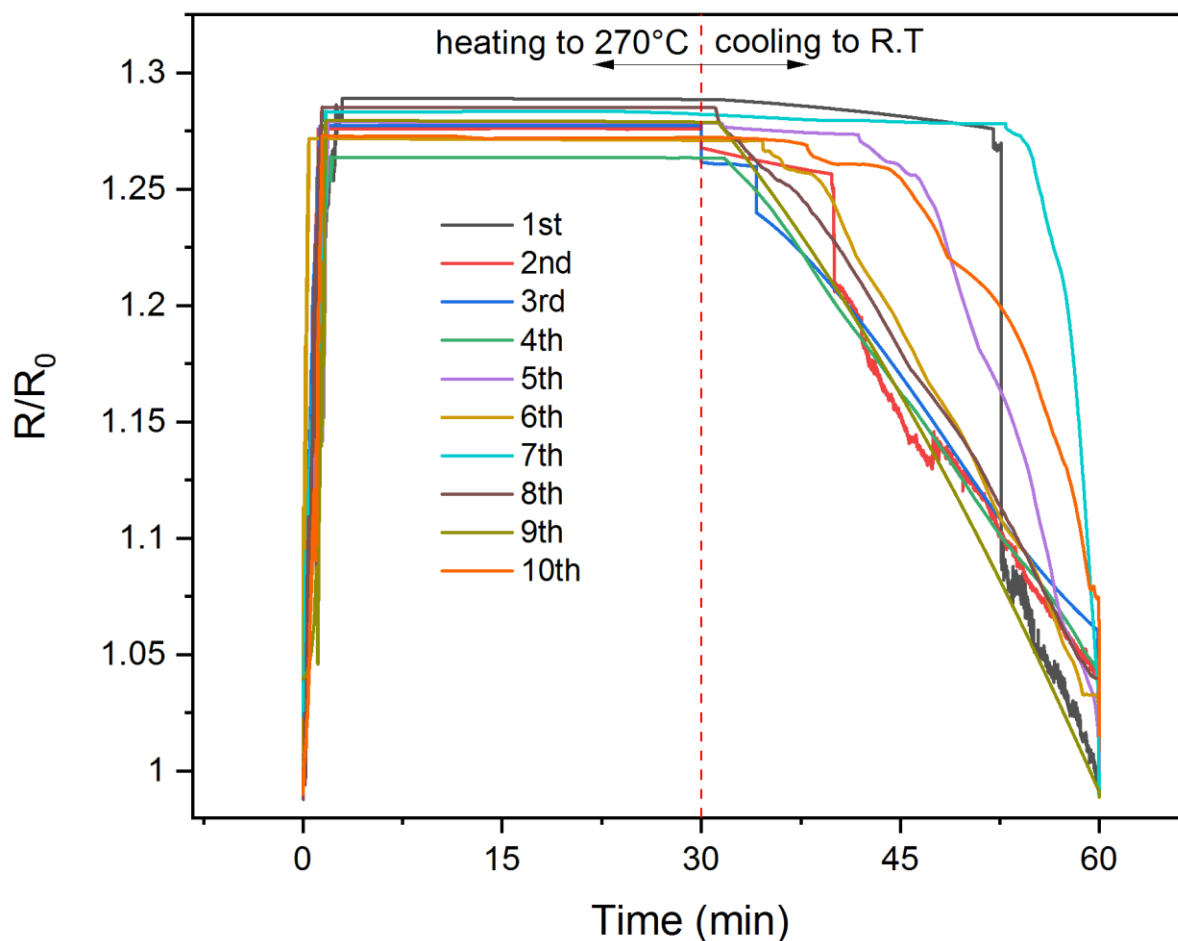
Figure 6.7 Transient resistance curves for a PEI-LIG sensor during heating and cooling cycles

6.3.3 Stability of PEI-LIG sensors over laundering cycles

As the end-of life sensor is intended to be integrated in a garment, one of the biggest challenges is related to launderability. During laundering, the abrasive and tensile stresses applied to a sensor may affect the electrical components of the sensors [177]. The conditions that a garment experiences during laundering also include elevated temperature, exposure to chemicals, and high moisture environment. These conditions can easily affect the functionality of textile-based sensors in an adverse manner. Therefore, it is important to encapsulate the sensor with a protective layer

to prevent possible damages during laundering; in the current study, the PEI-LIG sensor was encapsulated with a polyimide layer.

The stability of the PEI-LIG sensors under laundering was assessed by measuring their electrical resistance after selected numbers of washing cycles. In Fig. 6.8, the average normalized resistance of the encapsulated PEI-LIG sensors is plotted as a function of the washing cycles experienced. Their average resistance was 1.61 ± 0.62 kΩ before washing and it increased when they were subjected to laundering cycles. Normalized resistance values, R/R_0 of 1.30, 1.34, and 2.72 were obtained after 1, 3, and 5 cycles, respectively. After 10 cycles, one of the five sensors in the batch was severely damaged, showing an individual R/R_0 value of 11.5. The average normalized resistance was 2.33 when excluding the damaged sensor and 4.16 if it was included. The images of the PEG-LIG sensors inserted in Fig. 6.8 illustrate the typical damages observed on the sensors after the repeated laundering cycles.

A single factor ANOVA analysis excluding the damaged sensor was performed. It indicates that at least one of the washing conditions is different from the other washing conditions (It is noted that the p-value becomes 0.12 (n=25) when the damaged sensor is included, which supports the null hypothesis of 'no difference'; however, this result can be attributed to anomalously large sample variance of the group of sensors subjected to 10 washing cycles, and thus the interpretation seems more reasonable by excluding the outlier). We thus concluded that a significant change in resistance is produced when the sensors are subjected to 10 repeated washing cycles.
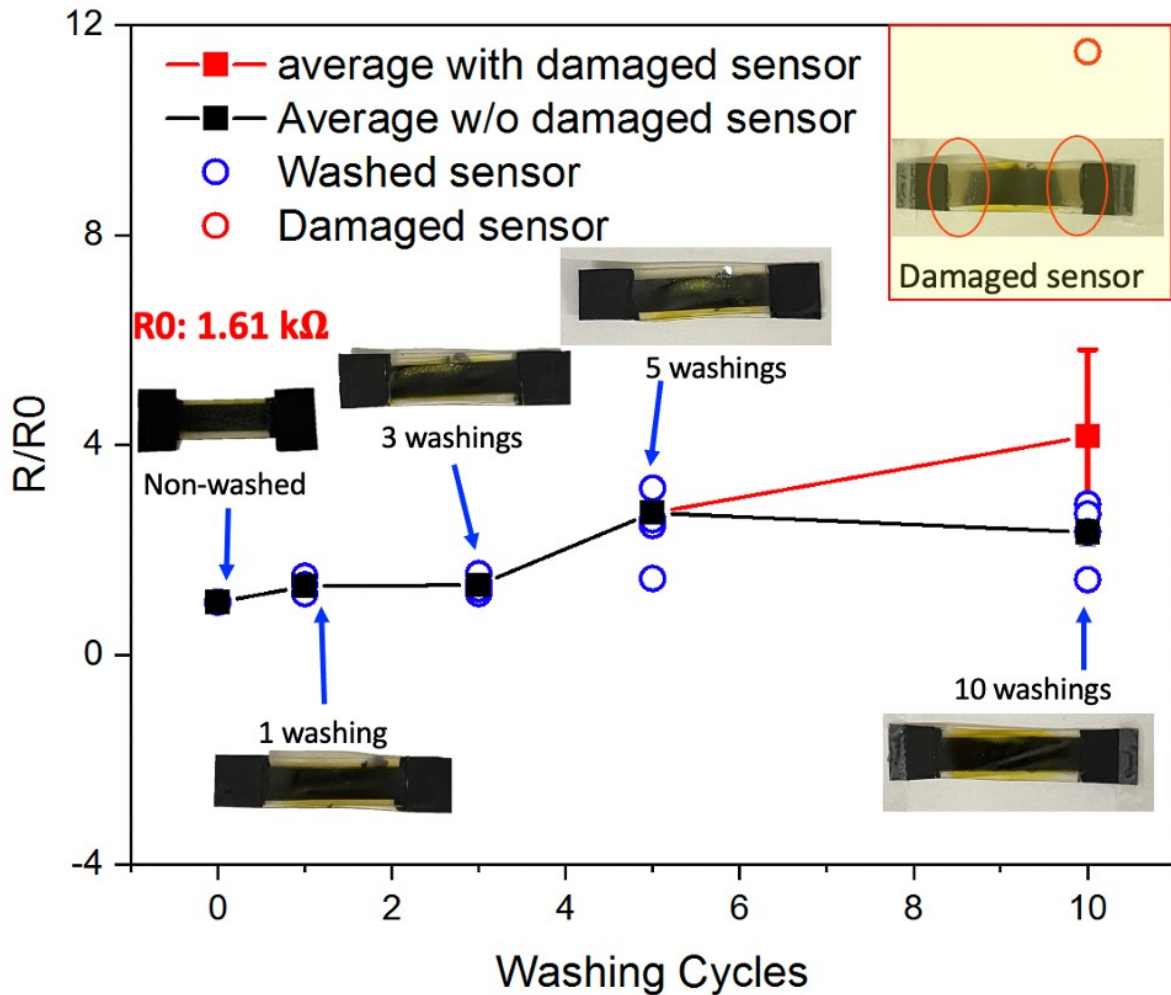
Figure 6.8 The resistance changes in PEI-LIG sensor over accelerated washing cycles. The resistance of individual sensor was plotted on blue circle.

According to the last edition of the relevant NFPA standard, advance cleaning of protective garments should be done at least every six months [62]. However, during fire operations, firefighters are exposed to various hazard chemicals, such as polycyclic aromatic hydrocarbons (PAH), carcinogenic chemicals in gas effluent, and smokes [260]. Therefore, recommendations in terms of the washing frequency of fire protective garments are expected to be increased to washing being performed after each fire-related operation to remove these hazard compounds from the fabrics [261]. Depending on the fire station, some protective garments may end up being subjected

to up to 25 laundering cycles in a year. Currently, it is recommended that the garments are retired before 10 years from their manufacturing date [62,73]. However, based on results showing significant loss in performance of Kevlar-based fabrics after 50 washing cycles (at 60 °C) [259], it it expected that the 10-year retirement recommendation will also have to be adjusted.

Nevertheless, to ensure that the sensor's stability against laundering is not the limiting factor (in other words, that it survive enough launderings to be able to 'die' due to thermal aging), a target of the sensor sustaining 100 washing cycles without significant change in resistance can be set. While this is an ambitious goal for a wearable sensor, future researches on sensor design and encapsulation techniques are critical.

6.4 Conclusions

A new non-destructive method for monitoring the residual condition of fire protective clothing was investigated; this approach aims to warn firefighters when the thermal aging of their protective garments has rendered it unsafe simply by measuring the electrical resistance of a PEI-LIG sensor located on their garment. The sensor was prepared by graphitizing the surface of PEI film was by laser scribing to produce a laser-induced graphene (LIG) layer. While the LIG layer is electrically conductive, the thermal aging of the PEI film will eventually deteriorate the stability of the LIG layer, resulting in an increase in its electrical resistance; this is the basic mechanism that enableed the PEI-LIG sensor to play a role of a thermal aging indicator. The PEI-LIG sensors were encapsulated using a polyimide layer to protect them against laundering.

Exposing the sensor to temperatures above the T_g of PEI led to an increase in its resistance. After short term aging (80 h at temperatures between 250 and 280 °C), the normalized resistance values R/R_0 reached between 1.4 and 2.1 as compared to the specimens before thermal aging. After long term aging (672 h at 270 °C), the R/R_0 the value exceeded 10. On the other hand,

heating/cooling cycle tests meant to mimic the situation experienced by firefighters in operation showed that the resistance of the PEI-LIG sensors remained stable when being repeatedly exposed to 270 ℃ followed by cooling at room temperature for 10 cycles. Washability tests using accelerated washing cycles revealed that an extensive reseach on sensor design and encapsulation materials is critically needed to ensure that the sensor survives enough of the repeated launderings experienced by the garments over its lifetime to play its role as a thermal end-of-life sensor.

It is to be noted that, in Chapter 5, the value of the activation energy of PEI (112kJ/mol), which was oberserved to be within the range of the outershell fabrics, was obtained at aging temperatures below the T_g of PEI. On the other hand, in this chapter (Chapter 6), the aging conditions that produced an increase in the resistance of the sensor were above PEI's T_g. This difference in behaviour may eventually be attributed to the fact that the change in resistance of the LIG layer is an indirect consequence of the effect of aging on PEI.

The sensor described in this work is simple to use. In addition, the simple production method that employs laser scribing provides an attractive solution as a low-cost, high-throughput fabrication technique. In the future, we plan to correlate the thermal aging of the PEI-LIG sensor with the degradation in the performance of the outershell fabrics of firefighters' garments. A precise tuning of the aging kinetics will allow the PEI-LIG sensor to provide an accurate indication of when to retire the protective garments by a simple observation by the firefighters themselves.

CHAPTER 7   Conclusions and Future work

7.1 Conclusions

The aim of this thesis was to develop a non-destructive method for the end-of-life monitoring of fire protective clothing. To achieve this goal, three main studies were conducted: (1) develop a stable rGO coating on the common outershell fabric material m-aramid with controlled conductivity loss as a platform for end-of life sensor for fire protective textiles, (2) investigate accelerated thermal aging behavior of high temperature resistance polyetherimide, (3) fabricate a thermal aging sensor for end-of-life sensor for fire protective clothing. Each sub-project is summarized as follows:

7.1.1 Electrical conduction of reduced graphene oxide coated meta-aramid textile and its evolution under aging conditions

This study presents a simple technique for the preparation of electrically conductive textiles that can be used as end-of-life sensors for fire protective fabrics. Graphene oxide was applied to the surface of the textile by dip-coating, and then converted to an electrically conductive material by a reduction process. Specific shape patterning was achieved using a wax layer to prevent the spreading of graphene oxide during dipping. This conductive layer patterning is an easy method to form of electrical circuit on textiles, and could potentially be used with a variety of fabric substrates.

The conductive layer (rGO) was deposited on m-aramid by dip-coating; a stable electrical conductivity was achieved after 10 dip coating cycles. These multiple rGO coatings resisted washing cycles and water immersion tests. Single and double side rGO tracks were also subjected to an abrasion test. The single side rGO tracks lost conductivity faster than the double side rGO

tracks after abrasion cycles. The two types of track patterning provide different applications for smart textiles. Single side patterning can be used to prepare end-of-life sensors and double side patterning offers stable and durable electrical conduction for e-textile applications.

7.1.2 Thermo-oxidative aging of polyetherimide and lifetime prediction at elevated temperature

In order to develop an end-of-life thermal sensor for outer shell fabrics, polyetherimide (PEI) was selected as the sacrificial polymer as it has a high temperature resistance and a similar thermal degradation behavior as m-aramid. The thermal aging behavior of PEI was studied over a range of temperatures below T_g in order to investigate the possible mechanisms by which PEI ages. It was evaluated in terms of mechanical and chemical property changes. The ultimate tensile strength (UTS) initially increased for short aging times; it was attributed to crosslinking reactions taking place during the initial stages of thermal aging. For longer aging times, the UTS decreased due to chain scission in the PEI network. Based on the UTS data obtained at 200 and 210 °C, a time-temperature superposition (TTS) master curve was constructed, leading to a value of the activation energy of 112 kJ mol^{-1}, which is very close to activation energy values reported for various outer shell fabrics in the literature. The lifetime of PEI corresponding to a 50% change in the UTS was estimated at 188 days at 200 °C and 113 days at 210 °C.

The chemical changes in PEI taking place during thermal aging were quantified by calculating the peak area of key functional groups in the FTIR spectrum at different aging times. Decreases in the FTIR peak areas of phthalimid and isopropylidene groups indicated chain scission in the PEI network, while an increase in the FTIR peaks of the carbonyl group area pointed towards the occurance of an oxidative reaction.

The thermal properties of PEI also changed due to thermal aging. The glass transition temperature initially increased but then decreased during aging, which may be attributed to crosslinking and chain scission reactions in the early and later parts of the aging process, respectively. Furthermore, the initial decomposition temperature and the temperature at the maximum decomposition rate decreased due to thermal aging, which also may be attributed to chain scission in PEI.

As a result of thermal aging, cracks formed on the PEI surface. The crack area increased both with aging time and temperature. On the other hand, PEI initially had a high surface roughness due to unique patterns from manufacturing and this surface roughness decreased during thermal aging. This decrease in surface roughness was attributed to irreversible deformations that took place during thermal aging.

This work clearly demonstrated that the potential of utilizing PEI in sensors for the assessment of thermal aging of outer shell fabrics in fire protective clothing. Compared to current aging assessments based on destructive methods, the PEI-based sensor can be used as a non destructive method for aging assessment by monitoring performance changes during thermal aging.

7.1.3 The fabrication of polyetherimide-based thermal aging sensors for outer shell fabrics

Based on the account that PEI has the same type of degradation by-products and similar decomposition temperature as m-aramid and the similar activation energy obtained here for PEI compared to various outer shell fabrics, it was proposed that PEI can be used as the sensory layer for the development of a thermal end-of-life sensor of fire protective clothing. This sensor will introduce simple way to monitor the aging level of polymeric materials under extreme environments. The sensor involves a conductive layer (graphitic layer, LIG) formed by laser

scribing on the PEI substrate, with copper strips connected to the LIG layer. The system is encapsulated by a polyimide layer to form a functional sensor.

The resistance of the PEI-LIG sensor was measured after short and long term thermal aging at elevated temperatures. When the sensor was aged below the glass transition temperature of PEI, its resistance first decreased quickly with time, then remained unchanged for the rest of the aging time (up to 80 hours). This initial drop in resistance was attributed to contact annealing between the copper strips and the LIG layer during thermal aging. At aging temperatures above PEI's Tg, the resistance increased consistently with aging time, and this increase became larger as aging temperature increased from 250 °C to 280 °C. The discrepancy between the range of aging temperatures that produced a change in the properties of the PEI film on one side and the electrical resistance of the PEI-LIG sensor on the other side can can be attributed to the fact that the change in the electrical resistance in the PEI-LIG sensor is an indirect consequence of the effect of thermal aging of PEI.

This sensor showed highly consistent normalized resistance values during 10 heating and cooling cycles. Furthermore, there was no effect of a temporarily cooling down to room temperature on the increase in resistance of the sensor due to thermal aging. On the other hand, the washing stability of the sensor still need to be improved.

7.2 Future work

In Chapter 5, changes in the mechanical and chemical properties of PEI were studied. Further investigations should be undertaken to perform more detailed FTIR characterizations. In particular, colloaborators from the Department of Chemistry will use the chemometrics technique to analysis the FTIR spectra after aging. This chemometrics analysis will provide an in-depth

investigation of the FTIR peak changes, and enable the aging mechanism of PEI to be more clearly understood. This will provide powerful information regarding the lifetime of PEI.

In Chapter 6, a LIG layer was deposited on the PEI film by laser irradiation. In order to minimize the variation of the initial resistance of the sensors, a consistant quality in the LIG layer should be achieved on all substrates. Raman spectroscopy will be used to identify the D and G peaks and allow optimizing the laser irradiation conditions. The sensor washing stability also needs to be improved, inparticular through a better sensor design and encapsulation.

Finally, the PEI-LIG sensor was exposed to a limited number of conditions corresponding to various temperatures over short and long term aging. In order to accurately estimate the lifetime of the sensor, it is necessary to perform long-term aging with multiple temperatures and produce a time-temperature-superposition master curve. This will allow investigating the correlation between the thermal aging behavior of the PEI-LIG sensors and that of the outershell fabrics to make this sensor practical for use in the field.

REFERENCES

(1)   Fahy, Rita, LeBlanc, Paul, Molis, J. Firefighter Fatalities in the United States. *Firef. Fatal. United States* **2015**.

(2)   Bourbigot, S.; Flambard, X. Heat Resistance and Flammability of High Performance Fibres: A Review. *Fire Mater.* **2002**. https://doi.org/10.1002/fam.799.

(3)   Dolez, P. I.; Tomer, N. S.; Malajati, Y. A Quantitative Method to Compare the Effect of Thermal Aging on the Mechanical Performance of Fire Protective Fabrics. *J. Appl. Polym. Sci.* **2019**, *136* (6), 47045. https://doi.org/10.1002/app.47045.

(4)   Ahmed, M.; Slater, K. Progressive Deterioration of Textile Materials. IV. The Effect of Accelerotor Abrasion on the Comfort Properties of Fabrics. *J. Text. Inst.* **1989**, *80* (2), 279–284.

(5)   Slater, K. Progressive Deterioration of Textile Materials. I. Characteristics of Degradation. *J. Text. Inst.* **1986**, *77* (No.2), 76–87.

(6)   *NFPA 1971 Standard on Protective Ensemble of Structural Firefighting*; Quincy, MA, 2007.

(7)   Moein, R. Evaulation of Performance of In-Use Firefighters' Protective Clothing Using Non-Destructive Tests, University of Saskatchewan, 2013.

(8)   Liu, S.; Fifield, L. S.; Bowler, N. Aging Mechanisms and Nondestructive Aging Indicator of Filled Cross-Linked Polyethylene (XLPE) Exposed to Simultaneous Thermal and Gamma Radiation. In *Minerals, Metals and Materials Series*; 2018. https://doi.org/10.1007/978-3-319-68454-3_6.

(9)   Rezazadeh, M.; Bespflug, C. J.; Torvi, D. A.; Noble, S. D.; Fulton, M. Predicting Mechanical Strength of In-Use Firefighter Protective Clothing Using Near-Infrared Spectroscopy. *Fire Technol.* **2018**. https://doi.org/10.1007/s10694-018-0766-3.

(10)   Thorpe, P. Assessment of In-Use Firefighter's Protective Clothing, University of Saskatchewan, 2004.

(11)   Lin, J.; Peng, Z.; Liu, Y.; Ruiz-Zepeda, F.; Ye, R.; Samuel, E. L. G.; Yacaman, M. J.; Yakobson, B. I.; Tour, J. M. Laser-Induced Porous Graphene Films from Commercial Polymers. *Nat. Commun.* **2014**. https://doi.org/10.1038/ncomms6714.

(12)   Slater, K. *TEXTILE DEGRADATION*; Taylor & Francis, 1991; Vol. 21.

(13)   Hatada, K.; Mita, I.; Fox, R. B.; Kahovec, J.; Maréchal, E.; Shibaev, V. Definitions of Terms Relating to Degradation, Aging, and Related Chemical Transformations of Polymers (IUPAC Recommendations 1996). *Pure Appl. Chem.* **1996**.

(14)   R.H.Atalla; R.H.Attalla. *Preservation of Paper and Textiles of Historic and Artistic Value. II*; Williams, J. C., Ed.; American Chemical Society, 1981.

(15)   Iskalieva, A.; Yimmou, B. M.; Gogate, P. R.; Horvath, M.; Horvath, P. G.; Csoka, L. Cavitation Assisted Delignification of Wheat Straw: A Review. *Ultrason. Sonochem.* **2012**, *19* (5), 984–993. https://doi.org/https://doi.org/10.1016/j.ultsonch.2012.02.007.

(16)   Okamba-Diogo, O.; Richaud, E.; Verdu, J.; Fernagut, F.; Guilment, J.; Fayolle, B. Investigation of Polyamide 11 Embrittlement during Oxidative Degradation. *Polymer (Guildf)*. **2016**.

(17)   Kulkarni, V. G. Influence of Nutrition on Some Properties of High- and Low-Crimp Merino Wools and Their Cellular Components. *Text. Res. J.* **1983**, *53* (11), 712–716.

(18)   Deshpande, S. D. Minimization of Damage during Chemical Modification of Keratin

Fibres. *Indian Text. J.* **1985**, *95* (No.12), 105–110.

(19)   Gacen, J.; Maillo, J.; Pepio, M.; Baixauli, J. J. Variation of Molecular Weight of Polyester as a Function of Setting Conditions (English). *Investig. e Inf. Text. y Tensioactivos* **1984**, *27* (No.4), 207–213.

(20)   Holmes-Brown, R. L.; Carnaby, G. R. Damage to Wool during Stock Dyeing. *Wool Res. Organ. New Zeal.* **1980**.

(21)   Herrling, J.; Zahn, H. *Effect of Dyeing with 1:1 Metal-Complex Dyes on the Chemical Composition of the Cell Membrane System of Wool (English)*; 1982; Vol. 1982.

(22)   Pavlov, P.; Lozanov, E. Study of Cellulose Degradation in Viscose Rayon Fibres during Crosslinking (English). *Tekst. Promyshlennost* **1983**, *32* (No.4), 155–157.

(23)   Hebeish, A.; Allam, E.; Bendak, A.; Tawfik, M. Mechanisms of Degradation of Cotton and Effects of Mercerization-Stretching upon the Course of These Mechanisms. IV. Ultraviolet Treatments. *Cellulose Chemistry & Technology*. January 1, 1981, pp 535–550.

(24)   Godon-Sadzik, J. Properties of Wool Stored in Non-Typical Conditions. *Gdynia Wool Fed.* **1977**.

(25)   Foldes, T. Degradation of Hungarian Wool during Storage (English). *Magy. Texttech.* **1985**, *38* (No.6), 308–316.

(26)   Tsanaka-Plivouri, A.; Vassiliadis, A. Effect of Certain Additives in Detergents on Wool Keratin (English). *Colloid Polym. Sci.* **1978**, *256* (No.1), 22–30.

(27)   Wolf, N.; Turkalj, D.; Krnic, M.; Bravar, M. Chemical Damage to Cotton Fibres during Laundering. *Tekst. J. Text. Cloth. Technol.* **1984**, *33* (No.1), 15–24.

(28)   Nishimura, H.; Yoshikawa, S.; Nozu, E. Studies on Detriment-Degradation of Synthetic Fibres Caused by Laundering. VI. Effect of Laundering Program (English). *Kochi Daigaku Kyoikugakubu Kenkyu Hokoku* **1977**, *92* (No.24).

(29)   Sadykova, F. .; Gintibidze, N. G. DETERMINATION OF PRESSURE EXPERIENCED BY CLOTH IN THE PROCESS OF WEARING. *Tekhnologiya Legk. Promyshlennosti* **1981**, *24* (3), 30.

(30)   WALL, M. J.; FRANK, G. C.; STEVENS, J. R. A Study of the Spectral Distributions of Sun-Sky and Xenon-Arc Radiation in Relation to the Degradation of Some Textile Yarns. II.Spectral Distribution Studies. *Text. Res. J.* **1971**, *41* (No.1), 38–43.

(31)   Simpson, W. S.; Page, C. T. *Inhibition of Light Tendering of Wool*; 1980.

(32)   Boboev, T. B.; Narzullaev, B. N.; Dadomatov, K. D. Photodegradation of Kapron Fibre and Natural Silk by Ultraviolet Radiation (English). *Mekh. Polim.* **1978**, *1978* (No.5).

(33)   Rizvi, M. S. Some Studies on Thermo-Oxidative Degradation of Polyester Fibre. *Karachi Univ. J. Sci.* **1983**, *11* (No.1).

(34)   Hanna, A. A. Thermal Degradation of Cotton Fibres Treated with Sodium Hydroxide. *Acta Polym.* **1984**, *35* (No.10), 656–659.

(35)   Peckett, N. J. Thermal Yellowing and Degradation of Wool. *Index to Theses Accept. High. Degrees by Univ. Gt. Britain Irel. Counc. Natl. Acad. Award.* **1979**.

(36)   Bartenev, G. M.; Savin, E. S. Degradation Mechanism of Mechanically Stressed Chemical Bonds in Polymer Fibres (English). *Vysokomol. Soedin. A* **1980**, *22* (No.6), 1420–1423.

(37)   M., B. G.; -., L. FRICTION AND WEAR OF POLYMERS. *Frict. WEAR Polym.* **1981**.

(38)   Kenney, M. C.; Mandell, J. F.; McGarry, F. J. Fatigue Behaviour of Synthetic Fibres, Yarns, and Ropes. *J. Mater. Sci.* **1985**, *20* (No.6).

(39)   Rabek, J. F. Physical Aspects of the Photodegradation of Polymers BT - Polymer Photodegradation: Mechanisms and Experimental Methods. In *Polymer

Photodegradation; Rabek, J. F., Ed.; Springer Netherlands: Dordrecht, 1995; pp 1–23.

(40)   Zhurkov, S. N.; Zakrevskyi, V. A.; Korsukov, V. E.; Kuksenko, V. S. Mechanism of Submicrocrack Generation in Stressed Polymers. *J. Polym. Sci. Part A-2 Polym. Phys.* **1972**, *10* (8), 1509–1520.

(41)   Casale, A.; Porter, R. S. Polymer Stress Reactions, Vol. 1: Introduction. *J. Polym. Sci. Polym. Lett. Ed.* **1978**, 118.

(42)   ACHHAMMER; B., G. Chemical Structure and Stability Relationships in Polymers. *Mod. Plast.* **1959**, 131–227.

(43)   Ehrenstein, G. W.; Pongratz, S. Part 1: Principles of Aging; Ehrenstein, G. W., Pongratz, S. B. T.-R. and S. of P., Eds.; Hanser, 2013; pp 1–138.

(44)   DE WITTE, E. Accelerated Aging, Photochemical and Thermal Aspects. *Stud. Conserv.* **1996**, *41* (3), 187.

(45)   Shimada, J.; Kabuki, K. The Mechanism of Oxidative Degradation of ABS Resin. Part I. The Mechanism of Thermooxidative Degradation. *J. Appl. Polym. Sci.* **1968**, *12* (4), 655–669.

(46)   Bresee, R. R. General Effects of Ageing on Textiles. *J. Am. Inst. Conserv.* **1986**.

(47)   Rajinipriya, M.; Nagalakshmaiah, M.; Robert, M.; Elkoun, S. Importance of Agricultural and Industrial Waste in the Field of Nanocellulose and Recent Industrial Developments of Wood Based Nanocellulose: A Review. *ACS Sustain. Chem. Eng.* **2018**, *6* (3), 2807–2828.

(48)   Okano, T.; Sarko, A. Mercerization of Cellulose. II. Alkali–Cellulose Intermediates and a Possible Mercerization Mechanism. *J. Appl. Polym. Sci.* **1985**, *30* (1), 325–332. https://doi.org/10.1002/app.1985.070300128.

(49)   Whelton, A. J.; Nguyen, T. Contaminant Migration From Polymeric Pipes Used in Buried Potable Water Distribution Systems: A Review. *Crit. Rev. Environ. Sci. Technol.* **2013**, *43* (7), 679–751.

(50)   Martin, J. R.; Gardner, R. J. Effect of Long Term Humid Aging on Plastics. *Polym. Eng. Sci.* **1981**, *21* (9), 557–565.

(51)   Smith, P.; Lemstra, P. J.; Pijpers, J. P. L. Tensile Strength of Highly Oriented Polyethylene. II. Effect of Molecular Weight Distribution. *J. Polym. Sci. Polym. Phys. Ed.* **1982**, *20* (12), 2229–2241.

(52)   Martin, J. R.; Johnson, J. F.; Cooper, A. R. Mechanical Properties of Polymers: The Influence of Molecular Weight and Molecular Weight Distribution. *J. Macromol. Sci. Part C* **1972**, *8* (1), 57–199.

(53)   De Focatiis, D. S. A.; Buckley, C. P.; Hutchings, L. R. Roles of Chain Length, Chain Architecture, and Time in the Initiation of Visible Crazes in Polystyrene. *Macromolecules* **2008**, *41* (12), 4484–4491.

(54)   Khaliq, Z.; Zulifqar, A. Textile Mechanics. *Handbook of Fibrous Materials*. April 27, 2020, pp 435–454. https://doi.org/doi:10.1002/9783527342587.ch17.

(55)   Hearle, J. W. S. Structural Mechanics of Fibers, Yarns and Fabrics (Chapter 4).Pdf. *John Wiley Sons, New York* **1969**.

(56)   Higginbotham, R. S. Deterioration of Textiles in Use. *Textiles* **1976**, *5* (No.2), 40–47.

(57)   Polikarpov, I. S. Investigation of Photo-Oxidative Degradation of Wool (English). *Tekhnologiya Legk. Promyshlennosti* **1977**, *1977* (116), 166–168.

(58)   Imabayashi, Y.; Yoshikawa, S. Decomposition Rate of Bleaching Agents and the Degradation of Nylon Fibres in Bleaching Process by Sodium Percarbonate (English). *J. Japan Res. Assoc. Text. End-Uses* **1984**, *25* (No.8), 400–405.

(59) J., M. R.; O., P. C.; N., B.; F.-M., K.; L., C.; L., M. R. HYDROLYTIC DEGRADATION OF KEVLAR 49 FIBERS. *Natl. SAMPE Symp. Exhib. Proc.* **1984**, 891.

(60) Health Canada. Personal Protective Equipment (PPE) https://www.canada.ca/en/health-canada/services/environmental-workplace-health/reports-publications/occupational-health-safety/whmis-quick-facts-personal-protective-equipment-health-canada-2008.html (accessed Nov 8, 2019).

(61) Mao, N. *High Performance Textiles for Protective Clothing*; Woodhead Publishing Limited, 2014.

(62) NFPA1851. *NFPA 1851 Standard on Selection, Care, and Maintenance of Protective Ensembles for Structural Fire Fighting and Proximity Fire Fighting*; 2020.

(63) Morton, W. E. E.; Hroudová, J.; Hearle, J. W. S.; Institute, T. *Physical Properties of Textile Fibres*, 4th ed.; CRC Press ;Cambridge, England: Boca Raton, FL, 2008; Vol. 68.

(64) Thorpe, P. Development of Non-Destructive Test Methods For Assessment of In-Use Firefighter's Protective Clothing, University of Saskatchewan, 2004.

(65) İşmal, Ö. E.; Paul, R. 17 - Composite Textiles in High-Performance Apparel. In *Woodhead Publishing Series in Textiles*; McLoughlin, J., Sabir, T. B. T.-H.-P. A., Eds.; Woodhead Publishing, 2018; pp 377–420.

(66) Day, M.; Cooney, J. D.; Suprunchuk, T. Durability of Firefighters' Protective Clothing to Heat and Light. *Text. Res. J.* **1988**, *58* (3), 141–147.

(67) Iyer, R. V; Vijayan, K. Decomposition Behaviour of Kevlar 49 Fibres: Part I. AtT≈Td. *Bull. Mater. Sci.* **1999**, *22* (7), 1013–1023.

(68) Iyer, R. V; Sudhakar, A.; Vijayan, K. Decomposition Behavior of Kevlar 49 Fibers: Part II. At T Values < Td. *High Perform. Polym.* **2006**, *18* (4), 495–517.

(69) Jain, A.; Vijayan, K. Thermally Induced Structural Changes in Nomex Fibres. *Bull. Mater. Sci.* **2002**, *25* (4), 341–346. https://doi.org/10.1007/BF02704129.

(70) Arrieta, C.; David, E.; Dolez, P.; Vu-Khanh, T. Thermal Aging of a Blend of High-Performance Fibers. *J. Appl. Polym. Sci.* **2009**, *115* (5), 3031–3039.

(71) TL, V. Post-Use Evaluation of Firefighter's Turnout Coats, University of Kentucky, 1996.

(72) McQuerry, M.; Klausing, S.; Cotterill, D.; Easter, E. A Post-Use Evaluation of Turnout Gear Using NFPA 1971 Standard on Protective Ensembles for Structural Fire Fighting and NFPA 1851 on Selection, Care and Maintenance. *Fire Technol.* **2015**.

(73) Rezazadeh, M.; Torvi, D. A. Assessment of Factors Affecting the Continuing Performance of Firefighters' Protective Clothing: A Literature Review. *Fire Technol.* **2011**, *47* (3), 565–599.

(74) Iyer, R. V; Vijayan, K. Identification of a New Parameter, Δt(T), Controlling the Thermally Induced Effects on Kevlar 49 Fibres. *Curr. Sci.* **1998**, *75* (9), 946–951.

(75) Thorpe, P.; Torvi, D. Development of Non-Destructive Test Methods for Assessing Effects of Thermal Exposures on Fire Fighters' Turnout Gear. *J. ASTM Int.* **2004**, *1* (6), 1–14. https://doi.org/10.1520/JAI12119.

(76) Ehrenstein, G. W.; Pongratz, S. Testing Methods; Hanser, 2013; pp 139–272. https://doi.org/https://doi.org/10.3139/9783446437098.002.

(77) Mahabadi, H. K.; Alexandru, L. Molecular Weight – Viscosity Relationships for a Broad Molecular Weight Distribution Polymer. *Can. J. Chem.* **1985**, *63* (1), 221–222. https://doi.org/10.1139/v85-035.

(78) Premnath, V.; Bellare, A.; Merrill, E. W.; Jasty, M.; Harris, W. H. Molecular Rearrangements in Ultra High Molecular Weight Polyethylene after Irradiation and Long-

Term Storage in Air. *Polymer (Guildf).* **1999**. https://doi.org/10.1016/S0032-3861(98)00438-8.

(79)   Brown, R.; Greenwood, J. H. *Practical Guide to the Assessment of the Useful Life of Plastics*; Rapra Technology Ltd: Shawbury, Shrewsbury [England], 2002.

(80)   Fleury, A.; Sugar, M.; Chau, T. E-Textiles in Clinical Rehabilitation: A Scoping Review. *Electronics* **2015**, *4* (1), 173–203. https://doi.org/10.3390/electronics4010173.

(81)   Stoppa, M.; Chiolerio, A. Wearable Electronics and Smart Textiles: A Critical Review. *Sensors (Switzerland)* **2014**, *14* (7), 11957–11992.

(82)   Park, S.; Mackenzie, K.; Jayaraman, S. The Wearable Motherboard: A Framework for Personalized Mobile Information Processing (PMIP). In *Proceedings 2002 Design Automation Conference (IEEE Cat. No.02CH37324)*; 2002; pp 170–174. https://doi.org/10.1109/DAC.2002.1012614.

(83)   Hughes-Riley, T.; Dias, T.; Cork, C. A Historical Review of the Development of Electronic Textiles. *Fibers* **2018**, *6* (2). https://doi.org/10.3390/fib6020034.

(84)   Shirakawa, H.; Louis, E. J.; MacDiarmid, A. G.; Chiang, C. K.; Heeger, A. J. Synthesis of Electrically Conducting Organic Polymers: Halogen Derivatives of Polyacetylene (CH). *J. Chem. Soc. Chem. Commun.* **1977**, No. 16, 578–580. https://doi.org/10.1039/C39770000578.

(85)   Ariyatum, B.; Holland, R. A Strategic Approach to New Product Development in Smart Clothing. *Proc. 6th Asian Des. Conf.* **2003**.

(86)   Van Langenhove, L.; Hertleer, C.; Schwarz, A. Smart Textiles: An Overview BT - Intelligent Textiles and Clothing for Ballistic and NBC Protection; Kiekens, P., Jayaraman, S., Eds.; Springer Netherlands: Dordrecht, 2012; pp 119–136.

(87)   Benito-Lopez, F.; Coyle, S.; Byrne, R.; Smeaton, A.; O'Connor, N. E.; Diamond, D. Pump Less Wearable Microfluidic Device for Real Time PH Sweat Monitoring. *Procedia Chem.* **2009**, *1* (1), 1103–1106. https://doi.org/https://doi.org/10.1016/j.proche.2009.07.275.

(88)   Vigneshwaran, N.; Kumar, S.; Kathe, A. A.; Varadarajan, P. V; Prasad, V. Functional Finishing of Cotton Fabrics Using Zinc Oxide-Soluble Starch Nanocomposites. *Nanotechnology* **2006**, *17* (20), 5087–5095. https://doi.org/10.1088/0957-4484/17/20/008.

(89)   Mondal, K. Recent Advances in Soft E-Textiles. *Inventions* . 2018. https://doi.org/10.3390/inventions3020023.

(90)   Karim, N.; Afroj, S.; Malandraki, A.; Butterworth, S.; Beach, C.; Rigout, M.; Novoselov, K. S. K.; Casson, A. J. A. J.; Yeates, S. G. All Inkjet-Printed Graphene-Based Conductive Patterns for Wearable e-Textile Applications. *J. Mater. Chem. C* **2017**, *5* (44), 11640–11648. https://doi.org/10.1039/C7TC03669H.

(91)   Shu, L.; Hua, T.; Wang, Y.; Qiao Li, Q.; Feng, D. D.; Tao, X. In-Shoe Plantar Pressure Measurement and Analysis System Based on Fabric Pressure Sensing Array. *IEEE Trans. Inf. Technol. Biomed.* **2010**. https://doi.org/10.1109/TITB.2009.2038904.

(92)   Mura, G. D.; Lorussi, F.; Tognetti, A.; Anania, G.; Carbonaro, N.; Pacelli, M.; Paradiso, R.; De Rossi, D. Piezoresistive Goniometer Network for Sensing Gloves. In *IFMBE Proceedings*; 2014.

(93)   Gonçalves, C.; Ferreira da Silva, A.; Gomes, J.; Simoes, R. Wearable E-Textile Technologies: A Review on Sensors, Actuators and Control Elements. *Inventions* **2018**, *3* (1), 14. https://doi.org/10.3390/inventions3010014.

(94)   Chatterjee, K.; Tabor, J.; Ghosh, K. T. Electrically Conductive Coatings for Fiber-Based

E-Textiles. *Fibers* . 2019. https://doi.org/10.3390/fib7060051.

(95) Little, B. K.; Li, Y.; Cammarata, V.; Broughton, R.; Mills, G. Metallization of Kevlar Fibers with Gold. *ACS Appl. Mater. Interfaces* **2011**, *3* (6), 1965–1973. https://doi.org/10.1021/am200193c.

(96) Liu, X.; Chang, H.; Li, Y.; Huck, W. T. S.; Zheng, Z. Polyelectrolyte-Bridged Metal/Cotton Hierarchical Structures for Highly Durable Conductive Yarns. *ACS Appl. Mater. Interfaces* **2010**, *2* (2), 529–535. https://doi.org/10.1021/am900744n.

(97) Castano, L. M.; Flatau, A. B. Smart Textile Transducers: Design, Techniques, and Applications BT - Industrial Applications for Intelligent Polymers and Coatings; Hosseini, M., Makhlouf, A. S. H., Eds.; Springer International Publishing: Cham, 2016; pp 121–146. https://doi.org/10.1007/978-3-319-26893-4_6.

(98) Jin, G.; Norrish, J.; Too, C.; Wallace, G. Polypyrrole Filament Sensors for Gases and Vapours. *Curr. Appl. Phys.* **2004**, *4* (2), 366–369. https://doi.org/https://doi.org/10.1016/j.cap.2003.11.050.

(99) Cho, G.; Jeong, K.; Paik, M. J.; Kwun, Y.; Sung, M. Performance Evaluation of Textile-Based Electrodes and Motion Sensors for Smart Clothing. *IEEE Sens. J.* **2011**, *11* (12), 3183–3193. https://doi.org/10.1109/JSEN.2011.2167508.

(100) Yoshioka, Y.; Jabbour, G. E. Desktop Inkjet Printer as a Tool to Print Conducting Polymers. *Synth. Met.* **2006**, *156* (11), 779–783. https://doi.org/https://doi.org/10.1016/j.synthmet.2006.03.013.

(101) Adanur, S. *Wellington Sears Handbook of Industrial Textiles*, 1st ed.; Routledge: New York, 1995.

(102) Kim, H.; Kim, Y.; Kim, B.; Yoo, H. A Wearable Fabric Computer by Planar-Fashionable Circuit Board Technique. In *2009 Sixth International Workshop on Wearable and Implantable Body Sensor Networks*; 2009; pp 282–285. https://doi.org/10.1109/BSN.2009.51.

(103) Böltau, M.; Walheim, S.; Mlynek, J.; Krausch, G.; Steiner, U. Surface-Induced Structure Formation of Polymer Blends on Patterned Substrates. *Nature* **1998**, *391* (6670), 877–879. https://doi.org/10.1038/36075.

(104) Sen, A. K. Coated Textiles: Principles and Applications. CRC Press ;Cambridge, England 2001.

(105) Yue, B.; Wang, C.; Ding, X.; Wallace, G. G. Polypyrrole Coated Nylon Lycra Fabric as Stretchable Electrode for Supercapacitor Applications. *Electrochim. Acta* **2012**, *68*, 18–24. https://doi.org/https://doi.org/10.1016/j.electacta.2012.01.109.

(106) Kim, B.; Koncar, V.; Dufour, C. Polyaniline-Coated PET Conductive Yarns: Study of Electrical, Mechanical, and Electro-Mechanical Properties. *J. Appl. Polym. Sci.* **2006**, *101* (3), 1252–1256. https://doi.org/10.1002/app.22799.

(107) Jeon, J. W.; Han, S.; Kim, B. H. Fabrication of Chromatic Electronic Textiles Synthesized by Conducting Polymer. *J. Korean Phys. Soc.* **2019**, *74* (2), 122–126. https://doi.org/10.3938/jkps.74.122.

(108) Xie, J.; Pan, W.; Guo, Z.; Jiao, S. S.; Ping Yang, L. In Situ Polymerization of Polypyrrole on Cotton Fabrics as Flexible Electrothermal Materials. *J. Eng. Fiber. Fabr.* **2019**, *14*, 1558925019827447. https://doi.org/10.1177/1558925019827447.

(109) Tran, T. N. T.; Qiu, S.; Chung, H. J. Potassium Ion Selective Electrode Using Polyaniline and Matrix-Supported Ion-Selective PVC Membrane. *IEEE Sens. J.* **2018**. https://doi.org/10.1109/JSEN.2018.2871001.

(110) Yetisen, A. K.; Qu, H.; Manbachi, A.; Butt, H.; Dokmeci, M. R.; Hinestroza, J. P.; Skorobogatiy, M.; Khademhosseini, A.; Yun, S. H. Nanotechnology in Textiles. *ACS Nano* **2016**, *10* (3), 3042–3068. https://doi.org/10.1021/acsnano.5b08176.

(111) Pang, S.; Gao, Y.; Choi, S. Flexible and Stretchable Biobatteries: Monolithic Integration of Membrane-Free Microbial Fuel Cells in a Single Textile Layer. *Adv. Energy Mater.* **2018**, *8* (7), 1702261. https://doi.org/10.1002/aenm.201702261.

(112) Alamer, F. A. Structural and Electrical Properties of Conductive Cotton Fabrics Coated with the Composite Polyaniline/Carbon Black. *Cellulose* **2018**, *25* (3), 2075–2082. https://doi.org/10.1007/s10570-018-1667-9.

(113) Shim, B. S.; Chen, W.; Doty, C.; Xu, C.; Kotov, N. A. Smart Electronic Yarns and Wearable Fabrics for Human Biomonitoring Made by Carbon Nanotube Coating with Polyelectrolytes. *Nano Lett.* **2008**. https://doi.org/10.1021/nl801495p.

(114) Mattana, G.; Cosseddu, P.; Fraboni, B.; Malliaras, G. G.; Hinestroza, J. P.; Bonfiglio, A. Organic Electronics on Natural Cotton Fibres. *Org. Electron.* **2011**. https://doi.org/10.1016/j.orgel.2011.09.001.

(115) Lee, H.; Glasper, M. J.; Li, X.; Nychka, J. A.; Batcheller, J.; Chung, H. J.; Chen, Y. Preparation of Fabric Strain Sensor Based on Graphene for Human Motion Monitoring. *J. Mater. Sci.* **2018**, *53* (12), 1–8.

(116) Yun, Y. J.; Hong, W. G.; Kim, W.-J. J.; Jun, Y.; Kim, B. H. A Novel Method for Applying Reduced Graphene Oxide Directly to Electronic Textiles from Yarns to Fabrics. *Adv. Mater.* **2013**, *25* (40), 5701–5705. https://doi.org/10.1002/adma.201303225.

(117) Zhao, C.; Shu, K.; Wang, C.; Gambhir, S.; Wallace, G. G. Reduced Graphene Oxide and Polypyrrole/Reduced Graphene Oxide Composite Coated Stretchable Fabric Electrodes for Supercapacitor Application. *Electrochim. Acta* **2015**, *172*, 12–19. https://doi.org/https://doi.org/10.1016/j.electacta.2015.05.019.

(118) Daoud, W. A.; Xin, J. H.; Szeto, Y. S. Polyethylenedioxythiophene Coatings for Humidity, Temperature and Strain Sensing Polyamide Fibers. *Sensors Actuators B Chem.* **2005**, *109* (2), 329–333. https://doi.org/https://doi.org/10.1016/j.snb.2004.12.067.

(119) Calvert, P.; Patra, P.; Sawhney, A.; Duggal, D.; Agrawal, A. Printed Conducting Polymer Strain Sensors for Textiles. *Int. Conf. Digit. Print. Technol.* **2007**, *23*, 831.

(120) Kim, H.; Kim, Y.; Kwon, Y.; Yoo, H. A 1.12mW Continuous Healthcare Monitor Chip Integrated on a Planar Fashionable Circuit Board. In *2008 IEEE International Solid-State Circuits Conference - Digest of Technical Papers*; 2008; pp 150–603. https://doi.org/10.1109/ISSCC.2008.4523101.

(121) Okuzaki, H.; Harashina, Y.; Yan, H. Highly Conductive PEDOT/PSS Microfibers Fabricated by Wet-Spinning and Dip-Treatment in Ethylene Glycol. *Eur. Polym. J.* **2009**, *45* (1), 256–261. https://doi.org/https://doi.org/10.1016/j.eurpolymj.2008.10.027.

(122) Wu, J. Synthesis, Characterisation and Applications of Conducting Polymer Coated Textiles, UNIVERSITY OF WOLLONGONG, 2004.

(123) Arapov, K.; Rubingh, E.; Abbel, R.; Laven, J.; de With, G.; Friedrich, H. Conductive Screen Printing Inks by Gelation of Graphene Dispersions. *Adv. Funct. Mater.* **2016**, *26* (4), 586–593. https://doi.org/10.1002/adfm.201504030.

(124) Huang, C.-T.; Shen, C.-L.; Tang, C.-F.; Chang, S.-H. A Wearable Yarn-Based Piezo-Resistive Sensor. *Sensors Actuators A Phys.* **2008**, *141* (2), 396–403. https://doi.org/https://doi.org/10.1016/j.sna.2007.10.069.

(125) Dominique, K. N. Advanced Screen Printing "Practical Approaches for Printable &

Flexible Electronics. In *3rd International Microsystems, Packaging, Assembly & Circuits Technology Conference*; 2008; pp 205–208.

(126) Blayo, A.; Pineaux, B. Printing Processes and Their Potential for RFID Printing. *Jt. sOc-EUSAI Conf.* **2005**. https://doi.org/10.1145/1107548.1107559.

(127) Lee, H.-H.; Chou, K.-S.; Huang, K.-C. Inkjet Printing of Nanosized Silver Colloids. *Nanotechnology* **2005**, *16* (10), 2436–2441. https://doi.org/10.1088/0957-4484/16/10/074.

(128) Trotter, M.; Juric, D.; Bagherian, Z.; Borst, N.; Gläser, K.; Meissner, T.; von Stetten, F.; Zimmermann, A. Inkjet-Printing of Nanoparticle Gold and Silver Ink on Cyclic Olefin Copolymer for DNA-Sensing Applications. *Sensors (Switzerland)* **2020**. https://doi.org/10.3390/s20051333.

(129) Mohammadi, M. M.; Gunturi, S. S.; Shao, S.; Konda, S.; Buchner, R. D.; Swihart, M. T. Flame-Synthesized Nickel-Silver Nanoparticle Inks Provide High Conductivity without Sintering. *Chem. Eng. J.* **2019**. https://doi.org/10.1016/j.cej.2019.04.141.

(130) Tang, Y.; He, W.; Wang, S.; Tao, Z.; Cheng, L. New Insight into the Size-Controlled Synthesis of Silver Nanoparticles and Its Superiority in Room Temperature Sintering. *CrystEngComm* **2014**. https://doi.org/10.1039/c3ce42439a.

(131) Ramli, M. R.; Ibrahim, S.; Ahmad, Z.; Abidin, I. S. Z.; Ain, M. F. Stretchable Conductive Ink Based on Polysiloxane-Silver Composite and Its Application as a Frequency Reconfigurable Patch Antenna for Wearable Electronics. *ACS Appl. Mater. Interfaces* **2019**. https://doi.org/10.1021/acsami.9b07671.

(132) Kumar, A.; Saghlatoon, H.; La, T.-G. G.; Mahdi Honari, M.; Charaya, H.; Abu Damis, H.; Mirzavand, R.; Mousavi, P.; Chung, H.-J. J. A Highly Deformable Conducting Traces for Printed Antennas and Interconnects: Silver/Fluoropolymer Composite Amalgamated by Triethanolamine. *Flex. Print. Electron.* **2017**, *2* (4), 45001. https://doi.org/10.1088/2058-8585/aa8d38.

(133) Qiu, S.; La, T.-G.; Zheng, L.; Cho, C.; Elias, A. L.; Rieger, J.; Chung, H.-J. Mechanically and Electrically Robust Stretchable E-Textiles by Controlling the Permeation Depth of Silver-Based Conductive Inks. *Flex. Print. Electron.* **2019**, *4* (2), 25006. https://doi.org/10.1088/2058-8585/ab2797.

(134) Capineri, L. Resistive Sensors with Smart Textiles for Wearable Technology: From Fabrication Processes to Integration with Electronics. *Procedia Eng.* **2014**, *87*, 724–727. https://doi.org/https://doi.org/10.1016/j.proeng.2014.11.748.

(135) Zeng, W.; Shu, L.; Li, Q.; Chen, S.; Wang, F.; Tao, X. M. Fiber-Based Wearable Electronics: A Review of Materials, Fabrication, Devices, and Applications. *Adv. Mater.* **2014**, *26* (31), 5310–5336. https://doi.org/10.1002/adma.201400633.

(136) Roh, J.-S. Textile Touch Sensors for Wearable and Ubiquitous Interfaces. *Text. Res. J.* **2013**, *84*, 739–750. https://doi.org/10.1177/0040517513503733.

(137) Pizarro, F.; Villavicencio, P.; Yunge, D.; Rodríguez, M.; Hermosilla, G.; Leiva, A. Easy-to-Build Textile Pressure Sensor. *Sensors* **2018**, *18* (4). https://doi.org/10.3390/s18041190.

(138) Teferra, M. N.; Ramos, J. S.; Kourbelis, C.; Newman, P.; Fleury, A.; Hobbs, D.; Reynolds, K. J.; Clark, R. A. Electronic Textile-Based Electrocardiogram Monitoring in Cardiac Patients: A Scoping Review. *JBI Database Syst. Rev. Implement. Reports* **2019**, *17* (10).

(139) Farina, D.; Lorrain, T.; Negro, F.; Jiang, N. High-Density EMG E-Textile Systems for the Control of Active Prostheses. In *2010 Annual International Conference of the IEEE*

Engineering in Medicine and Biology; 2010; pp 3591–3593.
https://doi.org/10.1109/IEMBS.2010.5627455.

(140) Carbonaro, N.; Mura, G. D.; Lorussi, F.; Paradiso, R.; Rossi, D. De; Tognetti, A. Exploiting Wearable Goniometer Technology for Motion Sensing Gloves. *IEEE J. Biomed. Heal. Informatics* **2014**, *18* (6), 1788–1795. https://doi.org/10.1109/JBHI.2014.2324293.

(141) Yang, C. M.; Huang, W.; Yang, T.-L.; Hsieh, M.; Liu, C. Textiles Digital Sensors for Detecting Breathing Frequency. In *2008 5th International Summer School and Symposium on Medical Devices and Biosensors*; 2008; pp 276–279. https://doi.org/10.1109/ISSMDBS.2008.4575073.

(142) Zhang, H.; Tao, X.; Yu, T.; Wang, S. Conductive Knitted Fabric as Large-Strain Gauge under High Temperature. *Sensors Actuators A Phys.* **2006**, *126*, 129–140. https://doi.org/10.1016/j.sna.2005.10.026.

(143) Pacelli, M.; Caldani, L.; Paradiso, R. Textile Piezoresistive Sensors for Biomechanical Variables Monitoring. In *2006 International Conference of the IEEE Engineering in Medicine and Biology Society*; 2006; pp 5358–5361. https://doi.org/10.1109/IEMBS.2006.259287.

(144) Castano, L. M.; Flatau, A. B. Smart Fabric Sensors and E-Textile Technologies: A Review. *Smart Mater. Struct.* **2014**, *23* (5), 53001. https://doi.org/10.1088/0964-1726/23/5/053001.

(145) Wijesiriwardana, R.; Dias, T.; Mukhopadhyay, S. Resistive Fibre-Meshed Transducers. In *Seventh IEEE International Symposium on Wearable Computers, 2003. Proceedings.*; 2003; pp 200–209. https://doi.org/10.1109/ISWC.2003.1241412.

(146) Axisa, F.; Schmitt, P. M.; Gehin, C.; Delhomme, G.; McAdams, E.; Dittmar, A. Flexible Technologies and Smart Clothing for Citizen Medicine, Home Healthcare, and Disease Prevention. *Trans. Info. Tech. Biomed.* **2005**, *9* (3), 325–336. https://doi.org/10.1109/TITB.2005.854505.

(147) Carlos, R.; Coyle, S.; Corcoran, B.; Diamond, D.; Tomas, W.; Aaron, M.; Stroiescu, F.; Daly, K. Web-Based Sensor Streaming Wearable for Respiratory Monitoring Applications. In *SENSORS, 2011 IEEE*; 2011; pp 901–903. https://doi.org/10.1109/ICSENS.2011.6127168.

(148) Marchand, G.; Bourgerette, A.; Antonakios, M.; Rat, V.; David, N.; Vinet, F.; Guillemaud, R. Development of a Dehydration Sensor Integrated on Fabric. In *2009 Sixth International Workshop on Wearable and Implantable Body Sensor Networks*; 2009; pp 230–233. https://doi.org/10.1109/BSN.2009.29.

(149) Sahin, O.; Kayacan, O.; Bulgun, E. Smart Textiles for Soldier of the Future. *Def. Sci. J.* **2005**, *55*, 195–205. https://doi.org/10.14429/dsj.55.1982.

(150) Acar, G.; Ozturk, O.; Golparvar, J. A.; Elboshra, A. T.; Böhringer, K.; Yapici, K. M. Wearable and Flexible Textile Electrodes for Biopotential Signal Monitoring: A Review. *Electronics* . 2019. https://doi.org/10.3390/electronics8050479.

(151) Wang, Q.; Markopoulos, P.; Yu, B.; Chen, W.; Timmermans, A. Interactive Wearable Systems for Upper Body Rehabilitation: A Systematic Review. *J. Neuroeng. Rehabil.* **2017**, *14* (1), 20. https://doi.org/10.1186/s12984-017-0229-y.

(152) Teplan, M. Fundamental of EEG Measurement. *Meas. Sci. Rev.* **2002**, *2*.

(153) Kirschstein, T.; Köhling, R. What Is the Source of the EEG? *Clin. EEG Neurosci.* **2009**, *40* (3), 146–149. https://doi.org/10.1177/155005940904000305.

(154) Chan, H.-L.; Kuo, P.-C.; Cheng, C.-Y.; Chen, Y.-S. Challenges and Future Perspectives on Electroencephalogram-Based Biometrics in Person Recognition . *Frontiers in Neuroinformatics* . 2018, p 66.

(155) Yapici, K. M.; Alkhidir, E. T. Intelligent Medical Garments with Graphene-Functionalized Smart-Cloth ECG Sensors. *Sensors* . 2017. https://doi.org/10.3390/s17040875.

(156) Takamatsu, S.; Lonjaret, T.; Crisp, D.; Badier, J.-M.; Malliaras, G. G.; Ismailova, E. Direct Patterning of Organic Conductors on Knitted Textiles for Long-Term Electrocardiography. *Sci. Rep.* **2015**, *5* (1), 15003. https://doi.org/10.1038/srep15003.

(157) Pola, T.; Vanhala, J. Textile Electrodes in ECG Measurement. In *2007 3rd International Conference on Intelligent Sensors, Sensor Networks and Information*; 2007; pp 635–639. https://doi.org/10.1109/ISSNIP.2007.4496917.

(158) Lee, S.; Kim, M.; Kang, T.; Park, J.; Choi, Y. Knit Band Sensor for Myoelectric Control of Surface EMG-Based Prosthetic Hand. *IEEE Sens. J.* **2018**, *18* (20), 8578–8586. https://doi.org/10.1109/JSEN.2018.2865623.

(159) Zhang, R.; Bernhart, S.; Amft, O. Diet Eyeglasses: Recognising Food Chewing Using EMG and Smart Eyeglasses. In *2016 IEEE 13th International Conference on Wearable and Implantable Body Sensor Networks (BSN)*; 2016; pp 7–12. https://doi.org/10.1109/BSN.2016.7516224.

(160) Matiko, J. W.; Wei, Y.; Torah, R.; Grabham, N.; Paul, G.; Beeby, S.; Tudor, J. Wearable EEG Headband Using Printed Electrodes and Powered by Energy Harvesting for Emotion Monitoring in Ambient Assisted Living. *Smart Mater. Struct.* **2015**, *24* (12), 125028. https://doi.org/10.1088/0964-1726/24/12/125028.

(161) La, T.-G.; Qiu, S.; Scott, D. K.; Bakhtiari, R.; Kuziek, J. W. P.; Mathewson, K. E.; Rieger, J.; Chung, H.-J. Two-Layered and Stretchable e-Textile Patches for Wearable Healthcare Electronics. *Adv. Healthc. Mater.* **2018**, *7* (22), 1801033. https://doi.org/10.1002/adhm.201801033.

(162) Nayak, R.; Houshyar, S.; Padhye, R. Recent Trends and Future Scope in the Protection and Comfort of Fire-Fighters' Personal Protective Clothing. *Fire Sci. Rev.* **2014**, *3* (1), 4.

(163) Rossi, R. M.; Bolli, W.; Stämpfli, R. Performance of Firefighters' Protective Clothing After Heat Exposure. *Int. J. Occup. Saf. Ergon.* **2008**, *14* (1), 55–60.

(164) Arrieta, C.; David, É.; Dolez, P.; Vu-Khanh, T. Hydrolytic and Photochemical Aging Studies of a Kevlar®-PBI Blend. *Polym. Degrad. Stab.* **2011**, *96* (8), 1411–1419.

(165) Fulton, M.; Rezazadeh, M.; Torvi, D. Tests for Evaluating Textile Aging. In *Advanced Characterization and Testing of Textiles*; Woodhead Publishing, 2018; pp 93–125. https://doi.org/10.1016/B978-0-08-100453-1.00006-4.

(166) Krishnamoorthy, K.; Navaneethaiyer, U.; Mohan, R.; Lee, J.; Kim, S.-J. Graphene Oxide Nanostructures Modified Multifunctional Cotton Fabrics. *Appl. Nanosci.* **2012**, *2* (2), 119–126.

(167) Molina, J.; Fernández, J.; Inés, J. C.; del Río, A. I.; Bonastre, J.; Cases, F. Electrochemical Characterization of Reduced Graphene Oxide-Coated Polyester Fabrics. *Electrochim. Acta* **2013**, *93*, 44–52.

(168) Shateri-Khalilabad, M.; Yazdanshenas, M. E. Preparation of Superhydrophobic Electroconductive Graphene-Coated Cotton Cellulose. *Cellulose* **2013**, *20* (2), 963–972.

(169) Shateri-Khalilabad, M.; Yazdanshenas, M. E. Fabricating Electroconductive Cotton Textiles Using Graphene. *Carbohydr. Polym.* **2013**, *96* (1), 190–195.

(170) Mikkonen, J.; Pouta, E. Flexible Wire-Component for Weaving Electronic Textiles. In *2016 IEEE 66th Electronic Components and Technology Conference (ECTC)*; 2016; pp 1656–1663.

(171) Chatterjee, A.; Nivas Kumar, M.; Maity, S. Influence of Graphene Oxide Concentration and Dipping Cycles on Electrical Conductivity of Coated Cotton Textiles. *J. Text. Inst.* **2017**, *108* (11), 1910–1916. https://doi.org/10.1080/00405000.2017.1300209.

(172) Li, X.; Chen, Y.; Kumar, A.; Mahmoud, A.; Nychka, J. A.; Chung, H. J. Sponge-Templated Macroporous Graphene Network for Piezoelectric ZnO Nanogenerator. *ACS Appl. Mater. Interfaces* **2015**, *7* (37), 20753–20760.

(173) Samad, Y. A.; Li, Y.; Alhassan, S. M.; Liao, K. Non-Destroyable Graphene Cladding on a Range of Textile and Other Fibers and Fiber Mats. *RSC Adv.* **2014**, *4* (33), 16935–16938. https://doi.org/10.1039/C4RA01373E.

(174) *CAN/CGSB-4.2 No. 58-2004 Textile Test Methods - Dimensional Change in Domestic Laundering of Textiles*.

(175) ASTM D-4966. Standard Test Method for Abrasion Resistance of Textile Fabrics (Martindale Abrasion. **2015**.

(176) Menezes, E.; Choudhari, M. Pre-Treatment of Textiles Prior to Dyeing. *Text. Dye.* **2011**, 221–241.

(177) Tao, X.; Koncar, V.; Huang, T. H.; Shen, C. L.; Ko, Y. C.; Jou, G. T. How to Make Reliable, Washable, and Wearable Textronic Devices. *Sensors (Switzerland)* **2017**, *17* (4).

(178) Alomayri, T.; Assaedi, H.; Shaikh, F. U. A.; Low, I. M. Effect of Water Absorption on the Mechanical Properties of Cotton Fabric-Reinforced Geopolymer Composites. *J. Asian Ceram. Soc.* **2014**, *2* (3), 223–230.

(179) Collier, B. J.; Bide, M. J.; Tortora, P. G. *Understanding Textiles*, 7th ed.; Pearson Prentice Hall: Upper Saddle River, N.J., 2009.

(180) Dupont®. *Moisture Effects and Processing Information for Nomex ® Paper Perform When the Heat's on*.

(181) Özdil, N.; Kayseri, G. Ö.; Mengüç, G. S. Analysis of Abrasion Characteristics in Textiles. *Abrasion Resist. Mater.* **2008**, 119–146. https://doi.org/10.5772/711.

(182) Ghosh, A.; Prithwiraj, M. Testing of Fibres, Yarns and Fabrics and Their Recent Development. In *Fibres to Smart Textiles Advances in Manufacturing, Technologies, and Applications*; Patnaik, A., Patnaik, S., Eds.; CRC Press: Boca Raton, 2019; p 242.

(183) Bhowmik, S.; Bonin, H. W.; Bui, V. T.; Weir, R. D. Modification of High-Performance Polymer Composite through High-Energy Radiation and Low-Pressure Plasma for Aerospace and Space Applications. *J. Appl. Polym. Sci.* **2006**. https://doi.org/10.1002/app.24230.

(184) Serfaty, I. W. Polyetherimide: A Versatile, Processable Thermoplastic BT - Polyimides: Synthesis, Characterization, and Applications. Volume 1; Mittal, K. L., Ed.; Springer US: Boston, MA, 1984; pp 149–161. https://doi.org/10.1007/978-1-4615-7637-2_10.

(185) Searle, O. B.; Pfeiffer, R. H. Victrex® Poly(Ethersulfone) (PES) and Victrex® Poly(Etheretherketone) (PEEK). *Polym. Eng. Sci.* **1985**. https://doi.org/10.1002/pen.760250808.

(186) Macocinschi, D.; Grigoriu, A.; Filip, D. Aromatic Polysulfones for Flame Retardancy. *Eur. Polym. J.* **2002**. https://doi.org/10.1016/S0014-3057(01)00253-1.

(187) Hill, H. W.; Brady, D. G. Properties, Environmental Stability, and Molding Characteristics of Polyphenylene Sulfide. *Polym. Eng. Sci.* **1976**.

https://doi.org/10.1002/pen.760161211.

(188) McKeen, L. W. 6 - Polyimides; McKeen, L. W. B. T.-T. E. of L. T. T. E. on P. and E., Ed.; William Andrew Publishing: Oxford, 2014; pp 117–137. https://doi.org/https://doi.org/10.1016/B978-0-323-22108-5.00006-0.

(189) Amancio-Filho, S. T.; Roeder, J.; Nunes, S. P.; dos Santos, J. F.; Beckmann, F. Thermal Degradation of Polyetherimide Joined by Friction Riveting (FricRiveting). Part I: Influence of Rotation Speed. *Polym. Degrad. Stab.* **2008**, *93* (8), 1529–1538. https://doi.org/https://doi.org/10.1016/j.polymdegradstab.2008.05.019.

(190) Carroccio, S.; Puglisi, C.; Montaudo, G. Thermal Degradation Mechanisms of Polyetherimide Investigated by Direct Pyrolysis Mass Spectrometry. *Am. Chem. Soc. Polym. Prepr. Div. Polym. Chem.* **2000**.

(191) Yilmaz, T.; Sinmazcelik, T. Effects of Hydrothermal Aging on Glass-Fiber/Polyetherimide (PEI) Composites. *J. Mater. Sci.* **2010**. https://doi.org/10.1007/s10853-009-3954-1.

(192) Tzounis, L.; Hegde, M.; Liebscher, M.; Dingemans, T.; Pötschke, P.; Paipetis, A. S.; Zafeiropoulos, N. E.; Stamm, M. All-Aromatic SWCNT-Polyetherimide Nanocomposites for Thermal Energy Harvesting Applications. *Compos. Sci. Technol.* **2018**, *156*, 158–165. https://doi.org/https://doi.org/10.1016/j.compscitech.2017.12.030.

(193) GE Plastics. ULTEM® PEI Resin Product Guide http://www-eng.lbl.gov/~shuman/NEXT/CURRENT_DESIGN/EP/ULTEMProductBrochure.pdf (accessed Apr 26, 2020).

(194) Batista, N. L.; Costa, M. L.; Iha, K.; Botelho, E. C. Thermal Degradation and Lifetime Estimation of Poly(Ether Imide)/Carbon Fiber Composites. *J. Thermoplast. Compos. Mater.* **2015**. https://doi.org/10.1177/0892705713484740.

(195) ISO. *ISO 527:2012 Plastics — Determination of Tensile Properties*; 2006.

(196) Shenton, M. J.; Herman, H.; Stevens, G. C. Chemometrics In The Study Of Polymer Degradation And Life Prediction By Spectroscopic Methods. In *Ageing Studies and Lifetime Extension of Materials*; 2001. https://doi.org/10.1007/978-1-4615-1215-8_39.

(197) Kumar, K. Principal Component Analysis: Most Favourite Tool in Chemometrics. *Resonance* **2017**, *22* (8), 747–759. https://doi.org/10.1007/s12045-017-0523-9.

(198) Bro, R.; Smilde, A. K. Principal Component Analysis. *Analytical Methods*. 2014. https://doi.org/10.1039/c3ay41907j.

(199) Christou, C.; Agapiou, A.; Kokkinofta, R. Use of FTIR Spectroscopy and Chemometrics for the Classification of Carobs Origin. *J. Adv. Res.* **2018**. https://doi.org/10.1016/j.jare.2017.12.001.

(200) Rohman, A.; Che Man, Y. B. Application of Fourier Transform Infrared (FT-IR) Spectroscopy Combined with Chemometrics for Authentication of Cod-Liver Oil. *Vib. Spectrosc.* **2011**. https://doi.org/10.1016/j.vibspec.2010.10.001.

(201) Matwijczuk, A.; Oniszczuk, T.; Matwijczuk, A.; Chruściel, E.; Kocira, A.; Niemczynowicz, A.; Wójtowicz, A.; Combrzyński, M.; Wiacek, D. Use of FTIR Spectroscopy and Chemometrics with Respect to Storage Conditions of Moldavian Dragonhead Oil. *Sustain.* **2019**. https://doi.org/10.3390/su11226414.

(202) Minguez, R.; Barrenetxea, L.; Solaberrieta, E.; Lizundia, E. A Simple Approach to Understand the Physical Aging in Polymers. *Eur. J. Phys.* **2019**. https://doi.org/10.1088/1361-6404/aaf244.

(203) Rychlý, J.; Rychlá, L. Modelling of Heat Release Rate-Time Curves from Cone

Calorimeter for Burning of Polymers with Intumescence Additives. *Polym. Degrad. Stab.* **1996**. https://doi.org/10.1016/s0141-3910(96)00050-x.

(204) Menczel, J. D.; Prime, R. B. *Thermal Analysis of Polymers: Fundamentals and Applications*; 2008. https://doi.org/10.1002/9780470423837.

(205) Chen, X. Y.; Romero, A.; Paton-Carrero, A.; Lavin-Lopez, M. P.; Sanchez-Silva, L.; Valverde, J. L.; Kaliaguine, S.; Rodrigue, D. Chapter 7 - Functionalized Graphene–Reinforced Foams Based on Polymer Matrices: Processing and Applications. In *Micro and Nano Technologies*; Jawaid, M., Bouhfid, R., Kacem Qaiss, A. el B. T.-F. G. N. and their D., Eds.; Elsevier, 2019; pp 121–155. https://doi.org/https://doi.org/10.1016/B978-0-12-814548-7.00007-6.

(206) Zhang, J.; Huang, Z.; Liu, D. Efficient Protein-Repelling Thin Films Regulated by Chain Mobility of Low-T g Polymers with Increased Stability via Crosslinking. *Appl. Surf. Sci.* **2017**. https://doi.org/10.1016/j.apsusc.2017.07.250.

(207) Abbasi, H.; Antunes, M.; Velasco, J. I. Polyetherimide Foams Filled with Low Content of Graphene Nanoplatelets Prepared by ScCO 2 Dissolution. *Polymers (Basel).* **2019**. https://doi.org/10.3390/polym11020328.

(208) Tcharkhtchi, A.; Farzaneh, S.; Abdallah-Elhirtsi, S.; Esmaeillou, B.; Nony, F.; Baron, A. Thermal Aging Effect on Mechanical Properties of Polyurethane. *Int. J. Polym. Anal. Charact.* **2014**, *19* (7), 571–584. https://doi.org/10.1080/1023666X.2014.932644.

(209) Wei, X. F.; Kallio, K. J.; Bruder, S.; Bellander, M.; Kausch, H. H.; Gedde, U. W.; Hedenqvist, M. S. Diffusion-Limited Oxidation of Polyamide: Three Stages of Fracture Behavior. *Polym. Degrad. Stab.* **2018**. https://doi.org/10.1016/j.polymdegradstab.2018.05.024.

(210) Gijsman, P.; Dong, W.; Quintana, A.; Celina, M. Influence of Temperature and Stabilization on Oxygen Diffusion Limited Oxidation Profiles of Polyamide 6. *Polym. Degrad. Stab.* **2016**. https://doi.org/10.1016/j.polymdegradstab.2016.05.024.

(211) Sang, L.; Wang, C.; Wang, Y.; Wei, Z. Thermo-Oxidative Ageing Effect on Mechanical Properties and Morphology of Short Fibre Reinforced Polyamide Composites-Comparison of Carbon and Glass Fibres. *RSC Adv.* **2017**. https://doi.org/10.1039/c7ra07884f.

(212) Yang, L.; Ohki, Y.; Hirai, N.; Hanada, S. Aging of Poly(Ether Ether Ketone) by Heat and Gamma Rays — Its Degradation Mechanism and Effects on Mechanical, Dielectric and Thermal Properties. *Polym. Degrad. Stab.* **2017**. https://doi.org/10.1016/j.polymdegradstab.2017.06.002.

(213) Mecheri, Y.; Boukezzi, L.; Boubakeur, A.; Lallouani, M. Dielectric and Mechanical Behavior of Cross-Linked Polyethylene under Thermal Aging. *Conf. Electr. Insul. Dielectr. Phenom. (CEIDP), Annu. Rep.* **2000**. https://doi.org/10.1109/CEIDP.2000.884022.

(214) Sirisinha, C.; Sae-Oui, P.; Guaysomboon, J. Mechanical Properties, Oil Resistance, and Thermal Aging Properties in Chlorinated Polyethylene/Natural Rubber Blends. *J. Appl. Polym. Sci.* **2002**. https://doi.org/10.1002/app.10171.

(215) Parkman, L. E. Viscoelastic Effects On A Polyetherimide Cylinder With Constant Radial Deformation, THE UNIVERSITY OF TEXAS AT ARLINGTON, 2015.

(216) Yin, W.; Xie, Z.; Yin, Y.; Yi, J.; Liu, X.; Wu, H.; Wang, S.; Xie, Y.; Yang, Y. Aging Behavior and Lifetime Prediction of PMMA under Tensile Stress and Liquid Scintillator Conditions. *Adv. Ind. Eng. Polym. Res.* **2019**. https://doi.org/10.1016/j.aiepr.2019.04.002.

(217) Anh, T. H.; Vu-Khanh, T. Effects of Thermal Aging on Fracture Performance of

Polychloroprene. *J. Mater. Sci.* **2005**. https://doi.org/10.1007/s10853-005-4418-x.

(218) Bernstein, R.; Gillen, K. T. Nylon 6.6 Accelerating Aging Studies: II. Long-Term Thermal-Oxidative and Hydrolysis Results. *Polym. Degrad. Stab.* **2010**. https://doi.org/10.1016/j.polymdegradstab.2010.06.018.

(219) Foreman, J. A.; Lundgren, C. J.; Gill, P. S. *MEASUREMENT OF THE PHYSICAL PROPERTIES OF ENGINEERING THERMOPLASTICS USING THERMAL ANALYSIS*.

(220) Jiao, L.; Xiao, H.; Wang, Q.; Sun, J. Thermal Degradation Characteristics of Rigid Polyurethane Foam and the Volatile Products Analysis with TG-FTIR-MS. *Polym. Degrad. Stab.* **2013**. https://doi.org/10.1016/j.polymdegradstab.2013.09.032.

(221) Romero, A. I.; Parentis, M. L.; Habert, A. C.; Gonzo, E. E. Synthesis of Polyetherimide/Silica Hybrid Membranes by the Sol-Gel Process: Influence of the Reaction Conditions on the Membrane Properties. *J. Mater. Sci.* **2011**. https://doi.org/10.1007/s10853-011-5380-4.

(222) Wan Nurul Huda, W. Z.; Ahmad, M. A. Effect of the Pyrolysis Soaking Time on CO2separation of Polyetherimide/Polyethylene Glycol-Based CMS Membranes. In *Developments in Sustainable Chemical and Bioprocess Technology*; 2013. https://doi.org/10.1007/978-1-4614-6208-8_39.

(223) Shah, S. S. A.; Nasir, H.; Saboor, A. Improved Dielectric Properties of Polyetherimide and Polyaniline-Coated Few-Layer Graphene Based Nanocomposites. *J. Mater. Sci. Mater. Electron.* **2018**. https://doi.org/10.1007/s10854-017-7929-8.

(224) Reddy, K. R.; Sin, B. C.; Yoo, C. H.; Sohn, D.; Lee, Y. Coating of Multiwalled Carbon Nanotubes with Polymer Nanospheres through Microemulsion Polymerization. *J. Colloid Interface Sci.* **2009**. https://doi.org/10.1016/j.jcis.2009.08.044.

(225) Jiang, X.; Ellis, N.; Zhong, Z. Characterization of Pyrolytic Lignin Extracted from Bio-Oil. *Chinese J. Chem. Eng.* **2010**. https://doi.org/10.1016/S1004-9541(09)60162-2.

(226) Saliba, J. B.; Faraco, A. A. G.; Yoshida, M. I.; de Vasconcelos, W. L.; da Silva-Cunha, A.; Mansur, H. S. Development and Characterization of an Intraocular Biodegradable Polymer System Containing Cyclosporine-A for the Treatment of Posterior Uveitis. In *Materials Research*; 2008. https://doi.org/10.1590/S1516-14392008000200016.

(227) Kurdi, J.; Kumar, A. Structuring and Characterization of a Novel Highly Microporous PEI/BMI Semi-Interpenetrating Polymer Network. *Polymer (Guildf).* **2005**. https://doi.org/10.1016/j.polymer.2005.06.057.

(228) Rajagopalan, M.; Oh, I. K. Fullerenol-Based Electroactive Artificial Muscles Utilizing Biocompatible Polyetherimide. *ACS Nano* **2011**. https://doi.org/10.1021/nn103521g.

(229) Pitchan, M. K.; Bhowmik, S.; Balachandran, M.; Abraham, M. Effect of Surface Functionalization on Mechanical Properties and Decomposition Kinetics of High Performance Polyetherimide/MWCNT Nano Composites. *Compos. Part A Appl. Sci. Manuf.* **2016**. https://doi.org/10.1016/j.compositesa.2016.06.025.

(230) Tunckol, M.; Hernandez, E. Z.; Sarasua, J. R.; Durand, J.; Serp, P. Polymerized Ionic Liquid Functionalized Multi-Walled Carbon Nanotubes/Polyetherimide Composites. *Eur. Polym. J.* **2013**. https://doi.org/10.1016/j.eurpolymj.2013.08.007.

(231) Musto, P.; Karasz, F. E.; MacKnight, W. J. Fourier Transform Infra-Red Spectroscopy on the Thermo-Oxidative Degradation of Polybenzimidazole and of a Polybenzimidazole/Polyetherimide Blend. *Polymer (Guildf).* **1993**. https://doi.org/10.1016/0032-3861(93)90618-K.

(232) Meftah, H.; Tamboura, S.; Fitoussi, J.; BenDaly, H.; Tcharkhtchi, A. Thermal Aging

Influence on the Damage Mechanisms of Fully Recycled Composite-Reinforced Polypropylene/Polyethylene Blend. *Polym. Compos.* **2019**. https://doi.org/10.1002/pc.25194.

(233) Bowles, K. J.; Jayne, D.; Leonhardt, T. A. Isothermal Aging Effects on PMR-15 Resin. *S.A.M.P.E. Q.* **1993**.

(234) Suresh, B.; Maruthamuthu, S.; Khare, A.; Palanisamy, N.; Muralidharan, V. S.; Ragunathan, R.; Kannan, M.; Pandiyaraj, K. N. Influence of Thermal Oxidation on Surface and Thermo-Mechanical Properties of Polyethylene. *J. Polym. Res.* **2011**. https://doi.org/10.1007/s10965-011-9628-0.

(235) Awaja, F.; Zhang, S.; Tripathi, M.; Nikiforov, A.; Pugno, N. Cracks, Microcracks and Fracture in Polymer Structures: Formation, Detection, Autonomic Repair. *Progress in Materials Science*. 2016. https://doi.org/10.1016/j.pmatsci.2016.07.007.

(236) Wang, W.; He, D.; Yang, K.; Liu, S.; Song, S.; Yi, D. Research of the Thermal Aging Mechanism of Polycarbonate and Polyester Film. *E-Polymers* **2017**. https://doi.org/10.1515/epoly-2016-0179.

(237) Jones, R. L.; Hu, T.; Soles, C. L.; Lin, E. K.; Reano, R. M.; Pang, S. W.; Casa, D. M. Real-Time Shape Evolution of Nanoimprinted Polymer Structures during Thermal Annealing. *Nano Lett.* **2006**. https://doi.org/10.1021/nl061086i.

(238) Jiang, Y.; Luo, B.; Cheng, X. Enhanced Thermal Stability of Thermoplastic Polymer Nanostructures for Nanoimprint Lithography. *Materials (Basel)*. **2019**. https://doi.org/10.3390/ma12030545.

(239) Statistics Canada. *Fire Statistics in Canada, Selected Observations from the National Fire Information Database 2005 to 2014*; 2017.

(240) *NFPA 1977 Standard on Protective Clothing and Equipment for Wildland Firefighting*; Quincy, MA, 2011.

(241) Torvi, D. A.; Hadjisophocleus, G. V; Hadjisophocleous, G. V. Research in Protective Clothing for Firefighters: State of the Art and Future Directions. *Fire Technol.* **1999**, *35* (2), 111–130.

(242) Davis, R. D.; Peng, J.; Chin, J. Accelerated Weathering of Firefighter Protective Clothing: Delineating the Impact of Thermal, Moisture, and Ultraviolet Light Exposures.

(243) Arrieta, C.; David, E.; Dolez, P.; Vu-Khanh, T. X-Ray Diffraction, Raman, and Differential Thermal Analyses of the Thermal Aging of a Kevlar®-PBI Blend Fabric. *Polym. Compos.* **2011**, *32* (3), 362–367.

(244) Fulton, M. Evaluating the Performance of Thermally and UV Aged Firefighters' Protective Clothing Using Both Destructive and Non-Destructive Methods, Department of Mechanical Engineering, 2017.

(245) *ASTM D5034-09(2017), Standard Test Method for Breaking Strength and Elongation of Textile Fabrics (Grab Test)*; West Conshohocken, PA, 2017.

(246) *ASTM D4533M-15 Standard Test Method for Trapezoid Tearing Strength of Geotextiles*; West Conshohocken, 2015. https://doi.org/10.1520/D4533_D4533M-15.

(247) *ASTM F903-18, Standard Test Method for Resistance of Materials Used in Protective Clothing to Penetration by Liquids*; West Conshohocken, PA, 2018.

(248) Rezazadeh, M.; Torvi, D. A. Non-Destructive Test Methods to Assess the Level of Damage to Firefighters' Protective Clothing. In *ASTM Special Technical Publication*; 2012. https://doi.org/10.1520/STP104097.

(249) Gauthier, M. M.; Committee, A. S. M. I. H. *Engineered Materials Handbook, Desk*

Edition; ASM Handbook; Taylor & Francis, 1995.

(250) Kuroda, S.; Terauchi, K.; Nogami, K.; Mita, I. Degradation of Aromatic Polymers—I. Rates of Crosslinking and Chain Scission during Thermal Degradation of Several Soluble Aromatic Polymers. *Eur. Polym. J.* **1989**, *25* (1), 1–7. https://doi.org/https://doi.org/10.1016/0014-3057(89)90200-0.

(251) Amancio-Filho, S. T.; Dos Santos, J. F. Joining of Polymers and Polymer-Metal Hybrid Structures: Recent Developments and Trends. *Polym. Eng. Sci.* **2009**. https://doi.org/10.1002/pen.21424.

(252) Brown, J. R.; Power, A. J. Thermal Degradation of Aramids: Part I—Pyrolysis/Gas Chromatography/Mass Spectrometry of Poly(1,3-Phenylene Isophthalamide) and Poly(1,4-Phenylene Terephthalamide). *Polym. Degrad. Stab.* **1982**, *4* (5), 379–392. https://doi.org/https://doi.org/10.1016/0141-3910(82)90044-1.

(253) Ye, R.; James, D. K.; Tour, J. M. Laser-Induced Graphene. *Acc. Chem. Res.* **2018**. https://doi.org/10.1021/acs.accounts.8b00084.

(254) Dosi, M.; Lau, I.; Zhuang, Y.; Simakov, D. S. A.; Fowler, M. W.; Pope, M. A. Ultrasensitive Electrochemical Methane Sensors Based on Solid Polymer Electrolyte-Infused Laser-Induced Graphene. *ACS Appl. Mater. Interfaces* **2019**. https://doi.org/10.1021/acsami.8b22310.

(255) Luo, S.; Hoang, P. T.; Liu, T. Direct Laser Writing for Creating Porous Graphitic Structures and Their Use for Flexible and Highly Sensitive Sensor and Sensor Arrays. *Carbon N. Y.* **2016**. https://doi.org/10.1016/j.carbon.2015.09.076.

(256) Chyan, Y.; Ye, R.; Li, Y.; Singh, S. P.; Arnusch, C. J.; Tour, J. M. Laser-Induced Graphene by Multiple Lasing: Toward Electronics on Cloth, Paper, and Food. *ACS Nano* **2018**. https://doi.org/10.1021/acsnano.7b08539.

(257) Cho, C.; Elias, A.; Batcheller, J.; Dolez, P.; Chung, H. J. Electrical Conduction of Reduced Graphene Oxide Coated Meta-Aramid Textile and Its Evolution under Aging Conditions. *J. Ind. Text.* **2019**. https://doi.org/10.1177/1528083719869387.

(258) Smith, J. T.; Franklin, A. D.; Farmer, D. B.; Dimitrakopoulos, C. D. Reducing Contact Resistance in Graphene Devices through Contact Area Patterning. *ACS Nano* **2013**. https://doi.org/10.1021/nn400671z.

(259) Dolez, P. I.; Malajati, Y. Resistance of Fire Protective Fabrics to Repeated Launderings. In *Performance of Protective Clothing and Equipment: Innovative Solutions to Evolving Challenges*; 2020. https://doi.org/10.1520/stp162420190079.

(260) Keir, J. L. A.; Akhtar, U. S.; Matschke, D. M. J.; Kirkham, T. L.; Chan, H. M.; Ayotte, P.; White, P. A.; Blais, J. M. Elevated Exposures to Polycyclic Aromatic Hydrocarbons and Other Organic Mutagens in Ottawa Firefighters Participating in Emergency, On-Shift Fire Suppression. *Environ. Sci. Technol.* **2017**. https://doi.org/10.1021/acs.est.7b02850.

(261) Stull, J. O.; Stull, G. G. Fundamental Changes Needed to Address Turnout Gear Contamination http://web.archive.org/web/20190610002417/https://www.ppe101.com/2018/03/fundamental-changes-needed-to-address-turnout-gear-contamination/.

(262) Studentized range q table https://www.stat.purdue.edu/~lingsong/teaching/2018fall/q-table.pdf.

Appendix

A1. Materials and specimen preparation

Each specimen was marked with a code "A-a-#", where "A" corresponds to the film number (A-H), "a" indicates the temperature condition (a: 190 °C; b: 210°C; c: 200 °C), and "#" indicates the aging time (from 1 to 10). In order to minimize the effect of any eventual inhomogeneity within the PEI films, the specimens corresponding to each condition had a different location for each film. In addition, three small square specimens were prepared for some initial control experiments with the FTIR characterization (labelled (A-H)-0, (A-H)-s-1, and (A-H)-s-2). Figures A1 to A8 show the distribution of the specimens on each of the 8 PEI films.
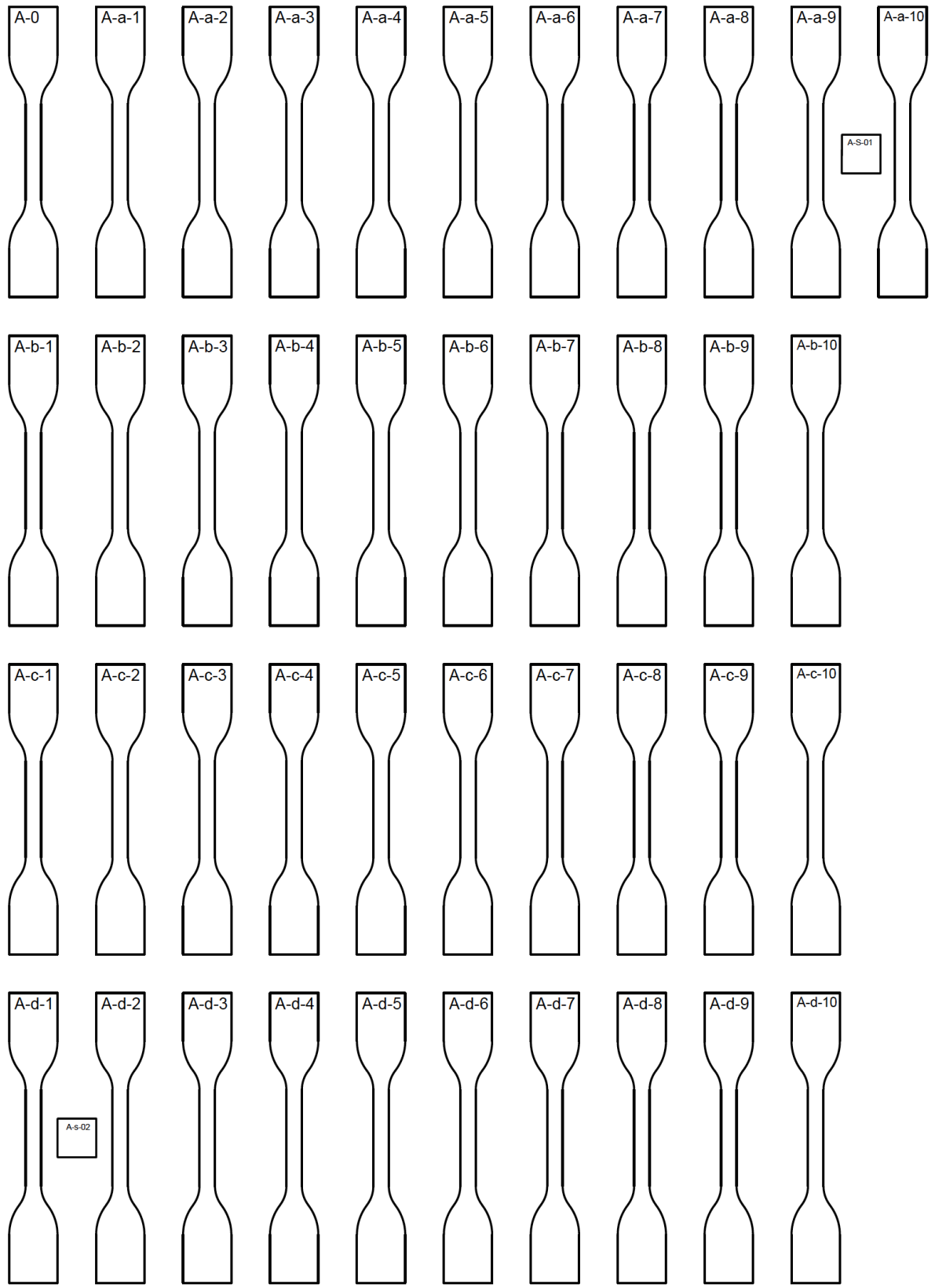
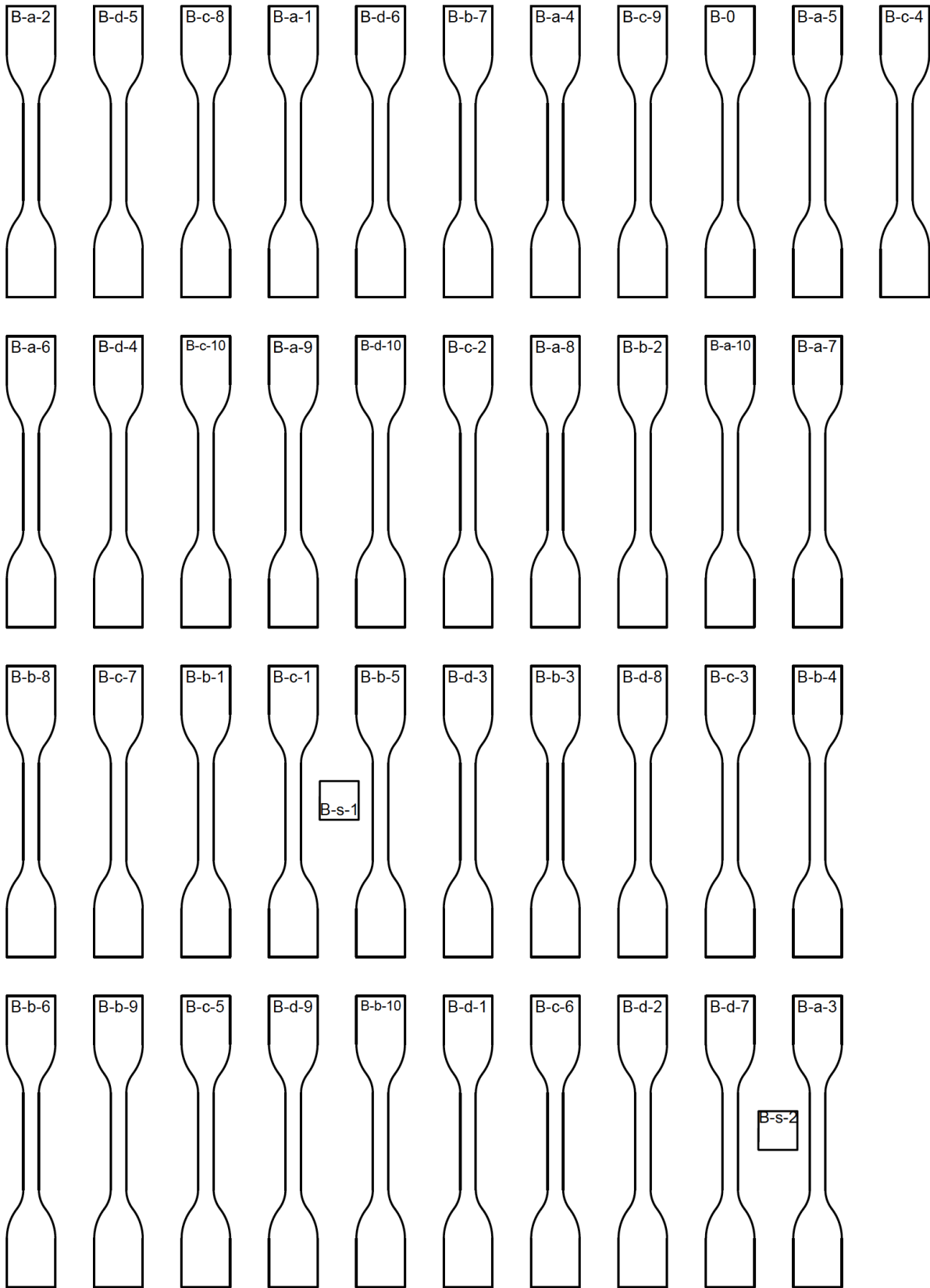Figure A1. Distribution of the specimens on film A

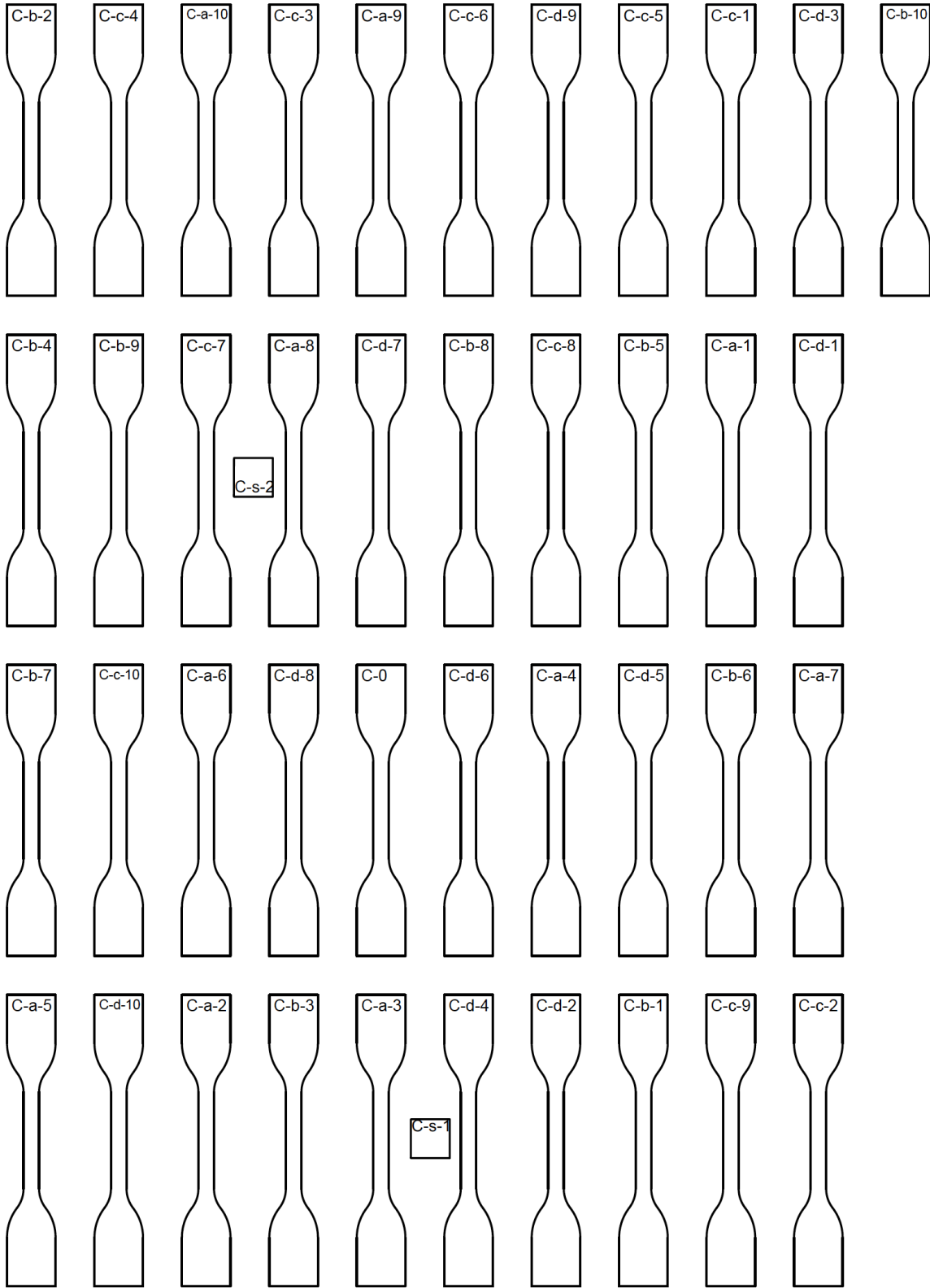Figure A2. Distribution of the specimens on film B

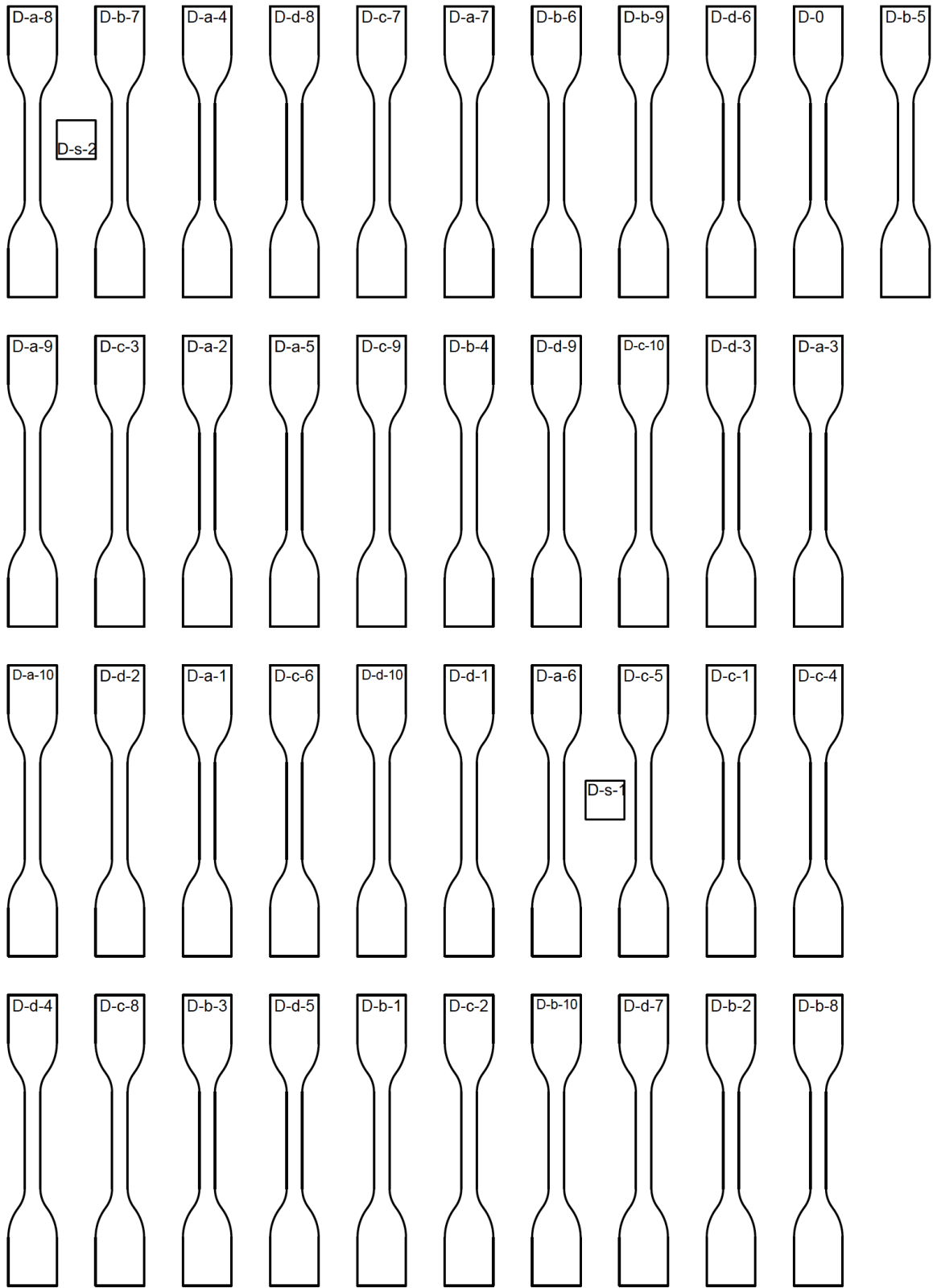Figure A3. Distribution of the specimens on film C

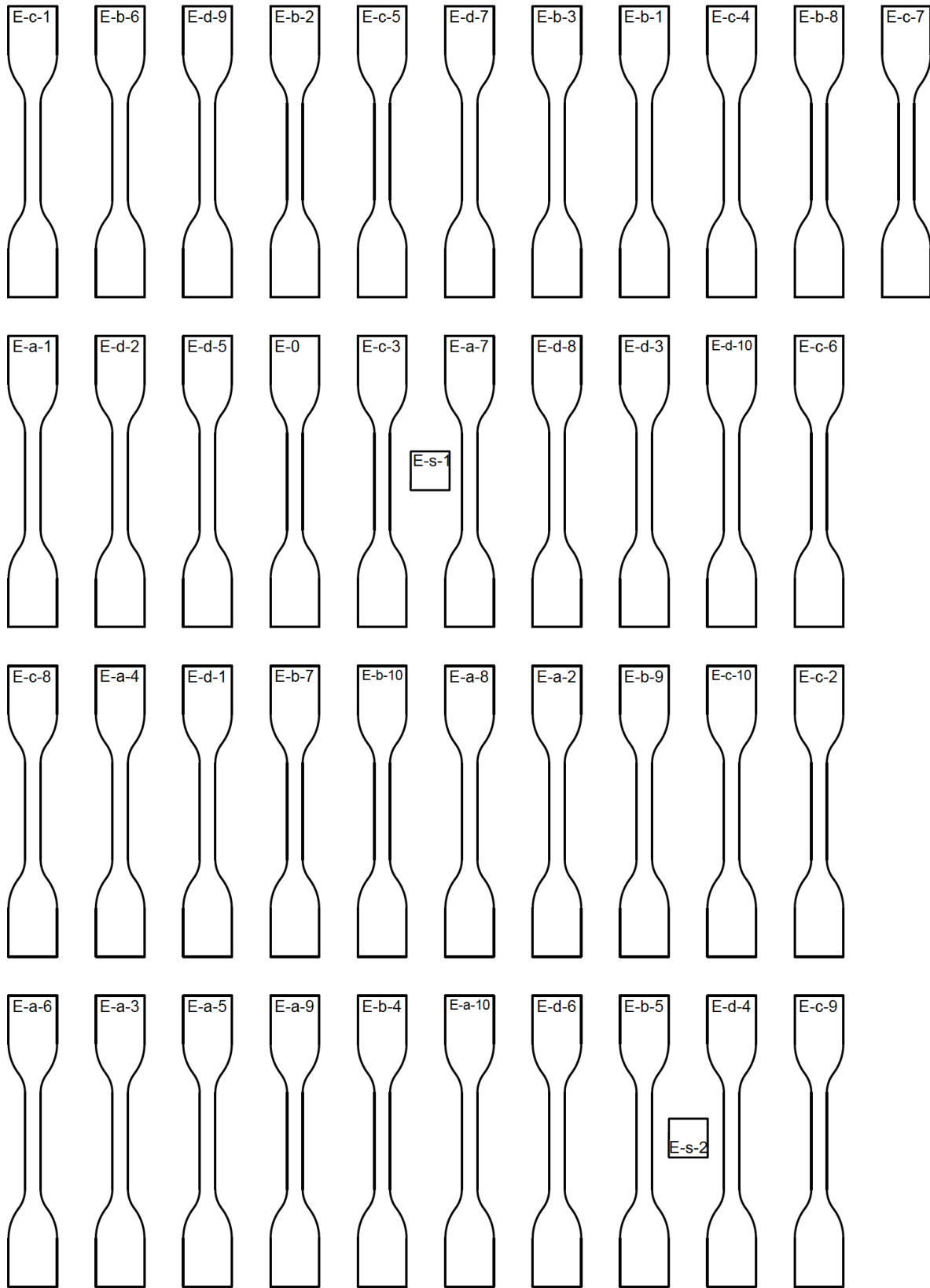Figure A4. Distribution of the specimens on film D

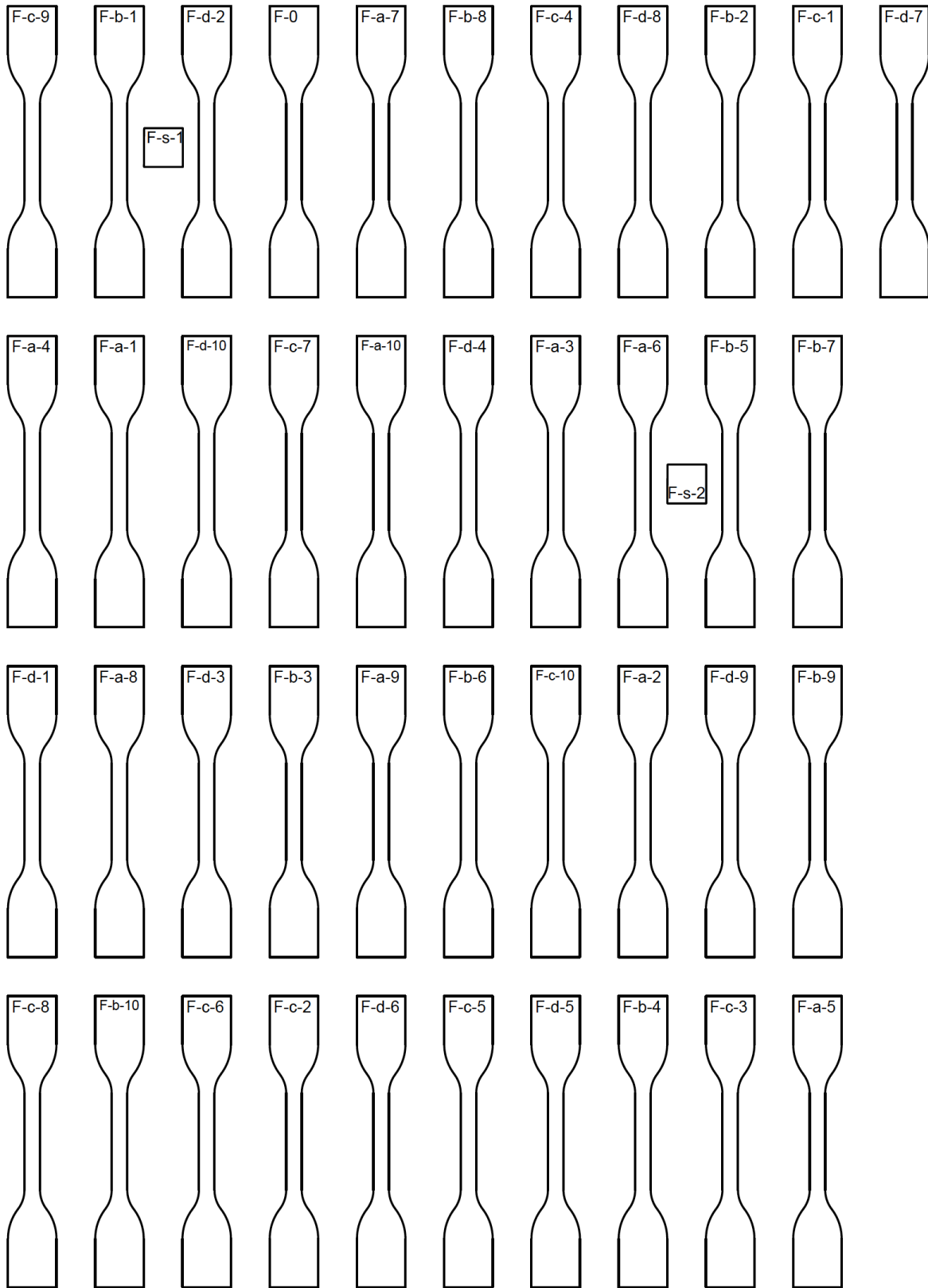Figure A5. Distribution of the specimens on film E
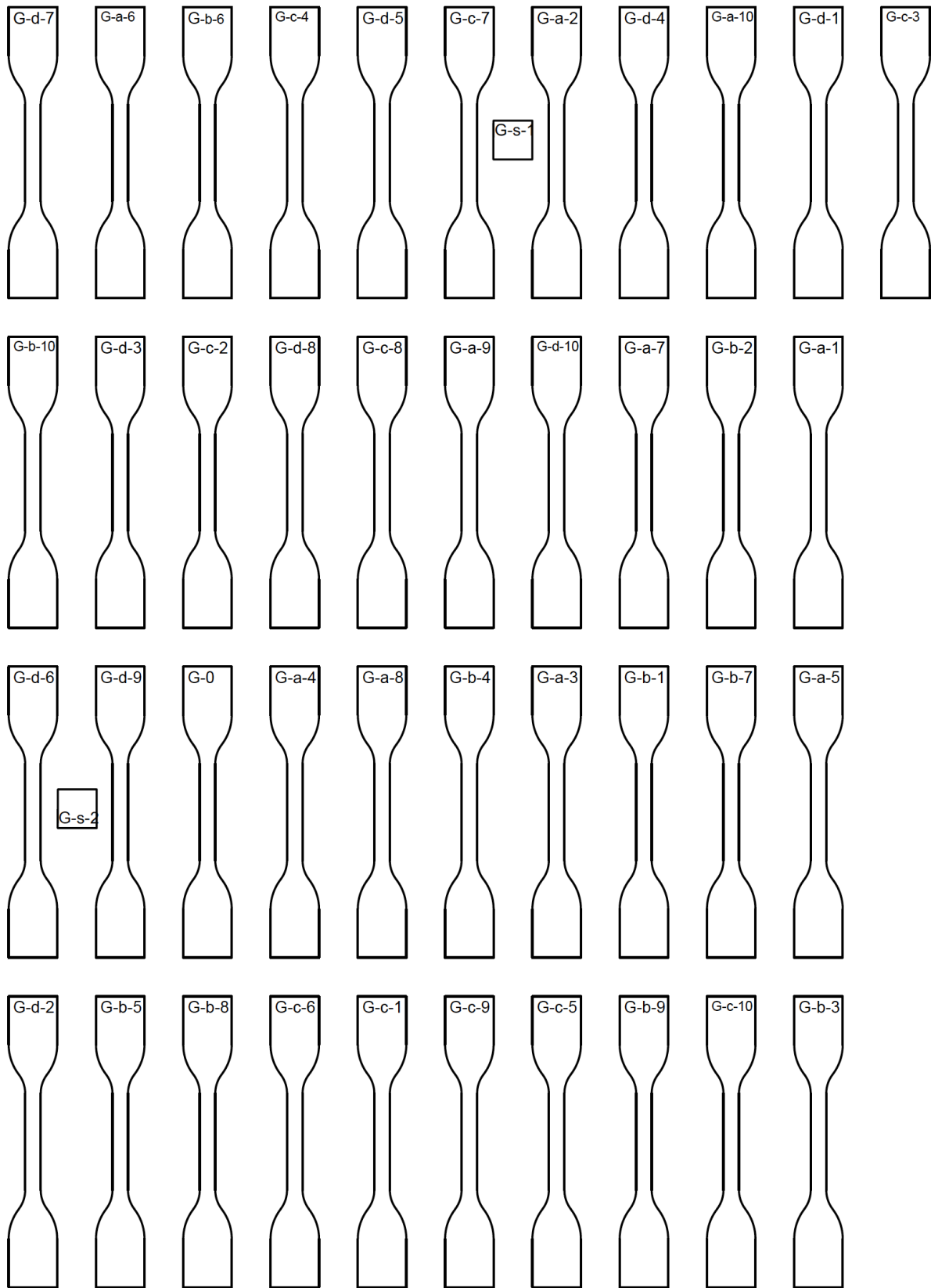
Figure A6. Distribution of the specimens on film F

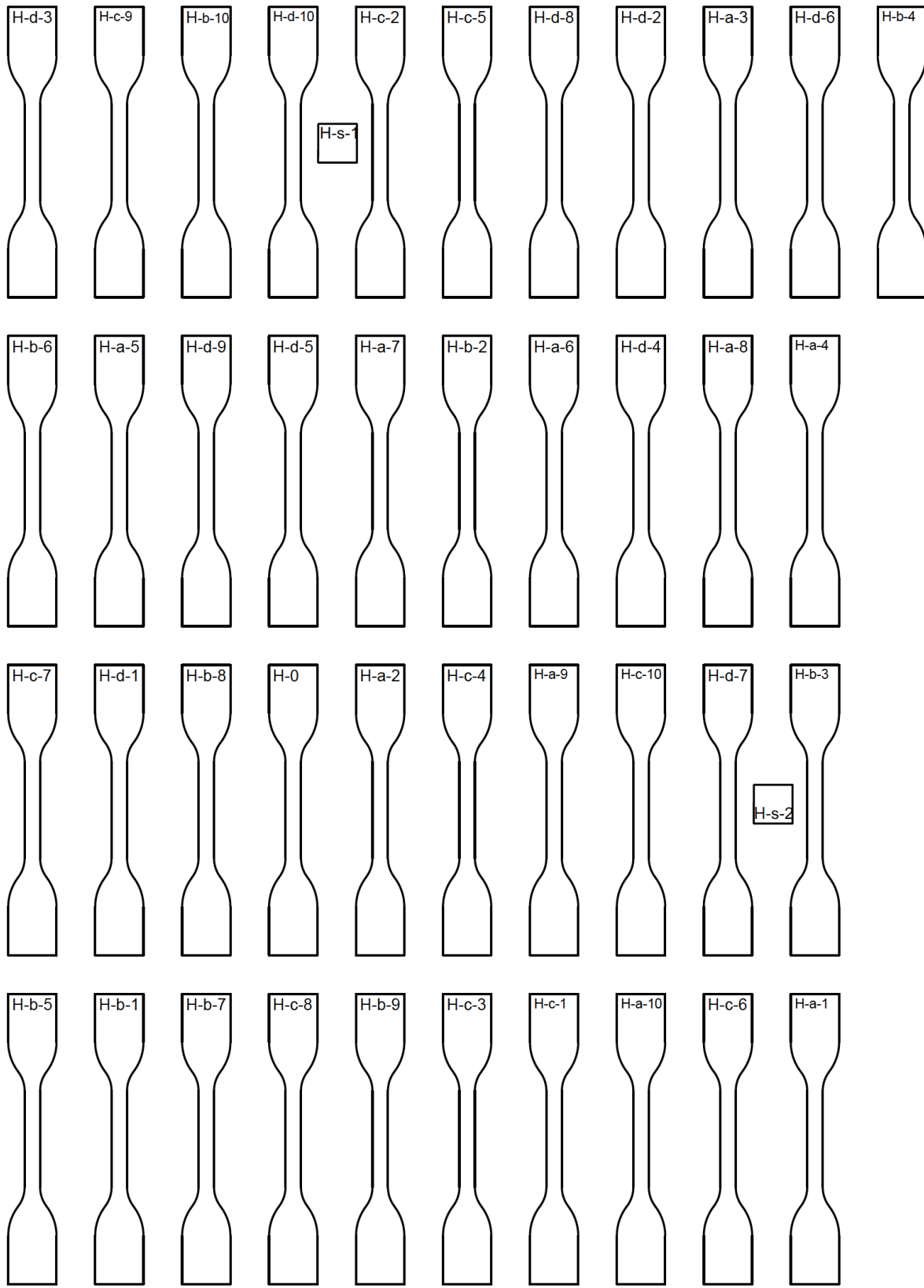Figure A7. Distribution of the specimens on film G

Figure A8. Distribution of the specimens on film H

A2. Accelerated thermal aging program

The convection oven has two shelves (Fig. A9); each shelf can hold 40 specimens. The temperature distribution in the oven was assessed using 8 thermocouples distributed throughout the oven[8] (Fig. A10) The measurement was done at the following temperatures: 50 °C, 100 °C, 150 °C, 200 °C, 250 °C and 300 °C. The measured temperatures are listed in Table A1.
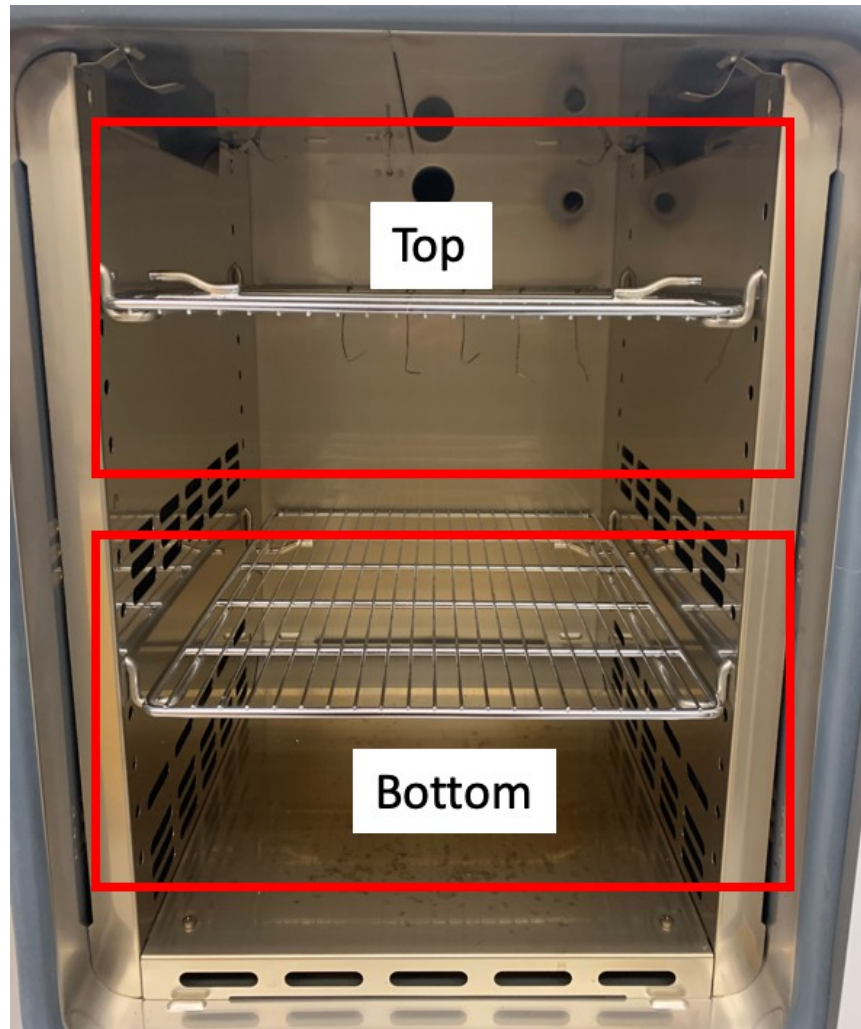

Figure A9. Convection oven used for the thermal aging of the PEI specimens

---

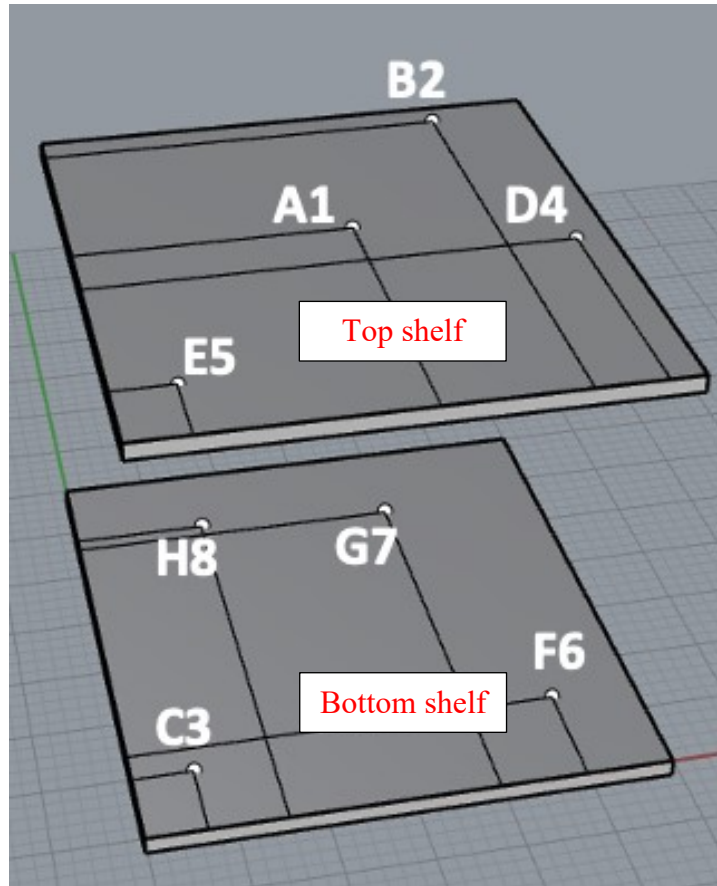[8] These measurements were performed by Research Assistant Lelin Zheng.

Figure A10. Distribution of the eight thermocouples on top and bottom shelf of the oven

An single factor ANOVA analysis was performed on the temperature data of the eight thermocouples at each oven set temperature (50 °C, 100 °C, 150 °C, 200 °C , 250 °C, and 300 °C). It shows that there is no significant difference in temperature between the different locations in the oven (p = 0.99, Total sample size N = 48). Table A1 also provides the average value of the temperatures recorded by the eight thermocouples. As there is a difference between the average temperature by the thermocouples and the set value in the oven, the correction was made to compensate for the difference between the oven set temperature and the temperature experienced by the specimens in the oven.

Table A1. Temperature data from the 8 thermocouples in the oven

Oven set temperature (°C)	50	100	150	200	250	300
Thermocouple 1	51.9	97.9	144.8	191.2	240.3	288.6
Thermocouple 2	50.9	91.3	142.8	188.9	239.6	286.7
Thermocouple 3	50.5	97.1	144.0	188.9	238.3	287.3
Thermocouple 4	51.9	96.2	141.8	186.4	232.8	265.3
Thermocouple 5	50.6	97.8	146.7	191.5	238.3	287.7
Thermocouple 6	50.3	97.0	143.1	188.6	233.8	280.2
Thermocouple 7	50.7	96.9	143.4	191.2	240.9	291.6
Thermocouple 8	51.6	98.5	146.1	193.4	243.0	293.0
Average temperature °C (thermocouple)	51.1 ± 0.6	96.5 ± 0.7	144.1 ±1.6	190 ±2	238 ±3	285±8

In addition, the temperature was recorded for 15 min after the door of the oven was opened and closed to simulate the operation associated with specimen collection (Fig. A11). A temperature drop was observed when the oven door was opened. But the temperature came back rapidly to the set value after closing the door. This opening and closing of the door when collecting the specimens is not expected to affect the aging of the specimens in the oven, especially since great care is taken in minimizing the time the door is left opened during the collection operation.
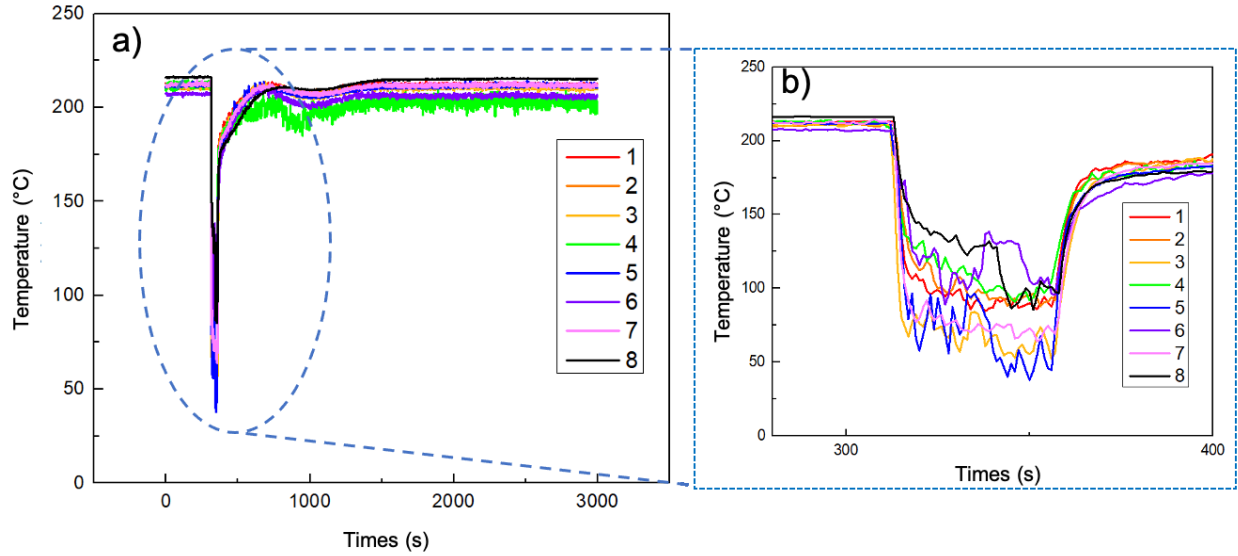
Figure A11. Variation in the temperature over time during the opening and closing of the oven door. The graph in b) provides a closeup view on the opening and closing event. The numbers in the legend correspond to the eight thermocouples.

In order to minimize any effect of temperature differences inside the oven, the specimens were positioned so that the replicates for each condition are distributed over the oven. This distribution is illustrated in Fig. A12 and Table A2. A special attention was also taken to maintain a certain distance between the specimens and with the oven walls. Tables A3 to A5 show the specimen codes for the different temperature and time conditions: the specimens were exposed at 190 °C for up to 12 weeks, at 200 °C for up to 16 weeks, and at 210 °C for up to 8 weeks.

Table A2. Distribution of the specimens in the convection oven. Samples shown in the grey area correspond to the top shelf while samples shown in the white area correspond to the bottom of the oven.

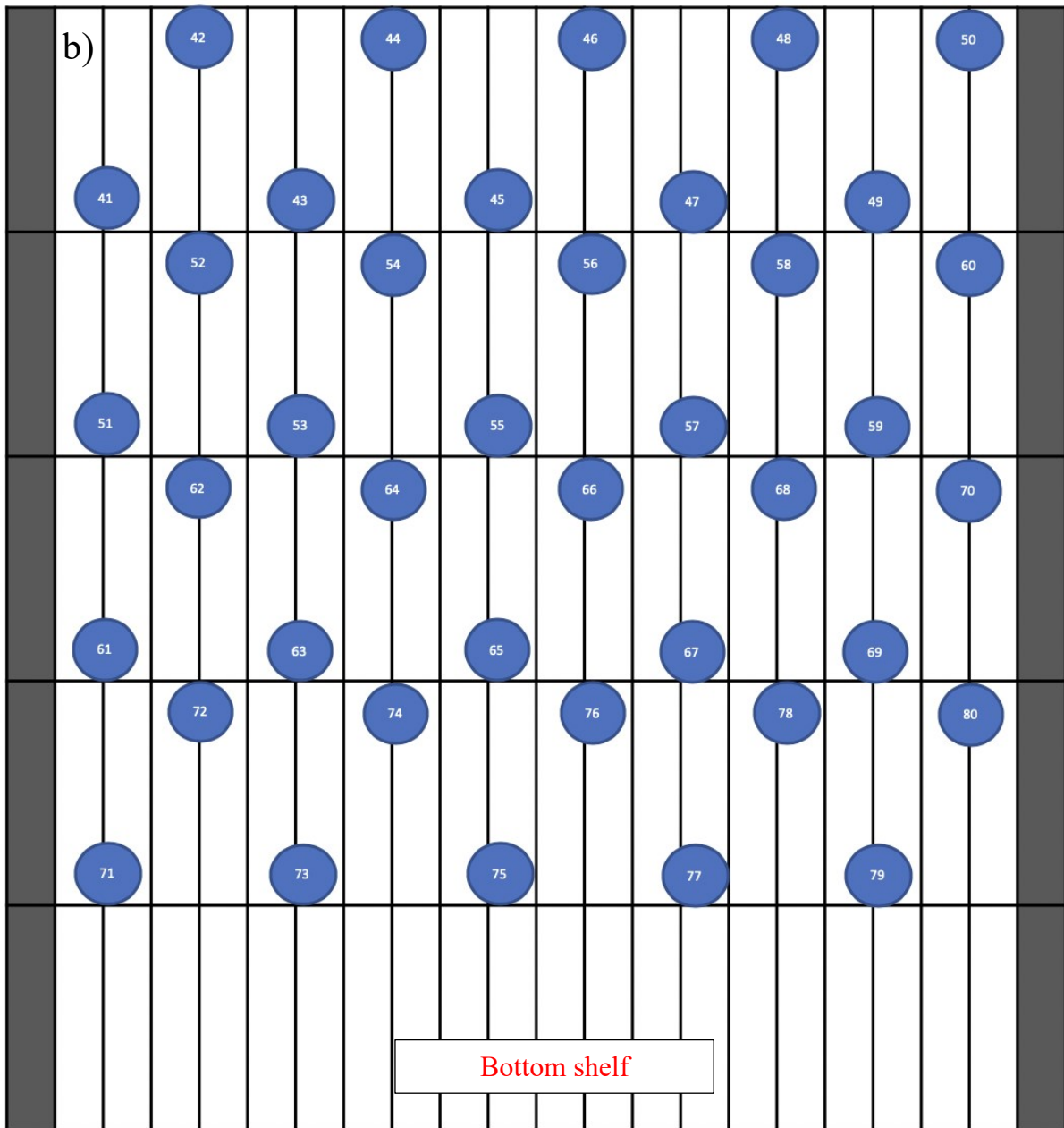| Sample # / Film #	(a-d)-1	(a-d)-2	(a-d)-3	(a-d)-4	(a-d)-5	(a-d)-6	(a-d)-7	(a-d)-8	(a-d)-9	(a-d)-10
A	1	2	3	4	5	6	7	8	9	10
B	13	16	12	20	17	14	11	15	18	19
C	22	27	26	23	30	28	29	24	25	21
D	36	33	37	31	32	40	34	39	38	35
E	48	45	43	44	49	42	47	41	50	46
F	54	58	55	59	51	57	52	53	56	60
G	69	61	70	65	68	64	66	67	63	62
H	80	79	78	77	76	75	74	73	72	71
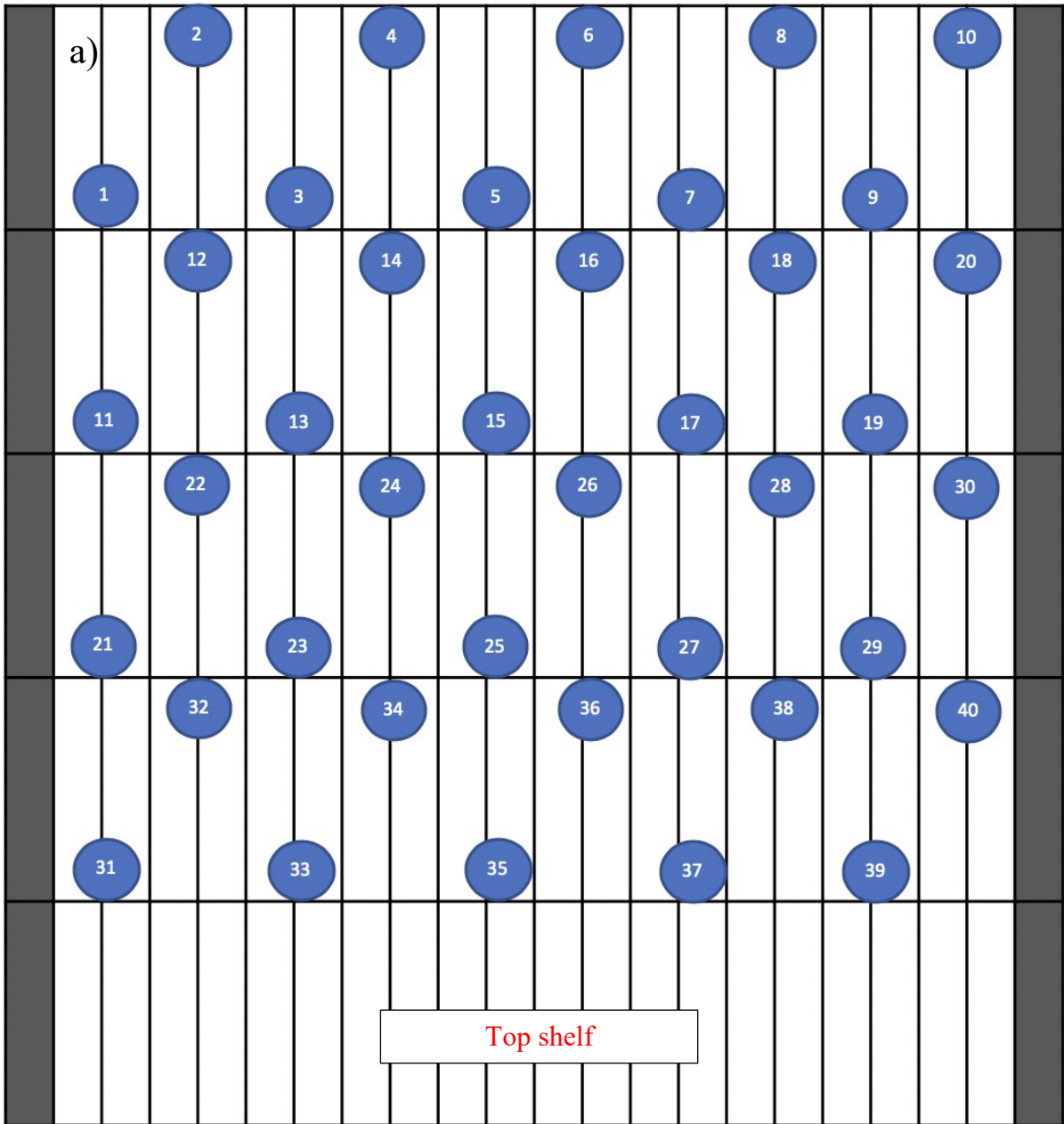
Figure A12. Specimen distribution a) on the top and b) bottom shelves of the oven

Table A3 Identification of the specimens subjected to thermal aging at 190 ℃.

Aging time (week) / Specimen	1	2	3	4	5	6	8	10	12
(A-H)-a-1	■								
(A-H)-a-2	■	■							
(A-H)-a-3	■	■	■						
(A-H)-a-4	■	■	■	■					
(A-H)-a-5	■	■	■	■	■				
(A-H)-a-6	■	■	■	■	■	■			
(A-H)-a-7	■	■	■	■	■	■	■		
(A-H)-a-8	■	■	■	■	■	■	■	■	■

Table A4 Identification of the specimens subjected to thermal aging at 200 ℃.

Aging time (week) / Specimen	2	4	6	8	10	12	13	14	15	16
(A-H)-b-1	■									
(A-H)-b-2	■	■								
(A-H)-b-3	■	■	■							
(A-H)-b-4	■	■	■	■						
(A-H)-b-5	■	■	■	■	■					
(A-H)-b-6	■	■	■	■	■	■				
(A-H)-b-7	■	■	■	■	■	■	■			
(A-H)-b-8	■	■	■	■	■	■	■	■		
(A-H)-b-9	■	■	■	■	■	■	■	■	■	
(A-H)-b-10	■	■	■	■	■	■	■	■	■	■

Table A5 Identification of the specimens subjected to thermal aging at 210 ℃.

Aging time(week) / Specimen	1	2	3	4	5	6	7	8
(A-H)-c-1	▨							
(A-H)-c-2	▨	▨						
(A-H)-c-3	▨	▨	▨					
(A-H)-c-4	▨	▨	▨	▨				
(A-H)-c-5	▨	▨	▨	▨	▨			
(A-H)-c-6	▨	▨	▨	▨	▨	▨		
(A-H)-c-7	▨	▨	▨	▨	▨	▨	▨	
(A-H)-c-8	▨	▨	▨	▨	▨	▨	▨	▨

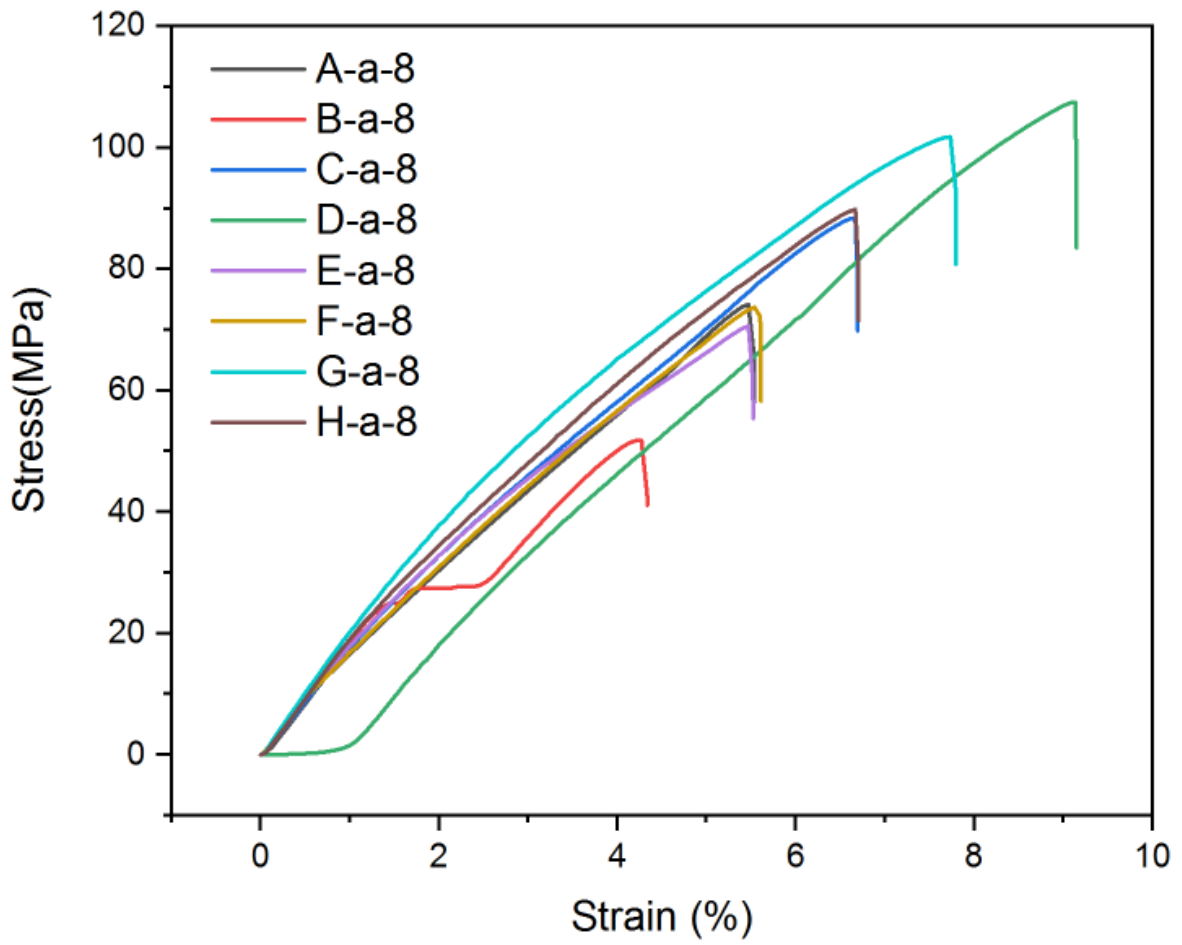**A3. The raw data of stress-strain curve in aged PEI specimen**

Figure A13. Stress-strain curve of 210 °C for 8 weeks of aged eight PEI specimens

A4. Statistical analysis (one-way ANOVA)

After evaluating statistical significance, the post-hoc analysis was performed to verify which condition showed statistically different from others. Tukey HSD (Honestly significant difference) test was used as a post-hoc analysis because it has been used to figure out which group is different from other groups. During Tukey analysis, critical q-value was required to determine statistical significance among groups, and was obtained from studentized range q table [262]. The HSD is larger or smaller than critical q-value, the difference of the means is significant or not significant at the 0.05 level. The q-value is calculated by following equation A-1.

$$HSD = q\sqrt{\frac{MS_w}{n}} \qquad\qquad A-1$$

where q is the critical q-value from studentized range table, MS_w is mean square within, and n is number in each group. If mean difference between two groups is larger than HSD value, two groups are statically different from each other.

A4.1 ANOVA analysis for changing in glass transition temperature

From a single factor ANOVA analysis, p-value of 1.7×10^{-7} was obtained (n=20), and 95% confidence interval is 217 to 220. The post-hoc analysis by Tukey's HSD test showed that the glass transition temperature was changed statistically significant during the thermal aging (Table A6). This analysis shows an agreement of mean-value comparision in the statement of section 5.3.1. At the beginning of thermal aging, crosslinking reaction happened in PEI network, which is also shown in UTS changes (Fig. 5.12). The glass transition temperature may be affected by crosslinking reaction due to restricted chain mobility. Since chain scission reaction becomes dominant in further aging, the glass transition temperature starts to decrease from 4 weels of aging, which is also agreed decreasing UTS in Fig 5.12.

Table A6 Post-hoc analysis for changing of glass transition temperature during thermal aging. The critical q value is 4.046.

Comparing condition	Mean difference	HSD value	Significance
4 weeks vs. 0 week	5.73		Yes
4 weeks vs. 0 week	1.90		Yes
4 weeks vs. 4 weeks	3.83		Yes
8 weeks vs. 0 week	0.39	1.83	No
8 weeks vs. 4 weeks	6.12		Yes
8 weeks vs. 4 weeks	2.29		Yes

A4.2 ANOVA analysis of various weight loss temperatures

Table A7 shows that the p-value of various weight loss temperatures and 95 % confidence intervals of each temperature. We observe that $T_{5\%}$ and $T_{initial}$ shows statistically significant changing during the thermal aging. The post-hoc analysis of $T_{5\%}$ and $T_{initial}$ explains only between 0 week vs. 8 weeks has significantly difference (Table A8 and A9). In other words, $T_{5\%}$ and $T_{initial}$ shows statistically insignificant upto 6 weeks of aging (1008 h) even though their mean-values has changed during thermal aging, and exhibits statistically difference in 8 weeks of aging (1344 h). On the other hand, $T_{2nd\ max\ rate}$ do not show statistically difference even though $T_{2nd\ max\ rate}$ has changed, and $T_{1st\ max\ rate}$ has no changes during thermal aging.

Table A7 The p-value of various weight loss temperatures and 95 % confidence intervals

Parameter \ Condition	$T_{5\%}$ (°C)	$T_{initial}$ (°C)	$T_{1st\ max\ rate}$ (°C)	$T_{2nd\ max\ rate}$ (°C)
p-value	0.02	0.01	0.24	0.4
95 % confidence interval	452 - 472	542 - 546	561 - 564	668 - 688

Table A8 Post-hoc analysis for $T_{initial}$ changes during thermal aging1. The critical q value is 4.529.

Comparing condition	Mean difference	HSD value	Significance
4 weeks vs. 0 week	19.62		No
6 weeks vs. 0 week	13.72		No
6 weeks vs. 4 weeks	5.90		No
8 weeks vs. 0 week	37.84	29.27	Yes
8 weeks vs. 4 weeks	18.22		No
8 weeks vs. 6 weeks	24.12		No

Table A9 Post-hoc analysis for $T_{5\%}$ changes during thermal aging1. The critical q value is 4.529.

Comparing condition	Mean difference	HSD value	Significance
4 weeks vs. 0 week	2.34		No
6 weeks vs. 0 week	3.66		No
6 weeks vs. 4 weeks	1.32		No
8 weeks vs. 0 week	7.47	29.26531	Yes
8 weeks vs. 4 weeks	5.13		No
8 weeks vs. 6 weeks	3.81		No

A4.3 ANOVA analysis of FTIR peak area changes

From figure 5.16, the 1215 cm^{-1} peak area changed was shown. The one-way ANOVA analysis showed p-value of 2.88×10^{-5} (n=24) and 95% confidence interval is 1.25 to 1.27. Based on p-value, among five conditions (unaged, 2, 4, 6, 8 weeks of aged) showed statistically significant. The post-hoc analysis shows that which group is different from other groups. In table A12, significance between five conditions was shown. The peak area of 8 weeks aged PEI showed statistically different from 0, 2, and 4 wks, but has no statistically different from the peak area of 6 weeks aged PEI. Except the peak area comparision between 6 week and 2 week aging, all other comparision between conditions(2 weeks vs. 0 week, 4 weeks vs. 0 weeks, 4 weeks vs. 2 weeks, 6 weeks vs. 0 weeks, 6weeks vs. 4 weeks, 8 weeks vs. 6 weeks) do not have statistical significance.

This represents that the C-N stretching in pthalimide ring groups do not changed during 6 weeks of aging, and starts to break their bonds from 6 weeks of aging due to chain-scission.

Table A10 Post-hoc analysis for peak area changing of 1215 cm^{-1}. The critical q value is 4.066.

Comparing condition	Mean difference	HSD value	Significance
2 weeks vs. 0 week	0.02		No
4 weeks vs. 0 week	0.01		No
4 weeks vs. 2 weeks	0.03		No
6 weeks vs. 0 week	0.03		No
6 weeks vs. 2 weeks	0.05		Yes
6 weeks vs. 4 weeks	0.03	0.04	No
8 weeks vs. 0 week	0.05		Yes
8 weeks vs. 2 weeks	0.07		Yes
8 weeks vs. 4 weeks	0.04		Yes
8 weeks vs. 6 weeks	0.02		No

The peak area changes in 1777 cm-1 has p-value of 3.3×10^{-6} for unaged vs. aged PEI specimens (n=40), and the 95% confidence interval is 3.1 to 3.14. The p-value indicate that the peak area changes during thermal aging shows statistically significant. In order to determine statistically significance among aging, calculated mean difference value between two conditions must be larger than HSD value from post-hoc analysis (Table A13). The peak area changes between 0 week vs. all aging conditions and the peak area changes between 6 weeks vs. 8 weeks showed shows statistically significant. However, the peak area changes between 2 weeks vs. 4 weeks and 4 weeks and 6 weeks do not show statistically significance. Therefore, the peak area changes in carbonyl group shows that carbonyl group has generagted until 2 weeks of aging due to thermo-oxidative reaction, no activities of consumption and generating of carbonyl group until 6 weeks of aging, and consumption of carbonyl group after 6 weeks of aging due to chain scission

reaction.

Table A11 Post-hoc analysis for peak area changing of 1777 cm^{-1}. The critical q value is 4.066.

Comparing conditions	Mean difference	HSD value	Significance
2 weeks vs. 0 week	0.09		Yes
4 weeks vs. 0 week	0.07		Yes
4 weeks vs. 2 weeks	0.02		No
6 weeks vs. 0 week	0.20		Yes
6 weeks vs. 2 weeks	0.03		No
6 weeks vs. 4 weeks	0.04		No
8 weeks vs. 0 week	0.06	0.05	Yes
8 weeks vs. 2 weeks	0.03		No
8 weeks vs. 4 weeks	0.01		No
8 weeks vs. 6 weeks	0.06		Yes

The peak area of isopropylidene group has p-value of 1.59×10^{-5} (n=40), the 95% confidence interval is 1.15 to 1.17. The obtained p-value showed that overall peak area of isopropylidene group was steady decreased. However, the statistical significance of peak area changes was only shown between 0 ~ 4 weeks of aging vs. 6 ~ 8 weeks of aging (Table A14). This explains that the peak area of isopropylidene group may starts break its structure after 4 weeks of aging, and no activity of chain scission until 8 weeks of aging.

Table A12 Post-hoc analysis for peak area changing of 1172 cm^{-1}. The critical q value is 4.066.

Comparing conditions	Mean difference	HSD value	Significance
2 weeks vs. 0 week	0.01		No
4 weeks vs. 0 week	0.03		No
4 weeks vs. 2 weeks	0.02		No
6 weeks vs. 0 week	0.05		Yes
6 weeks vs. 2 weeks	0.04	0.04	Yes
6 weeks vs. 4 weeks	0.03		No
8 weeks vs. 0 week	0.06		Yes
8 weeks vs. 2 weeks	0.05		Yes
8 weeks vs. 4 weeks	0.03		No
8 weeks vs. 6 weeks	0.01		No

A4.4 ANOVA analysis of washing stability of PEI-LIG sensor

Excluding damaged sensor provided p-value of 3.0×10^{-4} (n=24) and 95% confidence interval is 1.57 to 2.13). The post-hoc analysis in Table A13 shows that the resistance of LIG layer has not statistically changed between 0 to 3 washings, and 3 washings vs. 5 to10 washings showed significantly difference. This represents that the LIG layer may have damaged between 3 and 5 washings, therefore, the current washing stability of PEI-LIG senor is maximum 3 washings. In order to improve washing stability of PEI-LIG sensor, the quality of LIG layer has to be optimized by changing laser-scribing setting and better encapsulation method with modified sensor design.

Table A13 Post-hoc analysis for washing stability of PEI-LIG sensor. The critical q value is 4.253.

Comparing conditions	Mean difference	HSD value	Significance
1 washing 0 washing	0.38		No
3 washings 0 washing	0.34		No
3 washings 1 washing	0.05		No
5 washings 0 washing	1.04		Yes
5 washings 1 washing	1.42		Yes
5 washings 3 washings	1.38	0.87	Yes
10 washings 0 washing	0.65		No
10 washings 1 washing	1.03		Yes
10 washings 3 washings	0.99		Yes
10 washings 5 washings	0.39		No